

# Multiwavelength Observations of TeV Blazars in 2006-07

John Toner B.Sc.

Thesis submitted to the  
National University of Ireland, Galway  
for the award of Ph.D. in the  
School of Physics

Supervisors:

Dr. Mark Lang

Dr. Gary Gillanders

August 2008



# Contents

<b>1</b>	<b>Introduction</b>	<b>1</b>
1.1	VERITAS Collaboration . . . . .	3
1.2	Research Contribution . . . . .	6
1.3	Thesis Overview . . . . .	9
<b>2</b>	<b>Review of the Field</b>	<b>11</b>
2.1	Introduction and History . . . . .	11
2.2	The Physics of $\gamma$ -rays . . . . .	13
2.2.1	Production Mechanisms . . . . .	13
2.2.2	Interaction of $\gamma$ -Rays with Matter . . . . .	23
2.3	High Energy Astrophysics . . . . .	35
2.3.1	$\gamma$ -ray Astrophysics Overview . . . . .	35
2.4	TeV $\gamma$ -ray Sources . . . . .	43
2.4.1	Galactic Sources . . . . .	45
2.4.2	Extragalactic Sources . . . . .	57
2.4.3	Other Potential Sources . . . . .	61
<b>3</b>	<b>The Science of Active Galactic Nuclei</b>	<b>63</b>
3.1	Introduction . . . . .	63
3.2	Classification of AGN . . . . .	65
3.2.1	Blazars . . . . .	69
3.2.2	The Blazar Sequence . . . . .	74
3.2.3	Unification Scheme . . . . .	74
3.3	The Relativistic Jet . . . . .	76

## CONTENTS

	3.3.1 Relativistic Beaming . . . . .	77
	3.3.2 Superluminal Motion . . . . .	78
	3.3.3 Doppler Boosting . . . . .	80
3.4	Blazar Emission Models . . . . .	81
	3.4.1 Synchrotron Self Compton (SSC) . . . . .	82
	3.4.2 External Compton (EC) . . . . .	87
	3.4.3 Hadronic Models . . . . .	90
3.5	Multiwavelength Blazar Observations . . . . .	93
	3.5.1 Markarian 421 . . . . .	94
	3.5.2 Markarian 501 . . . . .	99
	3.5.3 1ES 2344+514 . . . . .	102
	3.5.4 H 1426+428 . . . . .	104
	3.5.5 1ES 1959+650 . . . . .	105
<b>4</b>	<b>The Whipple 10 m Telescope and Analysis</b>	<b>109</b>
4.1	Telescope Hardware . . . . .	109
	4.1.1 The Reflector . . . . .	109
	4.1.2 Camera . . . . .	115
4.2	Data Acquisition . . . . .	119
	4.2.1 Amplifiers . . . . .	120
	4.2.2 Current Monitor . . . . .	121
	4.2.3 Trigger Electronics . . . . .	121
	4.2.4 Signal-Recording Electronics . . . . .	122
	4.2.5 Timing Electronics . . . . .	123
4.3	Observation Strategies . . . . .	124
	4.3.1 ON-OFF Mode . . . . .	124
	4.3.2 TRACKING Mode . . . . .	125
4.4	Calibration and Analysis . . . . .	126
	4.4.1 Data Preparation . . . . .	126
	4.4.2 Parameterisation . . . . .	130
4.5	Supercuts Analysis . . . . .	133
	4.5.1 Pre-selection Cuts . . . . .	135

## CONTENTS

---

4.5.2	Shape and Orientation Cuts . . . . .	138
4.5.3	Length/Size Cut . . . . .	140
4.6	$\gamma$ -ray Rate and Significance Calculation . . . . .	140
4.6.1	ON-OFF Mode Calculation . . . . .	141
4.6.2	TRACKING Mode Calculation . . . . .	142
4.6.3	Spectral Analysis . . . . .	144
4.7	Post-analysis Corrections . . . . .	145
4.7.1	Zenith Angle Correction . . . . .	145
4.7.2	Throughput Correction . . . . .	147
<b>5</b>	<b>Optimisation of Supercuts &amp; <math>\gamma</math>-Ray Analysis Results</b>	<b>157</b>
5.1	Re-optimisation of Supercuts parameters . . . . .	157
5.1.1	Optimisation Methodologies . . . . .	158
5.1.2	Single Parameter Variation . . . . .	159
5.1.3	Cumulative Significance Method . . . . .	162
5.1.4	Test of Re-optimised Supercuts . . . . .	166
5.2	Tracking Ratio Calculation . . . . .	168
5.2.1	Data Selection . . . . .	169
5.2.2	Tracking Ratio Testing . . . . .	170
5.3	Analysis of Blazar Data . . . . .	172
<b>6</b>	<b>Optical Photometry</b>	<b>185</b>
6.1	Optical Monitoring Programme . . . . .	186
6.2	The FLWO 1.2 m Telescope . . . . .	188
6.3	Data Reduction . . . . .	189
6.4	Optical Photometry . . . . .	192
6.5	Error Estimation . . . . .	194
6.6	Variability . . . . .	196
6.7	Results . . . . .	196
6.7.1	Markarian 421 . . . . .	197
6.7.2	Markarian 501 . . . . .	201
6.7.3	H 1426+428 . . . . .	205

## CONTENTS

---

6.7.4	1ES 1959+650 . . . . .	209
6.7.5	1ES 2344+514 . . . . .	211
6.8	Photometric Normalisation . . . . .	215
<b>7</b>	<b>Variability &amp; Correlation</b>	<b>221</b>
7.1	Power Spectral Density Characteristics . . . . .	222
7.2	Variability Studies . . . . .	224
7.2.1	Fractional RMS Variability Amplitude . . . . .	224
7.2.2	Point-to-point Fractional RMS Variability Amplitude	225
7.2.3	Results . . . . .	226
7.3	The Structure Function . . . . .	230
7.3.1	Structure Function Calculation . . . . .	230
7.3.2	Structure Function Simulation and Fitting . . . . .	239
7.4	Correlation Analysis . . . . .	247
7.4.1	Flux-Flux Correlation . . . . .	248
7.4.2	Discrete Correlation Function . . . . .	248
7.4.3	DCF Limitations and Chance Probability . . . . .	252
7.4.4	Results . . . . .	257
<b>8</b>	<b>Interpretation and Conclusions</b>	<b>265</b>
8.1	Summary . . . . .	265
8.2	Discussion . . . . .	266
8.2.1	TeV $\gamma$ -ray Analysis . . . . .	266
8.2.2	Optical Data Analysis . . . . .	268
8.2.3	Correlation . . . . .	269
8.3	Interpretation and Conclusions . . . . .	270
8.4	Future Studies . . . . .	272
8.5	The Future of $\gamma$ -ray Astronomy . . . . .	274
<b>A</b>	<b>Data Files</b>	<b>279</b>

# Acknowledgements

I have been almost exclusively surrounded by enthusiastic and supportive people over the years. To all of you, I offer my thanks. I wish, however, to explicitly thank a number of people who have been instrumental in enabling me to produce this thesis.

First and foremost, I have enjoyed amazing supervision from Dr. Mark Lang and Dr. Gary Gillanders at NUI Galway. Without their guidance, I would never have finished this thesis. I am eternally grateful for their patience in dealing with me over the years. I would also like to thank the Science Foundation of Ireland (SFI) and the Harvard-Smithsonian Center for Astrophysics who generously provided financial support during my postgraduate studies.

My graduate student colleagues at NUI Galway were often a well of knowledge during my research. In particular, Gary Kenny, Michael Connolly, Nina Hanzlikova and Andrea Cesarini (from the VERITAS group), Don, Brendan, Caoilfhionn, Kieran, Alan, Leon, James and John, Patrick Carolan, Patrick Collins and Robert all deserve thanks for the help and the tea breaks! Arlene, thanks for friendship and good times. The staff of NUI Galway School of Physics also deserve thanks. In particular, I'd like to thank Tess, Conor and P.J. for help at every turn.

I owe a special debt of gratitude to Prof. Trevor Weekes for affording me the opportunity to spend a year in Arizona, as well as other shorter trips, over the course of my Ph.D. studies. It has always been a wonder to me just how approachable and enthusiastic Trevor is and if I have

---

picked up even a small semblance of that spirit while in his presence, I know I am a better man for it.

During my trips to Arizona, I was lucky enough to befriend and work with some incredible people. I must thank John Kildea for teaching me... well... pretty much everything I know about analysis! Jeremy, for consistently fixing everything that I broke. Oh, and teaching me Perl! Donna is the karaoke queen. To Ken Gibbs, Gene, Karen and Ginnee for all the help at basecamp, thank you.

I have gained much from the contact I have had with people throughout the VERITAS Collaboration. I would like to thank Peter Cogan, Deirdre Horan, Tulun Ergin, Glenn Sembroski, Mary Kertzman, Scott Hughes, Jim Buckley, Kuen (Vicky) Lee, Steve Fegan, Conor Dowdall and Jamie Holder for all of their helpful and insightful input. The Irish contingent, of course, also deserve special mention. In particular, I'd like to thank Victor Acciari for good company at the telescopes (and authoring all our papers!) as well as John E Ward for a number of crazy, memorable nights and lots of good music and laughs. Yes hoss!

I have to give a special mention to Andy Smith for everything, from helping me move to Arizona, to Dunkin Donuts at 2:30am, to introducing me to "Arnold Palmers" and that great CD... The list is endless. I wouldn't even know where to begin. All I can say is thanks for being such a good friend.

I have been fortunate to have had teachers who helped to inspire a love for scientific endeavour. In particular, I'd like to thank Mr. Farragher, Mr. McGonagle, Mr. Logue and Mrs. McGeady for their development and encouragement of my interest in Science and Mathematics. A special thanks to Mr. McCole for his words of wisdom.

I would like to thank my close friends, Eileen Byrne (and Jack!), Niamh Lardner, Patricia Martyn, Karina and Will. I would also like to say a special thanks to Edel De Paor. How you guys put up with me is a complete mystery. I'd like to thank Annaghdown GAA for being

---

a welcome distraction at times! Thanks to the Gibbons family for all of their help and kindness. A special thanks has to go to Eamon, who proofread my thesis. How he did it, I'll never know!

To my Karyn, who has been tremendously understanding, loyal and patient. You never allowed me to think twice about spending a year abroad, even though it meant us being apart, and you have bent over backwards to accommodate me in finishing this thesis. You truly are the most amazing girlfriend and I am so lucky to have met you again after being my childhood sweetheart. I love you.

Where do I even begin to thank my family? My brother Aidan and sisters Elaine, Breege and Maeve have done so much for me over the years. I owe them more than I can ever repay. Gerry's interest and discussions have been a source of wonder to me. You guys are amazing and I don't know where I'd be without you.

Simply put, words cannot describe the level of support, encouragement or motivation I have received from my parents, Anne and Patrick. More than anyone else, they have given me the values that have enabled me to realise my lofty goals. Nobody can have any idea of the strength I have gained from my parents and I can only be proud of who I am, and the things I have done, because I am a Toner.

*We set sail on this new sea  
because there is knowledge to be gained.*

– John F. Kennedy

---

---

To my family.

---

## Abstract

This thesis describes an investigation of the very high energy  $\gamma$ -ray emission of five northern hemisphere TeV blazars: Markarian 421, Markarian 501, 1ES 1959+650, 1ES 2344+514, H 1426+428. A rich  $\gamma$ -ray data set, obtained from the Whipple 10 m imaging atmospheric Cherenkov telescope during the 2006 - 2007 observing season, was analysed.

Parameter cuts, used in the analysis of the 2006 - 2007  $\gamma$ -ray dataset, were optimised by an extensive search of Hillas parameter space. Very high energy  $\gamma$ -ray emission was detected from Markarian 421 with a statistical significance of  $20.4\sigma$  at a mean flux of 31% of the Crab Nebula flux (in the same energy band). Variability was evident in the  $\gamma$ -ray light curve. Very high energy  $\gamma$ -ray emission was also detected from Markarian 501 at a statistical significance of  $7.7\sigma$ . The mean  $\gamma$ -ray flux was found to be 10% of the Crab Nebula flux in the same energy band. Markarian 501 was found to exhibit variability in the  $\gamma$ -ray band during the observing campaign. The  $\gamma$ -ray variability was characterised in the cases of Markarian 421 and Markarian 501. Very high energy  $\gamma$ -ray emission was not detected from 1ES 1959+650, 1ES 2344+514 or H 1426+428. Flux upper limits are presented for these sources.

Optical ( $r'$  band) data obtained from the Fred Lawrence Whipple 1.2m optical telescope during 2007 were reduced and analysed. These data were collected as part of a long-term multiwavelength blazar observing campaign. Differential photometry was carried out on the optical data set and variability was exhibited by all five blazars during the campaign. The optical variability was characterised in all cases. The sources were found to be more variable in the  $\gamma$ -ray band than in the optical band.

---

A discrete correlation function analysis was carried out to look for correlation between emission in the  $\gamma$ -ray band and the optical band. Statistical analysis of the discrete correlation analysis results was performed. There was no evidence for a correlation. The implications of this are discussed in terms of a Synchrotron Self-Compton emission model.

---

---

# Chapter 1

## Introduction

Recent developments in the field of Very High Energy (VHE) astrophysics have led to a dramatic increase in the number of detected sources of cosmic very high energy  $\gamma$ -rays (see Figure 1.1). A relatively new field of study,  $\gamma$ -ray astronomy has thus far given us an unprecedented view of some of the most violent and energetic phenomena in the Universe. While  $\gamma$ -ray astronomy will probably never command the same attention as optical astronomy, it has become a discipline with which all astronomers should have some degree of familiarity.

VHE astronomy has its roots in humble beginnings: the serendipitous detection, by Victor Hess, of cosmic rays with a simple detector on board a balloon flight in the early part of the 20<sup>th</sup> century. A definitive explanation of the origin of cosmic rays, which continually bombard the earth, has been elusive since their discovery. Cosmic rays with different energies have slightly different physical properties. Up to energies of  $\sim 10^{14}$ eV these electrically charged particles are deflected by interstellar magnetic fields, effectively erasing all point-of-origin information. The search for the source of this abundant radiation has long been held as one of the driving forces behind the development of VHE  $\gamma$ -ray astronomy due to the fact that  $\gamma$ -rays, which are a by-product of cosmic ray production (by  $\pi^0$  decay or inverse Compton scattering), carry no charge and thus travel

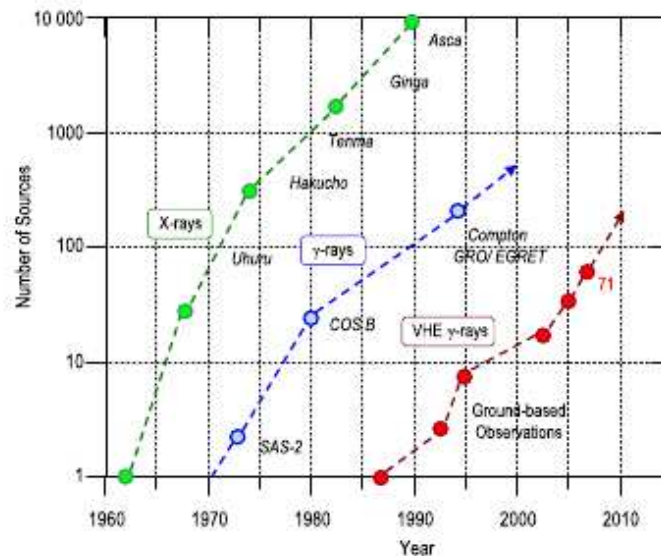


**Figure 1.1:** Comparison of the number of sources detected in the x-ray band, the high energy  $\gamma$ -ray band and the very high energy band against time. Figure taken from Hinton (2007).

to Earth from their site of production without deflection. It is thought that shock acceleration in the shells of supernova remnants is the source of cosmic rays at these energies.

Cosmic rays at energies  $> 10^{14}$ eV are not subject to as much deflection in magnetic fields and observations at the Pierre Auger Observatory in Argentina offer strong evidence that nearby active galactic nuclei may be the site of production of the highest energy cosmic rays (Abraham *et al.*, 2007, 2008).

Active galactic nuclei have been one of the cornerstones of  $\gamma$ -ray astronomy. Blazars – a type of active galactic nucleus – have attracted particular interest due to their variable and violent high-energy emission. The EGRET telescope, on board NASA’s Compton Gamma-Ray Observatory satellite, detected some 70 blazars (Hartman *et al.*, 1999). Spurred on by these discoveries, ground-based VHE telescopes detected the first TeV blazar, Markarian 421, in 1992 (Punch *et al.*, 1992). Cur-

## 1.1. VERITAS Collaboration

---

rently, there are 18 catalogued TeV blazars which been discovered since 1992 (see Tevcat catalogue: <http://tevcat.uchicago.edu/>).

### 1.1 VERITAS Collaboration

The Whipple 10 m reflector was built at the Fred Lawrence Whipple Observatory on Mt. Hopkins in southern Arizona, USA in 1968. It was the first large purpose-built atmospheric Cherenkov telescope for  $\gamma$ -ray astronomy (Fazio *et al.*, 1968). The telescope was operated and maintained by a group of international collaborating institutions, known collectively as the Whipple Collaboration. In 1998, the Whipple Collaboration expanded to become the VERITAS Collaboration (see Table 1.1). The VERITAS Collaboration now continues to operate the Whipple 10 m telescope, as well as the VERITAS array, which is an array of four 12 m imaging atmospheric Cherenkov telescopes (see Figure 1.2) located at the base of Mt. Hopkins.

The Whipple 10 m telescope has been a pioneering instrument in the field of VHE  $\gamma$ -ray astronomy. Many of the hardware features and analysis techniques currently employed by atmospheric Cherenkov observatories around the world were developed for use on the Whipple 10 m telescope. It was the first atmospheric Cherenkov telescope to successfully utilise the imaging atmospheric Cherenkov technique, detecting VHE  $\gamma$ -ray emission from the Crab Nebula in 1989 (Weekes *et al.*, 1989). The first detection of an extragalactic source of VHE  $\gamma$ -rays (Markarian 421; Punch *et al.*, 1992) was made by the Whipple 10 m telescope. Altogether, it has been credited with the detection of five sources of VHE  $\gamma$ -rays; more than any ground-based instrument prior to the current generation of observatories.

In 2005, construction of the first telescope in the VERITAS array was completed and the observing program at the Whipple 10 m telescope was redefined to concentrate almost exclusively on monitoring blazars. Since

## 1.1. VERITAS Collaboration

---

Member	Country
Smithsonian Astrophysical Observatory	USA
Purdue University	USA
Iowa State University	USA
Washington University in St. Louis	USA
University of Chicago	USA
University of Utah	USA
University of California, Los Angeles	USA
McGill University	Canada
University College Dublin	Ireland
University of Leeds	United Kingdom
Adler Planetarium	USA
Argonne National Lab	USA
Barnard College	USA
DePauw University	USA
Grinnell College	USA
University of California, Santa Cruz	USA
University of Iowa	USA
University of Massachusetts	USA
Cork Institute of Technology	Ireland
Galway-Mayo Institute of Technology	Ireland
National University of Ireland, Galway	Ireland

**Table 1.1:** List of VERITAS collaboration member institutions. The top part of the table lists member institutions that were involved at the inception of the collaboration, while the bottom part of the table lists collaborative institutions that have joined the collaboration since it formed. Associate members are not listed here.

## 1.1. VERITAS Collaboration

---



**Figure 1.2:** The VERITAS array, located at the base of Mt. Hopkins, Arizona, USA.

then, this monitoring programme has provided long-term deep exposures of blazars as well as triggers for observations of blazars with more sensitive instruments, such as the VERITAS array, when a blazar's flux was observed to be above a certain threshold. This approach makes for a more efficient use of the limited observing time available to the VERITAS array ( $\sim 800$  hours a year).

The design of the VERITAS telescopes is broadly based on the design of the Whipple 10 m telescope. However, the VERITAS telescopes have a larger aperture and more sophisticated electronics systems. The stereoscopic technique (using multiple telescopes in unison) employed by the VERITAS array offers many advantages over the single-telescope technique employed by the Whipple 10 m telescope. Advantages include better sensitivity, better angular resolution and a lower energy threshold.

Construction of the VERITAS array was completed in early 2007. The array has already made significant contributions to the field of VHE astronomy. Chief among the achievements of the collaboration thus far has been the recent detection of TeV  $\gamma$ -rays from two blazars, W Comae (Swordy, 2008a) and 1ES 0806+524 (Swordy, 2008b).

For the first two years of operation, 50% of observation time is being dedicated to four key science projects (Hanna *et al.*, 2008). The projects

## 1.2. Research Contribution

---

are as follows:

- A search for dark matter annihilation.
- A study of supernova remnants.
- A study of active galactic nuclei.
- A survey of the Cygnus Arm region of our galaxy.

The Whipple 10 m telescope is utilised within the framework of the active galactic nuclei key science project. Blazars that are known to emit VHE  $\gamma$ -rays are monitored by the Whipple 10 m telescope. If they are observed to be in a high-flux state, the VERITAS observers are alerted and may conduct more detailed observations. If the blazars are observed by the Whipple 10 m telescope to be in a low-flux state, the VERITAS observers continue to observe other potential VHE  $\gamma$ -ray sources.

## 1.2 Research Contribution

The research presented in this thesis was conducted as part of a large collaboration. Throughout the course of the project, the author has made contributions to the work of the collaboration.

A number of trips to the Fred Lawrence Whipple Observatory in Arizona, USA were undertaken, including two trips of 3-month and 12-month duration, respectively. Each trip involved extended spells of observing on the Whipple 10 m telescope. During the 12-month stay in Arizona, during the 2006-07 observing season, the author was responsible for the scheduling and time allocation of observations with the Whipple 10 m telescope, as well as maintenance of the telescope and debugging of unforeseen hardware problems which arose occasionally during observing. All of the  $\gamma$ -ray data presented in this thesis were obtained during this time (*i.e.* 2006-07) and a large portion of the dataset was obtained by the author himself.

## 1.2. Research Contribution

---

The data presented in this thesis were obtained as part of a large-scale multiwavelength observation campaign, which included observations at optical, radio, x-ray and  $\gamma$ -ray wavebands. It was the responsibility of the author to analyse the VHE  $\gamma$ -ray dataset obtained at the Whipple 10 m telescope during the 2006-07 observing season for the five blazars that were monitored during this campaign. In addition, the author also regularly liaised with observers at the Fred Lawrence Whipple Observatory 1.2 m optical telescope to ensure the relevant optical data were obtained for the multiwavelength campaign. These optical data were reduced and analysed by the author, using IRAF<sup>1</sup>.

The author has been involved in the construction of three of the four VERITAS telescopes. Knowledge of the underlying systems of the telescopes was gained. Contributions were made to the optimisation of the optical performance and pointing accuracy of the array as well as helping to trace and repair problems which occurred with the new electronic systems during commissioning.

The author was lead author on a paper presented at the 30<sup>th</sup> International Cosmic Ray Conference in 2007 on the characterisation and optimisation of the optical performance of the VERITAS telescopes. Furthermore, he has been a co-author for a number of refereed journal papers (see Table 1.2) and various papers in conference proceedings.

Observations of Markarian 421 by the Whipple 10 m telescope during the 2005-06 observing season are the subject of a journal paper that is currently in production (Horan *et al.*, 2009). The author of this thesis performed many of the  $\gamma$ -ray observations which comprise the subject matter of the paper, during a 3-month visit to Arizona in 2005, and has also made significant contributions to the analysis and interpretation of that data. The data presented in this thesis will be combined with multiwavelength data (optical/infrared, radio and x-ray) from other observatories and will be published in a number of journal papers, in a

---

<sup>1</sup>Image Reduction and Analysis Facility

Title	Reference
The First VERITAS Telescope	Holder <i>et al.</i> (2006)
Very High Energy Observations of $\gamma$ -Ray Burst Locations with the Whipple Telescope	Horan <i>et al.</i> (2007)
Observations of the Unidentified TeV $\gamma$ -Ray Source TeV J2032+4130 with the Whipple Observatory 10 m Telescope	Konopelko <i>et al.</i> (2007)
Whipple telescope observations of LSI +61 303: 2004-2006	Smith <i>et al.</i> (2007)
The Whipple Observatory 10 m $\gamma$ -Ray Telescope, 1997-2006	Kildea <i>et al.</i> (2007)
VERITAS Observations of the $\gamma$ -Ray Binary LSI +61 303	Acciari <i>et al.</i> (2008b)
Observation of Gamma-Ray Emission from the Galaxy M87 above 250 GeV with VERITAS	Acciari <i>et al.</i> (2008a)
Multiwavelength Observations of Markarian 421 in 2005-6	Horan <i>et al.</i> (2009)

**Table 1.2:** List of papers in refereed journals on which the author of this thesis is listed as a co-author.

### 1.3. Thesis Overview

---

similar way to those presented in Horan *et al.* (2009).

## 1.3 Thesis Overview

The work contained in this thesis is concerned with the TeV  $\gamma$ -ray and optical emission properties of five blazars that have been previously detected in the very high energy  $\gamma$ -ray band: Markarian 421, Markarian 501, 1ES 1959+650, 1ES 2344+514 and H 1426+428. Optical observations were taken at the Fred Lawrence Whipple 1.2 m optical telescope, while the  $\gamma$ -ray data were obtained at the Whipple 10 m telescope. Analysis of the data sets is outlined. In the cases of Markarian 421 and Markarian 501, comparisons are made between the  $\gamma$ -ray and optical characteristics with a view to finding correlated emission.

Chapter 2 gives an overview of the physical processes by which cosmic  $\gamma$ -rays are detected, the telescopes currently operating in this energy regime and the types of astrophysical objects which are known to emit at TeV energies. Chapter 3 offers a discussion of active galactic nuclei and their emission properties. A review of recent observations of the five blazars pertinent to this thesis is also given in Chapter 3.

Chapters 4 and 5 explain the air Cherenkov technique utilised by the Whipple 10 m telescope and outline the results of analysis of  $\gamma$ -ray data for the five blazars monitored in 2006-07. Chapter 6 gives a description, and results, of the analysis of optical (SDSS  $r'$  band) data collected in 2007. Statistical tests and temporal analysis of the  $\gamma$ -ray and optical data sets are presented in Chapter 7 along with a correlation analysis. The results are discussed in Chapter 8.

### 1.3. Thesis Overview

---

# Chapter 2

## Review of the Field

This chapter offers an overview of the field of very high energy  $\gamma$ -ray astrophysics.  $\gamma$ -ray production mechanisms and  $\gamma$ -ray interaction with matter are discussed in Section 2.2. Nomenclature associated with the field of high energy astrophysics and the properties of past and present experiments are discussed in Section 2.3. In Section 2.4, the physical properties of cosmic sources of TeV  $\gamma$ -rays are examined.

### 2.1 Introduction and History

The field of high energy astrophysics effectively has its roots in the accidental discovery of cosmic rays by Victor Hess in 1912. In a simple balloon experiment, he found that an electroscope discharged more quickly at higher altitudes in the atmosphere and attributed this to a previously unknown type of radiation entering the upper atmosphere from space. The radiation was initially thought to be electromagnetic in nature. Although subsequent work showed that they are not electromagnetic, cosmic “rays” remained the name of choice. Hess received the Nobel Prize in 1936 for the discovery.

Due to the fact that charged cosmic rays are deflected by magnetic fields as they travel through the Universe and seem to arrive isotropically

## 2.1. Introduction and History

---

up to energies of  $10^{18}$  eV, their origin has largely remained a mystery. Abraham *et al.* (2007) suggests that the highest-energy cosmic rays may have their origin in active galaxies. Active galactic nuclei (AGN) are already known to be sources of emission of VHE  $\gamma$ -rays, so this may be the solution to a mystery which has beleaguered high energy astrophysics for almost a century.

Many new fields of astronomy have been developed over a relatively short space of time. Until early in the twentieth century, astronomy at optical wavelengths was the predominant means of studying the cosmos. Development of radio, x-ray and higher-energy fields of astronomy have opened up the “visible” universe. VHE  $\gamma$ -ray astronomy has, in recent years, managed to establish itself as a distinct scientific field, opening a new and interesting window to the Universe. Correlating and intertwining knowledge at different wavelengths has led to new, exciting and sometimes unexpected discoveries.

The high-energy astrophysics disciplines have been relative latecomers, only undergoing noticeable development last in the 40 years. Until the launch of the first satellite observatory missions in the 1970’s,  $\gamma$ -ray astronomy was very much in its infancy. Experiments such as SAS-2 and COS-B made great strides in the field, but it was only after the launch of the highly successful Compton Gamma Ray Observatory (CGRO) in 1991 that  $\gamma$ -ray astronomy made its mark in mainstream astronomy. The COMPTEL, BATSE, and (in particular) EGRET instruments on board the satellite, and their immense contributions to the field, are discussed further in Section 2.3.1.

The CGRO mission ended in 2000 and has only recently been replaced by the Italian Astro-rivelatore Gamma a Immagini LEggero (AGILE) in 2007. NASA’s Gamma Ray Large Area Space Telescope (GLAST) was also launched in June 2008. These two missions promise to further the work of CGRO. The answer to the question of the origin of Gamma Ray Bursts (GRBs), for instance, could not be answered by CGRO. GRBs

## 2.2. The Physics of $\gamma$ -rays

---

are intense and short bursts of  $\gamma$ -rays that appear to come from random directions in the sky. They are discussed in more detail in Section 2.4.3.

One of EGRET's major successes was its affirmation of blazars, a subclass of AGN, as sources of  $\gamma$ -rays. Before EGRET,  $\gamma$ -rays had been detected from the active galactic nucleus 3C273 by the COS-B satellite. Some of the blazars initially detected by EGRET have since been detected at higher energies by ground-based telescopes. Also, some blazars for which only upper bounds could be produced by EGRET have been detected by ground-based telescopes. This suggests that, overall, blazars are complicated objects exhibiting different characteristics at different energies.

A shortcoming of EGRET, however, was its lack of angular sensitivity. Many source locations were only known to  $\sim 0.5^\circ$ . In many of these cases, a number of possible counterpart x-ray, radio and optical sources may be found within the  $0.5^\circ$  error circle around the position of the EGRET source. In fact, around 60% of the sources detected by EGRET have no firmly established counterpart at other wavelengths. AGILE and GLAST, which both have better angular resolution than EGRET, should be better able to constrain the exact location of these MeV - GeV  $\gamma$ -ray hotspots.

## 2.2 The Physics of $\gamma$ -rays

### 2.2.1 Production Mechanisms

Ramana Murthy & Wolfendale (1993) and Weekes (2003) give good overviews of the various  $\gamma$ -ray production mechanisms. These mechanisms can be separated into two classes: line emission mechanisms and continuum emission mechanisms. The following sections describe these briefly.

## 2.2. The Physics of $\gamma$ -rays

---

### Line Emission

Line emission mechanisms are more prevalent production mechanisms for lower-energy  $\gamma$ -rays, and are only discussed briefly here.

- *Particle/anti-particle annihilation*: When an  $e^+$  and an  $e^-$  collide,  $\gamma$ -rays are produced as follows:  $e^+ + e^- \rightarrow \gamma + \gamma$ . If both of the particles are at rest, the resulting  $\gamma$ -rays will both have energy of 511 keV. If the particles are in motion when the collision occurs, a continuous energy distribution will be produced. In this case, the energy of the collision is shared equally between the two resulting photons. It is also possible that three (or more) photons are produced in this annihilation but the probability of this occurring is much smaller than that of the two-photon scenario.
- *Neutron capture reactions*: In areas of high densities of hydrogen and in the presence of thermalised neutrons, the following interaction can produce 2.22 MeV  $\gamma$ -rays:  $n + {}^1\text{H} \rightarrow \gamma + {}^2\text{H}$ . This mechanism is common in solar flares and accretion disks due to their densities. Dense hydrogen is necessary to ensure that the neutrons do not decay before interaction and also to slow the neutrons. It is therefore not a common emission mechanism in the interstellar medium.
- *Collisions of energetic particles*: When nuclei are excited by energetic particle collision, and when the nuclei de-excite again after collision with energetic particles,  $\gamma$ -ray line emission is produced. Similarly, emission occurs when radioactive products of stellar ejecta material de-excite. This mechanism is common in the interstellar medium.
- *Landau transitions*: In the presence of strong magnetic fields, transitions between Landau levels (*i.e.* discrete cyclotron orbits which

## 2.2. The Physics of $\gamma$ -rays

---

may be occupied by charged particles in a magnetic field) can produce cyclotron emission lines.  $\gamma$ -ray line emission at an energy of  $11.6B$  keV (where  $B$  here is the magnetic field in units of  $10^{12}$  G) is produced as a result of the first-level transition, where emission lines begin at  $E > m_e c^2 = 511$  keV.

- *Elementary particle decay*: Some elementary particles can produce  $\gamma$ -rays when they decay. Unstable neutral pions ( $\pi^0$ ), for instance, decay into two  $\gamma$ -rays. If the decay happens while the pion is at rest, the resultant  $\gamma$ -ray energy will be  $0.5 m_{\pi^0} c^2$ , where  $m_{\pi^0}$  is the rest mass of the neutral pion. This is a very rare occurrence however. It is much more common for the pions to decay while moving. Neutral pions that decay while moving at relativistic speeds will produce  $\gamma$ -rays at  $>$ GeV energies. Such neutral pions are produced by many known interactions, most notably high-energy collisions of nucleons which are important in hadronic-initiated air showers.

### Continuum Emission

Continuum  $\gamma$ -ray spectra are generated by particles such as protons and electrons.  $\gamma$ -rays with TeV energies are produced by processes whereby these charged particles are accelerated. Some of these processes are discussed below:

- *Bremsstrahlung*: Any charged particle passing through the electric field of a nucleus, or an electrically charged particle, will produce radiation called bremsstrahlung or “braking radiation”. As the charged particle (*e.g.* an electron) moves through the electric field, it loses large amounts of energy, resulting in high-energy photons being emitted. The acceleration produced by a nucleus of charge ( $Z \times q_e$ ) on a particle of charge  $q$  and mass  $m$  is proportional to  $(Zq_e \times q)/m$ . This process is commonly associated with interstellar clouds due to concentration of ionized gas in them through which

## 2.2. The Physics of $\gamma$ -rays

---

electrons can pass. The  $\gamma$ -ray flux is directly proportional to the density of the ionized gas multiplied by the electron flux. If an electron population is responsible for the bremsstrahlung radiation and the population is characterised by a power-law spectrum with spectral index  $\Gamma_e$ , then the  $\gamma$ -ray spectrum that results will have a spectral index  $\Gamma_\gamma \approx \Gamma_e$ . This process is most important in the study of  $\gamma$ -ray emission in the energy range  $<200$  MeV.

- *Synchrotron radiation*: This is caused by the acceleration of relativistic particles in magnetic fields and yields a continuous spectrum. For this mechanism to produce TeV  $\gamma$ -rays, the particles must be accelerated in very strong magnetic fields. An object having a synchrotron component at lower energies in its spectrum indicates it has a population of relativistic electrons. TeV  $\gamma$ -rays may be produced by these relativistic electrons, but only if the electrons are energetic enough to produce  $\gamma$ -rays by bremsstrahlung or inverse Compton processes. Synchrotron radiation is highly polarised radiation which occurs as a continuum spectrum distributed about a critical (angular) frequency,  $\omega_c$  (see Figure 2.1).

The synchrotron radiation process is illustrated in Figure 2.2 for an electron. When the electron moves in a magnetic field at relativistic speeds, radiation is beamed within a narrow emission cone in the forward direction. The cone will have an opening angle  $\theta_o \simeq 1/\gamma$ , where  $\gamma$  is the Lorentz factor of the particle. An observer at the orbital plane of the electron will only see the radiation when the cone is pointed in that direction.

The frequency at which maximum power is emitted (*i.e.* the critical frequency) is given by

$$\omega_c = \frac{3}{2} \left( \frac{qB}{mc} \right) \gamma^2 \sin \phi \quad (2.1)$$

## 2.2. The Physics of $\gamma$ -rays

---

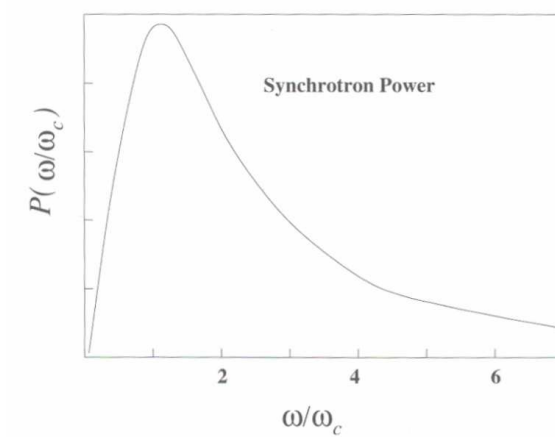


**Figure 2.1:** Illustrative example of a typical synchrotron power spectrum distributed about the critical frequency,  $\omega_c$ . (Weekes, 2003).

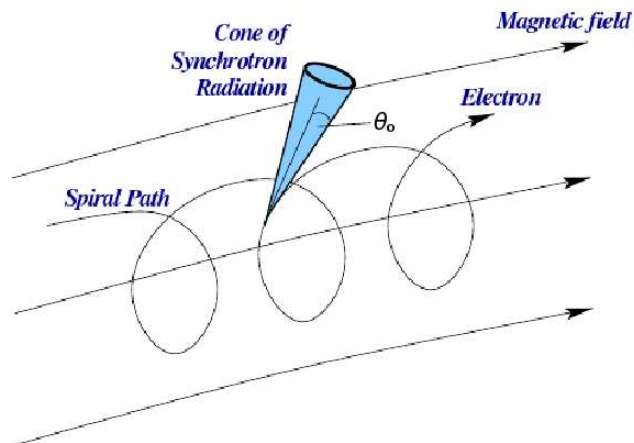


**Figure 2.2:** Synchrotron radiation from an electron as it moves in a spiral path in a magnetic field. The radiation is emitted at a tangent to the electron path with all of the radiation within a cone of opening angle ( $\theta_o$ ) due to the relativistic speed of the electron. (Weekes, 2003).

## 2.2. The Physics of $\gamma$ -rays

---

where  $\phi$  is the angle between the magnetic field and the direction of movement of the particle,  $q$  is the charge on the particle,  $B$  is the magnetic field strength,  $m$  is the mass of the charged particle and  $c$  is the speed of light (Weekes, 2003).

The energy loss is given by

$$-\frac{dE}{dx} = \frac{1}{c} \frac{dE}{dt} = \left( \frac{2q^4}{3m^2c^4} \right) \gamma^2 B^2 \quad (2.2)$$

where  $B$  is the magnetic field intensity at a right angle to the direction of motion of the particle in  $\mu\text{G}$ . Synchrotron emission is a more important process for electrons than it is protons due to the fact that the energy loss is inversely proportional to the square of the particle mass, with protons being much more massive than electrons.

The power distribution differs at frequencies,  $\omega$ , above and below the critical frequency,  $\omega_c$ , and is given by

$$P(\omega/\omega_c) = \begin{cases} 0.256 \sqrt[3]{(\omega/\omega_c)} & \text{for } \omega \leq \omega_c \\ \left(\frac{1}{16}\right) \sqrt{\pi\omega/\omega_c} \exp\left(\frac{-2\omega}{3\omega_c}\right) & \text{for } \omega > \omega_c \end{cases} \quad (2.3)$$

For a population of charged particles, all with identical opening angle,  $\theta_o$ , and Lorentz factor,  $\gamma$ , the spectrum of the synchrotron emission would take the form of the spectrum shown in Figure 2.3, with

$$\frac{dP}{d\omega} \propto \omega^{1/3} \quad (2.4)$$

in the low-frequency limit where  $\omega \ll \omega_c$ . In the case of real astrophysical sources of synchrotron radiation the shape of the spectrum is usually quite different, being more reasonably fitted by a power law with

## 2.2. The Physics of $\gamma$ -rays

---

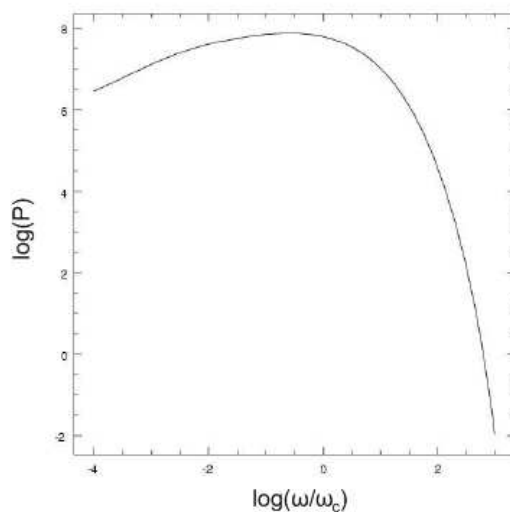


**Figure 2.3:** Typical synchrotron spectrum shape for a population of relativistic charged particles, all with identical opening angle and Lorentz factor.

$$\frac{dP}{d\omega} \propto \omega^{-s} \quad (2.5)$$

where  $s \neq -1/3$ . This is due to the fact that the emitting population of charged particles do not have the same energy, with high-energy particles being less common than low-energy particles within the population. Therefore, the shape of the synchrotron spectrum is highly dependent on the energy spectrum of the charged particles emitting the synchrotron radiation.

The total synchrotron power,  $P_t$ , from a relativistic particle of charge  $q$  undergoing acceleration  $a$  is

$$P_t = \frac{2}{3} \frac{q^2 \gamma^4 a^2}{c^3} \quad (2.6)$$

Using Equation 2.6 and considering relativistic particles with isotropically distributed velocity vectors, it can be shown that the total

## 2.2. The Physics of $\gamma$ -rays

---

synchrotron power for an isotropic distribution of emitting particles is

$$P_{sync} = \frac{4}{3} (\sigma_T c \beta^2 \gamma^2 U_B) \quad (2.7)$$

where  $\beta = v/c$  ( $v$  is the velocity of the particles),  $U_B = (B^2/8\pi)$  is the magnetic energy density and  $\sigma_T$  is the Thompson cross section – the cross section of interaction for the process. This is defined as

$$\sigma_T = \frac{8}{3} \pi r_0^2 \quad (2.8)$$

where  $r_0$  is the classical electron radius, given by

$$r_0 = \frac{q_e^2}{m_e c^2} \quad (2.9)$$

Electrons (or any charged particles) that are emitting synchrotron radiation are cooling down by *synchrotron cooling*. The time taken for this cooling to take place is

$$t_{sync} = \frac{E_e}{P_{sync}} \quad (2.10)$$

where  $E_e$  is the energy of the electrons, given by

$$E_e = \gamma m_e c^2 \quad (2.11)$$

Therefore, the synchrotron cooling time for electrons is given by

$$t_{sync} = \frac{3 m_e c^2}{4 \sigma_T c U_B \gamma \beta^2} \quad (2.12)$$

- *Inverse Compton scattering*: This is a process whereby a high-energy electron collides with a lower-energy photon, scattering the

## 2.2. The Physics of $\gamma$ -rays

---

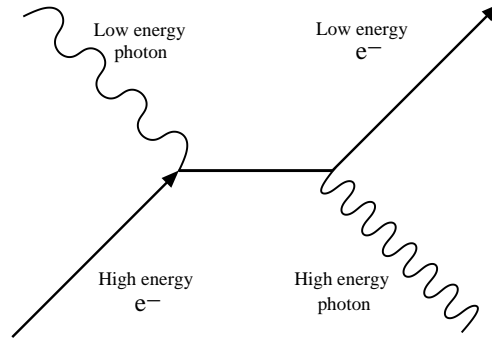


**Figure 2.4:** Feynman diagram for inverse Compton scattering. With two elements on either side of the interaction in the diagram, inverse Compton scattering is a second-order process.

photon to higher energies. Since the energy gained by the photon is substantial, it is thought that this is an important mechanism for high-energy  $\gamma$ -ray emission from astrophysical objects. It is further discussed in relation to blazars in particular in Chapter 3.

As the name of the process suggests, inverse Compton scattering is the opposite of Compton scattering, whereby a photon loses energy through interaction with a loosely-bound electron. Physically, inverse Compton scattering may be considered in terms of Compton scattering, but with a coordinate transformation to the rest frame of the electron. The incident photon has energy  $h\nu$ , the scattered photon has energy  $h\nu'$  and the electron loses energy  $E = \gamma m_e c^2$ , where  $\gamma$  is the Lorentz factor,  $m_e$  is the mass of the electron and  $c$  is the speed of light. We may define

$$x = \frac{h\nu}{m_e c^2} \quad (2.13)$$

*i.e.* the ratio of the incident photon energy to the rest energy of the electron. The energy of the scattered photon is given by

## 2.2. The Physics of $\gamma$ -rays

---

$$h\nu' = \frac{m_e c^2}{(1 - \cos\theta) + 1/x} \quad (2.14)$$

where  $\theta$  is the scattering angle of the photon relative to the path of the incident electron.

The cross section of the interaction is given by the Klein-Nishina cross section:

$$\sigma_{KN} = \pi r_0^2 \left[ \frac{(1/x^3) \ln(1 + 2x) + 2(1 + x)(2x^2 - 2x - 1)}{(x^2(1 + 2x)^2) + (8x^2/3(1 + 2x)^3)} \right] \quad (2.15)$$

For very small values of  $x$ , this reduces to the Thompson cross section (see Equation 2.8). For a population of relativistic electrons with a power-law distribution of energies  $N(E_e) \sim E^{-\alpha}$ , the resulting  $\gamma$ -rays will have characteristic energies of  $\gamma^2 h\nu$  in the Thompson regime or energies of  $\gamma h\nu$  in the Klein-Nishina regime, where  $h\nu$  is the initial energy of the photon being up-scattered. The resulting  $\gamma$ -rays have a spectrum of the form

$$N(E_\gamma) \sim E_\gamma^{-(\alpha+1)/2} \quad (2.16)$$

The power emitted in the case of an isotropic distribution of photons,  $P_{comp}$ , is given as

$$P_{comp} = \frac{4}{3} \sigma_T c U_{rad} \gamma^2 \beta^2 \quad (2.17)$$

where  $U_{rad}$  is the radiation energy density of the photon field before scattering. A typical inverse Compton spectrum is shown in Figure 2.5.

Inverse Compton scattering is the main process by which TeV  $\gamma$ -rays are produced from a population of relativistic electrons. The

## 2.2. The Physics of $\gamma$ -rays

---

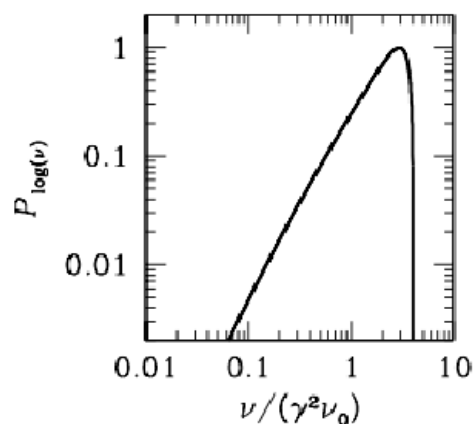


**Figure 2.5:** Example of a typical inverse Compton spectrum plotted on a log-log plot of power per logarithmic frequency range. Credit: Astrophysics II (FFYS4346) online lecture notes, Dr. C. Flynn, Tuorla Observatory, <http://www.astro.utu.fi/~cflynn/astroII/>.

electrons are assumed to be accelerated to high energies in relativistic shock waves. A process known as synchrotron self-Compton may take place whereby the energetic electrons, moving in magnetic fields, emit synchrotron radiation. These lower-energy synchrotron photons are then up-scattered to TeV energies by inverse Compton scattering.

### 2.2.2 Interaction of $\gamma$ -Rays with Matter

The detection of  $\gamma$ -rays depends on how they interact with matter.  $\gamma$ -rays interact with matter in different ways depending on the energy of the photons. Three interaction mechanisms are known to occur: photoelectric absorption, Compton scattering and pair production. Figure 2.6 shows the mass attenuation coefficients for the three different interaction mechanisms in a plastic scintillator. Although the actual values and the relative strengths of the processes differ from material to material the

## 2.2. The Physics of $\gamma$ -rays

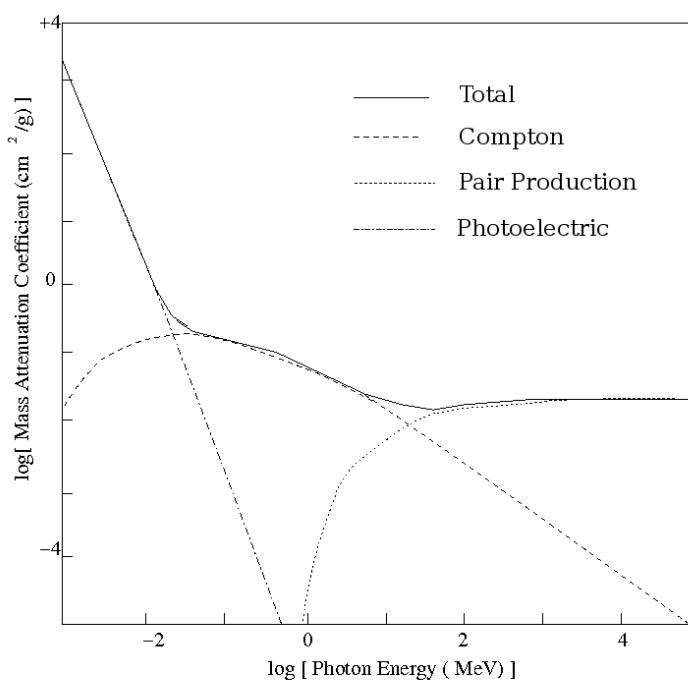


**Figure 2.6:** Graph of attenuation against energy for Compton scattering, pair production and photoelectric absorption in a plastic scintillator. The choice of scintillation material is arbitrary as the functional form is the same for all materials (*e.g.* air). (Weekes, 2003)

functional form is the same. These processes are explained below.

- *Photoelectric absorption:* An electron may be ejected from the inner shell (*i.e.* K-shell) of an atom by its interaction with a  $\gamma$ -ray. The energy of the  $\gamma$ -ray is transferred to the electron, causing it to unbind with energy  $E_{KE}$ , which is the difference between the energy of the photon and the binding energy of the electron. The gap left in the orbital shell of the atom is filled by an electron from a higher orbital shell, causing emission of an x-ray, which is absorbed in the material itself. This process is predominant at low  $\gamma$ -ray energies of  $E_\gamma < 0.1$  MeV. Materials with a high atomic number ( $Z$ ) are best

## 2.2. The Physics of $\gamma$ -rays

---

for absorbing low energy  $\gamma$ -rays as the probability of interaction varies approximately with  $Z^5$ .

- *Compton scattering*: This process occurs when a  $\gamma$ -ray interacts with a loosely-bound electron. The incident  $\gamma$ -ray loses some energy which is imparted to the electron. Another photon containing the remaining energy is emitted in a different direction to the initial  $\gamma$ -ray, conserving momentum. If the incident  $\gamma$ -ray has enough energy, it may begin a cascade of interactions. This is a dominant interaction process at intermediate energies of  $0.1 < E_\gamma < 10$  MeV. The probability of interaction of  $\gamma$ -rays by Compton scattering has no dependence on  $Z$ .
- *Pair production*: An electron-positron pair may be produced by a  $\gamma$ -ray photon interacting with a nucleus. It has a low energy threshold of  $E_\gamma = 1.022$  MeV (*i.e.*  $2 \times m_e c^2$ , where  $m_e$  is the rest mass of an electron/positron). Although this energy threshold is quite low, pair production is only significant for  $\gamma$ -rays with energies of several MeV. Above 30 MeV, pair production is the dominant attenuation process. At these energies, probability of interaction varies with  $\sim Z^2$ .

### Extensive Air Showers

Extensive air showers are cascades of ionised particles and electromagnetic radiation which occur in the Earth's atmosphere. The atmosphere is constantly bombarded by a mixture of high-energy particles, such as protons and nuclei, as well as a small flux of cosmic  $\gamma$ -rays. These incident particles and photons can interact with the atmosphere to initiate extensive air showers (EAS); cascades of particles and  $\gamma$ -rays which move down through the atmosphere until the initiator's energy has been depleted by processes such as bremsstrahlung and pair production (Weekes, 1988). The number of particles in the cascade multiplies as the shower

## 2.2. The Physics of $\gamma$ -rays

---

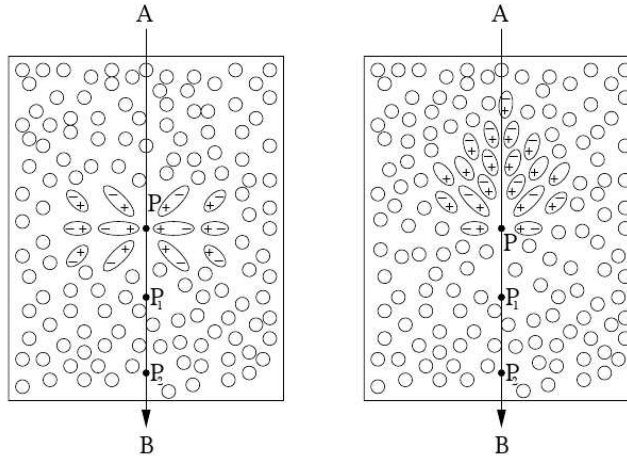


**Figure 2.7:** Charged particle (electron) moving through a dielectric medium. The left panel shows the particle moving relatively slowly through the medium. In the right panel, the particle moves at a speed comparable to the velocity of light in that medium. (Weekes, 2003)

develops, reaches a maximum and then dwindles as successive particles no longer have enough energy to induce further reactions. The interactions that take place within the cascade are discussed in more detail in the sections that follow. The depth of the shower maximum increases logarithmically with the energy of the primary. The number of particles in the shower maximum is also proportional to the energy of the initiator.

For most branches of astronomy, the Earth's atmosphere is a hindrance. At optical wavelengths, resolution is limited due to atmospheric turbulence. At other wavelengths (x-ray, ultraviolet) the atmosphere is opaque. However, for VHE astronomers, the atmosphere is essential to the detection technique. Cherenkov radiation from air showers generated high in the atmosphere by incident  $\gamma$ -ray photons may be detected on the ground, the atmosphere acting as a calorimeter. These processes are explained in more detail in the following sections.

## 2.2. The Physics of $\gamma$ -rays

---

**Cherenkov Radiation** When a charged particle moves through a dielectric medium at a greater velocity than the velocity of light in that medium, Cherenkov radiation may be produced. A comprehensive treatment of Cherenkov radiation may be found in Jelley (1958).

Figure 2.7 shows an electron moving through a dielectric medium. In the case where the electron moves slowly through the medium (left panel), the alignment of the molecules comprising the medium is distorted such that the positive charges within the atom are attracted to the moving electron. As the electron passes on through the medium, these molecules relax to their original alignment, causing a small electromagnetic pulse. The centre of polarisation moves on to points  $P_1$  and  $P_2$  as the electron moves through those positions. The polarisation field around the electron is symmetrical so there is no resultant radiation.

If the electron is moving through the medium at a velocity which is comparable to, or faster than, the speed of light in that medium (right panel of Figure 2.7), the symmetry of the polarisation field is not maintained. If the velocity of the electron is greater than the velocity of light in the medium, waves generated at each point along the track of the electron will be in phase and a coherent wave-front is generated at a well-defined angle to the path of the electron.

Figure 2.8 illustrates how a coherent Cherenkov wavefront is produced. The time taken for the charged particle to move from point X to point Y is the same as the time taken for the radiation emitted by the particle when it was at point X to reach point Z. If  $c$  is the speed of light in a vacuum,  $\beta c$  is the velocity of the charged particle as it moves through the medium. If  $n$  is the refractive index of the medium and  $\Delta t$  is the time taken for the charged particle to move from X to Y, then

$$|XY| = \beta c \Delta t \tag{2.18}$$

and

## 2.2. The Physics of $\gamma$ -rays

---

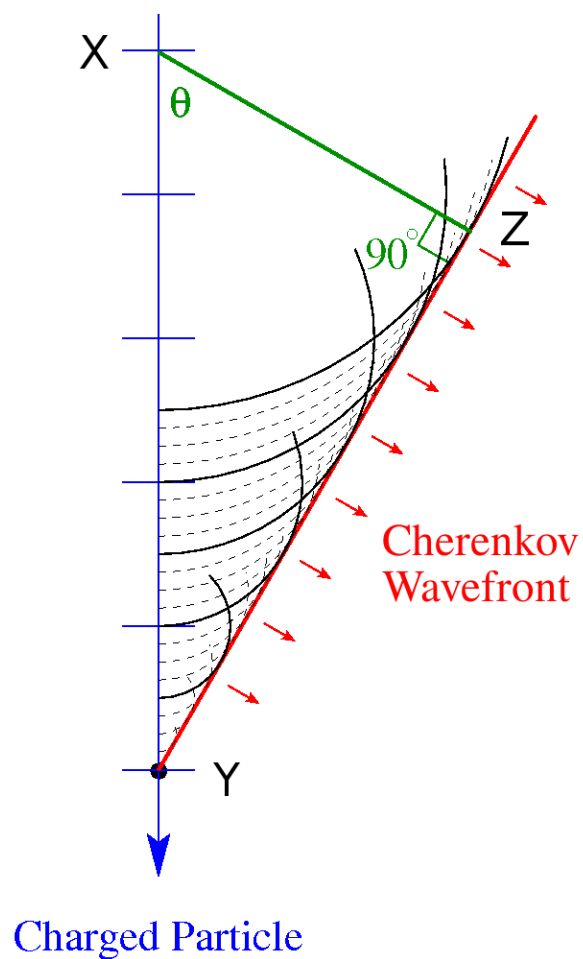


**Figure 2.8:** Coherent Cherenkov radiation production. The charged particle moves from X to Y in the same time it takes for emitted particles to get from X to Z. The Cherenkov angle,  $\psi$ , is shown.

## 2.2. The Physics of $\gamma$ -rays

---

$$|\text{XZ}| = \frac{c}{n} \Delta t \quad (2.19)$$

Using Equations 2.18 and 2.19, and noting that

$$\cos \psi = \frac{|\text{XZ}|}{|\text{XY}|} \quad (2.20)$$

we obtain the ‘‘Cherenkov relation’’, which describes the angle of Cherenkov emission:

$$\cos \psi = \frac{1}{\beta n} \quad (2.21)$$

There is a threshold velocity,  $\beta_{min} = (1/n)$ , below which Cherenkov radiation cannot take place. At this velocity, the radiation direction is the same as the direction of movement of the particle. The corresponding critical (or threshold) energy is:

$$E_t = \frac{m_0 c^2}{\sqrt{1 - \beta_{min}^2}} \quad (2.22)$$

where  $m_0$  is the mass of the particle. The maximum value Cherenkov angle,  $\psi_{max}$ , will occur when  $\beta = 1$ , giving the relation

$$\psi_{max} = \cos^{-1} \left( \frac{1}{n} \right) \quad (2.23)$$

For air at ground level, where  $n = 1.00029$ , the maximum Cherenkov angle is  $\psi_{max} = 1.3^\circ$  and the energy threshold is  $E_t = 21$  MeV. The threshold energy for muons is 4.4 GeV and the threshold energy for protons is 39 GeV. At higher altitudes the density of the air is lower so the Cherenkov angle is smaller.

Cherenkov radiation can only occur at wavelengths for which  $n > 1$  in the medium. In typical media,  $n < 1$  for x-rays and  $\gamma$ -rays meaning that Cherenkov radiation can only occur at microwave, infrared, visible and ultraviolet wavelengths.

The number of Cherenkov photons emitted per path length ( $dl$ ) per

## 2.2. The Physics of $\gamma$ -rays

---

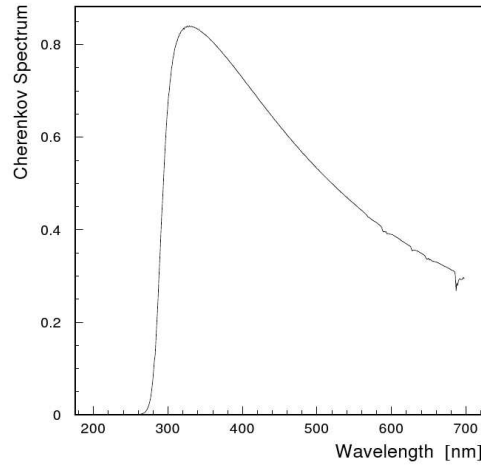


**Figure 2.9:** Typical spectrum of Cherenkov light generated by TeV air showers observed at 2200 m above sea level (in arbitrary units). The peak at  $\sim 350$  nm corresponds to blue/ultraviolet light. Adapted from Döring *et al.* (2001).

wavelength interval ( $d\lambda$ ) for a charged particle with charge  $Z$  is:

$$\frac{d^2 N}{dl d\lambda} = \frac{2\pi k Z^2}{\lambda^2} \left(1 - \frac{1}{\beta^2 n^2}\right) \quad (2.24)$$

where  $k$  is the fine structure constant (*i.e.* fundamental constant which characterises the strength of the electromagnetic interaction) (Dunlea, 2001) and  $n$  is the wavelength-dependent refractive index. This can be integrated for electrons, giving the number of photons emitted,  $N$ , in the wavelength range  $\lambda_1$  to  $\lambda_2$  over a distance  $l$  such that

$$N = 2\pi l k \left(\frac{1}{\lambda_2} - \frac{1}{\lambda_1}\right) \left(1 - \frac{1}{\beta^2 n^2}\right) \quad (2.25)$$

Therefore, the number of photons produced per wavelength interval is proportional to  $1/\lambda^2$  and, combined with the effects of atmospheric absorption and scattering phenomena, the peak of Cherenkov emission in air is observed to be in the blue-to-ultraviolet region of the spectrum. The observed spectrum of Cherenkov light in air is shown in Figure 2.9.

## 2.2. The Physics of $\gamma$ -rays

---

**Cherenkov Radiation from Air Showers** Cherenkov light is emitted by the charged particles that comprise air showers. The detection of this light forms the basis for the imaging atmospheric Cherenkov technique employed by many ground-based air Cherenkov telescopes. Hadronic cosmic rays initiate the vast majority of EAS, meaning the detection of  $\gamma$ -ray induced showers requires an efficient technique for separating them from the abundant hadronic background. The  $\gamma$ -hadron separation technique employed by imaging atmospheric Cherenkov telescopes is discussed in more detail in Chapter 4.

Hadron-initiated and photon-initiated air showers tend to have different morphologies. Figure 2.10 shows the development of both a 320 GeV  $\gamma$ -ray-induced shower and a 1 TeV proton-induced shower. When a high-energy  $\gamma$ -ray enters the atmosphere and passes very close to an atomic nucleus, it undergoes pair production, producing an electron-positron pair (*i.e.*  $\gamma \rightarrow e^- e^+$ ). This tends to happen near the top of the atmosphere. The electron-positron pair undergo bremsstrahlung which results in the production of high-energy  $\gamma$ -rays. Muons may also be produced in photonuclear reactions, though the probability of this happening is a lot lower than for pair production.

The cascade grows in an exponential fashion until shower maximum is reached. At this point, the electrons and positrons do not have enough energy to continue the cascade and rapidly lose energy by ionisation. This energy is known as the “critical energy” and has a value of  $\sim 84$  MeV for air. The cascade terminates and the charged particles are absorbed (Cranshaw, 1963). During the time that the electrons and positrons are moving through the atmosphere, they induce Cherenkov radiation. The radiation is emitted at a small angle to the direction in which the emitting particle is moving. A small percentage of the emission is directed at a different angle to the shower because some of the particles are spread by Coulomb forces so that the Cherenkov radiation is emitted over angles of  $\sim 20^\circ$ . The amount of emission at these larger angles is very small,

## 2.2. The Physics of $\gamma$ -rays

---

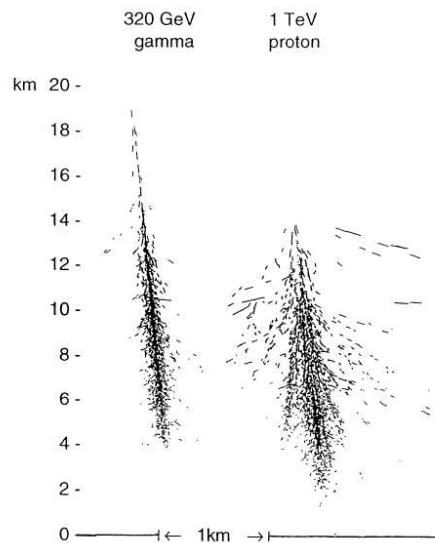


**Figure 2.10:** Simulations of extensive air showers. Shown here are the tracks of charged particles above the Cherenkov threshold for simulated showers generated by a 320 GeV  $\gamma$ -ray (left) and a 1 TeV proton (right) highlighting the differences in their development morphology. A 1 TeV proton was used for comparison as a 320 GeV proton-initiated shower rapidly dissipates, due to the mass of the proton, compared to a  $\gamma$ -ray-induced shower with an equivalent energy. Thus the showers shown here generate similar amounts of Cherenkov light. Figure from Hillas (1996).

however, and most of the light detected on the ground comes from the direction of the initiating particle movement. Therefore, a photon-induced shower, detected at mountain altitudes has a pool of light with a radius of  $\sim 125$  m, beyond which there is a rapid drop in light intensity. This can be explained by the difference in refractive index of the atmosphere at the beginning of the cascade compared to the refractive index of the atmosphere at (or near) sea level. Figure 2.11 shows this schematically, along with a typical intensity profile of the light pool.

The amount of light in a shower depends on the number of particles generated in the cascade. This light is not strongly attenuated by

## 2.2. The Physics of $\gamma$ -rays

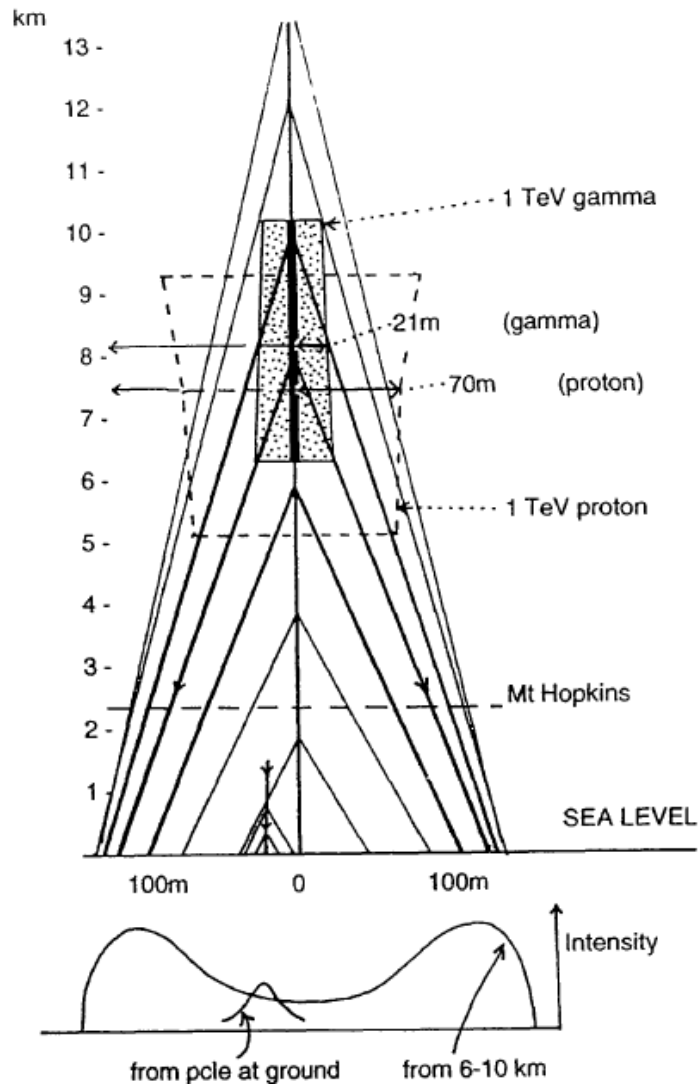


**Figure 2.11:** Typical change in Cherenkov emission angle throughout air shower. As the shower develops, the Cherenkov angle increases due to an increase in atmospheric density. The intensity profile of the resulting light pool is shown also. (Hillas, 1996)

## 2.2. The Physics of $\gamma$ -rays

---

the atmosphere between the site of Cherenkov emission and the ground. Therefore, the amount of light detected may be used to estimate the energy of the initiating photon.

Hadronic air showers are caused by the isotropic flux of cosmic rays incident on the Earth's atmosphere. When the cosmic rays collide with nuclei in the atmosphere, large numbers of elementary particles and radiation are produced, most of which are pions that decay through a series of decays as follows:

$$\begin{aligned}\pi^+ &\rightarrow \mu^+ + \nu_\mu \\ \pi^- &\rightarrow \mu^- + \bar{\nu}_\mu \\ \pi^0 &\rightarrow \gamma + \gamma\end{aligned}\tag{2.26}$$

The charged pions decay into neutrinos and muons. As muons do not interact strongly, most of the high-energy muons penetrate the remaining atmosphere and reach the Earth's surface. About a third of the pions produced are  $\pi^0$ . These decay into two  $\gamma$ -rays, which pair produce to begin electromagnetic cascades within the hadronic cascade. The electromagnetic cascade reaches maximum and is rapidly attenuated due to ionisation. Eventually, the energy of the hadronic cascade dissipates leaving only electromagnetic radiation and muons.

Due to the large transverse momentum of pions in strong interactions, the hadronic showers tend to be more laterally spread out, and more diffuse, than  $\gamma$ -ray showers. The differences in the profile of the showers, as seen from the ground, may be used as a means of discriminating  $\gamma$ -ray showers from hadron showers. In the imaging atmospheric Cherenkov technique, this is achieved by imaging the Cherenkov light given off by the showers using large reflectors and high-speed cameras.

### 2.3 High Energy Astrophysics

The study of the Universe – cosmological objects and their emission mechanisms – by means of looking at their non-thermal emission, is the mandate of high energy astrophysics. The emission mechanisms of these objects in different wavebands are often closely related. In particular, simultaneous studies of certain objects at x-ray and  $\gamma$ -ray wavelengths can prove interesting due to their supposed reliance on the same population of relativistic electrons for emission. In the case of blazars (a type of active galaxy), simultaneous observations across many wavelength bands have revealed interesting hints of correlated emission at different energies. Some noteworthy high-energy astrophysical observatories are described briefly in the following sections.

#### 2.3.1 $\gamma$ -ray Astrophysics Overview

$\gamma$ -rays cover a large part of the electromagnetic spectrum. As such, “ $\gamma$ -ray astronomy” is a far-reaching term, covering the observation of electromagnetic photons with energies from 511 keV (an electron’s mass) to the energies of cosmic rays ( $> 10^{20}$  eV), though cosmic  $\gamma$ -rays with these extremely high energies are rare due to low flux levels. As discussed in Section 2.2.2,  $\gamma$ -rays of different energies interact with matter in different ways. Weekes (1988) proposed a classification scheme whereby the field of  $\gamma$ -ray astronomy is subdivided roughly according to the energies over which the various detection techniques are effective. Although techniques have changed somewhat over the subsequent years, the classification has been largely adhered to and updated accordingly. Table 2.1 gives an outline of the nomenclature used in the field of high-energy  $\gamma$ -ray astrophysics for the subdivisions in the field, as proposed in Hoffman *et al.* (1999). One detector type cannot be used across the entire  $\gamma$ -ray energy range. The principal methods of detection and the various instruments used at these energies are described below.

Energy Range	Nomenclature	Detection Technique
10 MeV - 30 MeV	Medium Energy (ME)	Compton telescope (satellite)
30 MeV - 30 GeV	High Energy (HE)	Tracking detector (satellite)
30 GeV - 30 TeV	Very High Energy (VHE)	Atmospheric Cherenkov technique
30 TeV - 30 PeV	Ultra High Energy (UHE)	Air shower particle detector
30 PeV and up	Extremely High Energy (EHE)	Air shower particle/air fluorescence detector

**Table 2.1:** Nomenclature used in high-energy  $\gamma$ -ray astronomy.  
Adapted from Hoffman *et al.* (1999)

## 2.3. High Energy Astrophysics

---

### Space and Balloon Missions

The field of observational high-energy astrophysics essentially began with the balloon experiment by Hess in 1912 and the subsequent discovery of cosmic rays. The natural progression from balloon-based observation platforms was to build satellite-based telescopes.

The first  $\gamma$ -ray telescope which enjoyed success was SAS-2, launched by NASA in 1972. The European Space Agency soon followed with COS-B in 1975. These two missions demonstrated the potential of  $\gamma$ -ray astronomy. They mapped the  $\gamma$ -ray sky for the first time and the successes they enjoyed encouraged those working with ground-based instruments.

Following these experiments, the Compton Gamma Ray Observatory (CGRO) was launched by NASA in 1991. Its mission, which lasted a little over nine years, added enormously to the previous discoveries of SAS-2 and COS-B. The instruments on board CGRO and their effective energy bands were:

- *The Energetic Gamma Ray Experiment Telescope (EGRET)* provided sensitivity at the highest energies (20 MeV - 30 GeV) and had a large field-of-view ( $\pm 20^\circ$ ). As such, the catalogue of EGRET sources (Hartman *et al.*, 1999) is of most interest to those working with atmospheric Cherenkov telescopes.
- *The Compton Telescope (COMPTEL)* offered sensitivity in the range 1 - 30 MeV and a field of view of around one steradian. It mapped the sky in its energy range – the first instrument to do so.
- *The Oriented Scintillation Spectroscopy Experiment (OSSE)* had sensitivity in the energy range 0.05 - 10 MeV.
- *The Burst and Transient Source Experiment (BATSE)* was an array of eight detectors, designed to detect bursts of high-energy  $\gamma$ -rays and solar flares in the range 20 keV - 1.9 MeV. It could detect

### 2.3. High Energy Astrophysics

---

bursts over timescales of microseconds. BATSE also had a spectrometer, which was sensitive in the wider range 15 keV - 110 MeV, for measuring bursts' spectra.

CGRO was an incredibly successful mission. It was eventually retired due to a faulty gyroscope and manually de-orbited. Before this happened, it had accomplished most of its scientific goals and made some interesting discoveries in the process. EGRET, in particular, resolved over 270 sources of high-energy  $\gamma$ -rays in its sky survey. Of these sources, around 170 have not been definitively associated with counterparts at other wavelengths.

After the demise of CGRO in 2000, there was no equivalent observatory in orbit. Originally planned to fill the gap between CGRO and GLAST, the delay-stricken AGILE (Astro-rivelatore Gamma a Immagini LEggero) was constructed by the Italian Space Agency and launched in April 2007 (Feroci *et al.*, 2007). It is lighter and smaller than CGRO, but with comparable performance and instruments. Tavani *et al.* (2006) summarise the instruments on board and their respective capabilities.

NASA's Gamma-ray Large Area Space Telescope (GLAST) mission was launched in June 2008. Comprised of larger and more sensitive detectors than CGRO or AGILE, GLAST is capable of observing  $\sim 20\%$  of the sky at any one time, and the entire sky within a few hours. An outline of the various detectors on board GLAST is given in Carson (2007). More detailed descriptions are given in Steinle *et al.* (2006) and Latronico *et al.* (2007).

The instrument on board GLAST which is of particular interest to those working in the field of VHE  $\gamma$ -ray astronomy is the Large Area Telescope (LAT). Using technology similar to the technology used in the detectors of terrestrial particle accelerators (see Figure 2.12), the LAT will be sensitive to high-energy  $\gamma$ -rays in the energy range  $\sim 20$  MeV -  $\geq 300$  GeV with energy resolution of  $\leq 10\%$ . The GLAST Burst Monitor (GBM) will detect bursts of high-energy  $\gamma$ -rays in much the same

### 2.3. High Energy Astrophysics

---

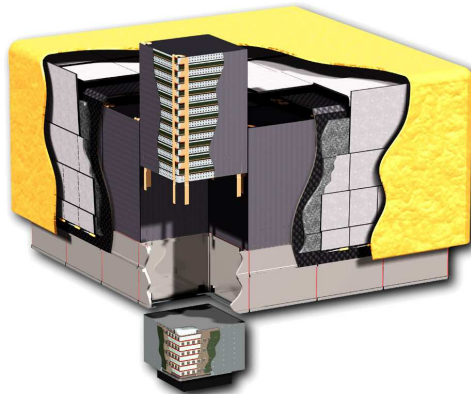


**Figure 2.12:** Cut-away image of the Large Area Telescope (LAT) aboard GLAST. The detector is comprised of an array of 16 columnar silicon strip detectors, similar to those used in detectors of particle accelerators. These are used to obtain highly accurate 2-dimensional coordinates on arrival of a high energy  $\gamma$ -ray by tracking the electron-positron pair that results from pair production in thin tungsten conversion foils between the columns. The third coordinate is obtained using adjacent columns to calculate the arrival direction. These silicon strip detectors sit atop a calorimeter. The entire detector is encased in an anti-coincidence shield. (Credit: NASA)

way as the BATSE instrument aboard CGRO did, alerting ground-based instruments of burst locations within minutes of their detection.

#### Ground-Based Experiments

The Earth's atmosphere may effectively be used as a detection medium for very high energy particles. Satellite  $\gamma$ -ray telescopes are ineffective in this energy range due to the low  $\gamma$ -ray flux at these energies and the relatively small size of telescopes which may be sent into orbit. VHE  $\gamma$ -rays are absorbed by the atmosphere and are therefore not directly detectable at ground-level. However, the effects of their absorption in the atmosphere are detectable on the ground. There are two means

### 2.3. High Energy Astrophysics

---

by which the incident  $\gamma$ -rays may be detected using ground-based techniques: detection of Cherenkov light from extensive air showers initiated by the  $\gamma$ -rays as the shower particles move through the atmosphere (see Section 2.2.2), and the direct detection of a shower of the secondary particles which comprise the cascade.

The detection of Cherenkov radiation is the method utilised by Imaging Atmospheric Cherenkov (IAC) telescopes in the 100 GeV - 50 TeV energy range. A large reflector is used to collect Cherenkov light photons produced in air showers that are initiated by high-energy  $\gamma$ -rays and cosmic rays which are incident on the atmosphere. The profile of the image of the Cherenkov light is then used to discriminate the  $\gamma$ -ray-induced air showers from the proton-induced air showers. The method employed is described in detail in Chapter 4.

Weekes & Turver (1977) suggested the use of imaging with the already-established Atmospheric Cherenkov Technique to discriminate  $\gamma$ -ray showers from hadronic showers. The first success of this technique came in 1989 with the detection of  $\gamma$ -rays from the Crab Nebula (Weekes *et al.*, 1989) by the Whipple Collaboration using the Whipple 10 m telescope at energies  $>700$  GeV. Since then, the Imaging Atmospheric Cherenkov Technique has proven itself as the most powerful technique for the detection of VHE  $\gamma$ -ray sources. The technique has developed significantly since the initial Crab Nebula detection and many observatories have been built to detect and monitor objects at these energies. Table 2.2, adapted from Catanese & Weekes (1999) and Hinton (2007), lists these observatories.

Stereo observatories (two or more IAC telescopes observing contemporaneously as an array), such as VERITAS and HESS, have added power to the technique, increasing collection area as well as improving sensitivity and angular resolution. Larger aperture IAC telescopes, such as MAGIC, also have lower energy thresholds so that more of the object's spectrum may be studied.

### 2.3. High Energy Astrophysics

Telescope	Location	$\mathbf{N}_T \times \mathbf{A}$ ( $\mathbf{N}_p$ )	Energy Threshold
Whipple 10 m	USA	1 × 10 m (379)	300 GeV
Crimea	Ukraine	6 × 2.4 m (37)	1 TeV
SHALON	Russia	1 × 4 m (144)	800 GeV
CANGAROO-I*	Australia	1 × 3.8 m (256)	500 GeV
HEGRA*	Spain	5 × 3 m (271)	500 GeV
CAT*	France	1 × 3 m (600)	250 GeV
Durham*	Australia	3 × 7 m (109)	250 GeV
7 Telescope Array*	USA	7 × 2 m (256)	500 GeV
TACTIC	India	1 × 3 m (349)	1.2 TeV
CANGAROO-II*	Australia	1 × 7 m (512)	400 GeV
CANGAROO-III	Australia	4 × 10 m (427)	300 GeV
MAGIC	Spain	1 × 17 m (574)	60 GeV
VERITAS	USA	4 × 12 m (499)	100 GeV
HESS	Namibia	4 × 12 m (960)	100 GeV

**Table 2.2:** Various imaging atmospheric Cherenkov observatories. The figures here represent the observatory’s current status (if still operating), though some observatories have utilised various camera configurations, *etc.*, during their lifetimes. \* indicates that an observatory is no longer operating.  $\mathbf{N}_T$  is the number of telescopes utilised by the observatory,  $\mathbf{A}$  is the aperture of each telescope and  $\mathbf{N}_p$  is the number of pixels contained in each of the telescope’s cameras. Thresholds quoted are trigger thresholds at zenith. (Adapted from Catanese & Weekes (1999) and Hinton (2007).)

### 2.3. High Energy Astrophysics

---

Cherenkov light detection techniques have also been used by non-imaging telescopes such as the Pachmarhi Array of Cherenkov Telescopes (PACT), based in Pachmarhi, India. This array of 25 telescopes uses wavefront sampling to reject background events. Bhat *et al.* (2000) gives a good overview of this technique.

Due to their large collection areas, and nightly availability, solar arrays have been used in Cherenkov detecting experiments such as CELESTE (France), STACEE (USA), Solar-2 (USA), CACTUS (USA) and GRAAL (Spain). These arrays of tracking mirrors focus Cherenkov light onto a single focal point. Arrival times are then used for shower reconstruction. Although the use of solar arrays offers large collection areas, and hence lower energy threshold, the background rejection is not very good, which affects sensitivity. None of these experiments are currently operating, since they have proven ineffective when compared to imaging telescopes.

The altitude at which maximum shower development occurs for 1 TeV  $\gamma$ -ray photon-initiated air showers is around 10 kilometres above sea level. However, a reasonable number of the tails of these showers (*i.e.* the parts of the air showers that continue beyond the shower maximum) may still be detectable at lower altitudes if the telescope's collection area is large enough. Exploiting this fact, particle shower arrays operate at slightly higher energies than air Cherenkov detectors. At these energies, enough particles remain at ground level to be directly detected.

There are two possible approaches for detecting  $\gamma$ -rays using air-shower arrays which directly detect the showers' particles. The first is to use an array of scintillation detectors which are widely spaced on the ground. An example of this approach is the Tibet Air-Shower Array (Tibet AS $\gamma$ ), which is located at an altitude of 4300 m above sea level (Amenomori *et al.*, 2000). The high altitude of this array helps to lower the energy threshold to  $\sim 3$  TeV. The second method does not have the detectors widely spaced but, rather, the entire ground is covered. This

## 2.4. TeV $\gamma$ -ray Sources

---

ensures a low energy threshold. Aielli *et al.* (2007) outlines the ARGO-YBJ experiment, which is located in Tibet and utilises this approach. It has an energy threshold of 2 TeV.

Water-Cherenkov detection has been used by the MILAGRO telescope, located in New Mexico, USA. This telescope began observations in 2000 and has been operating since. It consists of a large tank of water ( $>480$  m<sup>2</sup> surface area, 8 m depth) with 723 photomultiplier tubes (PMTs) deployed in two layers (Sullivan *et al.*, 2001). The arrival direction of the air shower is determined by relative timing of signals from the PMTs. Over the lifetime of the observatory, MILAGRO has had a duty cycle  $>90\%$ , with sensitivity at energies  $>1$  TeV. Outrigger water tanks were added to the telescope in 2003. These, coupled with improved analysis, have led to the detection of four sources (Abdo *et al.*, 2007). The new analysis techniques dramatically improve background rejection, but lead to an increase in energy threshold ( $\sim 20$  TeV). Some areas of extended  $\gamma$ -ray emission have been detected by MILAGRO, demonstrating one major advantage over IAC telescopes, whose fields of view are limited by comparison. The limited field of view of IAC telescopes results in relatively difficult analysis for extended  $\gamma$ -ray sources.

Although MILAGRO is nearing the end of its operational life, plans for a follow-up experiment are under way (Dingus, 2007). The High Altitude Water Cherenkov (HAWC) experiment will be located at 4300 m and will have a surface area of 22500 m<sup>2</sup>. Similar to MILAGRO, it will be an all-sky telescope, but will be  $\sim 15$  times more sensitive.

## 2.4 TeV $\gamma$ -ray Sources

The early days of VHE  $\gamma$ -ray astronomy were fraught with claims of detections which could not be verified. This was due to the discipline being so new, detector technology being rather primitive, and the fact that  $\gamma$ -ray “signal” is largely drowned out by hadronic background. Also,

## 2.4. TeV $\gamma$ -ray Sources

---

the detection medium being used (*i.e.* the atmosphere) can neither be controlled nor easily parameterised as atmospheric conditions vary. To overcome these inconsistencies, Weekes (2000) suggested that reported detections be graded based on a number of criteria. Firstly, the detection level must have a statistical significance  $\geq 5\sigma$ . Secondly, the source must be detected at a similar statistical level by a second experiment. The statistical significance of the detection should include a best estimate of systematic effects. If all of these criteria are met, the detection is awarded an “A” grade. If the detection is not verified by another experiment, but the detection has a statistical significance  $\geq 5\sigma$  and the systematic effects have been accounted for, the detection is awarded a “B” grade. A statistically significant detection with time variability, or other such factors which introduce degrees of freedom, would gain a “C” grade.

At the 30<sup>th</sup> International Cosmic Ray conference in Merida, Mexico in 2007, the number of “B” grade (or better) detections of VHE sources had risen to 71 (Hinton, 2007). The rise has been exponential and is seen to follow a similar trend to that experienced in the early days of both x-ray and HE  $\gamma$ -ray astronomy. This is a remarkable achievement, as Imaging Atmospheric Cherenkov telescopes are not wide-field instruments. Where satellites (x-ray and soft  $\gamma$ -ray) have the ability to survey swathes of the sky in relatively short periods of time with reasonable sensitivities, IAC telescopes have narrow fields of view (typically  $\leq 5^\circ$ ) and require long exposures to discern weaker sources from immense background. For this reason, careful candidate source selection based on emission models and observations at other wavelengths is necessary.

As the catalogue of TeV sources grows, a better understanding of the types of objects which might be good candidates for TeV emission is gained. In the case of blazars for instance, it was initially thought that detection at soft  $\gamma$ -ray energies was a good indicator of the potential for TeV emission. This selection criterion led to very limited success. However, after the detection of the first few VHE blazars, it became

## 2.4. TeV $\gamma$ -ray Sources

---

apparent that emission in the hard x-ray band is a better indicator that a blazar emits an observable VHE  $\gamma$ -ray component.

The current catalogue of TeV  $\gamma$ -ray sources includes a variety of different classes of object; both galactic and extragalactic. Galactic objects include supernova remnants (SNRs) – shell-type SNRs and pulsar wind nebulae (PWN) – and binary systems such as x-ray binaries and low-mass binaries. There are also galactic sources whose counterparts at other wavelengths are unclear. These are referred to as “unidentified sources”. Extragalactic sources mainly consist of active galactic nuclei of different types: High-Frequency BL Lacs (HBL), Low-Frequency BL Lacs (LBL), Flat Spectrum Radio Quasars (FSRQs) along with one other radio-loud non-blazar-type galaxy. These object classes are described in the following sections.

### 2.4.1 Galactic Sources

Many of the sources added to the catalogue of VHE  $\gamma$ -ray emitters in the last few years have been galactic. This has mainly been a result of surveys and observations of the Galactic Centre and its surrounds. The first of the current generation of instruments working at these energies to come online was HESS. Its location in the southern hemisphere allows for viewing of the Galactic Centre. A survey of the region by HESS, along with follow-up observations, has produced an unprecedented frequency of new source detections (Hoppe *et al.*, 2007).

Although many of the new galactic  $\gamma$ -ray sources have been associated with a counterpart at another wavelength, the majority are unidentified sources. Of the new sources which have been identified with counterparts, the majority are supernova remnants. The different classes of galactic sources are described in the sections that follow. Table 2.3 shows a list of the current catalogue of identified galactic sources of TeV  $\gamma$ -rays, as detected by IAC telescopes.

## 2.4. TeV $\gamma$ -ray Sources

Source	Type	Discoverer	Distance
Crab	PWN	Whipple	2.0 kpc
HESS J1640-465	PWN	HESS	8.6 kpc
IC443	PWN	MAGIC	1.5 kpc
Kookaburra Pulsar	PWN	HESS	5.6 kpc
Kookaburra (Rabbit)	PWN	HESS	5.6 kpc
HESS J1718-385	PWN	HESS	4.2 kpc
Vela	PWN	CANGAROO	0.29 kpc
MSH 15-52	PWN	HESS	5.2 kpc
Cas A	SNR SHELL	HEGRA	3.4 kpc
RX J1713.7-3946	SNR SHELL	CANGAROO	1 kpc
RX J0852.0-4622	SNR SHELL	CANGAROO	0.2 kpc
W 28	SNR SHELL	HESS	3.3 kpc
CTB 37B	SNR SHELL	HESS	10.2 kpc
WR20a	WR	HESS	8.0 kpc
PSR B1259-63	BIN	HESS	1.5 kpc
LS 5039	BIN	HESS	8.0 kpc
LS1 61+303	XRБ	MAGIC	2.0 kpc
Cen X-3	XRБ	Durham	8.0 kpc

**Table 2.3:** Galactic TeV  $\gamma$ -ray sources. All sources listed have a minimum “B class” detection and have been published in a refereed journal. WR, BIN and XRБ are Wolf-Rayet stars, binaries and x-ray binaries respectively. Table adapted from Tevcat (<http://tevcat.uchicago.edu/>).

## 2.4. TeV $\gamma$ -ray Sources

---

### Supernova Remnants (SNRs)

A supernova remnant (SNR) is the structure that remains in the aftermath of a stellar supernova explosion. A shockwave (*i.e.* a abrupt, propagating density change in a medium) carries gas and material (*i.e.* ejecta) away from the explosion site, sweeping up interstellar matter as it expands into space. As the shockwave interacts with interstellar matter, a high-temperature plasma is formed at the region of interaction.

There are thought to be two types of SNR. The first type – Pulsar wind nebulae (PWNe) – are thought to be powered by a relativistic wind that is generated by a central pulsar (*i.e.* highly-magnetised, rotating neutron star emitting beams of electromagnetic radiation). The Crab nebula is a typical member of this class. In the second type – shell-type SNRs – most of the observed radiation is thought to come from the site of interaction of the shell expanding into interstellar medium. They are not thought to be powered from a central power source. There are also thought to be SNRs with a mixture of these two morphologies.

### The Crab Nebula

The Crab Nebula is one of the best studied celestial objects, emitting at all wavelengths from radio through to VHE  $\gamma$ -rays. It is the brightest object in the night sky at many of these wavelengths. The supernova which created the Crab Nebula was observed by Chinese, Arab and Irish astronomers in 1054, when its brightness made it visible with the unaided eye during daytime for over three weeks.

The neutron star which powers the Crab Nebula was discovered to be an optical pulsar in 1967, with a period of 33 ms. The frequency of the pulsar is slowly decreasing. The energy lost by the pulsar is seen to be equal to the energy radiated by the nebula.

VHE  $\gamma$ -ray emission from the Crab Nebula was predicted long before a solid detection was achieved (Cocconi, 1959). Based on this predic-

## 2.4. TeV $\gamma$ -ray Sources

---

tion, many experiments set about trying to detect such emission, without credible success until 1989 when a clear steady signal was detected by the Whipple 10 m telescope after 60 hours of observation (Weekes *et al.*, 1989). Since then, as the sensitivities of various VHE experiments have improved, detecting the Crab Nebula has become a relatively simple endeavour. A  $5\sigma$  detection is currently possible within an hour of observation time on the Whipple 10 m telescope and within minutes with the latest generation of instruments, such as VERITAS.

Since the Crab Nebula is a steady source of TeV  $\gamma$ -ray emission, it has been adopted as the “standard candle” for the field. It is visible from both the northern and southern hemispheres, which is advantageous for the calibration of instruments around the world. At even higher energies, experiments such as MILAGRO (Atkins *et al.*, 2003) and Tibet AS $\gamma$  (Amenomori *et al.*, 2005) have detected emission from the Crab Nebula. The VHE  $\gamma$ -ray spectra measured by all experiments are in good agreement. Levels of emission in excess of that of the Crab Nebula have been detected from other objects, but these have always been variable sources. As an easily detectable source, the Crab has aided the refinement of instrumentation and analysis techniques for detecting other  $\gamma$ -ray sources.

The search for 33 ms pulsed  $\gamma$ -ray emission from the Crab in the TeV energy band by all IAC telescopes has been unsuccessful (*e.g.* Celik *et al.*, 2007; Nepomuk Otte *et al.*, 2007; Aharonian *et al.*, 2004b, 2007f). A number of IAC telescopes have been able to observe the 33 ms optical pulses of the Crab pulsar. Air-shower arrays have also been unsuccessful when trying to detect VHE  $\gamma$ -ray pulsing. The MAGIC Collaboration has recently announced detection of pulsed  $\gamma$ -ray emission from the Crab pulsar at  $> 25$  GeV energies. Using a modified trigger system which lowered the energy threshold of the MAGIC telescope from its normal threshold of 60 GeV, a pulsed  $\gamma$ -ray signal coinciding with the optical pulsar is evident (Aliu *et al.*, 2008; Teshima, 2008).

The TeV  $\gamma$ -ray emission of the Crab Nebula is understood to be a

## 2.4. TeV $\gamma$ -ray Sources

---

result of two processes: synchrotron emission from relativistic electrons in the pulsar wind shocks and inverse Compton scattering of electrons off neighbouring photons. The observed GeV - TeV emission is thought to arise from the inverse Compton processes.

### Pulsar Wind Nebulae (PWNe)

Recent observations by IAC telescopes, including a sky survey of the Galactic Centre region by HESS, have increased the number of pulsar wind nebulae (PWNe) that are known to emit VHE  $\gamma$ -rays. In fact, they are currently the largest population of identified galactic TeV sources. The Crab Nebula is one of the best examples of a PWN. As with the Crab, most of the PWNe detected have high spin-down velocities. Of the seven TeV  $\gamma$ -ray sources which have strong PWN associations, six have been detected since 2005. There is evidence for strong positional coincidence of TeV  $\gamma$ -ray nebulae with high spin-down luminosity pulsars above the expectation for chance coincidences (Carrigan *et al.*, 2007).

In addition to the PWNe listed in Table 2.3, HESS have also announced the detection of a further six VHE  $\gamma$ -ray sources with strong PWN associations: PSR J1846-0258, Kes 75, G 21.5-0.9, HESS J1809-193, HESS J1357-645 and HESS J1912+102 (Djannati-atai *et al.*, 2007b; Lemièrre *et al.*, 2007). These have not been included in Table 2.3 as their detections have yet to be confirmed by other observatories.

At higher energies, MILAGRO's sky survey has turned up an excess which is coincident with the location of Geminga (Abdo *et al.*, 2007), although the excess only has a significance of  $2.8\sigma$ . This detection is not definitive, but is noted as a tentative result - the first such result from a water Cherenkov detector.

## 2.4. TeV $\gamma$ -ray Sources

---

### Shell-Type Supernova Remnants

For many years now, shell-type supernova remnants (SNRs) have been the prime candidates for the acceleration of the bulk of the galactic cosmic ray protons and nuclei. The reasons why they are candidates are two-fold. Firstly, a supernova explosion has sufficient energy to accelerate the particles. In order for cosmic rays to be produced in the explosion, the efficiency of converting the supernova explosion's kinetic energy into relativistic particles must be around 10% (Drury *et al.*, 1989), which is thought to be possible. Secondly, the mechanism by which this explosion energy is transferred to particles with TeV - EeV energies is thought to be diffuse shock acceleration (Bell, 1978; Blandford & Ostriker, 1978) whereby shockwaves in ionised media (such as interstellar and interplanetary space) can accelerate energetic charged particles. Despite the fact that shell-type SNRs have been considered viable candidates for many years, evidence for the acceleration of particles in SNRs has only begun to emerge recently. Non-thermal x-ray radiation from objects such as SN1006 has been interpreted as synchrotron radiation. Based on this, it had been surmised that acceleration of electrons to  $\sim 100$  TeV is possible in SNRs (Koyama *et al.*, 1995).

Definitive evidence that this electron acceleration was taking place in SNRs only came with CANGAROO's detection of RX J1713.7-3946 and its subsequent detection by HESS with better spatial resolution (Muraishi *et al.*, 2000; Aharonian *et al.*, 2004d). X-ray emission from this young ( $\sim 2100$  years) SNR had already been detected by ROSAT (Pfeffermann & Aschenbach, 1996). Recent observations by the HESS Collaboration resulted in the detection of  $\gamma$ -ray emission from the region surrounding the SNR. It was then possible to resolve features in the SNR shell with a resolution of  $\sim 0.06^\circ$ . Aharonian *et al.* (2007d) outline similar observations that have been carried out on the shell-type SNR J0852.0-4622, which is also known by the name Vela Junior. Vela Junior's features are

## 2.4. TeV $\gamma$ -ray Sources

---

quite extended and the observed VHE  $\gamma$ -ray flux level is comparable to that of the Crab Nebula.

The recent observations of these two shell-type SNRs have presented problems to modellers who, until recently, had favoured an “electronic” model for VHE emission over a “hadronic” one. In the electronic model, inverse Compton scattering of energetic electrons on background microwave radiation is thought to produce the TeV emission. In the hadronic scenario, emission is due to decay of neutral pions that are produced in collisions within an energetic proton gas. The shape of emission spectra of both J1713.7-3946 and J0852.0-4622 seem to favour the hadronic model (Aharonian *et al.*, 2006b, 2007d). There is still a degree of ambiguity however. Plaga (2008) points out that flux levels from the centre of the SNR are 40 times higher than the flux level predicted by the hadronic model. Emission levels from the cloud are around 3 times lower than expected. The hadronic model favours the majority of the emission coming from the cloud complex, but this is not what has been seen in observations.

Cas A was originally detected by HEGRA (Aharonian *et al.*, 2001a) with 232 hours of data taken between 1997 and 1999. It has also been detected by MAGIC (Albert *et al.*, 2007d). The angular resolution of both HEGRA and MAGIC did not allow any features of the SNR shell to be resolved. Therefore, no morphological analyses can currently be carried out to examine features of the shell.

### **Binaries**

X-ray binaries are some of the most luminous objects at x-ray energies. Usually, the binary system consists of a relatively normal star orbiting a neutron star or black hole. The x-rays are produced when matter accretes onto the compact object from its companion star, releasing gravitational potential energy in the form of x-ray radiation with energy a few percent of its rest mass. An accretion disc is normally present around the

## 2.4. TeV $\gamma$ -ray Sources

---

compact object. It is thought that some of these objects may emit VHE  $\gamma$ -rays through outflow from relativistic jets, similar to emission from TeV blazars but on a much smaller scale. In this scenario, the compact object may act like the supermassive black hole of a regular quasar, with VHE photons produced in relativistic jets by processes similar to those that drive VHE emission from blazars. The jets must be aligned along the viewing axis from Earth in order for VHE  $\gamma$ -ray emission to be detected. Because of the obvious parallels with quasars, they are often called microquasars.

A number of  $\gamma$ -ray binary systems have been detected at TeV energies. The  $\gamma$ -ray emission is powered by a pulsar orbiting a massive, luminous Be star (luminous, blue star with strong Hydrogen emission lines). The pulsar wind interacts with the material and radiation around the Be star. Chadwick *et al.* (1998) outline the Durham group's detection of Centaurus X-3 (Cen X-3) in 1998 with a statistical significance of  $6.3\sigma$  in 10 hours of observation. This was the first firm detection of VHE  $\gamma$ -ray emission from an x-ray binary (XRB). There was no evidence for variability or pulsing of the  $\gamma$ -ray signal, though the compact object is a 4.8 second optical pulsar and the orbital period of the system is 2.1 days.

LSI 61+303 is a binary system which has been detected at TeV energies (Albert *et al.*, 2006e). It has been associated with a COS-B source, which was detected in 1978 (Gregory & Taylor, 1978). In the intervening years, radio and x-ray (Harrison *et al.*, 2000) flaring has been seen. X-ray outbursts are consistently seen during certain phases of the binary system's orbit (Harrison *et al.*, 2000). Periodicity at  $\gamma$ -ray energies has also been detected by MAGIC. Further observations of the system by the Whipple 10 m telescope provided flux upper limits at orbital phases where, at TeV energies, there had been none previously (Smith *et al.*, 2007). VERITAS conducted more sensitive observations of this object (in 2-telescope mode and 3-telescope mode, while the array was being built) as part of a multiwavelength campaign that included contempora-

## 2.4. TeV $\gamma$ -ray Sources

---

neous x-ray and HE  $\gamma$ -ray energies respectively (Acciari *et al.*, 2008b). Both x-ray and  $\gamma$ -ray datasets (after grouping the data by orbital phase – *i.e.* phase-folding) displayed a flux peak around apastron of the binary orbit (Smith *et al.*, 2008).

In their survey of the galactic plane, the HESS Collaboration detected the high-mass X-Ray Binary (XRB) LS 5039 (Aharonian *et al.*, 2005c). This binary system is a known x-ray emitter (Bosch-Ramon *et al.*, 2007) which has radio-resolved relativistic jets, putting it in the microquasar class of XRBs. 3.9 day flux modulation has been observed at TeV energies (Aharonian *et al.*, 2006a), corresponding to the orbital period of the system (Casares *et al.*, 2005). Both the  $\gamma$ -ray flux and spectrum are seen to vary as a function of phase (de Naurois, 2007). The flux displays a sinusoidal variation with orbital phase, which could be indicative of  $\gamma$ -ray absorption by pair production in the stellar photon field. Analysis of these phase-dependent modulations could also suggest that  $\gamma$ -ray emission occurs much closer to the compact object than previously thought. As such, it may not be a microquasar.

PSR B1259-63 is a binary system, comprised of a pulsar in an eccentric 3.4-year orbit around a large Be star. TeV emission was detected from this object at periastron in 2004 (Aharonian *et al.*, 2005b). It is thought that the emission arises from the interaction of the pulsar’s wind with the radiation and material field of the Be star. The Be star crosses the wind at periastron due to the orbital eccentricity of the system. VHE  $\gamma$ -ray emission was detected, as expected, during its 2007 periastron pass (Kerschhaggl *et al.*, 2007). Observations prior to periastron did not result in the detection of significant emission.

### Unidentified Sources

Many of the galactic TeV  $\gamma$ -ray sources discovered to date have no readily distinguishable counterpart at other wavelengths. These are often called “unidentified sources”. One of the reasons for the lack of counterparts

## 2.4. TeV $\gamma$ -ray Sources

---

for these sources is the fact that some objects may have a morphology at TeV energies that does not match their morphology when the object is viewed in other energy bands. The emitting objects may also be party to unknown physical processes that are responsible for the emission of VHE  $\gamma$ -rays. Unidentified sources are the subject of great interest at HE and VHE  $\gamma$ -ray energies. Around two-thirds of the EGRET catalogue of sources are unidentified. Due to its superior angular resolution, GLAST may help to identify many of these sources. The overlap in energy bands between GLAST and the current generation of imaging atmospheric Cherenkov telescopes should also offer new spectral information about these sources, which might be used to identify the physical processes involved in their emission.

Unidentified VHE  $\gamma$ -ray sources may be separated into two basic classes:

- Sources with a putative counterpart detected in other energy bands which is positionally coincident, but with no other strong evidence for an association. Some of these may be resolved with deeper observations or more detailed multi-wavelength analyses.
- Sources with no obvious counterpart in any other energy band. Often, these sources have GeV and TeV components, but are not visible at x-ray or lower energies. They are usually labelled “dark sources” or “dark accelerators”.

Many unidentified sources have been detected in the survey of the galactic plane by HESS (Aharonian *et al.*, 2006f). Prior to these discoveries, the only unidentified source was the dark accelerator TeV J2032+4130 which was discovered by the Crimean Astrophysical Observatory (Neshpor *et al.*, 1995) and later confirmed by HEGRA (Aharonian *et al.*, 2002a, 2005g). An analysis of archival Cygnus X-3 data taken by the Whipple 10 m telescope during the 1989 - 1990 season produced a  $3.3\sigma$  excess at a location  $0.6^\circ$  north of Cygnus X-3 (Lang *et al.*, 2004), which corresponds

## 2.4. TeV $\gamma$ -ray Sources

---

to the location of TeV J2032+4130. More recent observations by MAGIC have confirmed the detection (Albert *et al.*, 2008).

The Galactic Centre region has been shown by a number of observatories to emit TeV  $\gamma$ -rays although it is not entirely clear what type of object or objects (within the resolution of the instrument) may be driving the  $\gamma$ -ray emission. It was first reported by CANGAROO (Tsuchiya *et al.*, 2004). Subsequent observations by HESS (Aharonian *et al.*, 2004c), the Whipple 10 m telescope (Kosack *et al.*, 2004) and MAGIC (Albert *et al.*, 2006c) have shown reasonable excesses. Sagittarius A\* has been suggested as the source of this emission, though this association has not been substantially proven (Hinton *et al.*, 2007).

HESS J1023-575 is positionally coincident with Westerlund 2, the second largest stellar cluster in the Galaxy. Although an association cannot be definitively made yet, a confirmed association would suggest a new class of VHE  $\gamma$ -ray sources. The powerful stellar winds between the stars making up these clusters certainly have enough energy to generate VHE  $\gamma$ -ray photons. A definitive association remains to be seen however.

The unidentified sources of TeV  $\gamma$ -rays that have been detected by the HESS galactic plane sky survey are outlined in Table 2.4. Further to those sources detected in their survey, HESS have serendipitously discovered emission from HESS J1303-631 during observations of the binary system PSR B1259-63, which was also detected in the same field of view (Aharonian *et al.*, 2005f). Emission has been detected from HESS J0632+057 (Aharonian *et al.*, 2007g). Although this source is near the Monoceros Loop SNR, it is point-like within the angular resolution of HESS. It is unclear if the SNR is the source of this emission. Recent observations of the galactic plane has added exposure depth to their survey. This has resulted in the detection of a further six unidentified sources (Kosack *et al.*, 2007; Aharonian *et al.*, 2008c).

Seven years of “all-sky” data from the MILAGRO experiment have added three unidentified sources to the TeV catalogue: MGRO J2031+41,

## 2.4. TeV $\gamma$ -ray Sources

Source	RA	Dec.	Publication
<b>J0632+058</b>	06 <sup>h</sup> 32 <sup>m</sup> 58.0 <sup>s</sup>	+05° 48' 20"	Aharonian <i>et al.</i> (2007g)
<b>J1427-608</b>	14 <sup>h</sup> 27 <sup>m</sup> 52.0 <sup>s</sup>	-60° 51' 00"	Aharonian <i>et al.</i> (2008c)
<b>J1614-518</b>	16 <sup>h</sup> 14 <sup>m</sup> 19.0 <sup>s</sup>	-51° 49' 07"	Aharonian <i>et al.</i> (2005a)
<b>J1616-508</b>	16 <sup>h</sup> 16 <sup>m</sup> 23.6 <sup>s</sup>	-50° 53' 57"	Aharonian <i>et al.</i> (2005a)
<b>J1626-490</b>	16 <sup>h</sup> 26 <sup>m</sup> 04.0 <sup>s</sup>	-49° 05' 13"	Aharonian <i>et al.</i> (2008c)
<b>J1632-478</b>	16 <sup>h</sup> 32 <sup>m</sup> 08.6 <sup>s</sup>	-47° 49' 24"	Aharonian <i>et al.</i> (2006f)
<b>J1634-472</b>	16 <sup>h</sup> 34 <sup>m</sup> 57.2 <sup>s</sup>	-47° 16' 02"	Aharonian <i>et al.</i> (2006f)
<b>J1702-420</b>	17 <sup>h</sup> 02 <sup>m</sup> 44.6 <sup>s</sup>	-42° 04' 22"	Aharonian <i>et al.</i> (2005a)
<b>J1708-410</b>	17 <sup>h</sup> 08 <sup>m</sup> 14.3 <sup>s</sup>	-41° 04' 57"	Aharonian <i>et al.</i> (2006f)
<b>J1713-381</b>	17 <sup>h</sup> 13 <sup>m</sup> 58.0 <sup>s</sup>	-38° 12' 00"	Aharonian <i>et al.</i> (2006f)
<b>J1731-347</b>	17 <sup>h</sup> 31 <sup>m</sup> 55.0 <sup>s</sup>	-34° 42' 56"	Aharonian <i>et al.</i> (2008c)
<b>J1745-303</b>	17 <sup>h</sup> 45 <sup>m</sup> 02.2 <sup>s</sup>	-30° 22' 14"	Aharonian <i>et al.</i> (2006f)
<b>J1747-281</b>	17 <sup>h</sup> 47 <sup>m</sup> 23.2 <sup>s</sup>	-28° 09' 06"	Aharonian <i>et al.</i> (2006f)
<b>J1804-216</b>	18 <sup>h</sup> 04 <sup>m</sup> 31.6 <sup>s</sup>	-21° 42' 03"	Aharonian <i>et al.</i> (2005a)
<b>J1809-193</b>	18 <sup>h</sup> 10 <sup>m</sup> 31.0 <sup>s</sup>	-19° 18' 00"	Aharonian <i>et al.</i> (2007b)
<b>J1813-178</b>	18 <sup>h</sup> 13 <sup>m</sup> 36.6 <sup>s</sup>	-17° 59' 35"	Aharonian <i>et al.</i> (2005a)
<b>J1825-137</b>	18 <sup>h</sup> 26 <sup>m</sup> 03.0 <sup>s</sup>	-13° 45' 44"	Aharonian <i>et al.</i> (2005a)
<b>J1837-069</b>	18 <sup>h</sup> 37 <sup>m</sup> 37.4 <sup>s</sup>	-06° 56' 42"	Aharonian <i>et al.</i> (2005a)
<b>J1834-087</b>	18 <sup>h</sup> 34 <sup>m</sup> 46.5 <sup>s</sup>	-08° 45' 52"	Aharonian <i>et al.</i> (2005a)
<b>J1841-055</b>	18 <sup>h</sup> 40 <sup>m</sup> 55.0 <sup>s</sup>	-05° 33' 00"	Aharonian <i>et al.</i> (2008c)
<b>J1857+026</b>	18 <sup>h</sup> 57 <sup>m</sup> 11.0 <sup>s</sup>	+02° 40' 00"	Aharonian <i>et al.</i> (2008c)
<b>J1858+020</b>	18 <sup>h</sup> 58 <sup>m</sup> 20.0 <sup>s</sup>	+02° 05' 24"	Aharonian <i>et al.</i> (2008c)
<b>J1912+101</b>	19 <sup>h</sup> 12 <sup>m</sup> 49.0 <sup>s</sup>	+10° 09' 06"	Aharonian <i>et al.</i> (2008a)

**Table 2.4:** Unidentified galactic VHE  $\gamma$ -ray sources, as discovered by the HESS galactic plane survey.

## 2.4. TeV $\gamma$ -ray Sources

---

MGRO 2019+37 and MGRO J1908+06 (Abdo *et al.*, 2007). All three sources have fluxes at energies  $>20$  TeV approaching that of the Crab Nebula. MGRO J2031+41 and MGRO J2019+37 both appear to be extended beyond the  $1^\circ$  resolution of MILAGRO. These two sources have not been detected by ground-based imaging atmospheric Cherenkov telescopes. Although IAC telescopes have superior angular resolution to MILAGRO, their ability to detect extended sources is limited by their relatively small field of view.

HESS observations of MGRO J1908+06 have resulted in the detection of a point source (Djannati-atai *et al.*, 2007a). Spectral measurements by both experiments are in excellent agreement. This is the first case of a TeV  $\gamma$ -ray source detection by a non-IAC telescope being confirmed by an IAC telescope.

### 2.4.2 Extragalactic Sources

#### Active Galactic Nuclei (AGN)

Active galactic nuclei are the only extragalactic objects yet seen to emit VHE  $\gamma$ -rays. The bright core of an active galaxy far outshines the rest of the galaxy, often by a factor of  $\sim 1000$ . AGN were first identified in 1962, when a pattern of lines in the optical spectrum of 3C 273 was interpreted as the Balmer series of hydrogen lines, red-shifted to  $z = 0.158$  (Schmidt, 1963). 3C 273 had previously been catalogued as a star but, with such a redshift, the object could not be in our galaxy. It was termed a *quasi-stellar object* or “quasar”.

Quasars are now known to be a subset of the larger AGN population of extragalactic objects. Of the AGN which have been detected at TeV energies, most are of the *blazar* class. All of the blazars that have been detected fall into the category of *BL Lacertae* objects (BL Lacs) which are highly variable and are usually seen to be devoid of optical emission lines. BL Lacs are further subdivided into High-Frequency BL Lacs and

## 2.4. TeV $\gamma$ -ray Sources

---

Low-Frequency BL Lacs, based on whether they were discovered in x-ray surveys or radio surveys. Most of the blazars found to emit at VHE energies are HBLs. The science underlying the emission mechanisms, the taxonomy and other properties of AGN are discussed in detail in Chapter 3.

Markarian 421 was the first source of extragalactic TeV  $\gamma$ -rays discovered (Punch *et al.*, 1992). It was detected by the Whipple 10 m telescope in 1992, at a  $6\sigma$  level, with a flux of  $\sim 30\%$  that of the Crab Nebula. HEGRA confirmed the detection (Petry *et al.*, 1996). It has since been detected by many groups and is the best-studied TeV blazar. Observations of Markarian 421 were motivated by the detection of various flat-spectrum radio quasars by EGRET. The detection of FSRQs by EGRET turned attention onto other bright FSRQs such as 3C 273 and 3C 279, which were not detected.

Failure to detect FSRQs that had been detected by EGRET led to a re-evaluation of selection criteria for potential sources of extragalactic emission. Objects with similar characteristics to Markarian 421 were instead chosen. This led to the detection of VHE  $\gamma$ -ray emission from Markarian 501. The detection was first reported by the Whipple group (Quinn *et al.*, 1996) and was the first discovery of a new  $\gamma$ -ray source by a ground-based telescope. The initial detection was at the  $8.4\sigma$  level with a flux of around 10% of the Crab Nebula. Markarian 421 and Markarian 501 are considered “typical” TeV blazars. Since they are easier to detect than most other HBLs, much of what is known about the emission mechanisms of this class of blazar comes from studying them.

Table 2.5 lists the HBLs which have been thus far detected. The southern hemisphere blazar PKS 2155-304, which was initially detected by the Durham group during 1996 and 1997 (Chadwick *et al.*, 1999), is worth noting. It is a relatively distant HBL, with a redshift of  $z = 0.116$ . A  $6.8\sigma$  detection in 41 hours of data comprised the initial detection.

## 2.4. TeV $\gamma$ -ray Sources

Source Name	$z$	Publication
<b>Markarian 421</b>	0.031	Punch <i>et al.</i> (1992)
<b>Markarian 501</b>	0.034	Quinn <i>et al.</i> (1996)
<b>1ES 2344+514</b>	0.044	Catanese <i>et al.</i> (1998)
<b>Markarian180</b>	0.046	Albert <i>et al.</i> (2006b)
<b>1ES 1959+650</b>	0.047	Nishiyama (1999)
<b>PKS 0548–322</b>	0.069	Superina <i>et al.</i> (2007)
<b>PKS 2005–489</b>	0.071	Aharonian <i>et al.</i> (2005d)
<b>PKS 2155–304</b>	0.116	Chadwick <i>et al.</i> (1999)
<b>H 1426+428</b>	0.129	Horan <i>et al.</i> (2002)
<b>1ES 0229+200</b>	0.140	Aharonian <i>et al.</i> (2007e)
<b>H 2356–309</b>	0.165	Aharonian <i>et al.</i> (2006d)
<b>1ES 1218+304</b>	0.182	Albert <i>et al.</i> (2006a)
<b>1ES 1101–232</b>	0.186	Aharonian <i>et al.</i> (2006c)
<b>1ES 0347–121</b>	0.188	Aharonian <i>et al.</i> (2007c)
<b>1ES 1011+496</b>	0.212	Albert <i>et al.</i> (2007b)
<b>PG 1553+113</b>	>0.25	Aharonian <i>et al.</i> (2006e)

**Table 2.5:** List of high-frequency BL Lac objects that are confirmed VHE  $\gamma$ -ray emitters arranged in order of increasing redshift. List adapted from Tevcat (<http://tevcat.uchicago.edu>).

Variability within the dataset was also reported. Aharonian *et al.* (2005e) reported the confirmation of the source by HESS. HESS noted variability on small timescales. Emission levels varied from 10% to 60% of that of the Crab Nebula during these observations (July - October 2002 and June - September 2003). HESS later detected PKS 2155-304 in an extremely high state of activity in July 2006 (Aharonian *et al.*, 2007f). On one night of observation, average flux levels of  $\sim 7$  times that of the Crab Nebula were detected. Such high flux levels permitted variability and spectral studies with unprecedented time resolution. Fluxes measured with one-minute resolution exhibited peak values in excess of 14 times the Crab Nebula flux. Variability on timescales of  $< 4$  minutes was noted. No spectral variation was evident within the data.

The eponymous BL Lacertae (BL Lac) is currently the only confirmed

## 2.4. TeV $\gamma$ -ray Sources

---

low-frequency peaked BL Lac object to be detected at TeV energies. It was originally detected at the Crimean Astrophysical Observatory at a  $7.2\sigma$  level in 24 hours of observation (Neshpor *et al.*, 2001). This detection has been confirmed by the MAGIC group (Albert *et al.*, 2007a). A  $5.1\sigma$  level detection at around 3% of the Crab flux was noted in  $\sim 22$  hours of data in 2005. Follow-up observation in 2006 did not yield a detection from the entire 2006 data set and flaring was not evident during the observations. The non-detection was assumed to be due to the source being in a low state of emission which was below the sensitivity of the telescope. This lower state of activity at TeV energies in 2006 correlated with lower optical flux in the same period.

Another object worth noting is the giant radio (Fanaroff-Riley I or FRI) galaxy M87. Currently, it is the only non-BL Lac galaxy to be detected at TeV energies. An excess with significance of  $\sim 4\sigma$  was initially noted by the HEGRA group (Aharonian *et al.*, 2003b). Subsequent observations with the Whipple 10 m telescope only produced upper limits (Le Bohec *et al.*, 2004). More recent observations by HESS (Beilicke *et al.*, 2007; Beilicke, 2007) and VERITAS (Acciari *et al.*, 2008a) have confirmed the source as a VHE  $\gamma$ -ray emitter. M87 is a radio galaxy with large relativistic jets. However, the angle between the line-of-sight and the jet seems to be  $\sim 30^\circ$ , unlike the usual  $\sim 10^\circ$  of previously detected TeV blazars.

MAGIC have recently claimed a transient detection of the FSRQ 3C 279 which, at a redshift of  $z = 0.536$ , would be the most distant TeV blazar detected to date (Teshima *et al.*, 2007). Interestingly, observations of 3C 279 were triggered when its optical flux had risen significantly. Both Markarian 180 (Albert *et al.*, 2006b) and 1ES 1011+496 (Albert *et al.*, 2007b) were also detected by MAGIC when observations were triggered by high optical flux levels, although no definitive correlation has been found to exist between VHE  $\gamma$ -ray emission and optical emission for HBLs.

## 2.4. TeV $\gamma$ -ray Sources

---

Five HBLs have been studied in this thesis: Markarian 421, Markarian 501, 1ES 2344+514, 1ES 1959+650 and H 1426+428. Summaries of their initial detections, multiwavelength emission characteristics and past observation campaigns are given in Chapter 3.

### 2.4.3 Other Potential Sources

#### Gamma-Ray Bursts (GRBs)

GRBs were discovered serendipitously in 1967 when data from four Vela satellites, which were looking for bursts of radiation that might be caused by nuclear weapons, were analysed. Klebesadel *et al.* (1973) ruled out the Earth and the Sun as sources of these bursts. The likelihood of supernovae being their source was also discussed, but no correlations could be found.

GRBs are thought to originate in relativistic “fireballs” which occur after the core collapse of massive stars or the coalescence of compact objects. Although they are the most luminous objects in the Universe (Piran, 1999) and emission at  $\sim 20$  GeV has been detected by EGRET, no evidence of TeV emission exists either during the burst or the afterglow.

The Swift, HETE-II and INTEGRAL satellites all monitor the sky for GRBs. When a burst is detected and localised, coordinates are sent to the Gamma-ray bursts Coordinate Network (GCN) which alerts subscribing members. Although many imaging atmospheric Cherenkov telescopes subscribe to this network, the processing delay of a few seconds coupled with the relatively long slewing time makes it difficult to observe GRBs at TeV energies close to the time the burst occurs. HESS have serendipitously had a GRB occur in their field of view during observations of a different object (Aharonian *et al.*, 2008b). No significant  $\gamma$ -ray excess was detected, but the burst may have been an x-ray flare of galactic origin and not a GRB. The afterglows of many GRBs have been monitored by TeV telescopes. However, only flux upper limits have resulted. If GRBs

## 2.4. TeV $\gamma$ -ray Sources

---

have a TeV component, they still may not be detectable by ground-based instruments due to extragalactic background light (EBL) absorption and the large associated redshifts.

### Potential Extragalactic Sources

Currently, the only extragalactic objects detected at TeV energies have been active galactic nuclei (HBLs, LBLs, FSRQs and FRIs). However, there may be weaker types of extragalactic TeV emission which will be detectable by current or next generation ground-based instruments. Starburst Galaxies (Nagai *et al.*, 2003) and ultra-luminous infrared galaxies (ULIRGs) are chief among the candidates to be explored (Hinton, 2007). M82 is an archetypical starburst galaxy. A close encounter with nearby M81 has led to a high rate of star formation, with streams of hydrogen linking the two galaxies visible in radio maps of the region.

ULIRGS are large dusty galaxies. Ultraviolet light which is incident on the obscuring dust is absorbed and re-radiated as infrared radiation. Some x-ray observations of ULIRGs have suggested that they are double-cored. This may be because they are a result of merging of galaxies. There is also a suggestion that they are internally powered by AGN.

# Chapter 3

## The Science of Active Galactic Nuclei

### 3.1 Introduction

Active galactic nuclei are a type of galaxy for which the emission of the galactic core dwarfs that of the host galaxy. They are known to be bright and variable at almost all wavelengths observed. Although their emission is not yet entirely understood, it is thought that bright AGN core emission is due to accretion of matter onto a supermassive black hole (Rees, 1984). This matter is thought to orbit the black hole in an accretion disk. Matter falling onto the black hole loses angular momentum by turbulent or viscous forces. Thermal emission from the accretion disk is mainly at ultraviolet (and possibly soft x-ray) wavelengths. A dense dusty layer which bulges along the plane of the galaxy lies beyond the accretion disk. This layer tends to absorb optical and ultraviolet wavelengths along certain lines of sight. Perpendicular to the plane of the galaxy, collimated relativistic jets host some of the most energetic processes in the universe. The jets are thought to arise from distortions in space and time around the black hole, due to its mass, twisting magnetic fields into coils that can propel material outwards. Emission at wavelengths from radio to

### 3.1. Introduction

---

$\gamma$ -ray have been detected from these jets, offering an insight into the different emission processes taking place at the various regions comprising and surrounding the galaxy.

The above model for the composition of AGN adequately explains the line-of-sight dependence, in relation to the jet, for emission at higher energies. Blazars are a type of AGN whose collimated jets are aligned with our observation angle. They offer an opportunity to see some of these high-energy physical processes at work in a unique way. Coupling observations at TeV energies with those at other wavelengths may offer some constraint on models for emission which have been developed to explain the broadband properties of AGN.

Since 2005, the Whipple 10 m telescope has primarily been used to monitor the activity of a set of AGN which have previously been unambiguously detected at TeV energies (*e.g.* Kildea, 2007; Horan, 2007). These observations are part of a long-term multiwavelength campaign that was initiated by the VERITAS Collaboration and includes other participants at wavelengths from optical through to x-ray. Dedicating observation time to AGN, whether in a low or high state in any energy band, offers the possibility of unprecedented insights into the processes which underlie their emission as blazars are often only observed simultaneously at multiple wavelengths while in a heightened state of emission in a certain waveband.

In this chapter, the various types of AGN observed are summarised (Section 3.2). The collimated jets and processes they exhibit are described in Section 3.3. Various leptonic and hadronic models which have been developed to describe the observed emission from AGN are discussed in Section 3.4. Previous observations of the blazars monitored in this study are outlined (with an emphasis on very high energy and multiwavelength observations) in Section 3.5.

## 3.2 Classification of AGN

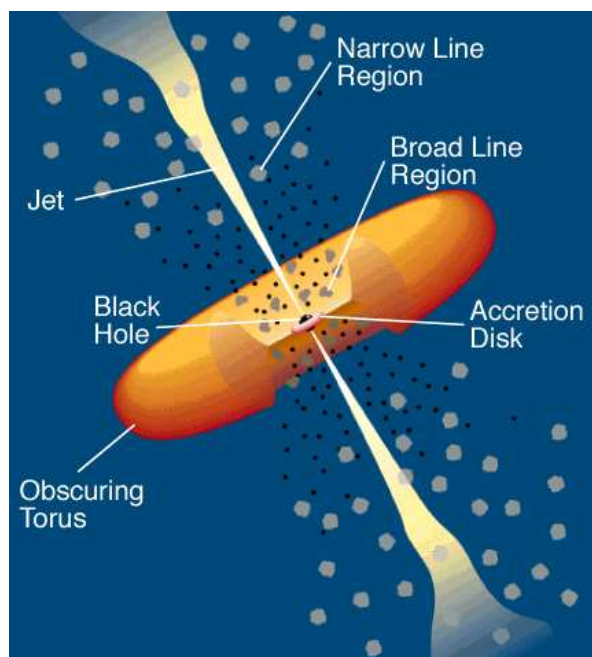
Comprising only a small percentage of all observed galaxies, AGN are characterised by their bright cores which outshine thermal emission from stars comprising the galaxy. Although AGN exhibit observable phenomena by which they could be subclassified, classification is complicated by the fact that there seems to be a large variation in the degree to which different AGN exhibit each feature. For instance, some AGN are radio-quiet (no jet) and some are radio-loud (have a jet). Some flare rapidly in certain wavebands across the electromagnetic spectrum while others are relatively steady emitters. Peak emission at radio, ultraviolet, x-ray or  $\gamma$ -ray wavelengths is another common differentiator.

Figure 3.1 shows the physical structure of an AGN, as is generally accepted (see Section 3.2.3 below). Emissions from certain regions of AGN are not observable due to the anisotropic radiation patterns. Other regions are simply obscured by the structure of the galaxy (*e.g.* the dusty obscuring torus, see Figure 3.1). Although the underlying emission processes remain somewhat mysterious, the main components comprising AGN are largely thought to be known (Urry & Padovani, 1995). The central supermassive black hole is the main energy source for the galaxy's emission. Transfer of gravitational potential energy from the black hole, as surrounding galactic matter falls onto it, is the main mechanism by which energy is released from this central engine. This method has been shown to be on the order of 100 times more efficient than nuclear fusion (Lynden-Bell, 1969).

Small, dense, fast-moving clouds of matter orbiting above (or below) the accretion disk of the black hole, due to the black hole's gravitational influence, exhibit broad optical emission lines (Holt *et al.*, 1980). The broadening is a result of Doppler effects. The strength and profile of these emission lines tends to vary on timescales on the order of around a year, suggesting that the sizes of the emitting regions are less than a light-year (Weedman, 1986). Larger clouds of matter, moving at a slower speed,

### 3.2. Classification of AGN

---



**Figure 3.1:** The broadly accepted model for the structure of AGN. Figure taken from Holt *et al.* (1992).

### 3.2. Classification of AGN

---

and farther from the black hole, exhibit narrow-line emission. These lines do not vary in shape or strength.

A large disk (or torus) of gas and dust resides outside both the accretion disk and the broad-line emission region. This torus tends to obscure the accretion disk and the broad-line region along most lines-of-sight. The narrow-line emission region is the only source of emission line information when the AGN is viewed along transverse lines-of-sight.

AGN are often classified as radio-loud or radio-quiet. Radio-loud AGN are relatively powerful radio emitters (*i.e.* in the  $10^{42}$  to  $10^{45}$  erg s<sup>-1</sup> range). Radio-quiet AGN are strong infrared emitters and only exhibit weak radio emission. Radio jets are often seen emanating from the central black hole of radio-loud AGN. Strong magnetic fields in the jet cause relativistic particles, which are present in the jet, to emit at radio to x-ray wavelengths by synchrotron radiation (*i.e.* radiation produced by electrons spiralling in the magnetic fields of the jets). These radio jets have been imaged on parsec-scales by large radio telescopes (Piner & Edwards, 2004). The jets have the effect of amplifying and concentrating the continuum emission in the directions perpendicular to the plane of the galaxy. Table 3.1 outlines some of the main properties of different AGN types.

The appearance of AGN (at most wavelengths) varies greatly with the orientation of the AGN relative to the line of sight of the observer. Intrinsically similar galaxies viewed at different viewing angles are often classified differently (Padovani, 1999). The confusing nature of these differences in emission properties lends itself to the classification system outlined in Figure 3.2. Some of the subdivisions used in this relatively simple classification system are largely historical.

All AGN detected at TeV energies thus far have been radio-loud (see Section 2.4.2). M87, a Fanaroff-Riley type 1 galaxy (also radio-loud), is the only non-blazar to be detected within this energy regime. Blazars are described in more detail in the sections that follow.

### 3.2. Classification of AGN

Class	Host Galaxy	Radio Emission	Optical Lines	Luminosity [ergs s <sup>-1</sup> ]
Blazar	E	Strong	Weak	10 <sup>45</sup> – 10 <sup>49</sup>
Radio-loud quasar	E	Strong	Broad	10 <sup>45</sup> – 10 <sup>49</sup>
Radio galaxy	E	Strong	Narrow	10 <sup>43</sup> – 10 <sup>45</sup>
Radio-quiet quasar	S/E	Weak	Broad	10 <sup>45</sup> – 10 <sup>49</sup>
Seyfert 1	S	Weak	Broad	10 <sup>43</sup> – 10 <sup>45</sup>
Seyfert 2	S	Weak	Narrow	10 <sup>43</sup> – 10 <sup>45</sup>

**Table 3.1:** Properties of important types of AGN. E and S stand for elliptical and spiral galaxy types respectively. Table taken from Rosswog & Brüggén (2007).

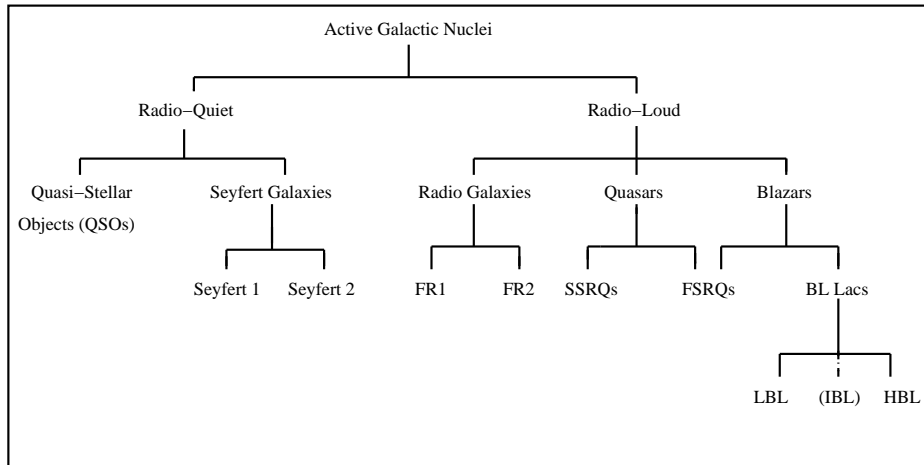


**Figure 3.2:** Classification of AGN types. FR1 and FR2 are Fanaroff-Riley galaxies (type 1 and type 2 respectively). FSRQs and SSRQs are Flat-Spectrum Radio Quasars and Steep-Spectrum Radio Quasars. LBL and HBL are Low-frequency-peaked and High-frequency peaked BL Lacertae objects. A class of objects which is sometimes considered to lie between these two object types, Intermediate-frequency peaked BL Lacs (IBL), is also shown in brackets. Adapted from Weekes (2003).

## 3.2. Classification of AGN

---

### 3.2.1 Blazars

An AGN is classified as a blazar if the relativistic jet emanating from its central black hole is aligned very close to the line of sight to the galaxy. They are the most powerful sources known. Blazars are always radio-loud due to the fact that the relativistic jet is pointed directly at us. They are also characterised by large variation and high luminosity at all wavelengths. The polarisation of emission at all wavelengths is also variable (Fossati *et al.*, 1998).

The spectral energy distributions (SEDs) of blazars are comprised of two broad emission peaks. The lower-energy peak normally occurs in the infrared to ultraviolet range, although this peak can sometimes occur in the x-ray band. The higher-energy peak occurs in the MeV - GeV band. Across the entire SEDs of blazars, the emission is dominated by non-thermal processes such as synchrotron emission and inverse Compton scattering. Blandford & Ostriker (1978) originally posited that this emission emanates from the dynamics of the relativistic jet pointed in our direction. An example of a blazar's spectral energy distribution is shown in Figure 3.3. Blazars exhibit properties which are consistent with relativistic beaming (*i.e.* emitting plasma moving at small angles to the line of sight). Due to beaming, superluminal motion (*i.e.* motion at an apparent speed greater than that of light in a vacuum) is also evident in the jet. These processes are described in more detail in Section 3.3.

Figure 3.2 shows how blazars are subclassified into BL Lacertae (BL Lac) objects and Flat-Spectrum Radio Quasars (FSRQs). The differences between these two classes of objects are as follows:

- *Emission Lines:* FSRQs exhibit strong, easily-discernible optical emission lines. BL Lacs have either very weak or indiscernible emission lines. This often makes the quantification of the redshift of BL Lac objects difficult or impossible.
- *Optical Polarisation:* The amount by which optical light from each

### 3.2. Classification of AGN

---

type of AGN is polarised differs (Ghisellini, 1999).

- *X-ray to Radio Ratio*: The ratio of x-ray flux to radio flux differs for the two types of object (Ghisellini, 1999).

Although these differences exist between the two classes of object, the differences are small and, overall, the distinction between them is not clear. A number of sources have been reported with properties which make their classification in one or other of these categories difficult (Fosati *et al.*, 1998). BL Lacs, their initial discovery, and their emission properties, are described in more detail below.

#### **BL Lacertae Objects (BL Lacs)**

Of the blazars detected at TeV energies to date, all but one are BL Lacs (M87 is the exception). As was the case with quasars, BL Lacs were discovered unexpectedly in the 1960s as counterparts to bright radio sources. The eponymous BL Lacertae was the first to be discovered (Schmitt, 1968), having mistakenly been reported as a variable star in 1928. Although the catalogue of quasars was growing rapidly at the time of BL Lacertae's initial discovery, classification of further objects as BL Lacs remained elusive, due mainly to their (almost) complete lack of optical emission lines (Giommi *et al.*, 2001).

BL Lacs are known to exhibit large-scale optical flux and polarisation variability. Thermal optical emission alone can not account for the observed level of variability. Synchrotron emission is largely responsible for the optical component of the BL Lac's spectrum. Non-thermal emission from BL Lacs spans over 20 decades of energy, from radio to TeV (Giommi *et al.*, 2000). Despite this, and unlike most other astronomical objects, BL Lacs have been almost exclusively discovered at either radio or x-ray energies. As those BL Lacs which were discovered in radio surveys displayed different physical properties from those discovered in x-ray surveys, they were initially designated either radio selected (RBL) or

### 3.2. Classification of AGN

---

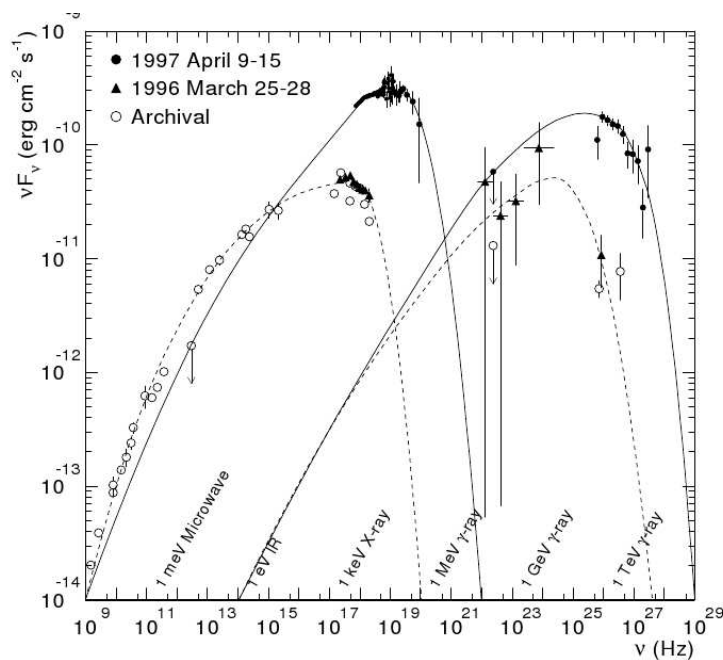


**Figure 3.3:** Spectral energy distributions for Markarian 501 from archival data with the relevant dates shown in the figure. The curves fitted to the data are only to guide the eye and do not represent model fits to the data. The double-peaked nature of the spectral energy distribution is clearly seen. The waveband relating to each data point is labelled in the figure. Figure adapted from Catanese & Weekes (1999) which contains references for the sources of the various data points.

### 3.2. Classification of AGN

---

x-ray selected (XBL). This designation scheme was later revised when it was realised that their discovery at various energies had more to do with the limitations of the detectors being used than the physical processes governing their emission.

Although BL Lacs usually do not exhibit emission lines, it is sometimes possible to discern them (the emission lines) if the optical luminosity of the galaxy's core drops. In these situations, the lines are usually quite faint making it difficult to ascertain the redshift of the galaxy with a high degree of accuracy. Also, such periods of low-luminosity optical emission are relatively rare. Some BL Lacs contain weak emission lines from the light of the surrounding host galaxy which may be used to determine the redshift. For many BL Lacs, the redshift has never been accurately obtained.

A small number of BL Lacs were discovered in the initial sky-surveys carried out by the first x-ray telescopes (Piccinotti *et al.*, 1982). The fact that only small numbers of BL Lacs were being discovered, relative to the overall number of AGN, fitted the hypothesis suggested by Blandford & Rees (1978) that BL Lacs and AGN were intrinsically the same, with their jets orientated differently. This hypothesis suggested that BL Lacs were a type of AGN which were orientated such that their jet pointed along our line of sight. Only a small fraction of them would be expected to exhibit this pointing by chance.

It had been expected that as the sensitivity of x-ray telescopes improved the number of BL Lac discoveries would increase. Surprisingly, this was not the case. Instead, as the sensitivities of x-ray observatories increased, the rate of discovery of BL Lacs dropped. It was found that BL Lacs showed negative cosmological evolution (*i.e.* BL Lacs either brighten with age or fewer of them existed in the past). Binning BL Lacs by the strength of their x-ray flux, Giommi *et al.* (2001) showed that the amount of negative cosmological evolution increases with increasing x-ray flux. This might be explained by the dependence of beaming on

### 3.2. Classification of AGN

---

the apparent luminosity, which could cause the K-correction (*i.e.* colour correction applied to compensate for reddening of galaxies due to wavelength shift) to depend artificially on the apparent luminosity. Even small amounts of incompleteness (*i.e.* small numbers of galaxies within the data set) at very faint fluxes can cause a correlation, similar to that outlined above, between negative evolution and x-ray flux (Giommi *et al.*, 2001, and references therein). Similar effects were seen in radio surveys as their sensitivities increased.

The nomenclature originally used to designate BL Lac types based on the band of their initial discovery (XBL and RBL) has been rejected in favour of the terminology suggested in Padovani & Giommi (1995). The term High-frequency peaked BL Lac (HBL) is used to describe a BL Lac with a strong x-ray component in its SED. Low-frequency peaked BL Lac (LBL) describes a BL Lac with a large radio component. Effectively, these terms represent a slight shift in nomenclature as BL Lacs tend to be discovered in the band where they were brightest.

Except for BL Lacertae itself, all BL Lac objects detected at TeV energies are HBLs. LBLs tend to have their upper energy peak in the MeV region making their detection with ground-based experiments difficult. They have been well studied by space-borne experiments, with EGRET detecting over 60 such objects. The ability to detect LBLs and HBLs depends heavily on the flux sensitivity and energy range of the observatory with which the object is observed. This has led some authors to suggest that the distinction between the two classes is purely due to selection effects and that there is no physical reason why there should not be a continuous range of peak energies within the blazar class (Padovani, 2007). The seeming lack of BL Lacs discovered to have an upper energy peak in the intermediate region (*i.e.* Intermediate-frequency peaked BL Lacs; IBLs) should be addressed by the launch of GLAST (see Section 2.3.1), with its energy sensitivity extending into the lower energy ranges of ground-based experiments such as VERITAS.

## 3.2. Classification of AGN

---

### Flat-Spectrum Radio Quasars (FSRQs)

Radio-loud quasars with broad emission lines and a radio spectral index of  $\leq 0.5$  are referred to as Flat-Spectrum Radio Quasars (FSRQs). This class of quasar makes up around 5-10% of all known quasars. In general, FSRQs are known to have large redshifts and are more luminous than BL Lacs (Fossati *et al.*, 1998). To date, no FSRQs have been detected at TeV energies (Falcone *et al.*, 2004b).

### 3.2.2 The Blazar Sequence

Blazar population studies have revealed a so-called “blazar sequence” which suggests that blazar luminosity depends on the location of the synchrotron peak. According to this sequence, HBLs are not as luminous as IBLs, which are less luminous again than LBLs. Fossati *et al.* (1998) initially put forward this notion after studying a dataset limited to  $\log_{10}(\nu_{peak}/\text{Hz}) = 15 - 19$  ( $\nu_{peak}$  is the frequency of peak emission for the blazar). A plot of luminosity against  $\log \nu_{peak}$  for a relatively small number of objects exhibited a general trend of increasing luminosity with increasing  $\nu_{peak}$ . However, Nieppola *et al.* (2006) conducted a more extensive study for a larger set of BL Lacs with  $\log_{10}(\nu_{peak}/\text{Hz})$  in the range of 13 - 21, introducing a lot more scatter to the plot of luminosity against  $\log \nu_{peak}$  in the process. This had the effect of invalidating the trend of decreasing luminosity of the blazar with increasing  $\log \nu_{peak}$  suggested in Fossati *et al.* (1998).

### 3.2.3 Unification Scheme

A unification scheme has been developed to describe the main characteristics that are common to all classes of AGN. Prototypical AGN are characterised as having the following characteristics (Urry, 2004):

- A central supermassive black hole, surrounded by an accretion disk. The disk is heated due to the force of friction dissipating gravita-

### 3.2. Classification of AGN

---

tional potential energy present near the black hole generating large amounts of broadband thermal radiation in wavebands from optical to x-ray. The mass of the black hole may be up to  $10^{10} M_{\odot}$ .

- An energetic electron population located above (and below) the accretion disk. This region emits in the x-ray band.
- A broad-line region which is made up of clouds of rapidly-moving gas close to the black hole. Optical emission characterised by broad emission lines is present in this region.
- An obscuring torus of gas and dust which surrounds the accretion disk.
- A narrow-line region, made up of clouds of moving gas beyond the obscuring torus. Optical emission from this region exhibits narrow emission lines.
- Relativistic jets emanating from the polar region of the black hole. The jets originate within a few hundred Schwarzschild radii. Only AGN with jets are radio-loud. The jets may be up to  $10^6$  parsecs in length.

Historical taxonomy schemes apart, all AGN types exhibit the features shown above (except for relativistic jets, which separate radio-loud and radio-quiet AGN). Differences in the observed properties of AGN are therefore thought to be exclusively due to the power and orientation of the AGN. Obscuration dominates the observed optical differences and beaming dominates the higher-energy features.

From this unification model, all AGN can be classified as one of just three types: Type 0, Type 1 and Type 2. The type classification is heavily dependent on the orientation of the AGN jet (if it exists) to the observer's line of sight. Type 0 describes any AGN whose observed emission is predominantly due to non-thermal processes. This is due to

### 3.3. The Relativistic Jet

---

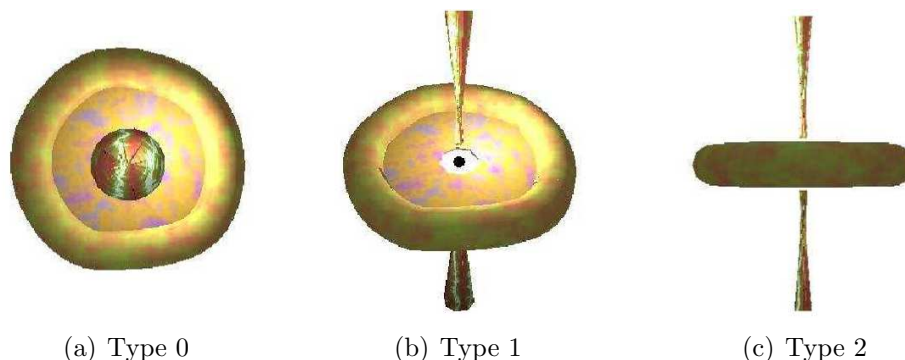


**Figure 3.4:** Types of AGN, based on their orientation. Type 0 have their jets pointed directly along the line of sight. Type 1 have their jets pointed at such an angle that is neither pointing directly at us nor are we viewing the galaxy “edge on”. Type 2 AGN are viewed “edge-on”.

the fact that the jet is oriented along the line of sight. These processes are discussed later in Section 3.4 and lend the AGN to detection at TeV energies by imaging atmospheric Cherenkov telescopes.

Type 1 AGN have their jets oriented at an angle to the line of sight such that the accretion disk is visible. Broad emission lines are therefore characteristic of this AGN type. Type 2 AGN are those whose accretion disks are viewed “edge-on”. Narrow emission lines are visible from this type of AGN and the broad-line region is obscured from view. The three types of AGN are shown in Figure 3.4

### 3.3 The Relativistic Jet

Although some AGN seem to have no discernible jet, many exhibit a large collimated outflow which is thought to be powered by gravitational potential energy of the infalling material in the gravitational field of the central black hole. Jet morphology has been studied in great detail by “parsec-scale” radio studies (Piner & Edwards, 2004; Giroletti *et al.*, 2004). These studies show that the jets are inhomogeneous in nature.

### 3.3. The Relativistic Jet

---

Areas of denser material, called knots, are seen to move along the jet. Their existence and motions may have a part to play in the variability of the source's emission. The movement of the knots is often relativistic, so the velocity is expressed in terms of the bulk Lorentz factor,  $\gamma$ , as follows:

$$\gamma = \frac{1}{\sqrt{1 - \frac{v^2}{c^2}}} \quad (3.1)$$

Here,  $c$  is the speed of light and  $v$  is the speed the knot is travelling relative to the galaxy's core. The fact that knots are seen to move with relativistic speeds is important in light of the relativistic beaming properties associated with jet dynamics. Relativistic beaming is thought to be responsible for many of the observed characteristics of high-energy emission from AGN jets. Chief among these characteristics are superluminal motion, rapid variability and high luminosity.

Relativistic beaming and its effects are discussed in more detail in the following section.

#### 3.3.1 Relativistic Beaming

If a plasma knot (*i.e.* source of photons) moves towards an observer along the line of sight (or very close to it) at a relativistic bulk velocity, the emission will be beamed in the forward direction of movement towards the observer. This beaming is a result of the flux density of the emitted radiation being increased (at the observer's location) due to relativistic effects.

For an emitting source, moving at a relativistic velocity, most of the emitted photons will be beamed into a cone with a half-opening angle of

$$\theta \approx \frac{1}{\gamma} \quad (3.2)$$

where  $\gamma$  is the Lorentz factor, defined in Equation 3.1. Relativistic beam-

### 3.3. The Relativistic Jet

---

ing is an important process with regard to blazar emission. Beaming has also been used to explain the apparent existence of a single jet in the case of some AGN. This jet oriented in our direction may be detected due to emission being beamed in our direction. Effectively, any emission oriented in the opposite direction would beam away from us, decreasing its observed luminosity from our point of view, much like a lighthouse beam is largely invisible to an observer when it is pointed away from that observer.

#### 3.3.2 Superluminal Motion

Superluminal motion is an *apparent* faster-than-light motion. Apart from radio galaxies and quasars, microquasars are also known to exhibit this effect (a central black hole being a common feature in all cases). Rees (1966) proposed the effect before it was observed by use of the VLBI (Very Long Baseline Interferometry) technique. The apparent velocity of a plasma knot is denoted  $v_a$ , where  $v_a > c$ , the speed of light. Relativity underlies the illusion: the source of the emitted photons pursues those photons after emission. In the observer's reference frame, the time between the emission of a photon and the emission of subsequent photons seems reduced as the source has started to "catch up" with the initially emitted photons before emitting again. This has the effect of giving the impression of superluminal motion.

Figure 3.5 illustrates how superluminal motion may be experienced in such relativistic circumstances. In the figure, the blue circles represent a knot moving from one position (at  $t = T_1$ ) to another position closer to the observer (at  $t = T_2$ ), at an angle  $\theta$  to the line of sight to the observer. After time  $\Delta t = T_2 - T_1$ , the knot will have moved an apparent distance,  $A = \beta ct \cos \theta$  towards the observer. The apparent transverse movement recorded would be  $B = \beta ct \sin \theta$ . Therefore, the apparent time taken for the knot to move from the first position (at  $T_1$ ) to the second (at  $T_2$ ) as seen by the observer,  $t_{obs}$ , is given by

### 3.3. The Relativistic Jet

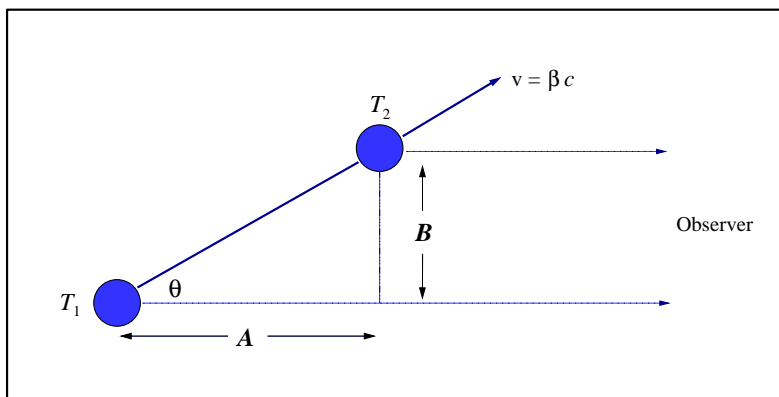


**Figure 3.5:** Schematic of the mechanisms causing the apparent superluminal motion observed in blazar jets. The knot (as represented by the blue circles) moves towards the observer ( $T_1 \rightarrow T_2$ ) at an angle  $\theta$  to the line of sight. The movement is at a speed of  $v = \beta c$  (see text) so the distance  $A = \beta c t \cos \theta$  and  $B = \beta c t \sin \theta$ .

$$t_{obs} = t - \beta t \cos \theta = t(1 - \beta \cos \theta) \quad (3.3)$$

The measured transverse velocity of the knot,  $v_{obs}$ , is then given by the ratio of the distance moved in the transverse direction,  $B$ , and the observed movement time,  $t_{obs}$ :

$$v_{obs} = \frac{B}{t_{obs}} = \frac{\beta c \sin \theta}{(1 - \beta \cos \theta)} \quad (3.4)$$

Then using  $\beta = v/c$  to convert to units of  $c$ ,

$$\beta_{obs} = \frac{\beta \sin \theta}{(1 - \beta \cos \theta)} \quad (3.5)$$

If  $\cos \theta = \beta$ , this function is maximised giving  $\beta_{obs} = \gamma \beta$ . Taking an example, if the velocity of the plasma movement is  $0.96c$ , and it is moving at an angle of  $\theta = 4^\circ$ , then the knot will appear to move at a velocity of  $\sim 1.44c$ . The effects of superluminal motion have been seen in the jets of many blazars (see for example, Giroletti *et al.*, 2004).

### 3.3. The Relativistic Jet

---

The detection of superluminal motion within a jet serves as evidence of relativistic beaming processes taking place.

#### 3.3.3 Doppler Boosting

Radiation emitted by a knot of plasma in the jet is Doppler boosted as it moves towards the observer. The observer detects much higher emission than if the plasma were emitting while stationary in the observer's reference frame due to the fact that the plasma – moving at relativistic speeds – catches up with the previously emitted photons while further emitting photons, causing a “pile up”. A large number of photons passing by an observer in a short interval of time may have been emitted over a comparatively long time in the source's rest frame. Thus, Doppler boosting has the effect of increasing the intrinsic luminosity of sources as well as shortening the variability timescales observed.

An important measure of the strength of boosting in this situation is the Doppler factor of the relativistically moving source, defined as:

$$\delta = \frac{\nu_e}{\nu_o} = \frac{1}{\gamma(1 - \beta \cos \theta)} \quad (3.6)$$

where  $\nu_e$  and  $\nu_o$  are the emitted frequency and the observed frequency respectively,  $\gamma$  is the Lorentz factor, as defined in Equation 3.1,  $\beta$  is the bulk velocity,

$$\beta = \frac{v}{c} \quad (3.7)$$

and  $\theta$  is the angle between the velocity vector of the source (*i.e.* the direction of the jet beaming) and the line of sight to the observer.

If  $L_{obs}$  is taken as the observed luminosity of the source and  $L_{rest}$  is taken as the intrinsic luminosity of the source in the rest frame, then  $L_{obs}$  is given by

$$L_{obs} = \delta^p L_{rest} \quad (3.8)$$

### 3.4. Blazar Emission Models

---

where  $\delta$  is the Doppler factor as defined in Equation 3.6,  $p = 2 + \alpha$  for a continuous jet (*i.e.* where there are no massive jet ejections) and  $\alpha$  is the spectral index of the source (Urry & Padovani, 1995).

Often, the high-energy emission from blazars dominates the emission at other wavebands. In the case of EGRET, many of the blazars detected exhibited  $\gamma$ -ray emission which was anywhere from 1 to 1000 times more luminous than emission at any other wavelength. Also, it is quite often the case that the GeV and TeV emission has been seen to increase and decrease by factors of 2 or 3 over a number of hours. Indeed, Aharonian *et al.* (2007a) described the extremely rapid and powerful flux variations exhibited by PKS 2155-304 (up to levels of  $\sim 15$  times the flux of the Crab Nebula in that energy band) while it was in a particularly active state.

## 3.4 Blazar Emission Models

The question of the origin of high-energy emission from blazars has challenged the field for many years. A number of competing models have emerged in order to explain this emission. Although there are many flavours of models, it is possible to break them down into three main groups, based primarily on the proposed dominant  $\gamma$ -ray production mechanism:

- Synchrotron Self Compton Models
- External Compton Models
- Hadronic Models

The first two types of model are considered *leptonic* in nature, whereby the non-thermal emission comes from a population of electrons in the jet, which are accelerated to relativistic energies within the jet plasma and are assumed to have a power-law spectrum. The observed SED shape

### 3.4. Blazar Emission Models

---

suggests an electron spectrum that steepens with increasing energy. The third set of models is, obviously, hadronic in nature. These models explain the emission of VHE  $\gamma$ -rays within a scenario that also allows for the origin of cosmic rays. The models are discussed here in detail.

#### 3.4.1 Synchrotron Self Compton (SSC)

Synchrotron radiation has been discussed in Section 2.2.1. Ginzburg & Syrovatskii (1969) first introduced Synchrotron Self Compton (SSC) models for astrophysical sources, based on previous related work by the same authors (Ginzburg & Syrovatskii, 1965). These theories were further developed for homogeneous spherical sources by Rees (1967) and Jones *et al.* (1974). SSC processes in relativistic jet scenarios were added to these models in later work (Konigl, 1981; Ghisellini & Maraschi, 1989; Marscher & Gear, 1985; Bloom & Marscher, 1996). Böttcher (2002) provides a good overview of viable SSC models.

In SSC models, the seed photons which are scattered to high energies by inverse Compton scattering are the photons produced by synchrotron radiation. The simplest form of an SSC model (Sikora & Madejski, 2001) – a one-component version – assumes that any emission is due to a single source or shock moving along the jet, accelerating electrons and positrons which emit synchrotron radiation. The synchrotron photons are boosted to higher energies by inverse Compton scattering with the same electron/positron population (thus, “*self* Compton”). The synchrotron radiation and Compton scattering, in this case, are assumed to take place in the same region. More realistic models require the use of multiple shells and are more complex in nature.

Following the treatment of Ghisellini *et al.* (1996) for the simple one-zone scenario, if the emitting region has a characteristic size,  $R$ , and moves at a relativistic speed of  $v = \beta c$  along a jet with a tangled magnetic field of strength  $B$ , the variability timescale,  $t_{var}$ , may be used to determine  $R$  as follows:

### 3.4. Blazar Emission Models

---

$$R = c t_{var} \frac{\delta}{1+z} \quad (3.9)$$

where  $z$  is the redshift of the blazar and  $\delta$  is the Doppler factor as defined in Equation 3.6. The Doppler factor is found here using the bulk Lorentz factor of the emitting zone (as defined in Equation 3.1).

Certain observable parameters may be ascertained from the blazar's SED, which is estimated from simultaneous observations at different wavelengths. Accurate measurement of these properties can then be used to determine some characteristics of the emission region of the blazar. The SSC model has the advantage of having only a relatively small set of these measurable free parameters, which are listed below:

$\nu_s$ : The frequency at which the synchrotron contribution to the SED peaks.

$\nu_c$ : The frequency at which the inverse Compton contribution to the SED peaks.

$\nu_b$ : The synchrotron break frequency arising from the assumed broken power-law spectrum of the relativistic electrons that drive the synchrotron emission.

$L_s$ : The total luminosity in the synchrotron regime.

$L_c$ : The total luminosity in the Compton regime.

The two peaks evident in the SED of VHE blazars are interpreted as being due to the maximum outputs of the synchrotron mechanism and the inverse Compton mechanism, respectively. The observed spectral shape requires that the relativistic electron spectrum steepens with increasing energy. This is usually approximated by a broken power law with different indices above and below a break energy,  $E_b$ . If the spectrum of the relativistic electrons is described by a broken power law with a spectral index less than 3 below the break frequency  $\nu_b$  (corresponding

### 3.4. Blazar Emission Models

---

to the break energy,  $E_b$ ) and greater than 3 above the break frequency  $\nu_b$ , then the maximum in the power per decade for both the synchrotron and inverse-Compton regimes is due to electrons of energy  $E_b$ . The frequency at which the synchrotron peak occurs in the SED is given by,

$$\nu_s \simeq \frac{4}{3} \frac{\delta \nu_B E_b^2}{(1+z)} \quad (3.10)$$

where  $\nu_B = 2.8 \times 10^6 B$  Hz is the Larmor frequency and  $E_b$  is the break energy in units of  $m_e c^2$ . The frequency that the inverse Compton peak occurs in the SED is given by,

$$\nu_c \simeq \frac{4}{3} E_b^2 \nu_s \quad (3.11)$$

If these two frequencies (*i.e.*  $\nu_s$  and  $\nu_c$ ) are determined from observations, the energy of electrons which contribute the most to the overall power output,  $E_{peak}$ , can be derived:

$$E_{peak} = E_b \simeq \sqrt{\frac{3\nu_c}{4\nu_s}} \quad (3.12)$$

Due to the fact that both the synchrotron and Compton frequencies are boosted by the same factor in this one-zone model, this equation does not depend on the Doppler factor. From this, it may be shown that:

$$B\delta \simeq (1+z) \frac{\nu_s^2}{3.7 \times 10^6 \nu_c} \quad (3.13)$$

where  $B$  is the magnetic field. By using a typical value of  $\delta \simeq 10$ ,  $B$ , can be estimated by

$$B \simeq \left( \frac{1}{37} \right) \frac{\nu_{s,14}^2}{\nu_{c,22}} \quad (3.14)$$

where  $\nu_{s,14}$  and  $\nu_{c,22}$  are the relevant frequencies in units of  $10^{14}$  Hz and  $10^{22}$  Hz respectively.

In SSC models, the high-energy emission is dominated by the first-order inverse Compton scattering (see Figure 2.4). The ratio of the lu-

### 3.4. Blazar Emission Models

---

minisities of the synchrotron and Compton peaks (*i.e.*  $\frac{L_s}{L_c}$ , where  $L_s$  and  $L_c$  are the synchrotron and the Compton peak luminosities respectively) gives the relative importance of each process to the overall emission. This ratio is related directly to the ratio of the magnetic energy density,  $U_B$ , to the radiation energy density of the synchrotron photons (as measured in the rest frame of the source),  $U'_s$ , as follows (Ghisellini *et al.*, 1996):

$$\frac{L_s}{L_c} \simeq \frac{U_B}{U'_s} = \frac{4 \pi R^2 c U_B \delta^4}{L_s} \quad (3.15)$$

If Equation 3.9 is used to estimate  $R$ , it can be shown that

$$B\delta^3 \simeq (1+z) \sqrt{\frac{2L_s^2}{L_c t_{var}^2 c^3}} \quad (3.16)$$

Now, expressing  $t_{var}$  in units of days (calling it  $t_d$ ) and using Equation 3.13 and Equation 3.16 to solve for  $\delta$  and  $B$  yields

$$\delta = (1.67 \times 10^4) \sqrt{\frac{\nu_c}{t_d \nu_s^2}} \sqrt[4]{\frac{L_{s,45}^2}{L_{c,45}}} \quad (3.17)$$

and

$$B = (2.14 \times 10^{-11})(1+z) \left( \frac{\nu_s^3 t_d^{\frac{1}{2}}}{\nu_c^{\frac{3}{2}}} \right) \sqrt[4]{\frac{L_{c,45}}{L_{s,45}^2}} \quad (3.18)$$

where  $L_{s,45}$  and  $L_{c,45}$  are the synchrotron and Compton luminosities in units of  $10^{45}$  erg  $s^{-1}$ . As can be seen, the determination (or good estimation) of  $\nu_c$ ,  $\nu_s$ ,  $L_c$  and  $L_s$  is important in fixing the physical properties which constrain the model. These data, if not taken simultaneously, are subject to a relatively large amount of variation which produces an error in the fit (Böttcher *et al.*, 2002).

This model serves as the simplest of a plethora of related models, all based on the fact that the high-energy photons are produced through inverse Compton scattering of lower-energy photons by the same electron population that produced the synchrotron emission. Since the same

### 3.4. Blazar Emission Models

---

population of electrons is involved in the bulk emission, fluctuations in the jet should produce variations which are correlated across multiple wavebands. Indeed, given simultaneous data at other wavelengths, the  $\gamma$ -ray flux prediction is very sensitive to small changes in the parameters of the model. Hence, uncertainties in the parameters lead to large uncertainties in the model prediction (Horan *et al.*, 2004). For instance, a thorough multiwavelength campaign to constrain parameters such as the magnetic field for BL Lacertae by Böttcher *et al.* (2003) resulted in a constraint of  $B \simeq 1.5 - 2$  G, indicating a wide range of uncertainty.

#### Parameter Variation in SSC Models

Bloom & Marscher (1996) found that, for a SSC model, varying the magnetic field strength alters the flux in both the synchrotron and self-Compton regime. Also, while below the Klein-Nishina (cross section of interaction) limit, the synchrotron and self-Compton cut-off energies are shifted. Above this limit, the influence of the magnetic field is suppressed. A similar effect is evident when the Doppler factor is varied. However, if the electron density is altered, asymmetric changes in the fluxes of the synchrotron and self-Compton components occur, with the Compton component being more affected by these changes.

Mastichiadis & Kirk (1997) showed that varying the amplitude of the spectrum of injected electrons results in flaring at ultraviolet/x-ray and TeV energies. Flares at optical and GeV energies lag prompt flares at ultraviolet/x-ray and TeV energies. It is suggested that this is because the higher-energy electrons have a shorter synchrotron cooling time so that the newly injected high-amplitude electron population cools first at high frequencies. The lower-frequency optical synchrotron and self-Compton photons cool later, causing the lag. However, this study also suggested that increasing  $\gamma_{max}$ , the maximum electron Lorentz factor, would result in flares restricted to x-ray and TeV  $\gamma$ -ray energies. Lower frequency emission would only vary slightly in this case.

### 3.4. Blazar Emission Models

---

Mastichiadis & Kirk (1997) also propose that an increase in the magnetic field strength would cause the peak frequency of synchrotron emission, as well as the luminosity, to increase. The Compton component of the SED would be reduced, compared to its quiescent level. Bloom & Marscher (1996) suggest contrasting behaviour. However, they allow the electron injection spectrum to vary, unlike Mastichiadis & Kirk (1997) who keep it constant in the changing magnetic field situation.

Seemingly different behaviour arising from changing parameters of the same or a similar model is commonplace and the various models can only be constrained and confirmed by accurate contemporaneous multiwavelength studies.

#### 3.4.2 External Compton (EC)

Unlike SSC models, the dominant source of seed photons for up-scattering (by relativistic electrons in the jet) in the inverse Compton process as explained by External Compton (EC) models are ambient photons from the accretion disk, the central accretion flow, the infrared background in the region, the broad-line region, the obscuring torus or some combination of these (Horan *et al.*, 2004). However, these models also predict that a single electron population is responsible for infrared to ultraviolet/x-ray emission due to synchrotron mechanisms and that inverse Compton processes are responsible for the emission at higher energies.

Dermer & Schlickeiser (1993) suggest that the seed photons could originate in the accretion disk of the blazar and enter the jet directly. The seed photons could also come from the circumnuclear material of the broad-line region (Dermer *et al.*, 1997). The broad-line region might then be illuminated by the jet (according to Ghisellini *et al.*, 1996), resulting in reprocessed soft x-ray photons being reflected back into the jet. Bednarek (1998) challenges this position, showing that the reflecting region would have to be inside the jet. Illumination of the broad-line region by the accretion disk (Blandford & Levinson, 1995) has also been suggested.

### 3.4. Blazar Emission Models

---

Another possible source of seed photons is the obscuring dusty torus around the blazar's accretion region (Wagner *et al.*, 1995; Arbeiter *et al.*, 2002).

For external Compton scattering to dominate over SSC emission processes, the energy density of the external radiation as measured in the reference frame of the moving jet plasma must exceed the jet's synchrotron radiation energy density. Extremely weak magnetic fields are required for the external Compton emission to be the dominant emission process (over synchrotron emission) (Sikora *et al.*, 1994). For small jet radii, attenuation of  $\gamma$ -rays by pair production would limit overall  $\gamma$ -ray emission from the jet. Typical distances, beyond the radiation source, where this type of emission might occur are on the order of  $10^{14}$  m (Maraschi *et al.*, 1992).

Under these schemes, as a shock-wave moves through the relativistic jet, electrons that are excited by the shock emit synchrotron radiation and up-scatter lower-energy (ultraviolet or infrared) photons which form a medium through which the jet is travelling. Assuming the external radiation energy density,  $U'_{ext}$ , is seen (from the point of view of the knot) to dominate the energy density of the internally produced synchrotron photons, then the typical frequency of isotropic ambient photons,  $\nu_o$ , will be up-scattered to a frequency of

$$\nu'_o = \gamma \nu_o \tag{3.19}$$

(Ghisellini *et al.*, 1996) where  $\gamma$  is the Lorentz factor (see Equation 3.1). If scattering by electrons with energy  $E_b$  (in units of  $m_e c^2$ ) takes place in the jet, then the observed frequency,  $\nu_c$ , of the resulting  $\gamma$ -rays will be

$$\nu_c = \left(\frac{4}{3}\right) \left(\frac{\delta}{(1+z)}\right) E_b^2 \gamma \nu_o \tag{3.20}$$

where  $z$  is, as before, the redshift of the blazar. Now the ratio of  $\nu_c$  to  $\nu_s$  yields a magnetic field of

### 3.4. Blazar Emission Models

---

$$B = (3.6 \times 10^8) \gamma \frac{\nu_s \nu_{o,15}}{\nu_c} \quad (3.21)$$

where  $\nu_{o,15}$  is  $\nu_o$  in units of  $10^{15}$  Hz. The ratio of the luminosity of the inverse Compton component of the spectrum to the luminosity of the synchrotron component is

$$\frac{L_c}{L_s} = \frac{U'_{ext}}{U_B} \simeq \frac{\delta^2 L_{ext}}{4\pi R_{broad}^2 c U_B} \quad (3.22)$$

in this case where photons originate in the broad-line region or the accretion disk (Ghisellini *et al.*, 1996).  $L_{ext}$  is the luminosity of the radiation emitted from the spherical region of radius  $R_{broad}$ , which is external to the jet. The  $\delta$  term makes allowance for the anisotropy of the Compton emission in the reference frame of the knot (Dermer, 1995). If Equation 3.21 is used for  $B$ , and setting  $\delta \simeq \gamma$ , then

$$\frac{L_c}{L_s} \simeq (5.14 \times 10^{-19}) \left( \frac{L_{ext,45}}{R_{broad,18}^2} \right) \left( \frac{\nu_c}{\nu_s \nu_{o,15}} \right)^2 \quad (3.23)$$

so that sources with self-Compton and synchrotron luminosities that are almost equal should have  $\frac{\nu_c}{\nu_s} \simeq 10^9$  (Ghisellini *et al.*, 1996). This is a simple first-order approach which gives initial insight into the model parameters involved in EC models.

Generally, SSC models have been favoured over EC models. However, leptonic models (those based on the up-scattering of photons to high energies by electrons) as a whole are not without problems. For instance, some leptonic models predict very weak magnetic fields on the order of  $10^{-4}$  G which may not be sufficient to confine the jet. Also, a cut-off in the electron spectrum is required to reproduce the observed shape of the lower-energy peak (*i.e.* slow fall off observed in synchrotron spectrum). As yet, there is no valid interpretation of this cut-off.

Sokolov & Marscher (2005) noted that the main cause of time lags between emission in different energy bands due to EC processes is radiative

### 3.4. Blazar Emission Models

---

energy loss which quenches any flares at the highest energies first. However, the EC flares at lower energies can incur time delays if the spectrum of electrons injected at the shock front (causing the flare) is characterised by a high value of the minimum electron energy (which depends on the minimum Lorentz factor cut-off). A positive spectral index for at least half of the flare duration would be necessary for this to happen whereas a SSC model would be characterised by a negative spectral index for the entirety of the flare.

#### Parameter Variation in EC Models

In Dermer *et al.* (1997), the effect of changing some of the physical parameters of EC models was investigated. The energy density of the external radiation field was kept constant while the effect of varying the soft photon energy was examined. If the energy of the soft photons was increased, the synchrotron break energy (*i.e.* the energy at frequency  $\nu_b$ ) increased by the same proportion as the photon energy increase. As the soft photon index was increased, the spectrum was found to steepen.

If the strength of the magnetic field was increased, the synchrotron flux was also found to increase. It was found that the flux of the inverse Compton component remained constant however. This is because the Compton regime is dominated by the energy density of the low-energy photons, which was held constant in this study.

#### 3.4.3 Hadronic Models

In hadronic models, protons are shock accelerated to relativistic energies and are injected into the highly magnetised environment of the jet (Mannheim, 1993, 1998). Proof that hadronic models explain TeV  $\gamma$ -ray emission may eventually come from indisputable evidence that these blazars are also the origin of extragalactic cosmic rays up to energies  $\sim 10^{20}$  eV. Hadronic models are based either on protons interacting with

### 3.4. Blazar Emission Models

---

some target, producing neutral pions ( $\pi^0$ ), or direct synchrotron radiation. In the former case, the neutral pions decay into a pair of  $\gamma$ -rays with energies that are determined by the initial energy of the neutral pion. *i.e.*

$$\begin{aligned} p + p &\rightarrow \pi^0 + \text{other hadrons} \\ \pi^0 &\rightarrow \gamma + \gamma \end{aligned} \tag{3.24}$$

Similar interactions would simultaneously be expected to produce neutrinos ( $\nu$ ) as well as electrons and positrons by the following series of interactions:

$$\begin{aligned} p + p &\rightarrow \pi^\pm + \text{other hadrons} \\ \pi^\pm &\rightarrow \mu^\pm \nu_\mu \\ \mu^\pm &\rightarrow e^\pm \nu_e \nu_\mu \end{aligned} \tag{3.25}$$

Two main families of hadronic models exist. The first involves beams of protons with energies in excess of  $10^{16}$  eV. The second requires beams of ultra-high-energy protons, with energies greater than  $10^{19}$  eV.

Dar & Laor (1997) consider clouds of gas with high column density crossing the jet of accelerated protons. The broad-line region is proposed here as the source of such clouds. The electrons and positrons generated by the decay of charged pions then cool by synchrotron radiation and inverse Compton scattering to produce wideband emission (optical through to TeV).

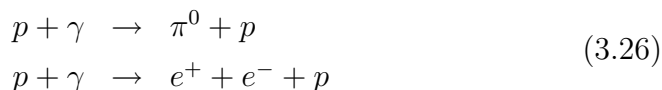
Pohl & Schlickeiser (2000) take a different approach, suggesting that an electron-proton beam sweeps up ambient matter. The model considers a similar approach to those of “expanding fireball” explanations for  $\gamma$ -ray bursts, whereby a blast of relativistic baryons is collimated by the magnetic field of the beam. Interacting with the interstellar medium, Alfvén waves (*i.e.* a type of magnetohydrodynamic wave) are generated which isotropise the interstellar protons and electrons. As these interstellar protons interact with the protons in the blast wave, pions (neutral

### 3.4. Blazar Emission Models

---

and charged) are generated. These further decay into  $\gamma$ -rays, electrons, positrons and neutrinos.

Within the family of ultra high-energy proton beam models, Mannheim (1993) suggests that both electrons and protons might be accelerated by multiple crossings of shock-waves in the jet. The protons can be accelerated to energies in excess of 100 TeV by this process. They can then lose energy by adiabatic expansion (proton pressure decreases as shock wave dissipates), synchrotron cooling, ionisation or by interaction with photons in the region by



The neutral pion here decays into a  $\gamma$ -ray pair (see above), but is scattered in the optically-thick jet. This produces an electromagnetic cascade, referred to as a proton-induced cascade, which in turn initiates a pair-synchrotron cascade. Both the lower and higher peaks in the blazar's SED can be explained by these cascades. The energy loss processes described in this model lead to the assumption of a second break in the seed proton and electron spectra - one break due to the intrinsic spectrum of the protons/electrons and another due to the energy loss effects. The photons with which the proton reacts are thought to come from the accretion disk for emission close to the supermassive black hole and from the broad-line region for emission from farther away.

Aharonian (2000) provides a good fit to observations of Markarian 421 and Markarian 501 using a model based on the synchrotron emission of  $10^{19}$ eV protons in a compact region of the jet which has a magnetic field of strength  $\sim 30 - 100$  G. This model can explain the spectral steadiness of the two sources (Markarian 421 and Markarian 501) during flaring.

Although observations can challenge both leptonic and hadronic models, neither can be convincingly ruled out. However, leptonic models (SSC and EC) are usually favoured over hadronic models. One reason for this

### 3.5. Multiwavelength Blazar Observations

---

is the strong correlation between observed x-ray and TeV fluxes. This correlation indicates that the same population of electrons is responsible for both the synchrotron and inverse Compton components of blazar SEDs. Also, the rapidity of the flaring exhibited by TeV blazars (often on the scale of minutes) is difficult to explain using hadronic scenarios as protons have considerably longer cooling times than electrons.

## 3.5 Multiwavelength Blazar Observations

In the last several years, various multiwavelength campaigns have been launched to monitor variability of blazars within a number of wavebands. The campaigns have varied in format from campaign to campaign, many waiting for the blazar to reach a threshold flux level in one wave-band before observations at other wavelengths were instigated. Other campaigns have been pre-planned, with observations carried out at prescribed times regardless of flux level. This type of campaign has usually been relatively short with sparse sampling. With only  $\sim 800$  hours of usable observation time every year, imaging atmospheric Cherenkov telescopes have rarely been able to expend a lot of time on this type of campaign.

Acquisition of good multiwavelength data has come up against difficulties as the sensitivity of TeV observatories requires that relatively large flares must be observed in order to obtain light curves which may be sampled on hour-long timescales (Rebillot *et al.*, 2006). In some cases, the fluxes have been sufficient but the sampling has been sparse due to weather or lunar-cycle limitations. However, the information gained from observations at  $\gamma$ -ray energies is important in the constraint of model parameters, as discussed in Section 3.4.

Since 2005, the Whipple 10 m  $\gamma$ -ray telescope has been primarily monitoring blazars as part of a large-scale multiwavelength campaign which includes observatories in radio, optical, infrared and x-ray bands. Long, well-sampled light curves and important spectral information are

### 3.5. Multiwavelength Blazar Observations

---

being gathered. Monitoring of the five blazars for which  $\gamma$ -ray and optical observations are presented in this thesis, is part of this campaign.

Table 3.2 lists those blazars which pertain to this thesis. All five are northern hemisphere high-frequency peaked BL Lacs which have been detected at TeV energies in the past at a significance greater than  $5\sigma$ . These blazars have also all been independently detected by a second experiment in the same energy band. In the following sections, the observation history of each source is discussed in the context of TeV  $\gamma$ -ray observations and multiwavelength observations along with recent findings.

#### 3.5.1 Markarian 421

Markarian 421 was the first source of extragalactic TeV  $\gamma$ -rays to be discovered by ground-based telescopes (Punch *et al.*, 1992). The initial detection indicated a  $6\sigma$  excess at a flux level (at energies  $>500$  GeV) of  $\sim 30\%$  that of the Crab Nebula. It is now one of the best-studied objects in the VHE sky, having been independently detected by all successful ground-based experiments in the interim (*e.g.* Petry *et al.*, 1996; Boone *et al.*, 2002; Amenomori *et al.*, 2003; Albert *et al.*, 2007e).

Shortly after the detection of Markarian 421 at TeV energies,  $\gamma$ -ray variability was reported (Kerrick, 1994; Schubnell, 1994). Since then, long term observation campaigns have revealed variation on timescales from minutes to years. Extreme and rapid flaring was detected for the first time in 1996 when flux levels were recorded at levels of  $\sim 10$  times that of the Crab Nebula over the course of 2 hours (Gaidos *et al.*, 1996). A weaker flare was detected in subsequent observations (a number of weeks later) which exhibited a doubling time of only 30 minutes.

Buckley *et al.* (1996) reported on multiwavelength observations carried out on Markarian 421 in the 1995 season. 62 nights of  $\gamma$ -ray data were complemented by target-of-opportunity observations in a number of different wavebands over a 27-day period. No steady emission was apparent and flares of the order of  $\leq 1$  day could be resolved. This rapid

Name	Right Ascension [hr:min:sec]	Declination [deg min sec]	$z$	Discoverer	Publication
Markarian 421	11:04:27.3	+38 12 32	0.031	Whipple	Punch <i>et al.</i> (1992)
Markarian 501	16:53:52.2	+39 45 36	0.034	Whipple	Quinn <i>et al.</i> (1996)
1ES 2344+514	23:47:04.8	+51 42 18	0.044	Whipple	Catanese <i>et al.</i> (1998)
H 1426+428	14:28:32.6	+42 40 21	0.129	Whipple	Horan <i>et al.</i> (2002)
1ES 1959+650	19:59:59.9	+65 08 55	0.048	Telescope Array	Nishiyama (1999)

**Table 3.2:** List of 5 blazars studied in this work. The Right Ascension in each case is J2000 epoch. The publication is the refereed journal publication reporting the initial detection at TeV energies.

### 3.5. Multiwavelength Blazar Observations

---

variability implied a small compact emission region with large Doppler boosting.

Multiwavelength observations of Markarian 421 in 1998 were discussed by Takahashi *et al.* (2000). BeppoSAX and the Whipple 10 m telescope both recorded a pronounced flare at the beginning of the campaign. Daily x-ray flares were observed. Correlation between the x-ray flares and  $\gamma$ -ray flares over the duration of this campaign was noted, again implying a co-located emission region. Temporal analysis provided evidence for flare timescales on the order of 1 day.

Takahashi *et al.* (2000) also reported complicated spectral variability for Markarian 421. In most previous studies hard x-ray flares were found to lead MeV - GeV flares (Takahashi *et al.*, 1996) while in other campaigns low-energy x-ray emission had been found to lead the high-energy x-ray emission (Fossati *et al.*, 2000). In the case of Takahashi *et al.* (2000), both types of behaviour were exhibited.

Spectral variations have been observed at TeV energies. Piron *et al.* (2001) discussed observations of flares by the CAT experiment which suggested spectral hardening at TeV energies while flaring. Systematic effects could not be ruled out as the cause of this behaviour, however, as the changes in spectral index were smaller than the systematic uncertainty associated with the spectral analysis. Krennrich *et al.* (2002) confirmed this behaviour definitively when flaring at levels of 0.4 - 13 times that of the Crab Nebula was recorded in 2000-2001. A tight correlation between spectral index and flux level was shown (see Figure 3.6). Similar behaviour was observed by HEGRA over the same period (Aharonian *et al.*, 2002c). Over the course of two nights in March of 2001, the flux levels observed at the Whipple 10 m telescope were sufficient for hour-scale spectral analysis. Spectral variation on timescales of  $\sim 15$  minutes was observed (Krennrich *et al.*, 2003).

Most multiwavelength campaigns in which TeV  $\gamma$ -ray telescopes were participants have had multiwavelength observations invoked by sufficient

### 3.5. Multiwavelength Blazar Observations

---

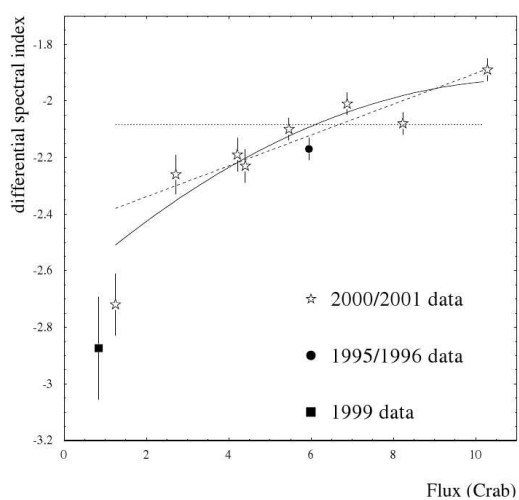


**Figure 3.6:** Plot of spectral index of Markarian 421 against flux for the 2000-2001 season (stars) as measured by the Whipple 10 m telescope. The dotted line represents a constant spectral index which did not fit the observations as the spectral index was seen to increase with flux. The data were better fitted by a linear relation (dashed) or a second-order polynomial (solid). (Krennrich *et al.*, 2002)

### 3.5. Multiwavelength Blazar Observations

---

flaring activity at TeV energies (Rebillot *et al.*, 2006; Fossati *et al.*, 2008) and usually did not last much longer than the durations of the TeV activity. A campaign carried out by Błażejowski *et al.* (2005) over a 16-month period in 2003-2004 did not require this trigger criterion however. Rather, regardless of flux at either wavelength,  $\gamma$ -ray observations were scheduled so that they matched the x-ray observation schedule as closely as possible. Although optical and radio data were also obtained, the campaign concentrated on the x-ray/ $\gamma$ -ray relationship. Rapid variability was again exhibited by the source in both bands. However, only a loose flux correlation was evident (*i.e.* correlations at lags of  $\pm 1$ -2 days). For one large flare, x-ray emission was found to peak a number of days after the  $\gamma$ -ray emission. A multi-component SSC approach was taken to model the emission.

X-ray flux correlation with  $\gamma$ -ray flux is discussed further in Fossati *et al.* (2008) in the context of observations of Markarian 421 in 2001. A tight x-ray flux/ $\gamma$ -ray flux correlation was confirmed, which backs up the postulation that emission at both of these bands is essentially from the same physical region and that the same electron distribution is responsible. The findings do offer a challenge in the modelling of the emission however. Two SSC models are considered to explain the emission processes and variability. One suggests that scattering takes place in the Klein-Nishina regime (see Section 2.2.1) and requires a Doppler factor of  $\delta \simeq 20$ . In the second model, scattering takes place in the Thompson regime and a Doppler factor of  $\delta \simeq 100$  is required.

The net result of these multiwavelength campaigns is that there is strong evidence for correlation between the observed x-ray flux and  $\gamma$ -ray flux for Markarian 421 (for example, see Buckley *et al.*, 1996; Błażejowski *et al.*, 2005). Most multiwavelength campaigns thus far have concentrated on the relationship between the x-ray and  $\gamma$ -ray variations. Correlations between  $\gamma$ -ray variations and variations at other wavelengths (radio, optical, *etc.*) have not been established. Correlations at these

### 3.5. Multiwavelength Blazar Observations

Year(s)	Publication
2001	Fossati <i>et al.</i> (2008)
2002 - 2003	Rebillot <i>et al.</i> (2006)
2003 - 2004	Błażejowski <i>et al.</i> (2005)
2005 - 2006	Horan <i>et al.</i> (2009)
2000 - 2006	Grube (2007)
2001 - 2006	Lee (2008)

**Table 3.3:** Outline of the publications presenting observations of Markarian 421 with the Whipple 10 m telescope since 2000.

other wavelengths may have been missed if flares occurred after the campaign had ended, or if a flare preceded the initial  $\gamma$ -ray or x-ray trigger.

Table 3.3 gives a summary of the recent observing campaigns (with associated publications) which have included observations taken at the Whipple 10 m telescope.

#### 3.5.2 Markarian 501

Markarian 501 was the second blazar with emission established at TeV energies. The initial detection was presented by Quinn *et al.* (1996) at a flux level of  $\sim 10\%$  of the Crab Nebula flux during observations in 1995. This was the first AGN source to be detected by a ground-based experiment without a previous detection by EGRET. The flux level also made it the weakest VHE  $\gamma$ -ray source detected at the time. Confirmation of the detection was provided by HEGRA (Bradbury *et al.*, 1997), subsequently by the Telescope Array (Hayashida *et al.*, 1998) and, more recently, by MAGIC (Albert *et al.*, 2007f).

Observations over a number of years following its initial discovery showed variation in the flux level from season to season. Average emission levels at this time were at a 10% - 50% Crab flux, though higher fluxes were also recorded during flaring. Observations in 1996 showed an

### 3.5. Multiwavelength Blazar Observations

---

average flux at twice the 1995 level, with considerably more month-scale variability (Quinn *et al.*, 1999). The average flux level in 1997 rose to  $\sim 1.4$  times that of the Crab Nebula. A peak nightly rate of 3.7 times that of the Crab Nebula was observed on one night. Significant hour-scale flaring was observed at this time, with flare maximum of  $\sim 5$  times that of the Crab Nebula. HEGRA's observations of Markarian 501 during 1997 revealed similar behaviour, with flares peaking at around 10 times the flux of the Crab Nebula (Aharonian *et al.*, 1999a,b) at energies greater than 1 TeV. The following season saw a return to flux levels of around 20% of the Crab flux.

The only other TeV blazar detected at the time, Markarian 421, had not previously exhibited yearly mean flux variation on a similar scale (Quinn *et al.*, 1999). Since their redshifts were similar, it was assumed that attenuation of an intrinsically strong and steady source could not be the reason for these differences. The variations were therefore thought to be intrinsic to the source itself.

An 11-day multiwavelength campaign was triggered by the high  $\gamma$ -ray activity observed in the 1997 season (Catanese *et al.*, 1997). This included high-energy  $\gamma$ -ray observations and x-ray observations as well as observations in optical wavebands. Correlations between the TeV  $\gamma$ -ray band, the soft x-ray band, and the hard x-ray band were evident in these observations, while Markarian 501 was not detected by EGRET in the soft  $\gamma$ -ray band. Although nothing conclusive could be stated about the significance of the observation, optical U-band flux was recorded at a level 10% above usual in that month.

In a similar manner to Markarian 421, many multiwavelength studies have been carried out on Markarian 501. These have traditionally concentrated on the x-ray/VHE  $\gamma$ -ray relationship. A long-term multiwavelength study of the x-ray and TeV  $\gamma$ -ray variation was reported in Gliozzi *et al.* (2006). RXTE data from 1997, 1998, 1999, 2000 and 2004 were compared to HEGRA data and Whipple 10 m data from the same

### 3.5. Multiwavelength Blazar Observations

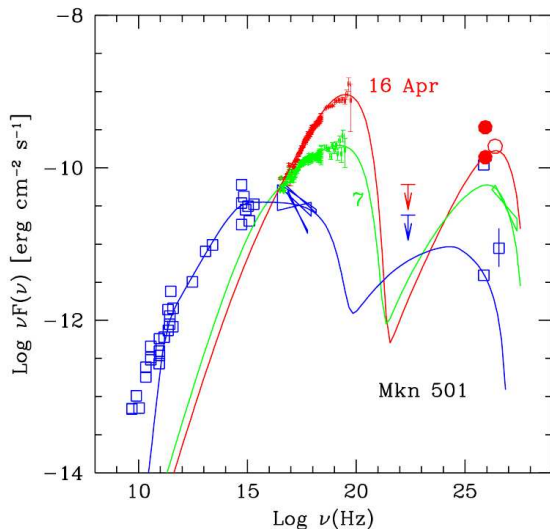


**Figure 3.7:** Plot of spectral energy distributions of Markarian 501 during varying levels of activity. (Pian *et al.*, 1998)

period. A strong flux correlation between the two bands was confirmed, the correlation being stronger when the source is brighter. Interestingly, some x-ray flares also seemed to have no TeV  $\gamma$ -ray counterpart.

Spectral variation has been observed in Markarian 501. The synchrotron peak was observed to shift to higher energies by a factor  $\geq 100$  during periods when higher  $\gamma$ -ray fluxes were observed (Pian *et al.*, 1998). Figure 3.7 shows this shift which moves the peak into the hard x-ray band. The spectral index above 1 TeV (as seen by HEGRA) was not seen to shift during this activity, although subsequent observations in 1998-1999 exhibited a softer low-state energy spectrum. The CAT telescope, which had a lower energy threshold of 0.25 TeV, did detect spectral variability during the 1997 outburst (Piron *et al.*, 2000; Djannati-Atai *et al.*, 1999).

Albert *et al.* (2007f) reported MAGIC's observations of Markarian 501 over 21 nights in 2005. On all nights, the source was detected. On two of the nights covered, the flux level reached  $>3$  times that of the Crab Nebula. A 20-minute flare was recorded which indicated a  $4 \pm 1$  minute

### 3.5. Multiwavelength Blazar Observations

---

time delay between the peak flux at energies  $<0.25$  TeV and the peak flux at energies  $>1.2$  TeV. This might indicate that electrons are being progressively accelerated within the plasma knot. The spectral peak shifted with luminosity, so spectral variability was confirmed. Although these observations offered insight into the TeV activity of the source, no simultaneous x-ray observations were obtained, meaning that the SSC model for the SED could not be constrained. The results did restrict the Doppler factor to the  $\delta = 25 - 50$  range and the magnetic field to  $B = 0.05 - 0.50$  Gauss. During the campaign, flux variability (measured using the fractional variability amplitude,  $F_{var}$ , as per Vaughan *et al.* (2003)) was seen to increase with the  $\gamma$ -ray energy.

Stickel *et al.* (1993) reported variability over 1.3 magnitudes in optical wavebands. Over the course of 2 weeks of observation, Heidt & Wagner (1996) saw variations of 0.31 magnitudes per day. Fast variation was reported in Ghosh *et al.* (2000) when 10 nights of intense observation resulted in the detection of rapid variability on 7 of the nights. On one night the variability was as much as 0.13 magnitudes within 12 minutes. Gupta *et al.* (2008) reported on minute-scale to day-scale variability over a 12-night observing campaign. B-, V- and R-band observations were obtained. A 0.05 magnitude R-band variation was observed over 15 minutes in one night. From these measurements, the central black hole was constrained to a mass of  $\sim 1.2 \times 10^8 M_{\odot}$ .

#### 3.5.3 1ES 2344+514

Observations of 1ES 2344+514 for four months between October 1995 and January 1996 led to its initial detection by the Whipple 10 m telescope (Catanese *et al.*, 1998). The evidence for emission came mostly from the detection of an apparent flare on one night. The source exhibited a  $6\sigma$  excess with a flux of  $>60\%$  that of the Crab Nebula. Removing this one night of data resulted in a  $4\sigma$  excess over the other four months, giving a mean flux of  $\sim 11\%$  of the Crab Nebula flux. Follow-up observa-

### 3.5. Multiwavelength Blazar Observations

---

tions, reported in Catanese *et al.* (1998), in the 1996-1997 season yielded no significant detection and gave an upper limit of around 8% of the Crab flux. The assumption was that, like Markarian 421 and Markarian 501, the quiescent emission of 1ES 2344+514 was below the sensitivity threshold of the telescope and emission could only be detected from the source when it went into a high state of activity.

Konopelko (1999) reported on observations of 1ES 2344+514 by the HEGRA array which resulted in only tentative hints ( $>3\sigma$ ) of a signal in 25 hours of data. After further observations were taken, and data from three seasons were combined, a  $4.4\sigma$  detection at just over 3% of the Crab flux resulted (Aharonian *et al.*, 2004a).

Schroedter *et al.* (2005) reported on the spectrum of 1ES 2344+514 during the 1995 flare. Due to low statistical significance of the spectrum, the spectral cut-off feature expected to be present in the observed spectrum due to attenuation by extragalactic background light (*e.g.* Aharonian *et al.*, 2001b; Krennrich *et al.*, 2001a) could not be measured and compared to those of Markarian 421 and Markarian 501. As there were no contemporaneous observations at other wavelengths, nothing could be said about the SED during the flare. However, x-ray observations were conducted by BeppoSAX about a year after the 1995 TeV  $\gamma$ -ray flare (Giommi *et al.*, 2000). A sizeable flare and large spectral variations were detected over a 5-day period. The shape of the spectrum was seen to vary depending on the intensity of emission, the spectrum hardening with increasing brightness. As with Markarian 501, the synchrotron peak was also seen to shift into the hard x-ray band when the source had brightened. Simultaneous observations at TeV energies did not reveal a detection, thus limiting the possibility of constraining emission models.

More recently, MAGIC has detected 1ES 2344+514 in a low, steady state of emission (Albert *et al.*, 2007c). 23 hours of data taken over a 5-month period in 2005 produced a  $11\sigma$  detection at a level of  $(10 \pm 1)\%$  of that of the Crab Nebula (at  $E \geq 200$  GeV). No significant variability was

### 3.5. Multiwavelength Blazar Observations

---

exhibited at TeV energies with the detected “baseline” corresponding to a level  $\frac{1}{6}$  of that of the 1995 flare detected by the Whipple 10 m telescope. R-band optical observations were also obtained. A one-zone SSC model was used to fit archival data which were split into low state and flare state based on the TeV emission at the time the data were obtained. Radio data were omitted as they were not well fitted by the model. Values of  $\delta = 8.4$  and  $B = 0.095$  G for low-state and  $\delta = 15.2$  with  $B = 0.075$  G for high-state (Doppler factor and magnetic field respectively) fitted the observational data.

The relativistic jet of 1ES 2344+514 has been studied in great detail with VLBI radio telescopes (Piner & Edwards, 2004). The resolution achieved has permitted imaging and velocity measurements of individual plasma knots as they move through the jet. It is thought that the site of radio emission is farther along the jet than the site of higher-energy emission.

#### 3.5.4 H 1426+428

The detection of H 1426+428 at TeV energies (Horan *et al.*, 2002) was of great significance due to its redshift ( $z = 0.129$ ). At the time of its detection, it was the most distant TeV blazar detected by a long way. Its discovery was confirmed by a number of experiments (Aharonian *et al.*, 2002b; Djannati-Ataï *et al.*, 2002). The initial detection at the Whipple 10 m telescope was at a  $5.8\sigma$ -level of significance based on 44 hours of data. The source is known to be weak. Although year-on-year variability has been exhibited, no major flaring events have been detected. Observations at the Whipple 10 m telescope between 1995 and 1998 did not reveal a significant signal. More extensive observations were carried out between 1999 and 2001. The observations in 2000 resulted in a  $3.1\sigma$  excess with the 2001 data exhibiting a  $5.5\sigma$  excess. The synchrotron emission peak was found to be at a higher frequency than any of the previously detected blazars. It has thus been labelled an “extreme” HBL.

### 3.5. Multiwavelength Blazar Observations

---

Aharonian *et al.* (2002b) reported similar results for HEGRA observations in the 1999 and 2000 seasons which resulted in a  $5.8\sigma$  accumulated excess over the two years. The 1999 data set showed a  $2.4\sigma$  excess, with the 2000 data set amounting to a  $5.3\sigma$  excess. H 1426+428's spectrum was also found to be very steep - steeper than any previously detected HBL. This was confirmed by Petry *et al.* (2002). The steep spectrum implied attenuation by extragalactic background light, but a steep intrinsic source spectrum could not be ruled out.

The CAT telescope observed H 1426+428 from 1998 to 2000, resulting in an accumulated  $5.2\sigma$  excess from 26 hours of data (Djannati-Ataï *et al.*, 2002). The mean flux measured was  $\sim 20\%$  of that of the Crab Nebula at  $E \geq 250$  GeV. Observations by CELESTE in 2000 resulted in an upper limit of  $<50\%$  of the Crab at 100 GeV (Smith *et al.*, 2006).

RXTE observations of H 1426+428 from March to June of 2002 revealed information about the synchrotron peak region of the SED (Falcone *et al.*, 2004a). Variability was observed in all x-ray bands, albeit at lower levels than typical for other TeV blazars. Changes in the observed spectral index over the course of the campaign, if due to shifts in the low-energy peak position, would imply that it sometimes shifts to  $>100$  keV energies, while falling into the 2.9 - 24 keV region (*i.e.*, within the sensitivity of the Proportional Counting Array on board RXTE) at others. No significant detections at TeV energies were made during this campaign, making model constraint difficult.

#### 3.5.5 1ES 1959+650

Low redshift and a hard x-ray spectrum made 1ES 1959+650 a prime candidate for TeV observations before it was initially detected at a  $3.9\sigma$  significance level by the Utah Seven Telescope Array in 1998 (Nishiyama, 1999). The mean flux level recorded by the Seven Telescope Array for the 1998 season was comparable to the Crab Nebula flux. Two periods of higher activity were detected at significance levels of  $5.3\sigma$  and  $5.0\sigma$ .

### 3.5. Multiwavelength Blazar Observations

---

HEGRA detected 1ES 1959+650 during the 2000 and 2001 observing seasons with a significance of  $5.2\sigma$ , at a flux level of 5.3% of the Crab Nebula’s flux (Aharonian *et al.*, 2003a).

Whipple 10 m telescope observations of the source in May of 2002 showed 1ES 1959+650 to be in a high state of activity (Holder *et al.*, 2003). The source was monitored into July resulting in 39 hours of data, giving a mean flux of  $>60\%$  of the Crab flux. Night-by-night rates exhibited large amounts of variability, reaching levels  $>3$  times the flux of the Crab. Prompted by these observations, HEGRA observed 1ES 1959+650 and detected it at a  $23\sigma$  statistical significance with flux levels up to  $>2$  times that of the Crab Nebula flux (Aharonian *et al.*, 2003a).

A steep spectral index ( $\alpha = 2.83 \pm 0.14_{stat} \pm 0.08_{sys}$ ) was recorded by HEGRA when 1ES 1959+650 was not in a high state. While flaring, the SED was seen to exhibit a curved profile (*i.e.* slope of the SED varied with energy) and deviated from the previously recorded spectrum. Spectral analysis of the Whipple 10 m data was complicated by a drop in telescope efficiency during the time of observations. However, these complications were resolved and Daniel *et al.* (2005) reported a spectral index which was in agreement with the HEGRA value during flaring. There was no evidence for a spectral cut-off. Spectral variation as a function of flux level was not evident, unlike in the cases of Markarian 421 and Markarian 501.

Flaring detected by the Whipple 10 m telescope triggered target-of-opportunity observations in the radio, optical and x-ray wavebands (Krawczynski *et al.*, 2004). The correlation analysis for the x-ray band and  $\gamma$ -ray band presented the most interesting result: although a correlation existed between the x-ray data and  $\gamma$ -ray data, an “orphan”  $\gamma$ -ray flare was also detected which had no accompanying x-ray flare. This challenges models which suggest that the emission in both bands originates in the same region of the jet. The radio flux stayed steady during the flare within the sensitivity of the instruments used. Optical varia-

### 3.5. Multiwavelength Blazar Observations

---

tion was detected during the campaign. However, no correlation between the optical bands and the higher-energy bands was observed. Data were obtained in the V-, R- and I-bands, each showing variations of about 0.1 magnitude on timescales of about 10 days. There was a difference of 0.1 magnitudes between the mean brightness in the last two weeks of the campaign and the mean brightness in the first 4 weeks. Although a slow overall increase in flux occurred in the x-ray band during the two weeks when the optical flux was higher, no definite correlations could be seen. Previous studies of the optical characteristics of 1ES 1959+650 had shown it to be capable of high variability. Villata *et al.* (2000) found rapid changes in brightness, including a 0.28 magnitude decrease over only 4 days. However, similar studies at optical wavelengths have not always seen this level of variability (*e.g.* Poggiani, 2006).

The low-energy component of 1ES 1959+650's SED had been shown to peak at around 4 keV by BeppoSAX in 1997 (Beckmann *et al.*, 2002). However, as with other HBLs, this peak frequency is known to vary depending on its flux. Analysis of the x-ray data taken at the time of the 2002 flare showed the peak moving to different energies above and below 10 keV during the observations (Krawczynski *et al.*, 2004). X-ray observations of 1ES 1959+650 in 2000 (Giebels *et al.*, 2002) showed threefold increases in flux on timescales of a few days. These increases in flux were correlated with spectral hardening, indicating that the lower-energy peak was shifting towards higher energies at the time.

More recent observations of 1ES 1959+650 with MAGIC (Albert *et al.*, 2006d) while in a low state of TeV activity have resulted in a  $\sim 8\sigma$  significance level detection with a flux of around 20% that of the Crab Nebula. No large-scale or significant variability was detected. X-ray observations in the same period showed that the source was similarly in a low state of activity in this band. Optical observations also showed flux at a lower level than its 2-year average flux. Spectral analysis of the TeV  $\gamma$ -ray data gives a differential spectrum which is well fitted by a power-

### 3.5. Multiwavelength Blazar Observations

---

law and is in reasonable agreement with HEGRA's measurements of a "low-state" spectrum for this object (*i.e.* from Aharonian *et al.*, 2003a) when the emission level was comparable to that observed by MAGIC. A simple one-zone SSC emission scenario seems improbable for this source due, mainly, to the "orphan" flares detected at TeV energies in the past. Either additional high-energy electron populations or proton synchrotron models seem much more likely to be the cause of the emission.

# Chapter 4

## The Whipple 10 m Telescope and Analysis

### 4.1 Telescope Hardware

The Whipple 10 m Atmospheric Cherenkov Telescope was built in 1968. It is located on Mount Hopkins in southern Arizona, USA at an altitude of  $\sim 2300$  m above sea level. It is comprised of a large tessellated reflector with a camera at the focal plane. It was the first large atmospheric Cherenkov telescope to be built for the study of  $\gamma$ -ray astronomy (Fazio *et al.*, 1968). Since 1982, it has operated as an Imaging Atmospheric Cherenkov telescope. An altitude-over-azimuth mount is used to drive the reflector with a slewing speed of around  $1^\circ \text{ s}^{-1}$ . Tracking resolution is  $0.01^\circ$ .

#### 4.1.1 The Reflector

The telescope's reflector has an aperture of 10 m. It is of Davies-Cotton design (Davies & Cotton, 1957), employing many small spherical mirror facets, each with a focal length that is equal to the radius of curvature of the optical support structure (OSS) on which they are mounted. This has the effect of providing the same effective collection area as a single

## 4.1. Telescope Hardware

---

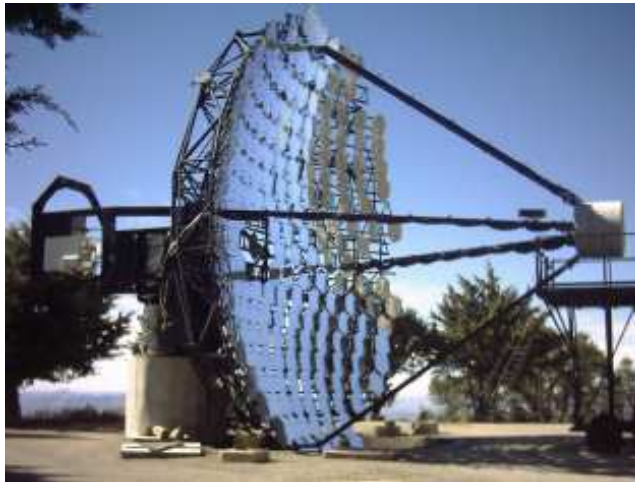


**Figure 4.1:** The Whipple 10 m reflector, located on Mt. Hopkins in southern Arizona, USA.

large 10 m-diameter mirror. The OSS that holds the facets is made of tubular steel, is spherical and has a radius of curvature of 7.3 m (*i.e.* the effective focal length of the reflector). The Davies-Cotton optical design offers the advantages of straightforward alignment procedure and good off-axis performance. A disadvantage is that the system is not isochronous. This means that photons in an ideally flat wavefront which is incident on the telescope perpendicular to the optic axis will be spread out by  $\sim 6$  ns when they arrive at the camera. Discussion of the optical aberration and characteristics of the Whipple 10 m reflector is presented in Lewis (1990).

The reflective surface is composed of 248 hexagonal glass facets which are made of solid ground and polished glass of 1 cm thickness. They are hexagonal in shape to minimise gaps and overlaps in the reflective surface, which has an area of around  $75 \text{ m}^2$ . Each facet is fixed to the OSS on a triangular mount by three adjustable bolts located at the corners of the mount. These bolts are adjustable to allow for optical alignment of each facet.

Each facet is front-aluminised and anodised to give high reflectivity

## 4.1. Telescope Hardware

---

in the blue/ultraviolet part of the spectrum. The anodization hardens the front surface of the facet. This is necessary since the mirrors are not covered in any way that might protect them from exposure to the environment. Although anodization helps protect the reflective surface of the facets, degradation still occurs over the course of a number of years. For this reason, the mirrors are removed, stripped and re-coated every few years to ensure a high level of reflectivity is maintained. The reflectivity of the mirrors is also adversely affected on shorter timescales by a build-up of various environmental contaminants such as dust, water spots and bird droppings. This is overcome by monthly washing of the reflector with water and mild detergent. Investigations have shown that this method helps to maintain reflectivity over a longer period of time and has no noticeable corrosive effect on the reflective surface (Badran & Weekes, 2001). The reflectivity of the Whipple 10 m telescope facets is typically  $> 80\%$  across the visible spectrum but peaks at around 400 nm.

### Alignment

Each mirror facet comprising the telescope's optics is individually adjustable. By adjusting each facet in turn, the reflector's overall optics can be modified. A semi-automated alignment system has been built to measure the adjustment necessary to align each mirror facet. When measuring the alignment of the telescope, this system is set up at a point which is 14.6 m (*i.e.* twice the focal length of the mirror facets) from the OSS along the optic axis of the reflector. This point is referred to as the "2f-point". Adjustments to each facet's alignment are carried out while the telescope is stowed at its home position facing north at an elevation of  $0^\circ$ . The alignment device is then mounted on a purpose-built platform at the 2f-point. The alignment device is pictured in Figure 4.2 and consists of:

- A computer-controlled pan-tilt unit

## 4.1. Telescope Hardware

---

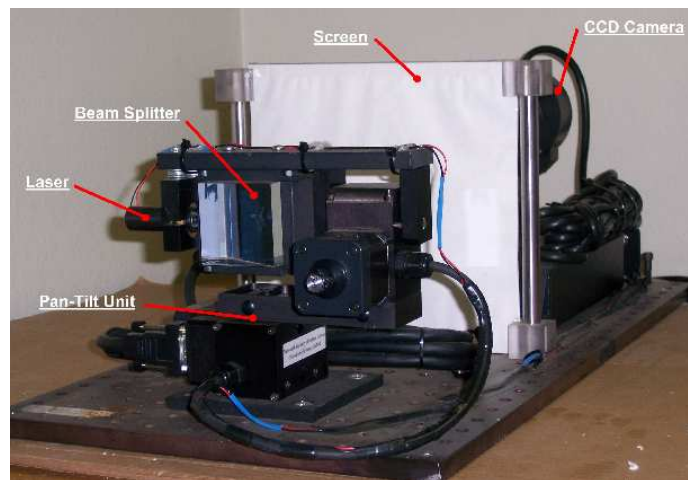


**Figure 4.2:** The semi-automated alignment system (cover removed for clarity) used to align the reflectors of the VERITAS telescopes. The Whipple 10 m alignment system is similar in design.

- A laser and beam-splitter assembly
- A SBIG ST-5C CCD camera
- A translucent screen

The pan-tilt unit, controlled by a custom computer program, is used to direct the outgoing laser beam onto each mirror facet in turn. Due to the Davies-Cotton optics employed by the telescope reflector, the beam reflected from the mirror should then return along its own outgoing path when the mirror is correctly aligned. With all mirrors aligned in this manner, light from a source at infinity should converge to a point at the focal plane of the telescope. Figure 4.3 illustrates this schematically.

Part of the outgoing laser beam is back-reflected by the beam-splitter onto the screen, forming a reference beam. This gives a reference point on the screen corresponding to the desired position of the reflected beam when the facet is aligned correctly. Using an image of the screen obtained with the CCD camera, the program can determine the centroid locations

## 4.1. Telescope Hardware

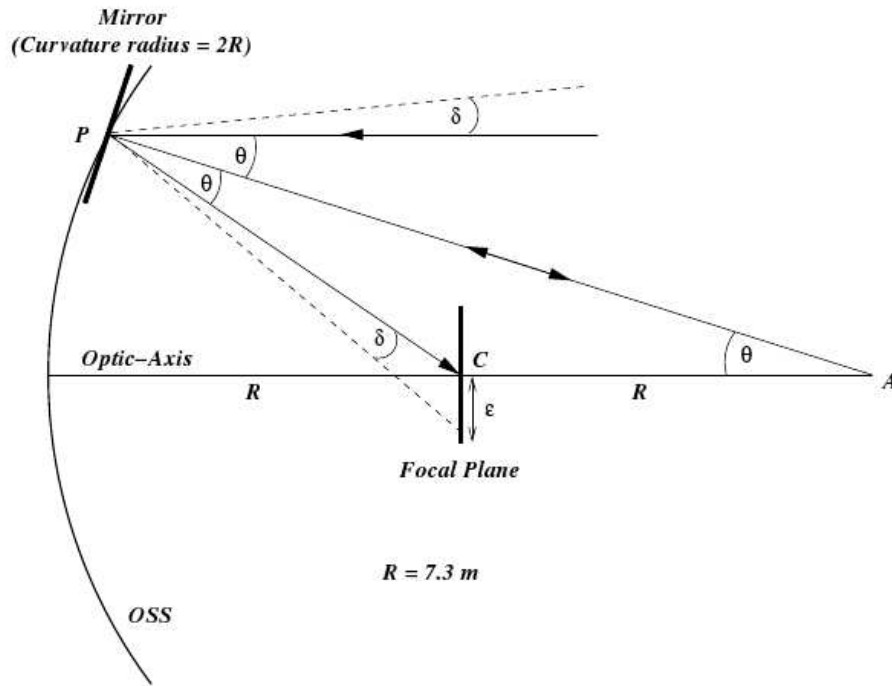


**Figure 4.3:** For a reflector (such as the Whipple 10 m reflector) utilising the Davies-Cotton design, when each mirror facet is correctly aligned, the triangle  $APC$  will be isosceles. Light which is incident parallel to the optic axis of the reflector will be focused at the centre of the focal plane. Light from the point  $A$  will reflect back along its own path. Light incident at an angle  $\delta$  from the optic axis will be displaced from the centre of the focal plane by an amount  $\epsilon$ . Figure from Kildea *et al.* (2007).

## 4.1. Telescope Hardware

---

of both the back-reflected beam and the reflected beam. These positions are used to determine how far the reflected beam is from the reference position on the screen and then to calculate what adjustments must be made to the facet mounting bracket in order to align the mirror correctly. This is then repeated for each of the mirror facets on the reflector. Once aligned, it is not necessary to re-align the facets more frequently than once a year.

### **Bias Alignment**

When the telescope moves in elevation, gravity has the effect of moving each mirror facet slightly relative to the other mirrors. The arms which hold the camera and its housing at the focal point of the reflector also put stresses and strains on the OSS, which distort its shape. Both of these effects lend themselves to a broadening of the reflector's point spread function (PSF) at typical observing elevations. Any image formed at the focal plane of the telescope is a convolution of the ideal object image with the optical response of the telescope. As such, it is desirable to optimise the optical response of the reflector at observing elevations. The effects of the sagging can be measured and, as they happen in a reproducible way, can be corrected for.

In order to correct for the sagging, the movement experienced by each facet must be characterised. To do this, a small, light-weight laser unit is attached to a facet. The laser beam is directed onto the focal plane of the telescope and a CCD image of the focal plane is obtained. The telescope is then raised to the elevation of desired best focus at  $65^\circ$ , which is a typical observing elevation. Another CCD image is obtained. The amount by which the laser spot moves on the focal plane is measured by comparing the images taken at the two different telescope positions. The laser beam's movement on the focal plane is due to the fact that the facet on which it is mounted has moved, relative to the optic axis of the telescope, due to sagging, thus the movement of the facet can

## 4.1. Telescope Hardware

---

be characterised. This process is repeated for all mirror facets in the reflector.

A file is produced containing the movement characteristics of each mirror facet. This file is used by the alignment program to negate the effects of sagging. To do this, each facet is purposely misaligned while the telescope is parked at its stow position. The deliberate misalignment is equal in magnitude to that of the measured movement of the facet due to sagging but in the opposite direction to the motion due to sagging. This ensures that the mirrors fall into alignment at typical observing elevations, thus sharpening the point spread function (Schroedter, 2002, 2004). Typically, mirrors require corrections of  $\leq 0.1^\circ$ , with more movement (due to sagging) observed in the mirrors surrounding the arms that support the camera housing in the focal plane of the telescope.

### Performance

To test the alignment of the reflector, a CCD image of the focal plane of the telescope is acquired while the telescope tracks a bright star. Images like these are acquired for a series of bright stars at various elevations. The bright stars are considered point-sources at infinity. The PSF at each elevation is measured by finding the full-width-half-maximum for a 2-D Gaussian fitted to the stars' images. A comparison of the PSF values obtained before and after bias alignment of the Whipple 10 m reflector is shown in Figure 4.4. This technique has also been employed to optimise the optical response of the four telescopes comprising the VERITAS telescope array (Toner *et al.*, 2007).

### 4.1.2 Camera

The telescope's camera is housed in a cylindrical container at the focal plane of the reflector. The container is held in this position by four steel arms. The camera consists of a tightly-packed array of photomultiplier tubes (PMTs). Over the life of the telescope, the focal plane detector has

## 4.1. Telescope Hardware

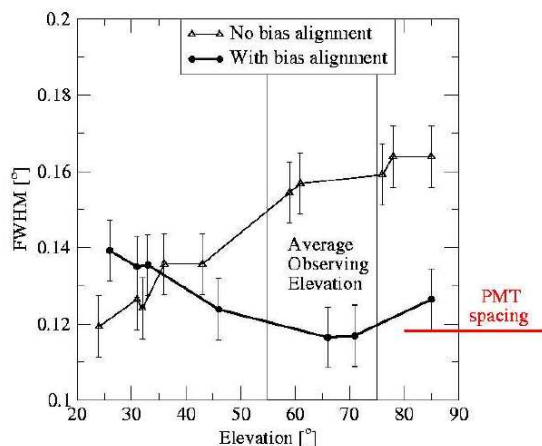


**Figure 4.4:** PSF measurements for the Whipple 10 m reflector over a range of elevations both before and after bias alignment. After bias alignment, the PSF is seen to improve around the average range of observing elevations. The spacing of the PMTs which make up the imaging camera of the telescope is also indicated. Figure from Kildea *et al.* (2007).

been modified and upgraded a number of times. Figure 4.5 shows the layouts of the various imaging cameras employed on the telescope since 1982. Prior to 1982, a single non-imaging 2-inch PMT was used, giving a  $1^\circ$  field of view. Various characteristics of each camera are outlined in Table 4.1. The current camera consists of 379 PMTs (see Figure 4.6), each viewing  $0.12^\circ$  of the sky.

Power is supplied to each individual PMT from a high-voltage module located to the rear of the telescope’s reflector. The voltage applied to the PMTs can be controlled in software via an ethernet connection, with different voltages being applied to each PMT. The voltages are adjusted every year to maintain a relatively constant gain across the camera; typically on the order of  $5 \times 10^6$ . The gain of each tube varies slightly from night to night, however. These small differences are corrected for during offline analysis.

As the PMTs are round, they cannot be packed in such a manner that

## 4.1. Telescope Hardware

---

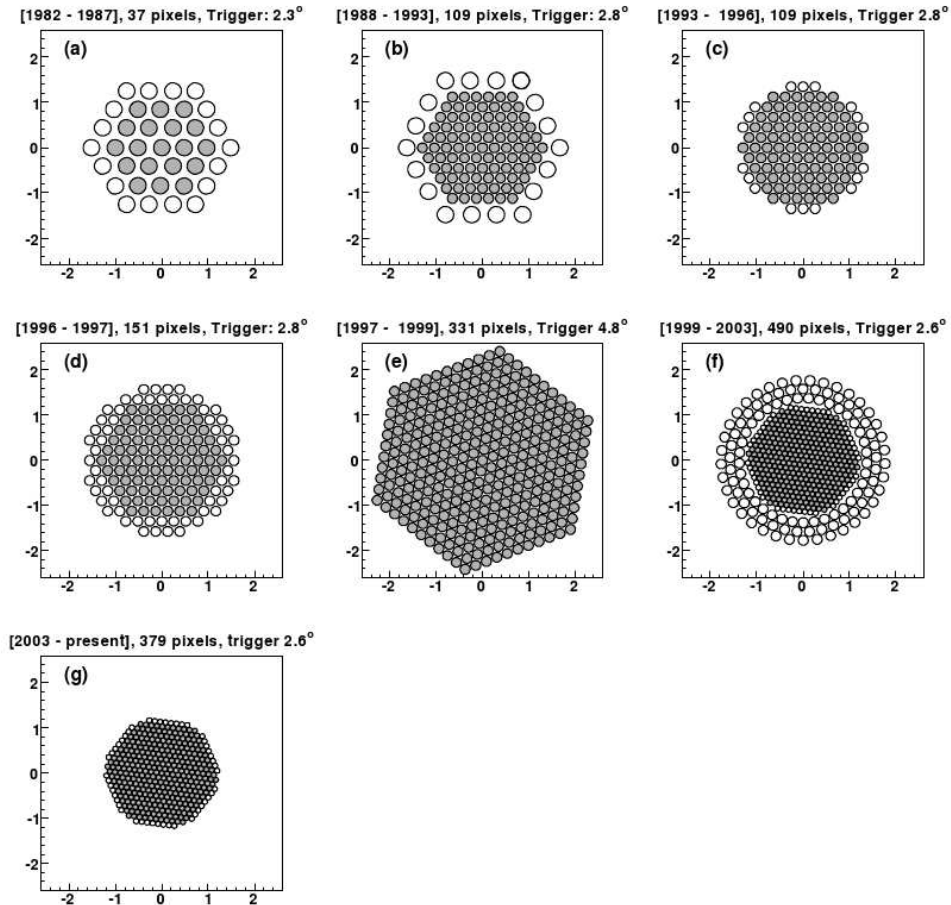


**Figure 4.5:** Layouts of various imaging PMT cameras deployed on the Whipple 10 m telescope from 1982 to present. The shaded pixels were/are included in the telescope's triggering electronics. (Kildea *et al.*, 2007)

## 4.1. Telescope Hardware

---



**Figure 4.6:** The 379-pixel high-resolution PMT camera of the Whipple 10 m telescope. Light cones are mounted in front of the PMTs to collect light that would otherwise fall in the gaps between the pixels.

## 4.2. Data Acquisition

Years	Inner Pixels	Outer Pixels	Pixel FOV	Total FOV	Threshold <sup>1</sup> [GeV]
1982-1987	37	0	0.52°	3.3°	700
1988-1993	91	18	0.26°/0.52°	3.75°	500
1993-1996	109	0	0.26°	3.0°	500
1996-1997	151	0	0.26°	3.5°	500
1997-1999	331	0	0.26°	4.8°	500
1999-2003	379	111	0.12°/0.26°	3.8°	300
2003-present	379	0	0.12°	2.8°	300

**Table 4.1:** Specifications of various imaging cameras used over the lifetime of the Whipple 10 m telescope. Some configurations of the camera were comprised of a set of pixels which contributed to the triggering of the telescope (*i.e.* Inner Pixels) and pixels whose integrated charge in pulses were read out only when the telescope was triggered (*i.e.* Outer Pixels).<sup>1</sup> The energy threshold is defined as the energy at which a peak occurs in the detector’s response to a spectrum similar to that of the Crab Nebula. Table adapted from Kildea *et al.* (2007).

they have no gaps between them. To improve the collection efficiency of the camera, light-concentrating cones are mounted in front of the PMTs at the focal plane of the telescope. The lightcones collect some of the light photons that would otherwise fall on these gaps by reflecting them onto a PMT. Le Bohec & Holder (2003) found a 27% improvement in light collection efficiency when using the lightcones, compared with data obtained before the lightcones were fitted to the camera. This analysis is based solely on experimental data and does not rely on simulations.

## 4.2 Data Acquisition

The telescope’s triggering and data acquisition electronics are located in an air-conditioned room located in the control building close to the

## 4.2. Data Acquisition

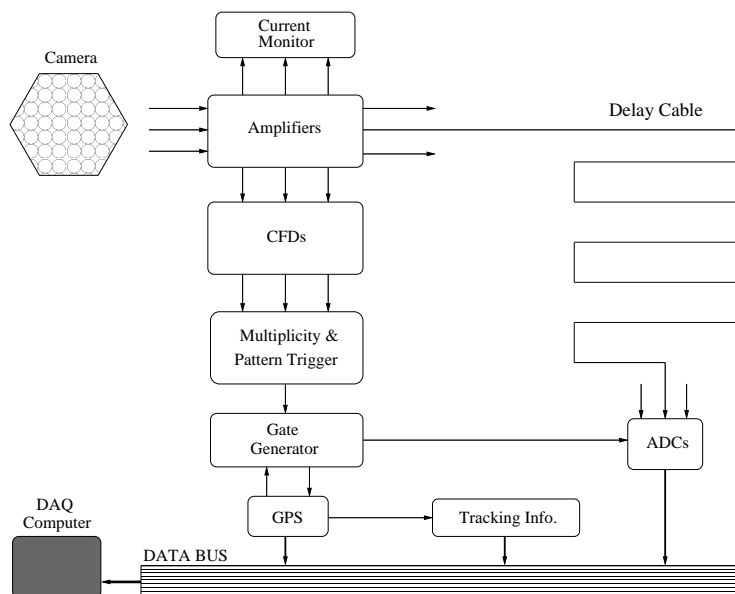


**Figure 4.7:** Outline of the electronics involved in data acquisition for the Whipple 10 m telescope.

telescope. The electronics are comprised of modules connected to a CAMAC data bus system (Rose *et al.*, 1995). Each of the modules is part of a subsystem that is involved in telescope triggering and data read-out. Figure 4.7 outlines the details of the data acquisition electronics diagrammatically. The various electronics subsystems are discussed in the following sections.

### 4.2.1 Amplifiers

Each of the camera's PMTs are connected to amplifiers by 50 m of RG-58 coaxial cable. The signal is amplified by a factor of 10. The amplifiers themselves are modified LeCroy 612A modules with three outputs for every input signal. The first output is connected to the current monitor. The other two outputs are AC coupled. This is done to act as a filter for night-sky background picked up by the PMTs. One of the two outputs is connected to an analogue-to-digital converter (ADC) through a long

## 4.2. Data Acquisition

---

delay cable. The other is connected, by a much shorter cable, to the trigger electronics.

### 4.2.2 Current Monitor

The amplified DC component of the signal from each PMT is fed into a series of ADC data acquisition boards. These boards have a current resolution on the order of  $1\ \mu\text{A}$  and are read in parallel by the custom software which controls the high-voltage supply to the camera. The anode current for each PMT is monitored in this way. In the case of a high anode current, due to a star in the field-of-view or some unexpected background light, the PMT's high-voltage supply can be switched off by the observer.

### 4.2.3 Trigger Electronics

Imaging atmospheric Cherenkov telescopes operate by recording an event when a rapid pulse of photons is incident on the PMTs in the camera within a short integration time ( $\sim 20\ \text{ns}$ ). The telescope's trigger electronics are set to minimise the number of false random trigger events from night-sky background that are recorded.

To trigger the digitisation and recording of an event, certain criteria must be met. In order for a telescope to register a triggered event, the signal in a minimum number of pixels in the camera must exceed a preset threshold number of photoelectrons. The pixels must exceed this threshold within a short coincidence window of a few nanoseconds – the time smearing occurring mainly due to air shower development time and the non-isochronous nature of the Whipple 10 m reflector. Further false triggers due to night-sky background (ambient night-sky photons) or PMT after-pulsing are suppressed by requiring that the triggering pixels must have a certain proximity in the camera.

The Whipple 10 m telescope utilises constant-fraction-discriminators

## 4.2. Data Acquisition

---

(CFDs), one per pixel, to test if the amplified signals from the PMTs have reached a threshold voltage. CFDs remove the pixel-to-pixel time jitter which is inherent in fixed-threshold triggering of pulses with different amplitudes. This allows the coincidence window to be reduced below what it would be if fixed-threshold triggering was used. The CFD triggers at a level of one third of the input amplitude. The incoming pulse (typically with a length of the order of 15 ns) is gated by a voltage comparator with an adjustable threshold between -20 mV and 1 V. The CFD unit, therefore, functions like an ordinary discriminator. The CFD thresholds are set to the same voltage for all PMTs in order to maintain a uniform response across the camera. The level is adjusted annually after the camera has been flat-fielded by varying the PMT cathode voltages (Section 4.1.2).

The geometry of the triggered pixels is then tested by the pattern selection trigger. The pattern selection trigger is a logic device that tests if those pixels which have exceeded the hardware trigger level, within the time coincidence window, are adjacent to each other. The pattern of signals from the discriminators is compared with a pre-programmed memory containing mappings of all possible trigger decisions (Bradbury & Rose, 2002). An event is only recorded if three or more of the pixels passing threshold criteria are adjacent to each other, as per the pattern criterion. In using a pattern selection trigger, the coincidence window (within which the pixel values must exceed the threshold number of photoelectrons) is reduced to  $\sim 5$  ns.

### 4.2.4 Signal-Recording Electronics

When an event triggers the telescope, digital count values are recorded from 10-bit (*i.e.* 0 - 1023 d.c.) ADCs for every PMT. The output from the amplifiers to the ADCs is delayed by 120 ns by travelling through long coaxial delay lines. This delay allows the signal to arrive at the ADC in coincidence with the trigger gate pulse produced if an event

## 4.2. Data Acquisition

---

passes the trigger criteria outlined above (Section 4.2.3). The gate pulse width is 20 ns, over which time the PMT signals are integrated by the ADCs. This relatively long integration window is used to allow for the anisochronous nature of the reflector which introduces an intrinsic spread in the arrival times of photons at the camera plane. A GPS time-stamp, telescope azimuth and elevation are appended to the event before it is read out. The ADCs read out their values in digital counts. Typically, the ratio of digital counts to photoelectrons for the PMTs in the camera is  $\sim 3.2$  d.c./photoelectron although this value was not measured during the 2006-2007 observing season.

Due to the 20 ns ADC integration time, some signal from night-sky background is introduced. This is accounted for in offline analysis by use of a regularly injected pedestal. The pedestal of a channel is a measure of its mean integrated charge in the absence of a Cherenkov signal. To measure the pedestal in each channel, forced triggers are injected into the data stream at a rate of 1 Hz. A baseline pedestal of 20 digital-counts is set for each ADC channel, which allows for both negative and positive fluctuation of the AC-coupled signal to be measured. The pedestal events then provide a measure of the fluctuation of the signal about this 20 digital-count level. If no background light is incident on a PMT the distribution will be very narrow, fluctuations being caused predominantly by electronic noise. When exposed to the night sky the distribution widens as more variation is observed in the channel. The width of this distribution is therefore used as a measure of night-sky background in a channel when analysing the data offline.

### 4.2.5 Timing Electronics

Every event has timing information appended to the record. A TrueTime GPS clock provides this information. The inherent accuracy of the clock is 250  $\mu$ s but, through the use of a Canberra 10 MHz oscillator, the GPS time is interpolated to 0.1  $\mu$ s accuracy. Pulses from the oscillator

### 4.3. Observation Strategies

---

are also counted by two 48-bit scalers to provide an elapsed time and a livetime since the start of the data run for each event. The deadtime can be measured using these values (*i.e.* deadtime = elapsed time – live time). Deadtimes for typical data runs are on the order of 1% - 2% with a Cherenkov event rate of  $\sim 25$  Hz.

## 4.3 Observation Strategies

The aim of atmospheric Cherenkov  $\gamma$ -ray astronomy is to detect  $\gamma$ -rays of cosmic origin from celestial objects by means of detecting the Cherenkov light which is generated by extensive air showers (EAS) resulting from  $\gamma$ -rays pair producing in the field of a nucleus as they enter the atmosphere. These  $\gamma$ -ray initiated showers must be separated from a much larger background component. The background comes in the form of local muons, hadron-initiated EAS and light from night-sky background.

The Imaging Atmospheric Cherenkov Technique has proven itself the most powerful method to date for the selection of  $\gamma$ -ray initiated events in the VHE range. Simulations show that the technique offers close to 100% background rejection while retaining close to 50% of the genuine  $\gamma$ -ray events (Fegan, 1997).

There are two main modes of observation employed at the Whipple 10 m telescope: ON-OFF mode and TRACKING mode. The type of observation strategy utilised depends on factors such as atmospheric conditions at the time of observation and time constraints. Both modes are explained in the sections which follow.

#### 4.3.1 ON-OFF Mode

Data taken in ON-OFF mode consist of an “on-source” run and an “off-source” run, referred to as a pair. The on-source run is a data scan with the candidate  $\gamma$ -ray source placed at the centre of the field-of-view. The off-source run is a scan of an area of the sky which is offset from

### 4.3. Observation Strategies

---

the source area by 30 minutes in right ascension. The off-source scan does not contain a  $\gamma$ -ray source and is taken over the same elevation and azimuth range as the on-source scan. The number of  $\gamma$ -ray like events in the OFF run are used as an estimate of the background for the ON run.

The normal duration for both the ON run and OFF run is 28 minutes each. The OFF run is obtained either before or after the ON run with a 2-minute gap between runs to allow for the slew time of the telescope. As they are taken so closely in time, the atmospheric conditions are usually similar for both runs. Also, pixels with star light in them are usually switched off during ON-OFF observations to maintain parity between the on-source and off-source fields. However, ON-OFF mode observations are not taken in variable weather conditions due to the fact that the ON and OFF scans will not be well matched, so the background estimation will not be accurate.

ON-OFF mode is a highly effective means of detecting new sources and determining accurate flux upper limits. However, one of the disadvantages of this mode of observation is that only 50% of the total observation time is spent monitoring the candidate source. For sources displaying variability on short timescales it is desirable that maximum observation time is spent on-source.

#### 4.3.2 TRACKING Mode

TRACKING mode requires that the telescope exclusively tracks the candidate  $\gamma$ -ray source with no accompanying background-estimating data scan. When data are taken in this mode, characteristics of the on-source scan are used to make a good estimate of the expected background. The background estimation method will be outlined in Section 4.6.2.

One obvious advantage of this method of observation is that all of the available observation time is spent on-source. This allows for more comprehensive short-term variability studies than ON-OFF mode can offer if a source's flux varies on short timescales. TRACKING mode

---

## 4.4. Calibration and Analysis

---

data may be used when atmospheric conditions are not of a suitably high quality for ON-OFF observations. The majority of the data used in this work were taken in TRACKING mode.

### 4.4 Calibration and Analysis

In the Imaging Atmospheric Cherenkov Technique, the image of a shower that triggers the telescope is characterised on the basis of its angular compactness (*shape*) and on the direction from which it came (*orientation*) for  $\gamma$ /hadron separation. Events which meet certain criteria based on the shape and orientation of the image are accepted as “ $\gamma$ -ray like”. All other events are rejected as background. The criteria which define  $\gamma$ -ray like events are set using simulations and optimised with data taken on the Crab Nebula.

The analysis of data consists of a number of stages, as follows:

- Data preparation
- Parameterisation
- $\gamma$ -ray/hadron separation
- $\gamma$ -ray rate and significance calculation

These steps are described in more detail in the following sections.

#### 4.4.1 Data Preparation

Before the data can be further analysed, each image recorded by the camera must be prepared by removing night-sky fluctuation effects (*i.e.* pedestal subtraction), accounting for the gain differences across the camera (*i.e.* gain matching) and cleaning images by removing aberrant pixels (*i.e.* image cleaning). These methods are further explained in the following sections.

## 4.4. Calibration and Analysis

---

### Pedestal Subtraction

Each PMT in the camera is AC coupled to remove the effects of night-sky background current and other effects such as dark current in the PMT. Positive and negative current fluctuations about the average, which occur within the 20 ns ADC integration window due to fluctuations in the brightness of the night sky, are measured using pedestals (see Section 4.2.4). To measure these fluctuations, a pedestal current of 20 digital counts is added to each channel's signal at the ADCs so that negative fluctuations (of up to 20 digital counts value) in the PMT signal still result in a positive ADC value when integrated over the gate.

When data are being acquired, a forced read-out of the PMT signals is recorded once every second (Section 4.2.4). The system is triggered by a 1 Hz signal from the GPS clock. The assumption is made that all ADC counts in these images are from night-sky background only. Around 1600 such events are recorded, along with the triggered events, in a standard 28-minute scan. A calculation of the mean signal gives the size of the pedestal for each channel. The pedestal variance is, therefore, a measure of the fluctuation of the night-sky background light for each channel.

When the pedestal variance for each channel has been found, the median value is calculated. A high pedestal variance ( $>1.5 \times$  the median pedestal variance) is indicative of the PMT having a bright region of the sky (*e.g.* a star) in its field of view (note that pixels are switched off for very bright stars). A low pedestal variance ( $<0.6 \times$  the median pedestal variance) indicates the pixel was switched off or is not functioning correctly. High and low pedestal variance channels (which meet the above criteria) are disregarded by the software when further analysing the data.

### Gain Matching

At the beginning of each observing season, the gain of each PMT in the telescope's camera is adjusted so that the response of each pixel is similar. However, the response of each pixel varies slightly from night to

## 4.4. Calibration and Analysis

---

night due to factors such as temperature differences.

The gains of the camera pixels are characterised by “flat fielding” before observing commences each night. This involves uniformly illuminating the camera with a light source pulsed at a frequency of around 1 kHz. The pulses have a fast rise time (a few nanoseconds) and the light is of a wavelength similar to that of atmospheric Cherenkov light ( $\sim 400$  nm). Around 4000 pulses are recorded over the course of a 1-minute run and the average signal is found for each PMT. A gain correction factor for each channel is calculated, using the average values, so that the same signal is found for each channel. The gain correction factor for each channel is used to scale the ADC values for every pixel in all events recorded that night.

A nitrogen arc lamp had been used for this purpose. It was located at the centre of the reflector and pointed directly at the camera plane. A spark-gap in a pressurised nitrogen bulb discharged at high frequency. In March 2007, this was replaced by a laser/diffuser set-up. The laser, which is housed in the control building adjacent to the 10 m reflector, produces light pulses at a wavelength of 337 nm. These pulses are passed through a dye which fluoresces at around 400 nm. An optical fibre carries the pulses outside to the telescope. The fibre is coupled to a diffuser located at the centre of the reflector. This diffuser spreads the pulse so that it illuminates the entire camera uniformly.

### Image Cleaning

After pedestals are subtracted and gain corrections have been applied, images are “cleaned” using picture/boundary cleaning. The assumption is made that pixels which are part of a shower image have more signal than those with only a night-sky background contribution. Pixels in which the signal is likely to have been caused entirely by noise are, therefore, removed from the image. The standard deviation of the pedestals,  $\sigma_{ped}$ , is calculated for each tube. This provides a measure of the average

#### 4.4. Calibration and Analysis

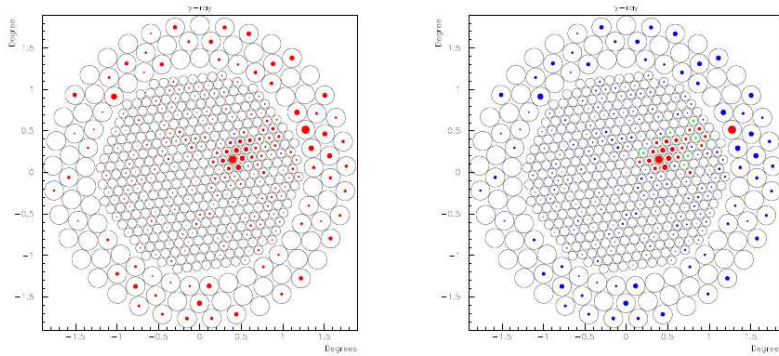


**Figure 4.8:** Illustration of picture/boundary cleaning of a simulated  $\gamma$ -ray image. The left panel shows the uncleaned image. The right panel shows the image after cleaning with the picture tubes coloured red, the boundary tubes coloured green and all other zeroed tubes coloured blue. (Dunlea, 2001).

fluctuation due to sky noise for that run.

“Picture tubes” must next be identified. These are channels in which the signal is not likely to be entirely due to noise. A “picture threshold” value,  $T_{pict}$ , is defined such that the signal in a tube must exceed  $T_{pict} \times \sigma_{ped}$  in order to be considered a picture tube. For this work, the standard picture threshold value of 4.25 was used (Punch *et al.*, 1991).

Next, the “boundary tubes” are identified. Again, a “boundary threshold”,  $T_{bound}$ , is defined. This threshold is lower than  $T_{pict}$  because a tube may only be considered a boundary tube if the signal exceeds  $T_{bound} \times \sigma_{ped}$  and the tube is adjacent to a picture tube. If a channel meets these two criteria, the signal is assumed to be due to an event and not entirely comprised of noise. The standard boundary threshold value of 2.25 (Punch *et al.*, 1991) was used in this work.

All tubes which are not picture tubes or boundary tubes have their signal set to zero. Picture/boundary cleaning is illustrated in Figure 4.8.

## 4.4. Calibration and Analysis

---

### Padding

When data are acquired in ON-OFF mode (*i.e.* a scan of an on-source region, with an accompanying off-source scan), differences in the night-sky brightness in the two regions of the sky that are scanned can introduce some bias when the data are analysed. This bias can be measured, however, and can be reduced. The technique is known as noise padding (Cawley, 1993). To do this, for each pixel the standard deviation of the pedestal is compared for the ON run and the OFF run. Some artificial Gaussian noise is added to the less noisy of the two pixels until the standard deviations match.

### 4.4.2 Parameterisation

After pedestal subtraction, flat-fielding and image cleaning are completed, images are parameterised using a moment-fitting routine. The first, second and third moments of the distribution of light in the camera plane are calculated so that an ellipse is fitted to the image of each event. This procedure is outlined in Appendix A of Reynolds *et al.* (1993).

The image is parameterised by defining the shape (*length, width*), location (*distance, miss, azwidth*) and orientation (*alpha*) of the ellipse fitted to the image. The parameters are collectively called Hillas parameters (Hillas, 1985). The Hillas parameters are outlined in Table 4.2 and illustrated diagrammatically in Figure 4.9.

In addition to the above Hillas parameters, some further parameters are defined based on the brightness of the image. These are mainly used to select events in the early stages of analysis. The *size* parameter is a measure of the total number of digital counts in the cleaned image. The *max1*, *max3* and *max3* parameters are defined as the ADC signals recorded in the tubes which recorded the highest, second highest and third highest ADC values respectively for the event. These parameters depend on the brightness of the Cherenkov light from the shower which

#### 4.4. Calibration and Analysis

---

Parameter	Definition
<i>Size</i>	Sum of the ADC digital count values in all of the pixels in the image, corresponding to the total light content of the image.
<i>Frac3</i> *	Percentage of the total light content of the image contained in the three pixels with the highest digital count values.
<i>Length</i> *	RMS spread of light along the image's major axis.
<i>Width</i> *	RMS spread of light along the image's minor axis.
<i>Azwidth</i> *	RMS spread of light perpendicular to the line connecting the image centroid with the centre of the field of view.
<i>Miss</i> *	Perpendicular distance between the image's major axis and the centre of the field of view.
<i>Distance</i> *	Distance from the image centroid to the centre of the field of view.
<i>Alpha</i>	Angle between the major axis of the image and a line joining the image centroid to the centre of the field of view.
<i>Assymetry</i>	Measure of the asymmetry of the light distribution of the image along the major axis.
<i>Max1, Max2, Max3</i>	ADC digital count values for the three highest pixels.
<i>Length/size</i>	Measure of the image compactness relative to its light content.

**Table 4.2:** Outline of the different Hillas parameters used in the parameterisation of Cherenkov events. \* denotes a parameter which was included as one of the six original Hillas parameters from (Hillas, 1985).

## 4.4. Calibration and Analysis

---

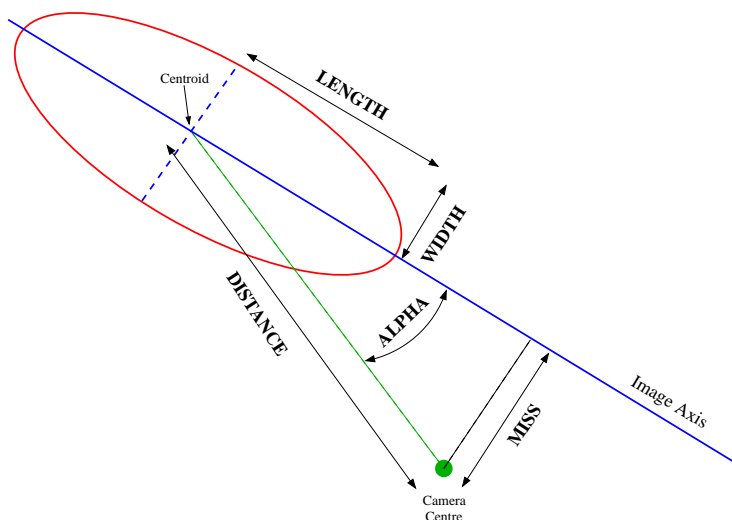


**Figure 4.9:** Schematic outline of the Hillas parameters.

produced the image. Images produced by showers of higher energy have a larger *size*. Therefore, the *size* parameter is related to the energy of the incident photon.

The *alpha* parameter measures the angle between the major axis of the fitted ellipse and a line drawn from the centre of the field-of-view of the camera to the centre of the ellipse. Measuring the parameter in this way assumes that any possible source of cosmic  $\gamma$ -rays is at the centre of the field-of-view for the duration of the data-scan. Ellipses fitted to images of showers caused by  $\gamma$ -rays emanating from the centre of the field-of-view should have major axes that point towards the centre of the camera, giving them a small *alpha* value.

A further parameter is defined by taking the ratio of the *length* to the *size* of the fitted ellipse. This parameter is simply referred to as *length/size* (Fegan, 1997). It is used to help reject events triggered by local muons which dominate the background at lower energies. Muon images usually contain a constant amount of light per unit *length*. The *length/size* parameter was used in this work.

The *asymmetry* parameter quantifies how the light in the image is

## 4.5. Supercuts Analysis

---

distributed along the major axis of the ellipse (Lessard *et al.*, 2001). An image of a  $\gamma$ -ray event will tend to have more light in the direction in which the shower is pointing, and less in the direction from which it came, when compared to images of background events. This parameter is most useful for cameras with larger fields-of-view ( $> 3^\circ$ ). It was, therefore, not used for this work as the camera currently employed on the Whipple 10 m telescope has a  $2.8^\circ$  field-of-view (see Table 4.1).

Hillas parameterisation and event selection, based on the above parameters, are discussed in more detail in the following section.

## 4.5 Supercuts Analysis

One of the core requirements of the Imaging Atmospheric Cherenkov Technique is a scheme to separate  $\gamma$ -ray air-shower images from those of cosmic ray background air showers. Schemes based on Hillas parameterisation have proven to be very powerful. Smaller transverse momentum of particles and electromagnetic interactions of a more regular nature, in  $\gamma$ -ray air showers than in hadronic background showers, mean that  $\gamma$ -ray images are typically narrower and more uniformly shaped than background images. If the shower is generated by a  $\gamma$ -ray emanating at the centre of the field of view of the camera, the major axis of the image of the shower will point towards the centre.  $\gamma$ -ray images may, therefore, be separated from hadronic images based on their shape and orientation. This approach to  $\gamma$ -ray/hadron separation is known as Supercuts (Punch *et al.*, 1992).

Using Monte Carlo simulations of  $\gamma$ -ray initiated showers following the spectrum of the Crab Nebula (and real data as background), upper and lower limits (referred to as “cuts”) were derived for each of the parameters such that a large number of  $\gamma$ -ray images are retained while also rejecting the majority of the background events. These parameter cuts are optimised every observing season on data from the Crab Neb-

## 4.5. Supercuts Analysis

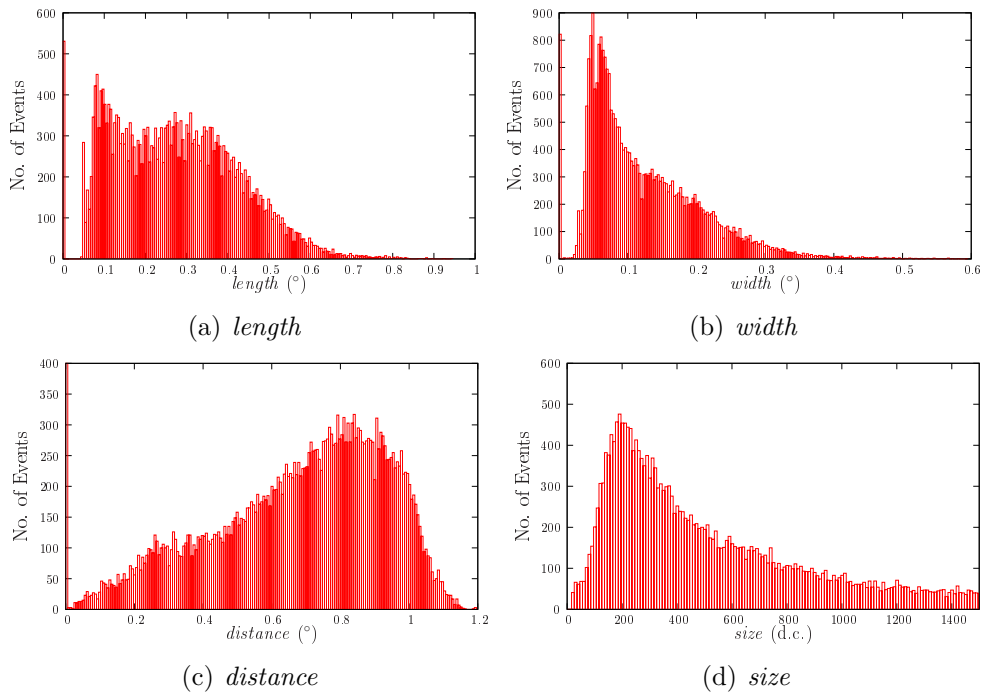


**Figure 4.10:** Parameter distributions for a typical 28-minute on-source (Crab Nebula) data scan using the Whipple 10 m telescope.

ula to allow for slight differences in the telescope or trigger electronics configuration. Studies of simulations show that this scheme rejects over 99% of the background events while retaining more than 50% of the true  $\gamma$ -ray events. The set of optimised cuts used in the analysis for this thesis are discussed further in Section 5.1. Figure 4.10 shows some example parameter distributions for a single 28-minute on-source data scan of the Crab Nebula.

The standard method traditionally employed in the analysis of data from the Whipple 10 m telescope is the *Supercuts* analysis technique (Punch *et al.*, 1991; Reynolds *et al.*, 1993). This technique calls for the Hillas parameterisation of each event recorded within the field of view of the telescope. Probable  $\gamma$ -ray events are then selected based on their shape (*i.e.* *width* and *length*) and orientation (*i.e.* *distance* and *alpha*).

## 4.5. Supercuts Analysis

Cut	Lower Bound	Upper Bound
<i>size</i>	0	$\infty$
<i>max1</i>	30 d.c.	-
<i>max2</i>	30 d.c.	-
<i>max3</i>	-	-
<i>frac3</i>	-	0.98
<i>width</i>	$0.05^\circ$	$0.12^\circ$
<i>length</i>	$0.13^\circ$	$0.25^\circ$
<i>distance</i>	$0.40^\circ$	$1.00^\circ$
<i>alpha</i>	-	$15.0^\circ$
<i>length/size</i>	-	$0.0004^\circ/\text{d.c.}$

**Table 4.3:** Values of Supercuts 2000.

Bounds are set on these parameters such that an area of Hillas parameter space may be defined as a “ $\gamma$ -ray domain”. If an event falls within this domain, it passes the analysis as a probable  $\gamma$ -ray event. Other events are rejected as probable hadron events. This technique has been described in Section 4.4.2.

The Supercuts technique is optimised for particular telescope configurations using ON-OFF data. A standard set of Supercuts criteria (Supercuts 2000) has been developed for the current 379-pixel camera. These are often used as a starting point when looking for a  $\gamma$ -ray signal from a probable source, or high-state activity of a variable source, before being optimised further on a seasonal basis. The Supercuts 2000 criteria are listed in Table 4.3. Each of the selection cuts are described further.

### 4.5.1 Pre-selection Cuts

The raw data are filtered by means of some pre-selection cuts before the *shape* and *orientation* cuts are applied to the data. Only those events passing these pre-selection criteria are passed to Supercuts.

## 4.5. Supercuts Analysis

---

### Software Trigger Cut

These cut criteria will only pass events in which the two tubes (*max1* and *max2*) or the three tubes (*max1*, *max2*, *max3*) with the highest signals have digital count values above certain defined thresholds. This is quite similar to the hardware trigger, rejecting small background events. However, the hardware trigger threshold of 30 photoelectrons (spread over three pixels), equating to  $\sim 10$  digital counts, is lower than the 60 digital count threshold imposed by Supercuts 2000 (*i.e.*  $max1 = 30$  d.c.,  $max2 = 30$  d.c.,  $max3 = 0$  d.c.). If an event does not satisfy the software trigger criteria, it is excluded from further analysis, thus considerably reducing the number of events which are tested by the Supercuts analysis.

Although the *max3* criterion is an available option in any Supercuts analysis, it is not included in the Supercuts 2000 selection criteria. The use of a *max3* cut was examined for the optimisation outlined in Chapter 5.

### *Frac3* Cut

For an event to pass the *frac3* cut, the percentage of light in the three tubes with the three highest digital count values must be below a certain value (*i.e.* below a set percentage of the *size* of the image). This excludes small events in which the total signal is confined to three tubes (most likely adjacent to one another due to the hardware pattern trigger constraints) or fewer. Such events are often a result of cosmic rays passing directly through the telescope camera and are also difficult to parameterise meaningfully.

### *Size* Cut

The *size* cut allows one to effectively select events based on their energy (*i.e.* showers initiated by higher-energy photons or cosmic rays are brighter than those initiated by lower-energy photons or cosmic rays).

## 4.5. Supercuts Analysis

---

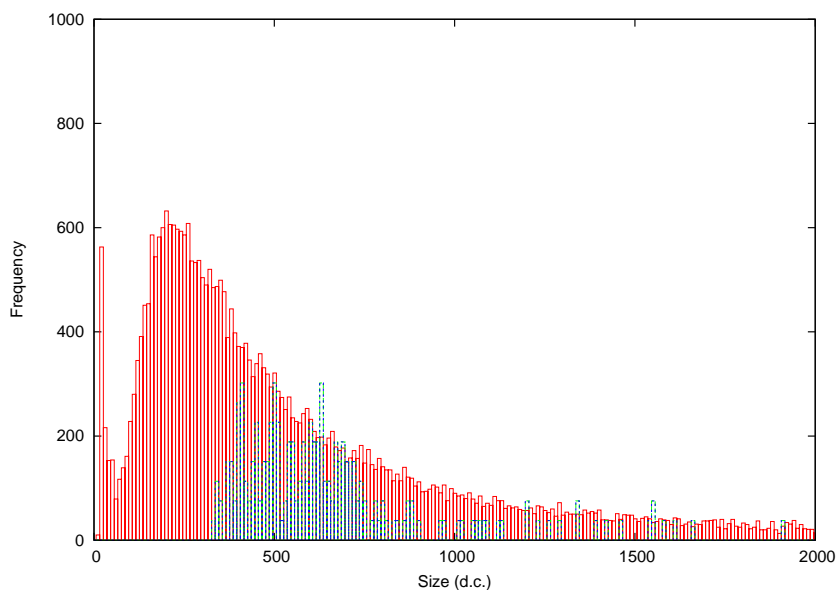


**Figure 4.11:** Plot of *size* distribution for one data scan before (larger, red distribution) and after (smaller, blue distribution) Supercuts 2000 have been applied. Although no lower *size* cut has been employed, events with small *size* (<340 d.c. here) are removed by pre-selection cuts. The vertical scale for the “after cuts” *size* distribution has been multiplied by a scalar multiple (*i.e.* 40) so that the distribution is visible on this plot.

Standard Supercuts 2000 does not explicitly employ a *size* cut. However, due to the use of other pre-selection cuts which deal with aspects of each event’s *size*, an effective lower *size* cut is implicitly imposed (see Figure 4.11).

No explicit lower *size* cut was imposed in the analysis of data in this work. In one optimisation methodology which was investigated, *max1*, *max2*, *max3* and *frac3* cuts were all optimised, effectively placing an implicit lower *size* cut on the data. No upper *size* cut was used so that events of all energies (within the sensitive range of the telescope) were analysed.

## 4.5. Supercuts Analysis

---

### 4.5.2 Shape and Orientation Cuts

It can be shown that *length* and *width* for  $\gamma$ -ray events tend to be smaller than those for background events (hadron-initiated showers, *etc*) since  $\gamma$ -ray-induced EAS tend to have a tighter profile (Hillas, 1985). Figure 4.12 shows some examples of typical events recorded by the Whipple 10 m telescope. For Supercuts, upper and lower bounds are placed on the *length* and *width* parameters such that the image of the events which pass are regarded as having a  $\gamma$ -ray-like *shape*.

In the analysis of data from point sources, *distance* and *alpha* are the parameters used to define an event's orientation. The *distance* cut selects events for which the centroid of the image lies within a certain angular distance of the centre of the camera.  $\gamma$ -rays from a point source at the centre of the field-of-view of the telescope should exhibit small *alpha* values. As such, in Supercuts analysis, events which have small values of *alpha* ( $< 15^\circ$  in the case of Supercuts 2000) are passed as  $\gamma$ -ray-like events. No lower limit value is used since  $\gamma$ -ray-like events should have an *alpha* value which tends to  $0^\circ$ .

Events with a small (or  $0^\circ$ ) *distance* have a small impact parameter and do not allow for an accurate definition of *alpha*. A lower *distance* cut rejects these events. The maximum *distance* of any event is determined by the telescope camera's field-of-view. However, an explicit upper *distance* cut is utilised to reduce the effects of truncation of event images which extend beyond the field-of-view of the camera. This upper *distance* limit is given a value which places it far enough inside the camera's edge that only images of showers which do not have a lot of the shower truncated pass while many events which are missing information about the shower itself are rejected, reducing the telescope's effective area.

## 4.5. Supercuts Analysis

---

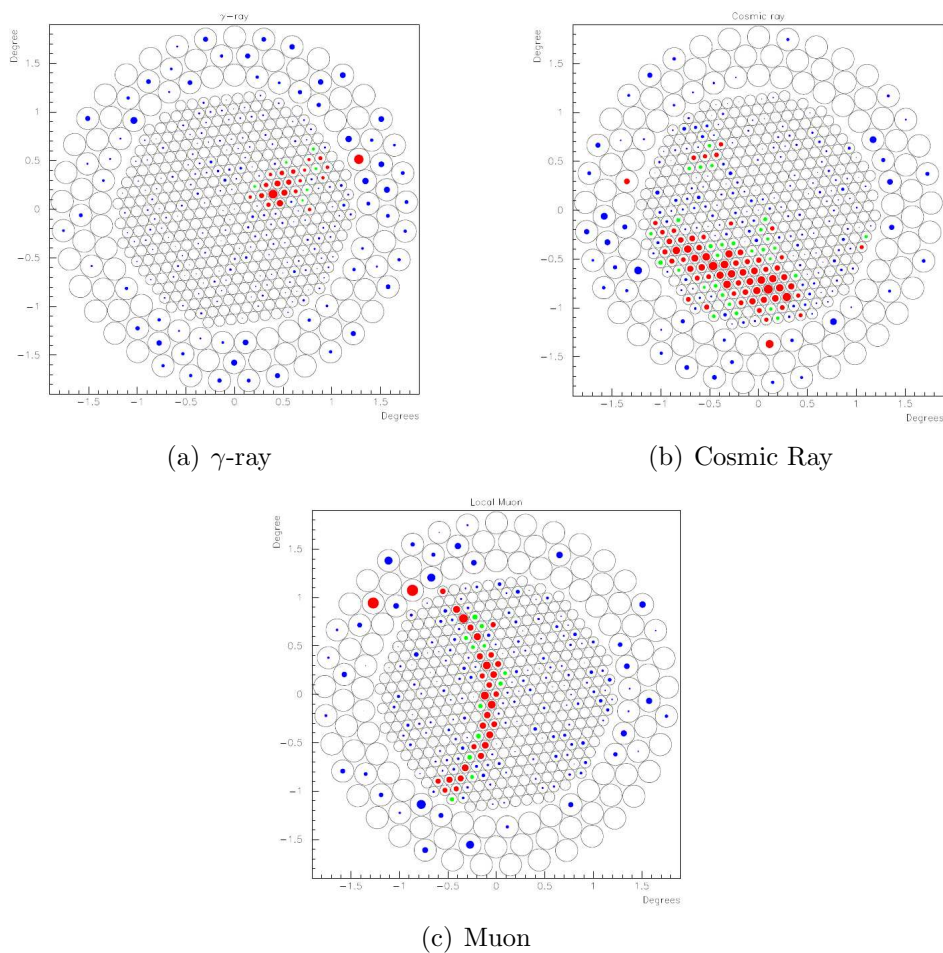


**Figure 4.12:** Typical images recorded by the Whipple 10 m Telescope. Image (a) is a  $\gamma$ -ray candidate event due to its compact nature and orientation towards the centre of the camera. Image (b) is a cosmic ray event; more spread out and scattered across the camera. Image (c) is a segment of the ring of light generated by a local muon. Images from Dunlea (2001).

---

## 4.6. $\gamma$ -ray Rate and Significance Calculation

---

### 4.5.3 Length/Size Cut

The *length/size* criterion was developed in Catanese *et al.* (1995) and included in Supercuts as a way of reducing the number of single muon events (*i.e.* Cherenkov light, emitted by a single local muon, that triggers the telescope) passing selection criteria. Muon events dominate at the lower end of the telescope's energy range. Images of muon events are ring-shaped. Truncated arcs produced by these events (see Figure 4.12(c)) can easily resemble  $\gamma$ -ray events if oriented towards the centre of the field-of-view. These events tend to have less light per pixel than  $\gamma$ -ray images. They also tend to be very elongated by comparison. Since these qualities (*image size* and *length*) are measured for each event, a selection is made rejecting events with a certain ratio of *length* to *size* (those  $< 0.0004$  for Supercuts 2000). From simulations, it can be shown that this has the effect of reducing the number of muon events which pass as  $\gamma$ -ray-like. This cut also tends to reject a lot of real  $\gamma$ -ray events ( $\sim 50\%$ ; Moriarty *et al.*, 1997).

## 4.6 $\gamma$ -ray Rate and Significance Calculation

Results of an analysis may be presented graphically in an “*alpha* plot” where *alpha* values for events passing all cuts, except for the *alpha* cut, are binned and plotted on a histogram. Since  $\gamma$ -ray images have low values of *alpha*, a larger number of events would be expected in the small-*alpha* region of the plot for a scan which contains a  $\gamma$ -ray source when compared to an area of the sky not containing a  $\gamma$ -ray source.

For data taken in ON-OFF mode, the *alpha* plot for the OFF scan is superimposed on the *alpha* plot for the ON scan on the same graph. An example of an *alpha* plot for ON-OFF data which contain a  $\gamma$ -ray signal (the Crab Nebula) is shown in Figure 4.13.

## 4.6. $\gamma$ -ray Rate and Significance Calculation

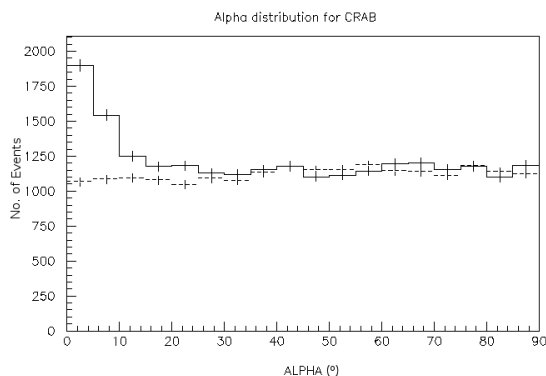


**Figure 4.13:** *Alpha* plot for a set of Crab Nebula data exhibiting a positive excess of  $\gamma$ -ray events. Both the ON plot (solid) and the OFF plot (dashed) are shown. An obvious excess is seen in the ON plot at lower *alpha* values.

A number of events will pass all of the cuts, even in the absence of a  $\gamma$ -ray signal. This background must be quantified in order to calculate the statistical significance of any excess of  $\gamma$ -rays detected. There are two methods for estimating the background level depending on what mode of observation was used to take the data.

### 4.6.1 ON-OFF Mode Calculation

Data taken in this mode consist of a “pair” of scans; one scan of the region of the sky containing the candidate  $\gamma$ -ray source (the ON region) and a scan of the same range of elevation and azimuth when it no longer contains the candidate source (the OFF region). The OFF region is used as a control, providing an estimate of the number of  $\gamma$ -ray like events expected from the ON scan if the source were removed. The data are usually software padded (Section 4.4.1). The  $\gamma$ -ray rate,  $\phi$ , and the statistical uncertainty in the rate,  $\Delta\phi$ , are defined as:

$$\phi = \frac{N_{ON} - N_{OFF}}{t_{exp}} \quad (4.1)$$

---

## 4.6. $\gamma$ -ray Rate and Significance Calculation

---

$$\Delta\phi = \frac{\sqrt{N_{ON} + N_{OFF}}}{t_{exp}} \quad (4.2)$$

where  $N_{ON}$  and  $N_{OFF}$  are the number of  $\gamma$ -ray like events in the ON and OFF scans respectively, and  $t_{exp}$  is the exposure time of each of the scans. The significance,  $\sigma$ , of any excess which may be present is defined as:

$$\sigma = \frac{\phi}{\Delta\phi} = \frac{N_{ON} - N_{OFF}}{\sqrt{N_{ON} + N_{OFF}}} \quad (4.3)$$

### 4.6.2 TRACKING Mode Calculation

Scans taken in TRACKING mode have no counterpart scan which may be used to estimate the background level of  $\gamma$ -ray like events. The estimation of this background level is necessary to characterise the excess of  $\gamma$ -ray like events emanating from a candidate  $\gamma$ -ray source.

To estimate the background level in TRACKING data, the shape of the *alpha* plot is used. A large number of scans of “darkfield” regions – regions of the sky with no detected  $\gamma$ -ray source – are analysed. The result of this analysis is an *alpha* plot with the shape expected when no  $\gamma$ -rays are present in a data set.

Truncation of images located at the edge of the camera and finite pixel size means that the *alpha* plot may not be entirely flat. Truncation phenomena particularly affect events which lie in the  $> 65^\circ$  region of the plot. This region of the plot is not considered for use in background estimation due to its instability. However, the shape of *alpha* plots in the  $0^\circ - 65^\circ$  region for darkfield data remains stable from scan to scan.

Since  $\gamma$ -ray images will tend to have low *alpha* values (source at the centre of the field-of-view), those events with *alpha* greater than  $20^\circ$  are assumed to be independent of any potential  $\gamma$ -ray source. A ratio of the number of events which pass the *alpha* cut in the darkfield data to the number of events which lie in the  $20^\circ - 65^\circ$  region is calculated. This

#### 4.6. $\gamma$ -ray Rate and Significance Calculation

---

ratio – the tracking ratio,  $\rho$  – is then used to scale the number of events in the  $20^\circ$  -  $65^\circ$  region of an *alpha* plot for a TRACKING scan to the expected background level of events passing the *alpha* cut for that scan. The tracking ratio,  $\rho$ , and the associated statistical uncertainty,  $\Delta\rho$ , are calculated as follows (Catanese *et al.*, 1998; Quinn *et al.*, 1996):

$$\rho = \frac{N_{source}}{N_{control}} \quad (4.4)$$

$$\Delta\rho = \sqrt{\frac{N_{source}}{N_{control}^2} + \frac{N_{source}^2}{N_{control}^3}} \quad (4.5)$$

where  $N_{source}$  is the number of events in the darkfield data which pass all cuts, including the *alpha* cut.  $N_{control}$  is the number of events in the same darkfield data which have *alpha* values between  $20^\circ$  and  $65^\circ$  and pass all other cuts.

The rate and associated statistical uncertainty calculations for data obtained in TRACKING mode then require that the number of events passing all cuts (including the *alpha* cut),  $N_{on}$ , and the number of events with *alpha* values between  $20^\circ$  and  $65^\circ$  (while passing all other cuts),  $N_{off}$ , be ascertained. The  $\gamma$ -ray rate,  $\phi$ , and statistical uncertainty in the rate,  $\Delta\phi$ , are then given by:

$$\phi = \frac{N_{on} - \rho N_{off}}{t_{exp}} \quad (4.6)$$

$$\Delta\phi = \frac{\sqrt{N_{on} + \rho^2 N_{off} + \Delta\rho^2 N_{off}^2}}{t_{exp}} \quad (4.7)$$

where  $t_{exp}$  is the exposure time for a scan. The significance of an observed excess is again given by Equation 4.3.

### 4.6.3 Spectral Analysis

The energy spectrum of a source offers an important insight into the emission processes responsible for the emission of VHE  $\gamma$ -rays. As spectral analysis has not been performed as part of this work, only a brief description of the process is provided. Mohanty *et al.* (1998) offers a more robust description of the analysis methodology.

For each  $\gamma$ -ray detected, an estimation of the energy is made using a polynomial function that is dependent on the log of the image *size* and the *distance* parameter. The energy-dependent collection area of the telescope is found using Monte Carlo simulations of  $\gamma$ -ray-induced electromagnetic cascades. The source spectrum is then found using the estimated energy distribution, the collection area of the telescope and the livetime of the observation.

The differential flux,  $\frac{dF}{dE}$ , is defined as the number of particles per unit area, energy and time and is given by

$$\frac{dF}{dE} = \frac{1}{t_{live}} \frac{dN_{\gamma}}{dE} \quad (4.8)$$

where  $A(E)$  is the energy-dependent collection area of the telescope which is calculated using Monte Carlo simulations.  $N_{\gamma}$  is the number of  $\gamma$ -rays detected during the live time,  $t_{live}$ , of the observation. The simplest source spectrum model is a power law of the form

$$S(E) dE = K E^{-\alpha} dE \quad (4.9)$$

where  $K$  is the flux constant,  $\alpha$  is the spectral index for the source and  $S(E) dE$  is the number of  $\gamma$ -rays per unit area per unit time (*i.e.* flux) in the infinitesimal interval  $dE$  at energy  $E$ . The integral flux is found by integrating  $S(E) dE$  over all energies.

## 4.7 Post-analysis Corrections

In practice, data are taken at a range of different zenith angles and in weather conditions which may be different on a night-by-night or a run-by-run basis. These differences can have an effect on the outcome of the analysis. Corrections may be applied to try to compensate for these effects.

The methods used for zenith angle and throughput correction are outlined in the sections that follow, since these corrections were investigated during the analysis of data presented in this thesis. Changes in the trigger configuration of the telescope throughout the 2006-2007 observing season meant that these corrections could not be applied to the data, however, as the corrections could not be justified. The reasons for this conclusion are also outlined in the following sections.

### 4.7.1 Zenith Angle Correction

Figure 4.14 shows schematically the emission of Cherenkov light in the atmosphere. The Cherenkov angle,  $\psi$ , is given by  $\cos(\psi) = \frac{1}{n}$  where  $n$  is the refractive index of the atmosphere at the altitude at which the Cherenkov emission occurs. We can see from Figure 4.14 that the radius of the Cherenkov wavefront, perpendicular to the axis of the shower, at the detector is  $R = \frac{H - H_{tel}}{\cos \theta_z} \tan \psi$ . By use of a small angle approximation, it can be shown that (Le Bohec & Holder, 2003):

$$R = \frac{H - H_{tel}}{\cos \theta_z} \sqrt{546 \times 10^{-6} e^{-\frac{H}{8.5}}} \quad (4.10)$$

When  $H$  is small,  $R$  will increase with  $H$ . For larger values of  $H$ ,  $R$  will decrease with  $H$ .  $R$  must, therefore, take a maximum value,  $R_{max}$ . Differentiating and solving for  $\frac{dR}{dH} = 0$  gives:

$$R_{max} = \frac{17}{\cos \theta_z} \sqrt{546 \times 10^{-6} e^{-\frac{(17+H_{tel})}{8.5}}} \quad (4.11)$$

## 4.7. Post-analysis Corrections

---

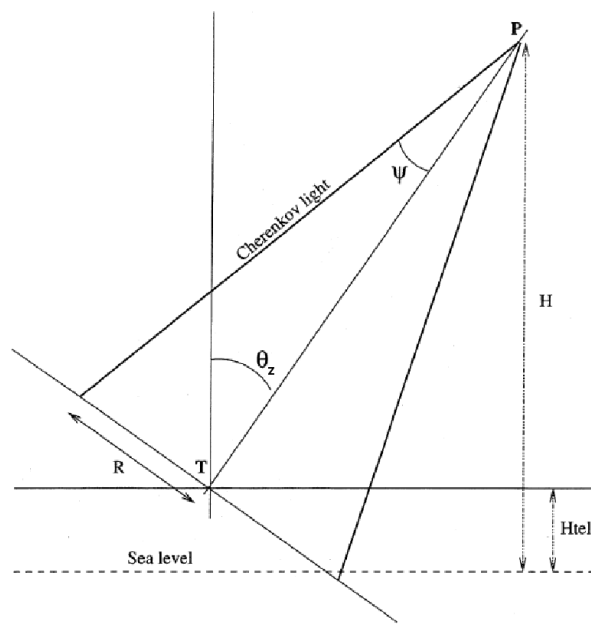


**Figure 4.14:** Figure from Appendix A of Le Bohec & Holder (2003) showing the emission of Cherenkov light in the atmosphere.

## 4.7. Post-analysis Corrections

---

Now taking  $H_{tel} = 2$  km (the approximate altitude of the Whipple 10 m telescope):

$$R_{max} \approx \frac{130}{\cos \theta_z} \quad (4.12)$$

Since  $R_{max}$  scales as  $\frac{1}{\cos \theta_z}$ , the effective collection area should scale as  $\frac{1}{\cos^2 \theta_z}$ . This shows that the observed rate is intrinsically zenith angle dependent. Although the zenith angle dependence is more ideally calculated using Monte Carlo simulations, this analytical model provides a good approximation for this application (Le Bohec & Holder, 2003).

Since the effective collection area,  $A$ , and the energy threshold,  $E_{th}$ , are proportional to  $\frac{1}{\cos^2 \theta_z}$ , the  $\gamma$ -ray rate  $\phi \propto (\cos \theta_z)^{2(\alpha-1)}$ , where  $\alpha$  is the integral  $\gamma$ -ray power-law spectral index for the source being observed. Hillas *et al.* (1998) gives  $\alpha = 1.5$  for the Crab Nebula and so

$$\phi \propto \cos \theta_z \quad (4.13)$$

For a set of data taken at different zenith angles, this approximation can be used to correct the measured  $\gamma$ -ray rate of each run to the rate expected if each run were taken at the same zenith angle. One data scan is chosen as a reference, and the rates for all other runs in the dataset are corrected using this approximation as if they were taken at the same zenith angle as the reference run (*i.e.*  $\theta_{ref}$ ). This gives a list of zenith angle corrected rates,  $\phi_{ref}$ , which are further corrected for differences in throughput on a run-by-run basis.

### 4.7.2 Throughput Correction

In general terms, each Cherenkov event recorded at a telescope can be characterised by its luminosity,  $Q$  (in units of J/s). The luminosity of a Cherenkov event is defined as the amount of Cherenkov light energy radiated per unit time over the duration of the electromagnetic cascade. A relative throughput factor,  $F$ , may then be defined as the ratio of

## 4.7. Post-analysis Corrections

---

luminosities recorded for the same atmospheric shower observed at the same zenith angle but under different conditions.

In the case of the Whipple 10 m Telescope, the brightness of an event (*i.e.* the *size* of an event) is defined as the sum of the ADC signals in all of the photomultiplier tubes which contributed to the image (Reynolds *et al.*, 1993). The *size* of an image may therefore be used as a measure recorded luminosity of an event due to the fact that the integration time of each recorded image is the same. The conditions which may differ for different observations include mirror reflectivities, atmospheric transparency and point spread function. In order to estimate the throughput factor, the cosmic ray spectrum is assumed to be constant over the energy range of the telescope (Gaisser, 1990) such that differences in distributions of  $Q$  for events recorded at the same zenith angle are solely due to some variation in the overall light collection efficiency and gain of the telescope system.

Since the *size* parameter may be used as a measure of the luminosity of events, distributions of *size* may be thought of as histograms of  $Q$ . One data scan from a specific night is used to construct a *size* distribution which is then used as a reference for all other runs. A similar histogram is then produced for all other data scans in a dataset. Each histogram is multiplied by a scalar factor,  $F$ , such that

$$F \times Q_{run} = Q_{ref} \tag{4.14}$$

where  $Q_{run}$  is the *size* histogram for the run being examined and  $Q_{ref}$  is the *size* histogram for the reference run. In practice, the “equality” of Equation 4.14 is found using minimisation of a  $\chi^2$  fit. The zenith angle at which this reference run is obtained is noted for zenith angle correction (see Section 4.7.1).

We may consider cosmic rays, incident at an angle,  $\theta_z$  to the vertical, initiating air showers in atmosphere that is not very dense. For these showers, the Cherenkov emission per unit track length is lower than the

## 4.7. Post-analysis Corrections

---

emission per unit track length for air showers initiated in dense atmosphere. However, for the showers initiated in atmosphere that is not dense, the total track length to the telescope is longer by an amount which compensates for this so that the total amount of Cherenkov light produced in the air shower is similar in both cases (*i.e.* rare and dense atmosphere cases) and, hence, does not depend on the zenith angle. The Cherenkov light pool extends over a larger radius on the ground, however, for cosmic rays incident at an angle to the vertical. Therefore, the light detected at the telescope is more diluted, with the luminosity scaling as  $\cos^2 \theta_z$ .

When calculating throughput in practice, the luminosity distribution is compared over a number of elevations. The content of a specific bin in the luminosity distribution will be affected by a factor of  $\frac{1}{\cos^2 \theta_z}$ , corresponding to the change in effective collection area of the telescope, and by a factor of  $\cos^{2\alpha} \theta_z$ , corresponding to the luminosity of the event scaled for a luminosity distribution of power-law index  $\alpha = 2.3$  (as measured by the Whipple 10 m telescope). If these two factors are combined and raised to the power of  $1/\alpha$  (Le Bohec & Holder, 2003), the expected throughput factor should scale as

$$F \propto (\cos \theta_z)^{\frac{2(\alpha-1)}{\alpha}}. \quad (4.15)$$

Using Equation 4.15 and accounting for atmospheric attenuation of the Cherenkov light as it travels from the site of emission to the telescope, the throughput factor is expected to vary as

$$F \propto (\cos \theta_z)^{2\left(\frac{\alpha-1}{\alpha}\right)} \times e^{-\frac{K}{\cos \theta_z}} \quad (4.16)$$

where the exponential term describes how the atmosphere attenuates Cherenkov light (*i.e.*  $K$  is a variable related to the atmospheric attenuation). Using a value of  $\alpha = 2.3$ , gives

## 4.7. Post-analysis Corrections

---

$$F \propto (\cos \theta_z)^{1.13} \times e^{-\frac{K}{\cos \theta_z}} \quad (4.17)$$

As throughput factor varies with zenith angle, the expected throughput factor,  $F_{exp}$ , must be calculated for each data scan, normalised to the zenith angle of the reference run,  $\theta_{ref}$  such that:

$$F_{exp} = \left( \frac{\cos \theta_z}{\cos \theta_{ref}} \right)^{1.13} \quad (4.18)$$

This is equivalent to Equation 4.17 without the exponential term describing how the atmosphere attenuates Cherenkov light. The throughput correction automatically incorporates correction for atmospheric effects. The rate is corrected using

$$\phi_{corr} = \frac{\phi_{ref}}{\left( \frac{F_{meas}}{F_{exp}} \right)^\alpha} \quad (4.19)$$

where  $\phi_{corr}$  is the throughput corrected and zenith angle corrected  $\gamma$ -ray rate with regard to a reference run at zenith angle,  $\theta_z$ , and  $\alpha$  is the integral  $\gamma$ -ray power-law spectral index of the source.

The application of these corrections was explored for this work. In order to do this, the corrections were applied to a set of data from observations of the Crab Nebula. A set of 29 data scans taken between the 30<sup>th</sup> September 2006 and 16<sup>th</sup> March 2007 were used. The Crab Nebula is known to be a steady source of TeV  $\gamma$ -rays. Therefore, fluctuations in the recorded  $\gamma$ -ray rate for these observations should be entirely due to the zenith angle of observation, the atmospheric conditions during the observations and statistical fluctuations.

Data selection was made based on the quality of the data:

- Observations which were taken in A class weather (very clear, no cloud) or B class weather (clear, little or no cloud), which was determined by the observer, were used.

## 4.7. Post-analysis Corrections

---

- Only observations taken at zenith angles smaller than  $35^\circ$  were used.
- Data scans with large fluctuations in the raw event rate were discarded.
- If only part of a data scan was affected by bad weather or hardware problems, then only that part of the scan which was unaffected was analysed.

These data were representative of the type of data presented later in this work as the same quality selections were applied. The zenith angle of the observation was defined as the zenith angle at the middle of the scan (or useable part thereof). That is,

$$\theta_z = \frac{\theta_{begin} + \theta_{end}}{2} \quad (4.20)$$

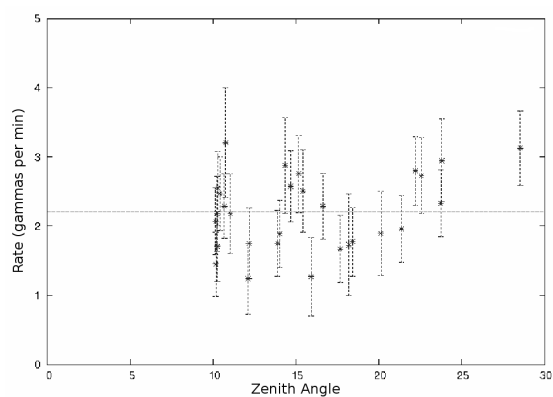
The average zenith angle for the observations was found to be  $15.7^\circ$  so a run with an observation zenith angle of  $\theta_z = 15.7^\circ$  (*i.e.* the closest to the average) was selected as the reference run.

Figure 4.15 shows the changes in rates after each correction has been applied. The rate should be expected to become independent of zenith angle, exhibiting less scatter. Table 4.4 shows that this is not the case however. The application of zenith angle correction has an almost unnoticeable effect on the rates. This is because the data are selected to be in a relatively small range of zenith angles due to the quality selection criteria.

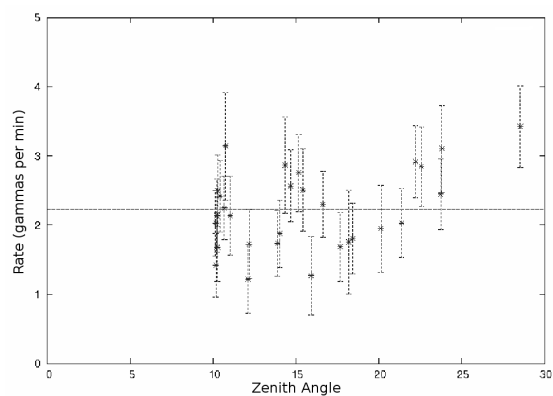
The application of zenith angle correction is highly dependent on the selection of the reference run. While investigating the reason for the increase in scatter after the throughput corrections had been applied, it was found that the trigger criteria for the telescope had been altered for a one-month period. In this alternate trigger configuration, four adjacent pixels were required to trigger an event (as opposed to the usual

## 4.7. Post-analysis Corrections

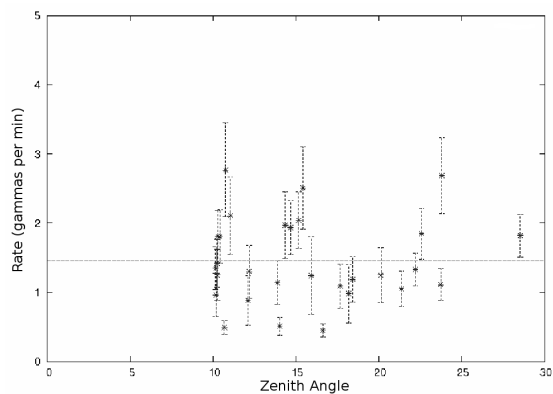
---



(a) Uncorrected



(b) Zenith Angle Corrected



(c) Zenith/Throughput Corrected

**Figure 4.15:** Three plots showing the observed rates as a function of zenith angle (for a set of 2006-07 season Crab Nebula data) before and after the application of corrections. The horizontal line indicates the mean rate value for each plot. Error bars were scaled using the same scaling factor applied in the rate correction.

#### 4.7. Post-analysis Corrections

Correction	Mean Rate [ $\gamma \text{ min}^{-1}$ ]	RMS [ $\gamma \text{ min}^{-1}$ ]
No Corrections	2.21	0.53
Zenith Angle	2.23	0.54
Throughput/ Zenith Angle	1.46	0.65

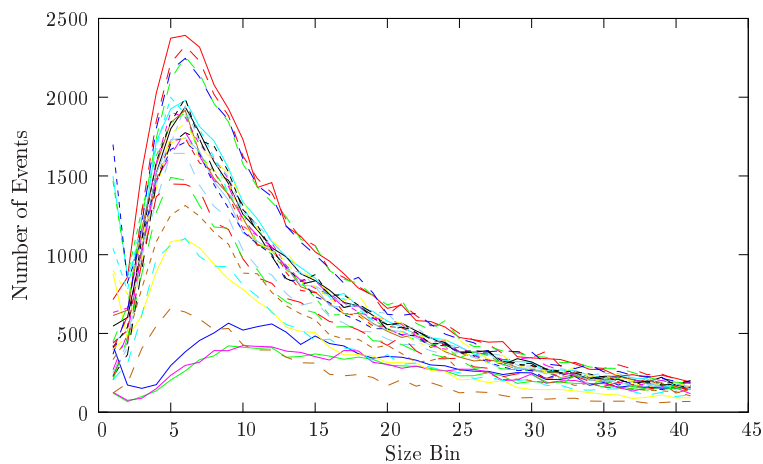
**Table 4.4:** Results of performing zenith angle and throughput corrections on 2006-2007 data from the Crab Nebula. The scatter in the rate is seen to increase with the application of the correction.

configuration which requires only three). This had the effect of changing the profile of the *size* distribution, upon which the calculation of the throughput factor is based. Figure 4.16 and Figure 4.17 show these differences graphically.

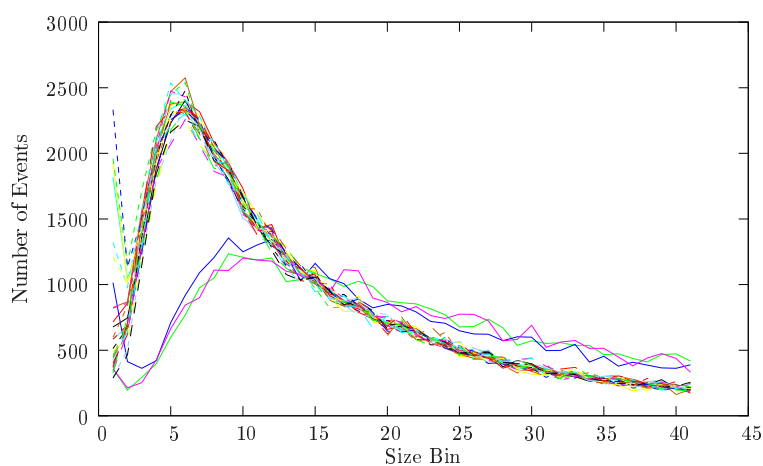
An extra scaling factor had to be added to take account of the exposure time differences for those runs which were not of 28-minute length. This may have diluted the statistics used in the calculation of the throughput factor, thus adding to the error in the corrected rate.

Due to the differing trigger conditions over the course of the season, it was felt that this correction should not be applied to the data used in the work of this thesis. The variation in the observed  $\gamma$ -ray rate during the times when the trigger condition had varied was examined. The Crab Nebula data were again examined. During the month when the telescope required a 4-fold trigger, the average  $\gamma$ -ray rate was found to be  $2.16 \pm 0.61 \gamma \text{ min}^{-1}$ . When the telescope required a 3-fold trigger, the rate was found to be  $2.21 \pm 0.53 \gamma \text{ min}^{-1}$ . Since the 4-fold value lies within the range of uncertainty of the “normal” 3-fold values, no correction was applied for any other data taken in that month by way of accounting for the difference in trigger condition.

## 4.7. Post-analysis Corrections



(a) Unscaled



(b) Scaled

**Figure 4.16:** The top panel shows the *size* distributions (*i.e.*  $Q_{run}$ ) for a collection of 29 Crab Nebula data scans. The lower panel shows the same *size* distributions multiplied by their respective throughput factors (*i.e.*  $F \times Q_{run}$ ) so that they are normalised to the reference run. The distributions which do not match the others were taken while the trigger criteria had been altered. Sizes were binned in 25-digital count bins.

## 4.7. Post-analysis Corrections

---

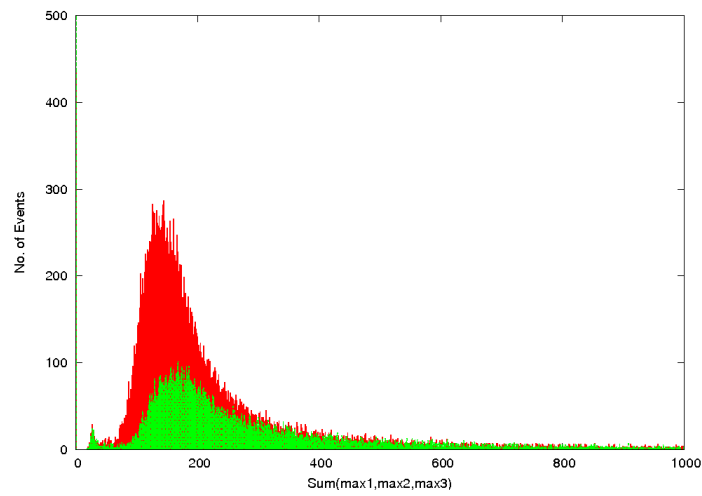


**Figure 4.17:** Comparing the sum of the *max1*, *max2* and *max3* distributions for two runs using different trigger criteria. The larger distribution uses a 3-fold trigger while the smaller one uses a 4-fold trigger. Indicative of this are the facts that there are fewer events recorded in the 4-fold case and the peak is shifted toward more luminous events.

## 4.7. Post-analysis Corrections

---

# Chapter 5

## Optimisation of Supercuts & $\gamma$ -Ray Analysis Results

The Supercuts criteria used for the selection of  $\gamma$ -ray events were optimised for the Whipple 10 m data from the 2006-2007 observing season. Two methods of optimisation are outlined in Section 5.1. The calculation of the tracking ratio for the 2006-2007 observing season is discussed in Section 5.2. The results of the Supercuts analysis of  $\gamma$ -ray data for five TeV blazars are presented in Section 5.3.

### 5.1 Re-optimisation of Supercuts parameters

Supercuts 2000 has proven to be sufficient for providing detections of  $\gamma$ -ray sources. However, from year to year the telescope configuration slowly changes in ways that require a re-optimisation of the Supercuts criteria for that specific observing season. Changes include:

- Variation in constant fraction discriminator threshold on a yearly basis

---

## 5.1. Re-optimisation of Supercuts parameters

---

- Fluctuation in performance of camera pixels (gain variation due to aging, pixels becoming damaged, *etc.*)
- Changes in the reflectivity and alignment of the telescope's optics
- Loss of channels due to electronic failures

Since Supercuts 2000 was developed using data obtained in the 2000 observing season, and the telescope has undergone considerable changes since then, a newly optimised set of parameter constraints was determined and used in this work.

Parameter cuts may also be optimised for the detection of sources with certain spectra (*i.e.* hard spectra or soft spectra, for instance). This may be achieved using simulated data with different spectral indices. No assumptions were made about the spectra of the sources investigated in this thesis, so cuts were optimised to find the highest signal-to-noise ratio using a strong source – the Crab Nebula.

### 5.1.1 Optimisation Methodologies

The traditional methodology for optimising Supercuts has been to choose a relatively large dataset which is known to have a significant  $\gamma$ -ray excess. This dataset is divided into two parts: an optimisation dataset and a control dataset. The optimisation dataset is optimised, using a pre-determined method, so that the highest statistically significant detection (or rate) is obtained. Crab Nebula data from the 2006-2007 observing season were used for the optimisation presented in this thesis.

The newly optimised Hillas parameters are then applied to the control dataset, which should also show an increase in significance (or rate) when compared to the unoptimised parameters. This is done to ensure that the selection criteria values are not due to some bias in the optimisation dataset.

The objective of the re-optimisation Supercuts was to obtain the highest possible excess significance (above background) over the entire energy

---

## 5.1. Re-optimisation of Supercuts parameters

---

range of the Whipple 10 m telescope. Small loss in  $\gamma$ -ray rate was therefore deemed acceptable.

A number of methods for Supercuts optimisation have been examined in the past. Some of these include the single parameter variation method (Lessard, 1999), the simplex algorithm (Moriarty *et al.*, 1997), and the grid search method (Quinn, 1997). Most of these optimisation methods select a contiguous region of Hillas parameter space. The use of non-contiguous cuts has been examined in the past but yielded similar results to schemes employing contiguous cuts. Hence, both the Single Parameter Variation method and the Cumulative Significance method, outlined in the following sections, select contiguous regions of Hillas parameter space to define cuts for the season.

### 5.1.2 Single Parameter Variation

This method was used as it is intuitive and not very computer intensive. A “brute-force” optimisation, whereby all permutations of cut values over the entirety of Hillas parameter space were tested, was also undertaken but this was shown from the outset to be resource intensive and slow when optimising nine parameters for a reasonably large dataset. The single parameter variation method is explained here.

Each of the cuts is initialised to an “open” value which allows most events to pass. One parameter is varied through a range of values in discrete steps while the other parameter cut values are held constant. The value of the varied cut for which the highest significance is achieved is selected and assigned this high-significance cut value. The next parameter is varied through a range of values in a similar manner until all of the parameters have been optimised.

This initial iteration gives a “best-estimate” value for all cuts. The same process is repeated with the “best-estimate” values replacing the initial “open” values of the first iteration. After this iteration, the new “best-estimate” is used as the starting point for the next iteration, and so

---

### 5.1. Re-optimisation of Supercuts parameters

---

on. Three iterations of this process were seen to result in a convergence to a maximum significance and the values of each parameter were then re-optimised Supercuts. Table 5.1 outlines these newly re-optimised Supercuts.

The *max3* cut was included in the re-optimisation. This was seen to have the effect of only slightly increasing the significance. A single parameter variation re-optimisation was attempted without the inclusion of a *max3* cut. The optimum *max1* and *max2* values remained the same as those shown in Table 5.1. The significance was found to be higher than the significance achieved by a Supercuts 2000 analysis, but slightly lower than when the *max3* cut was included. The  $\gamma$ -ray rate dropped (compared to a Supercuts 2000 analysis) by a similar amount regardless of whether a *max3* cut was included or not.

Although the  $\gamma$ -ray rate was found to fall significantly when using the single parameter variation cuts shown in Table 5.1, the excess significance increased by a large amount. *Length/size* was also included in the optimisation. As mentioned earlier, this has the effect of removing a lot of the muon events. However, Krennrich *et al.* (2001b) suggested that the effect this cut had on the 490-pixel camera in 2000 was to raise the energy threshold from 300 GeV when not utilising the cut to 520 GeV when utilising it.

The newly optimised cuts, when applied to the two Crab datasets, yield the results outlined in Table 5.2. The results of the analysis of the same datasets using Supercuts 2000 are also shown for comparison.

When the optimisation dataset and the control data set were analysed using Supercuts 2000 and the optimised cuts, there was a large discrepancy regarding both the significance and rate obtained. This indicates that the cuts obtained by this method of optimisation may not give the expected results (an increase in significance of  $\gamma$ -ray excess) for all data sets.

Using these re-optimised cuts, the “Crab rate” (*i.e.* the average  $\gamma$ -

## 5.1. Re-optimisation of Supercuts parameters

---

Cut	SC2000	SPV-Optimised Cuts
<i>size</i>	0 - $\infty$	0 - $\infty$
<i>max1</i>	> 30 d.c.	> 88 d.c.
<i>max2</i>	> 30 d.c.	> 56 d.c.
<i>max3</i>	-	> 52 d.c.
<i>frac3</i>	< 0.98	< 1.00
<i>width</i>	0.050° - 0.120°	0.043° - 0.110°
<i>length</i>	0.130° - 0.250°	0.114° - 0.228°
<i>distance</i>	0.400° - 1.000°	0.396° - 1.004°
<i>alpha</i>	< 15.0°	< 9.5°
<i>length/size</i>	< 0.00040°/d.c.	< 0.00032°/d.c.

**Table 5.1:** Comparison of cuts optimised for the 2007 season using the Single Parameter Variation (SPV) method with Supercuts 2000 (SC2000).

	Optimisation Dataset	Control Dataset
<b>Supercuts 2000</b>		
Significance	13.4 $\sigma$	13.5 $\sigma$
Rate	3.16 $\pm$ 0.24 $\gamma$ min <sup>-1</sup>	3.14 $\pm$ 0.23 $\gamma$ min <sup>-1</sup>
<b>SPV cuts 2007</b>		
Significance	19.8 $\sigma$	15.7 $\sigma$
Rate	2.07 $\pm$ 0.11 $\gamma$ min <sup>-1</sup>	1.65 $\pm$ 0.11 $\gamma$ min <sup>-1</sup>
Exposure	390.80 mins	372.20 mins

**Table 5.2:** Results of Single Parameter Variation re-optimisation of selection cuts, comparing results of analysis against Supercuts 2000.

---

## 5.1. Re-optimisation of Supercuts parameters

---

ray rate for the season’s observations of the Crab Nebula) was taken as the rate obtained using the optimised cuts on the control data set. This yielded a rate of  $1.65 \pm 0.11 \gamma \text{ min}^{-1}$ . This is a considerably lower rate than the Crab rate obtained using Supercuts 2000 on the same data set and is due to the increase in the energy threshold of the analysis due to considerably higher *max1*, *max2* and *max3* cuts which remove small, low-energy events.

### 5.1.3 Cumulative Significance Method

In order to determine an optimised set of cuts which would be more suitable for all data sets used in this thesis, a different approach was taken: the cumulative significance method.

As mentioned in Section 4.5, a “ $\gamma$ -ray domain” within a multi-dimensional parameter space (one dimension for each parameter) may be defined by the bounds, placed on each parameter, that are used to select  $\gamma$ -ray like events. A simple two-dimensional illustration of this is shown in Figure 5.1. This concept is expandable to all parameters used for the selection of  $\gamma$ -ray like events, although it is difficult to visualise.

To use this concept of domains within parameter space for the optimisation of selection parameters, the optimisation dataset is first parameterised and all events are binned in parameter space. This was done in two arrays; one for ON runs and one for OFF runs (*i.e.* *ON* and *OFF* arrays). For this work, four parameters were optimised using this method: *width*, *length*, *distance* and *alpha*. The optimisation of more parameters would require an unreasonably large amount of computer memory as the arrays used for binning events become quite large if they are constructed with fine resolution (*i.e.* fine bin widths) in multiple dimensions. The pre-selection cuts in *standard* Supercuts 2000 were used for the other parameters.

A “sum array” was next constructed for both the ON and the OFF data (*i.e.* *ON<sub>sum</sub>* and *OFF<sub>sum</sub>*). These were constructed so that the

## 5.1. Re-optimisation of Supercuts parameters

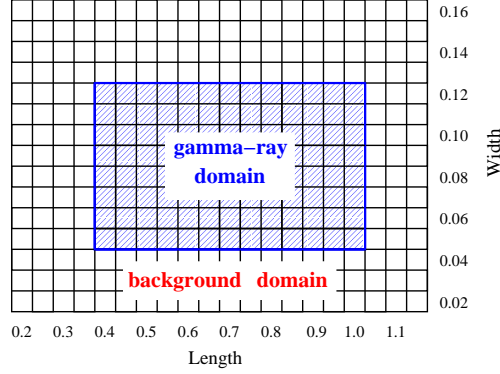


**Figure 5.1:** Schematic of a two-dimensional simplification of parameter space. Any event that has a *length* and *width* parameter which places it in the blue box is retained as a  $\gamma$ -ray like event. Otherwise, it falls in the background domain and is rejected by the analysis.

value in each cell of the array (*e.g.*  $ON_{sum}(w, l, d, a)$ , where  $w, l, d$ , and  $a$  are coordinates in the different dimensions of the array) was the sum of the events in the cells which form a contiguous space beginning at the origin (*e.g.*  $ON_{sum}(0, 0, 0, 0)$ ) and ending at the cell in question. So, for the  $ON$  array,

$$ON_{sum}(w, l, d, a) = \sum_{h=0}^w \sum_{i=0}^l \sum_{j=0}^d \sum_{k=0}^a ON(h, i, j, k) \quad (5.1)$$

A similar equation applied for the construction of the  $OFF_{sum}$ . A two-dimensional illustration of this is shown in Figure 5.2. After the  $ON_{sum}$  and  $OFF_{sum}$  arrays had been constructed in this manner, a four-dimensional significance array ( $SIG_4$ ) was constructed. This array had a calculated significance in each cell,  $SIG_4(w, l, d, a)$ , using ON and OFF counts from the corresponding cells in the  $ON_{sum}$  and  $OFF_{sum}$  arrays by

$$SIG_4(w, l, d, a) = \frac{ON_{sum}(w, l, d, a) - OFF_{sum}(w, l, d, a)}{\sqrt{ON_{sum}(w, l, d, a) + OFF_{sum}(w, l, d, a)}} \quad (5.2)$$

## 5.1. Re-optimisation of Supercuts parameters

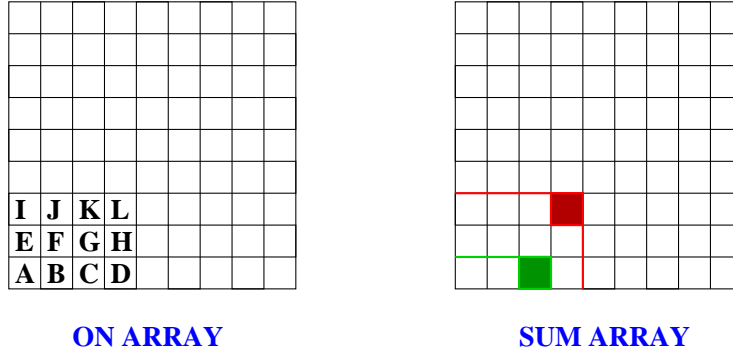


**Figure 5.2:** Two-dimensional example of the summing method used in finding the upper bounds of the parameters optimised using the cumulative significance technique. The value of the green cell in the sum array is found by adding  $A + B + C$  in the *ON* array. To find the value of the red cell in the sum array the values of cells *A* to *L* in the *ON* array are summed. In reality, this method was expanded to four dimensions and used to find upper bounds for four corresponding selection parameters.

where  $w, l, d$  and  $a$  are coordinates on the *width*, *length*, *distance* and *alpha* axes of the arrays.  $SIG_4$  was systematically searched so that the cell with the highest significance was found. The coordinates of this maximum significance cell,  $w', l', d'$  and  $a'$ , then acted as the upper bounds for the *width*, *length*, *distance* and *alpha* parameters respectively.

Next, the lower bounds for the parameters were found. The *alpha* parameter does not have a lower bound so the *ON* and *OFF* arrays were “collapsed” along their *alpha* axis, leaving them with only three dimensions. So for the collapsed *ON* array,

$$ON(w, l, d) = \sum_{k=0}^{x-1} ON(w, l, d, k) \quad (5.3)$$

where there are  $x$  divisions along the *alpha* axis.

Three-dimensional sum arrays were constructed for both the *ON* and *OFF* data. This was done by using the upper bounds, which had pre-

### 5.1. Re-optimisation of Supercuts parameters

Cut	SC2000	CSM-Optimised Cuts
<i>size</i>	0 - $\infty$	0 - $\infty$
<i>max1</i>	> 30 d.c.	> 30 d.c.
<i>max2</i>	> 30 d.c.	> 30 d.c.
<i>max3</i>	-	> - d.c.
<i>frac3</i>	< 0.98	< 0.98
<i>width</i>	0.050° - 0.120°	0.058° - 0.127°
<i>length</i>	0.130° - 0.250°	0.135° - 0.236°
<i>distance</i>	0.400° - 1.000°	0.463° - 0.975°
<i>alpha</i>	< 15.0°	< 9.5°
<i>length/size</i>	< 0.0004°/d.c.	< 0.0004°/d.c.

**Table 5.3:** A comparison of cuts optimised for the 2007 season using the Cumulative Significance method (CSM) and Supercuts 2000 (SC2000).

viously been found for *width*, *length* and *distance* (*i.e.*  $w'$ ,  $l'$  and  $d'$ ), as a starting point. The *ON* and *OFF* array cells were summed from this point back along each axis towards the origin, by

$$ON_{back}(w, l, d) = \sum_{h=w'}^0 \sum_{i=l'}^0 \sum_{j=d'}^0 ON(h, i, j) \quad (5.4)$$

A simplified two-dimensional representation is shown in Figure 5.3.

The sum arrays for *ON* and *OFF* data were calculated using this method for all cells from the upper bound values to the origin of each array. A three-dimensional significance array,  $SIG_3$ , was constructed using the values of these arrays and filling each cell using the three-dimensional equivalent of Equation 5.2 (*i.e.* excluding the *alpha* coordinates). The coordinates of the cell with the highest significance in  $SIG_3$  were then used as the lower bounds for *width*, *length* and *distance*. The optimised cuts found using the cumulative significance method are shown in Table 5.3 with Supercuts 2000 values shown for comparison. The effect of using the newly optimised cuts on the optimisation and control datasets

## 5.1. Re-optimisation of Supercuts parameters

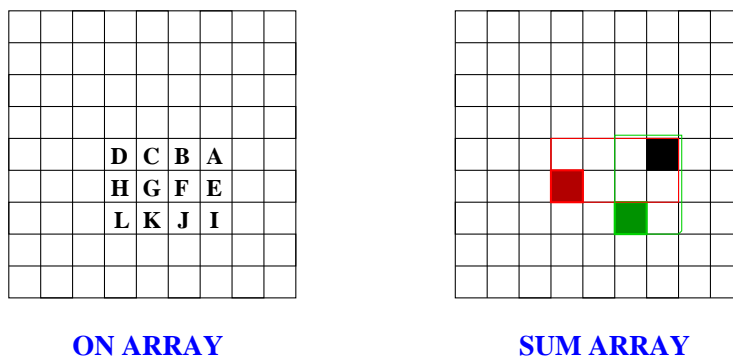


**Figure 5.3:** Two-dimensional illustration of the summing method used in finding the lower bounds for selection parameters being optimised with the cumulative significance technique. The value of the red cell in the sum array is found by summing  $A, B, C, D, E, F, G$  and  $H$ . The value in the green cell is found by  $A + B + E + F + I + J$ .

is shown in Table 5.4

The result of the cumulative significance optimisation was to increase the significance of the  $\gamma$ -ray signal in both the optimisation and control data sets. The increase in significance is smaller than that found with the single parameter variation method. However, the drop in  $\gamma$ -ray rate is not as severe. Also, the results after using the cumulative significance method cuts on both the optimisation data set and the control data set are more consistent than those found using the single parameter variation cuts. Analysis of the control data set using the optimised cuts resulted in a  $14.1\sigma$  excess for a  $\gamma$ -ray rate of  $2.50 \pm 0.18 \gamma \text{ min}^{-1}$  (*i.e.* the “Crab rate” for the season). This compared with an excess of  $13.5\sigma$  and a rate of  $3.14 \pm 0.23 \gamma \text{ min}^{-1}$  when the same data were analysed with Supercuts 2000.

### 5.1.4 Test of Re-optimised Supercuts

As a test of the two optimisation methods outlined above, the two sets of optimised cuts were applied to Markarian 421 data taken in the 2006-

### 5.1. Re-optimisation of Supercuts parameters

	Optimisation Dataset	Control Dataset
<b>Supercuts 2000</b>		
Significance	13.4 $\sigma$	13.5 $\sigma$
Rate	$3.16 \pm 0.24 \gamma \text{ min}^{-1}$	$3.14 \pm 0.23 \gamma \text{ min}^{-1}$
<b>CSM cuts 2007</b>		
Significance	14.4 $\sigma$	14.1 $\sigma$
Rate	$2.53 \pm 0.18 \gamma \text{ min}^{-1}$	$2.50 \pm 0.18 \gamma \text{ min}^{-1}$
Exposure	390.80 mins	372.20 mins

**Table 5.4:** Results of Cumulative Significance re-optimisation of selection cuts, comparing results of analysis against Supercuts 2000.

2007 season and the results were compared with those obtained for an analysis using standard Supercuts 2000. Data were selected on the basis of quality, as outlined previously in Section 4.7.2. Although the vast majority of the Markarian 421 data taken in the 2006-2007 season were taken in TRACKING mode, only the ON-OFF data were used in this test. The reasons for this were that:

- The aim of the test was not to look for, or measure, the variability of the source, but rather to determine the set of cuts that gave the highest significance of any excess of  $\gamma$ -ray-like events which could be detected for a known source of  $\gamma$ -rays.
- When using TRACKING data, a tracking ratio must be determined (see Section 4.6.2). By using ON-OFF data, the test is not subject to possible uncertainties in the tracking ratio.

The dataset contained 25 ON-OFF pairs taken between November 2006 and May 2007 over a range of elevations from 56° to 83°. A comparison of the results of analyses using the different sets of selection criteria may be found in Table 5.5.

## 5.2. Tracking Ratio Calculation

	Supercuts 2000	SPV Cuts 2007	CSM Cuts 2007
<b>Significance</b>	6.90 $\sigma$	9.21 $\sigma$	8.01 $\sigma$
<b>Rate</b> [ $\gamma$ min <sup>-1</sup> ]	1.02 $\pm$ 0.15	0.50 $\pm$ 0.05	0.91 $\pm$ 0.11
<b>% Crab Rate</b> <sup>1</sup>	0.33 $\pm$ 0.05	0.27 $\pm$ 0.03	0.36 $\pm$ 0.05

**Table 5.5:** Test of re-optimised  $\gamma$ -ray selection criteria by applying each set of cuts to Markarian 421 pairs. <sup>1</sup> %  $\gamma$ -ray rate from the Crab in the 2006-07 season.

As can be seen, the significance is increased from the nominal Supercuts 2000 values when using either of the two sets of optimised cuts. Using the single parameter variation cuts, the  $\gamma$ -ray rate is reduced significantly. Although the increase in significance using the cumulative significance method cuts is not as dramatic, the  $\gamma$ -ray rate is mostly retained. For weak, variable sources, the retention of rate sensitivity is important since variations in the detected rate are harder to discern when they are all consistently low. If rate sensitivity is not retained, variation in the detected  $\gamma$ -ray rate may not be large in comparison to the uncertainty in the rate. The retention of rate sensitivity exhibited when using the cumulative significance method cuts is, therefore, favourable and this set of cuts was adopted as Supercuts 2007 for all  $\gamma$ -ray analysis in this thesis.

## 5.2 Tracking Ratio Calculation

The tracking ratio is defined as the ratio of events passing cuts in a “source region”, to those passing cuts in a “control region” region for data containing no source of  $\gamma$ -rays. This has been explained in more detail in Section 4.6.2. Figure 5.4 shows where these *source* and *control* regions have been defined on an *alpha* plot (see Section 4.6).

Since observations taken in ON-OFF mode are only 50% time efficient

## 5.2. Tracking Ratio Calculation

---

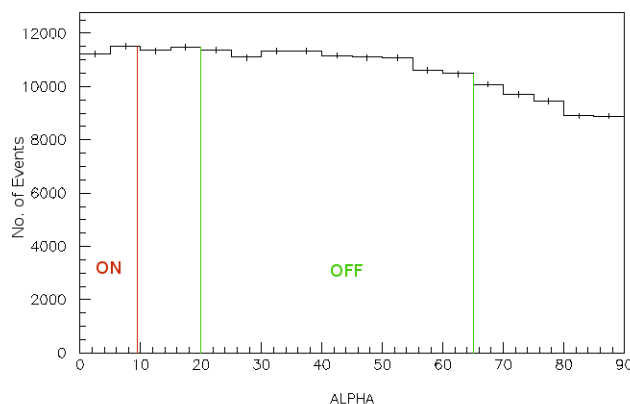


**Figure 5.4:** ON region ( $0^\circ - 9.5^\circ$ ) and OFF region ( $20^\circ - 65^\circ$ ), as defined for the calculation of a tracking ratio. The axis labelled “ALPHA” is in units of degrees. The distribution tapers from  $60^\circ - 90^\circ$  due to the fact that the optimised cuts were used. The appearance of tapering beyond the OFF field of *alpha* plots is common when cuts have been optimised.

(*i.e.* only 50% of the observation time is spent observing the object), most of the blazar monitoring observations in the 2006-2007 season were taken in TRACKING mode. This offered more on-source time. However, this also means that the determination of a tracking ratio (and its accuracy) becomes important. An inaccurate tracking ratio may lead to an underestimate or an overestimate of the background, which can artificially increase or reduce the statistical significance of a detection.

### 5.2.1 Data Selection

A large collection of OFF data scans from different regions of the sky (*i.e.* darkfield data) were used to determine the tracking ratio, as they were known to have no  $\gamma$ -ray signal. These data were selected using the criteria listed in Section 4.7.2 whereby only good quality data from observations at zenith angles  $<35^\circ$  in good non-variable weather were used.

## 5.2. Tracking Ratio Calculation

---

The amount of atmosphere between the telescope and the point at which an EAS is initiated increases with zenith angle. Therefore, only higher-energy particles can generate showers which are luminous and extensive enough to overcome the attenuation of Cherenkov light from showers initiated by the particle and register a trigger at the telescope for observations at these larger zenith angles. More importantly, however, the photon density of light pools generated by showers observed at increased zenith angle is lower than those observed at smaller zenith angle due to geometric spread (see Section 4.7.1). Observations taken at larger zenith angles will thus be of a different character to those taken closer to zenith, lending themselves to different selection criteria. This will have the effect of changing the tracking ratio for large zenith angle data. The effect of this atmospheric attenuation is rather negligible at zenith angles  $\leq 40^\circ$ . With the exception of observations of 1ES 1959+650, all blazar observations presented in this work were taken at zenith angles  $\leq 35^\circ$ . For this reason, only darkfield data at zenith angles less than  $35^\circ$  were used to determine a suitable tracking ratio for the season's data.

After applying the above criteria to the dataset, 265 darkfield scans remained for the 2006-2007 observing season. A source region of  $alpha = 0^\circ - 9.5^\circ$  and a control region of  $alpha = 20^\circ - 65^\circ$  were defined, as shown in Figure 5.4. From these, a tracking ratio of  $0.2162 \pm 0.0017$  was determined for the season.

### 5.2.2 Tracking Ratio Testing

The stability of the tracking ratio as a function of observation angle was tested by splitting up the entire darkfield dataset into  $5^\circ$  elevation bands and finding the tracking ratio (and associated uncertainty) for each of these data subsets. The results are plotted in Figure 5.5. The tracking ratio was found to be stable over the tested range of elevations.

In order to test the accuracy of the derived tracking ratio, a set of ON-OFF data was analysed. The ON runs from this dataset were then

## 5.2. Tracking Ratio Calculation

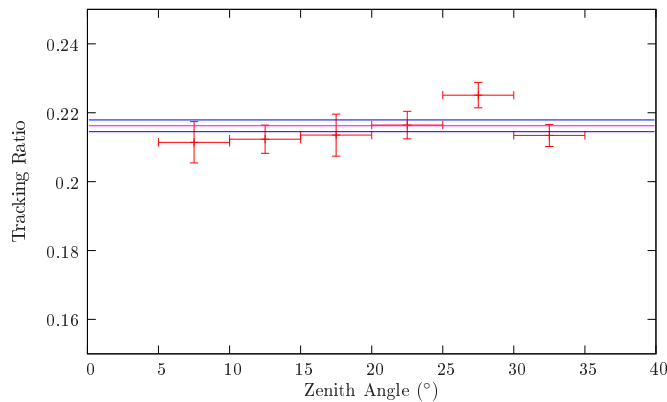


**Figure 5.5:** Tracking ratio calculated for  $5^\circ$  bins from zenith angles of  $5^\circ$  to  $35^\circ$ . The solid red line is the tracking ratio calculated using all of the darkfield data and the blue lines are the corresponding  $1\sigma$  uncertainty for this value.

analysed as if they were observations taken in TRACKING mode, using the previously calculated tracking ratio to estimate the background. The results were then compared. If the background estimation is correct (*i.e.* the tracking ratio has been correctly determined) then both results should have similar significances and rates since the background estimated using the tracking ratio should be similar to the real background from the OFF data.

A total of 30 pairs of ON-OFF observations (some shorter than 28 mins) of the Crab were used for comparison, giving a total exposure of 765.5 mins ( $\sim 12.8$  hrs). The data were analysed using the cumulative significance optimised cuts and a tracking ratio of  $0.2162 \pm 0.0017$  which was determined as outlined above.

The statistical significance was found to be slightly higher when the data were analysed as TRACKING runs. It is possible that statistical fluctuations within the control region of the *alpha* distribution, for a number of runs, have led to a determination of the background estimate which does not match the true (OFF run) background well.

### 5.3. Analysis of Blazar Data

	Pairs Analysis	Tracking Analysis
<b>Significance</b>	20.52 $\sigma$	22.03 $\sigma$
<b>Rate</b> [ $\gamma \text{ min}^{-1}$ ]	2.52 $\pm$ 0.12	2.41 $\pm$ 0.11

**Table 5.6:** Test of 2007 observing season tracking ratio. Crab ON-OFF data were analysed as pairs. The ON runs were then analysed as TRACKING data for the tracking analysis results shown.

### 5.3 Analysis of Blazar Data

The five TeV blazars, which were monitored as part of this work, are listed with their right ascensions and declinations and their respective redshifts, giving an indication of their relative distances, in Table 3.2. A review of recent observations of each object may be found in Section 3.5.

Four of the objects (1ES 1959+650 was the exception) had suitable declinations for observations at zenith angles  $<35^\circ$ , so all data for these objects were selected based on an observing zenith angle of less than  $35^\circ$ . For 1ES 1959+650, observations were all made in the  $34^\circ - 40^\circ$  band of zenith angles. Recent tests of the pointing accuracy of the Whipple 10 m telescope have shown that it has a small systematic pointing error. The pointing error is known to depend on the zenith angle of the telescope. However, any effect this pointing error might have on the analysis of the 2006-07 blazar data will be minimised by the selection of data obtained over a relatively small range of zenith angles.

Both TRACKING mode observations and ON-OFF mode observations were taken on all objects. An observing scheme of two TRACKING runs to every ON-OFF pair was employed when weather permitted (pairs were usually only taken in good weather). This ensured there were sufficient darkfield data throughout the season to determine an accurate tracking ratio. Data quality criteria outlined in Section 5.2.1 were used to select the datasets. Table 5.7 outlines the numbers of hours of data

### 5.3. Analysis of Blazar Data

Object	Dates [MJD]	No. of Nights	Pairs <sup>1</sup> [hours]	Track [hours]	Total [hours]
Markarian 421	54064-54260	44	10.8	38.1	48.9
Markarian 501	54148-54275	48	8.7	33.9	42.6
1ES 2344+514	54003-54118	36	5.6	25.1	30.7
1ES 1959+650	53998-54275	26	5.2	15.5	20.7
H 1426+428	54116-54272	57	12.7	37.6	50.3

**Table 5.7:** Datasets for each target investigated in this work. 1ES 1959+650 was observed at the beginning (53998 - 54031) and towards the end (54236 - 54275) of the observing season with a gap in between. This is because it was not visible at a suitable elevation from the Whipple observatory in the middle of the season. <sup>1</sup> One hour of pairs data means one hour on-source with an hour of corresponding off-source observations.

selected after data selection was made for each source based on the criteria outlined in Section 5.2.1 (*i.e.* the data which were subsequently analysed).

#### Markarian 421

Markarian 421 is known to exhibit large flaring at TeV energies. It has shown both rapid variability (day-scale) and long-term variability (on scales of months or years) in the past.

The entire set of over 48 hours of on-source data (*i.e.* TRACKING runs and ON runs analysed as TRACKING data) produced a  $20.44\sigma$ -level detection with a rate of  $0.79 \pm 0.04 \gamma \text{ min}^{-1}$  or  $\sim 31\%$  of the Crab rate. Variability is evident at significant levels in the light curve shown in Figure 5.6. A  $\chi^2$  test was performed to compute the chance probability of the variation in  $\gamma$ -ray rate being due to random fluctuations about the mean rate for the season. This resulted in a fit of  $\chi^2/dof = 144.4/43$ , corresponding to a chance probability of  $7 \times 10^{-13}$ . Two 28-minute data

### 5.3. Analysis of Blazar Data

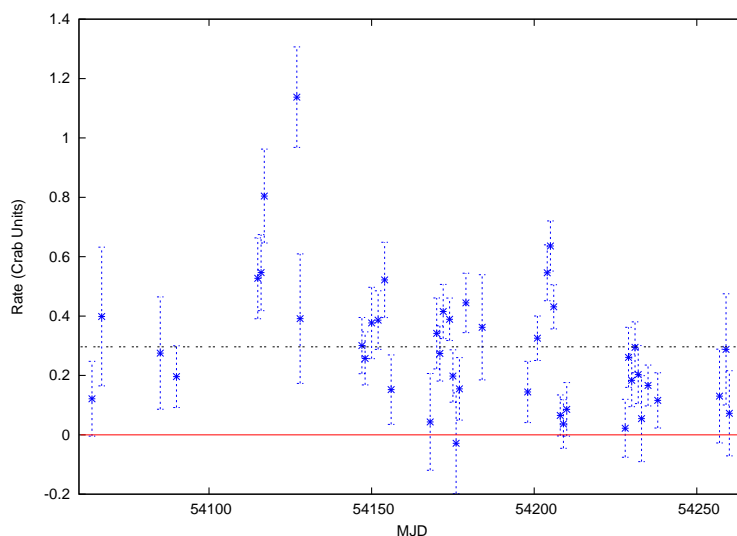


**Figure 5.6:** Markarian 421 nightly light curve for the 2006-07 observing season. Data shown here were taken between 25<sup>th</sup> November 2006 and 9<sup>th</sup> June 2007. Rates are shown in units of fraction of the Crab rate. The dashed horizontal line represents the mean  $\gamma$ -ray rate for the campaign.

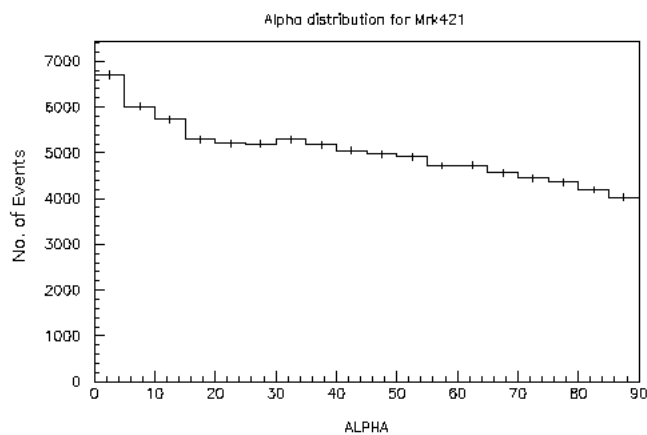


**Figure 5.7:** *Alpha* plot for all Markarian 421 TRACKING and ON data from the 2006-07 observing season. An excess of events is visible at lower *alpha* values. *Alpha* is in units of degrees.

### 5.3. Analysis of Blazar Data

---

scans on MJD 54127 exhibited rates of  $2.87 \pm 0.57 \gamma \text{ min}^{-1}$  and  $2.84 \pm 0.56 \gamma \text{ min}^{-1}$  (both  $\sim 1.3$  times the Crab rate) respectively. This night also had the highest nightly average rate of 1.1 times the Crab rate at a significance of  $6.7\sigma$ . This is more than three times the average rate for Markarian 421 during the season. A detailed quantitative analysis of the variability exhibited by Markarian 421 during the 2006-07 observing season will be presented in Chapter 7. The *alpha* plot for the TRACKING analysis of all Markarian 421 data for the season is shown in Figure 5.7. A clear excess of events with small values of *alpha* is evident in the plot.

#### Markarian 501

Markarian 501 is another often-detected TeV blazar. It has exhibited extraordinary flaring activity in the past, having exhibited flux levels in excess of the Crab Nebula. Section 3.5.2 gives an outline of previous Markarian 501 observations at  $\gamma$ -ray energies.

In the 2006-2007 season, Markarian 501 was detected with a high statistical significance of  $7.73\sigma$  in  $\sim 42$  hours of on-source data (TRACKING data and ON data). Figure 5.8 shows the *alpha* plot for these data with an excess clearly visible at small *alpha* angles.

The mean  $\gamma$ -ray rate for Markarian 501 during the 2006-07 season was found to be  $0.26 \pm 0.03 \gamma \text{ min}^{-1}$ , which corresponds to a little over 10% of the Crab rate for the season. As with Markarian 421, the rate varied on a nightly basis. A  $\chi^2$  test for consistency with steady emission from the source resulted in a fit of  $\chi^2/dof = 146.5/46$  which corresponds to a chance probability of  $2 \times 10^{-12}$ . On a single night (MJD 54213), Markarian 501 was detected at  $8.4\sigma$  and the average  $\gamma$ -ray rate was 56% of that of the Crab Nebula. This represented more than a 5-fold increase in the average Markarian 501  $\gamma$ -ray rate for the season. One 28-minute data scan on this night alone exhibited a  $\gamma$ -ray rate of  $\sim 90\%$  that of the Crab Nebula with a significance of  $6.2\sigma$ . The rate then fell to around 50% of the Crab rate within the next 2 hours.

### 5.3. Analysis of Blazar Data

---

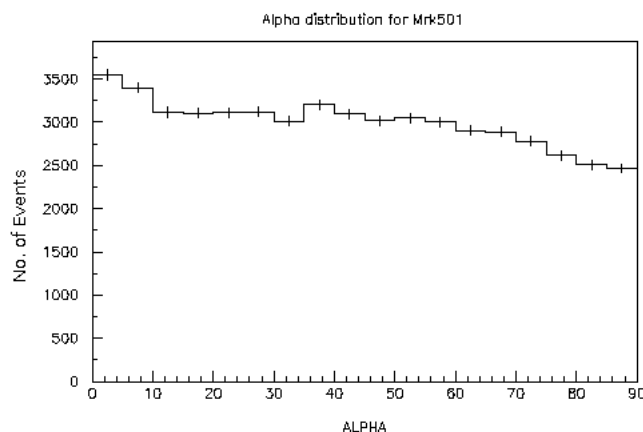


**Figure 5.8:** *Alpha* plot for Markarian 501 on-source data (analysed as TRACKING data) in the 2006-07 observing season. An excess of events is visible at lower *alpha* values. *Alpha* is in units of degrees.

This type of variability is evident in the light curve shown in Figure 5.9. Long-term and short term variability are characterised more quantitatively in Chapter 7.

#### 1ES 2344+514

1ES 2344+514 has only been detected once by the Whipple 10 m telescope (Catanese *et al.*, 1998). An apparent flare on one night of observation was detected, with follow-up observations only providing hints of a signal. More recent observations in 2005 by the more sensitive MAGIC telescope have detected quiescent emission from 1ES 2344+514 (see Section 3.5.3).

There was no significant  $\gamma$ -ray excess observed in the 2006-07 observations of this campaign. Analysis of 30.7 hours of on-source data only resulted in a  $\sim 2\sigma$  excess. The *alpha* plot for this analysis (Figure 5.10) does not show any evidence for a statistically significant excess at small

### 5.3. Analysis of Blazar Data

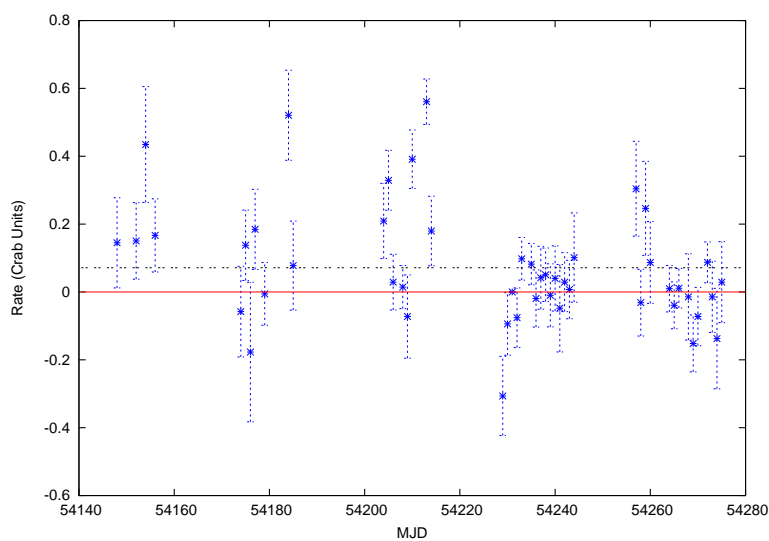


**Figure 5.9:** Markarian 501 light curve for the 2006-07 observing season. Each point in the plot represents a nightly average  $\gamma$ -ray rate in Crab units. The dashed horizontal line shows the average  $\gamma$ -ray rate (in Crab units) for Markarian 501 for the season. The data shown in this plot were obtained between 17<sup>th</sup> February and 24<sup>th</sup> March, 2007.

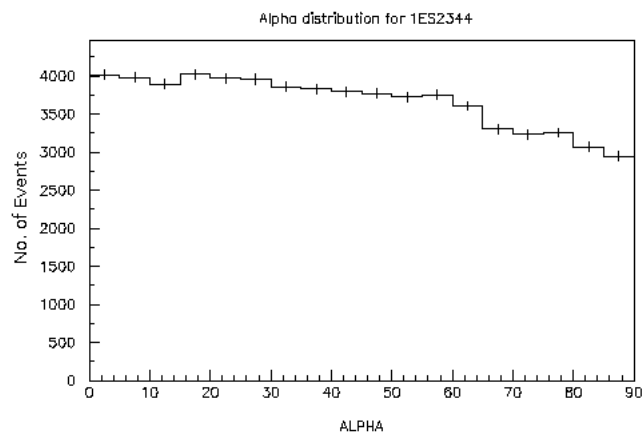


**Figure 5.10:** *Alpha* plot for all 2006-07 season 1ES 2344+514 on-source data (analysed as TRACKING data). No excess is evident in the plot. *Alpha* is in units of degrees.

### 5.3. Analysis of Blazar Data

---

values of *alpha*.

$3\sigma$  upper limits were calculated following the Bayesian method of Helene (1983). This method calculates the highest rate value the rate could have been while remaining below the sensitivity threshold of the telescope given the statistical insignificance of the excess detected. An upper limit of  $0.25 \gamma \text{ min}^{-1}$ , or around 10% of the Crab Nebula rate, was found for 1ES 2344+514 using this method.

Although the entire data set did not exhibit a statistically significant  $\gamma$ -ray excess, the variable nature of TeV blazars means that there may have been flaring of the source on shorter timescales at levels above the sensitivity threshold of the telescope. However, run-by-run and night-by-night examinations of the data did not show evidence for any flares.  $\chi^2/dof = 19.4/32$  for a straight-line fit to the data, corresponding to a chance probability of 0.96, suggests that the light curve does not exhibit variability. It is, of course, possible that there was quiescent emission from 1ES 2344+514 below the threshold of the Whipple 10 m telescope. This has been the case in the past, with detections only occurring when it was in a high state of activity. The night-averaged light curve produced from the analysis of the 1ES 2344+514 data is shown in Figure 5.11.

#### **1ES 1959+650**

1ES 1959+650 has only previously been detected by the Whipple 10 m telescope while flaring (see Section 3.5.5). During this campaign, there was no evidence of flaring and only a  $2.8\sigma$   $\gamma$ -ray excess was observed for the entire data set of  $>20$  hours of data. The *alpha* plot for data set is shown in Figure 5.12.

The data set for 2006-07 is comprised of two separate sets of data: 9 hours of data from early in the season (MJD 53998 - 54031) and 11.7 hours taken towards the end of the season (MJD 54236 - 54275). Neither of these data sets, in their own right, exhibited a significant excess. The reason for the gap in coverage between these two sets of observations

### 5.3. Analysis of Blazar Data

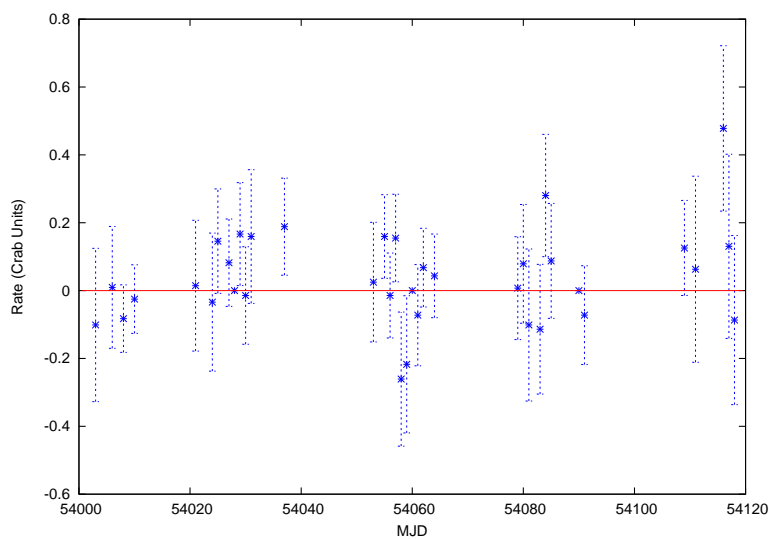


**Figure 5.11:** 1ES 2344+514 light curve for the 2006-07 observing season. There is no evidence of flaring. The data shown in this plot were obtained between 22<sup>nd</sup> of September 2006 and 17<sup>th</sup> of January 2007.

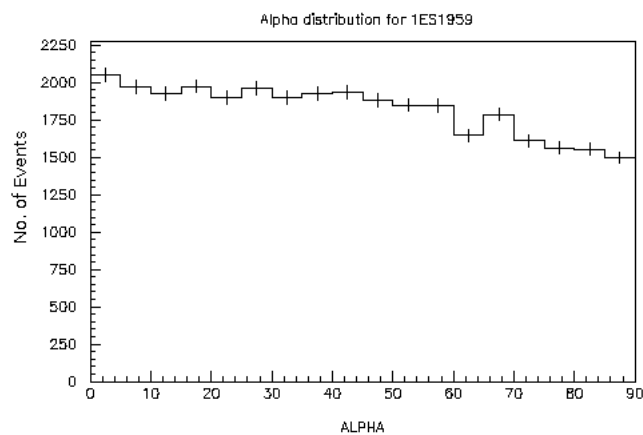


**Figure 5.12:** *Alpha* plot for all 2006-07 season 1ES 1959+650 on-source data (analysed as TRACKING data). There is no evidence of a significant  $\gamma$ -ray excess in the plot. *Alpha* is in units of degrees.

### 5.3. Analysis of Blazar Data

---

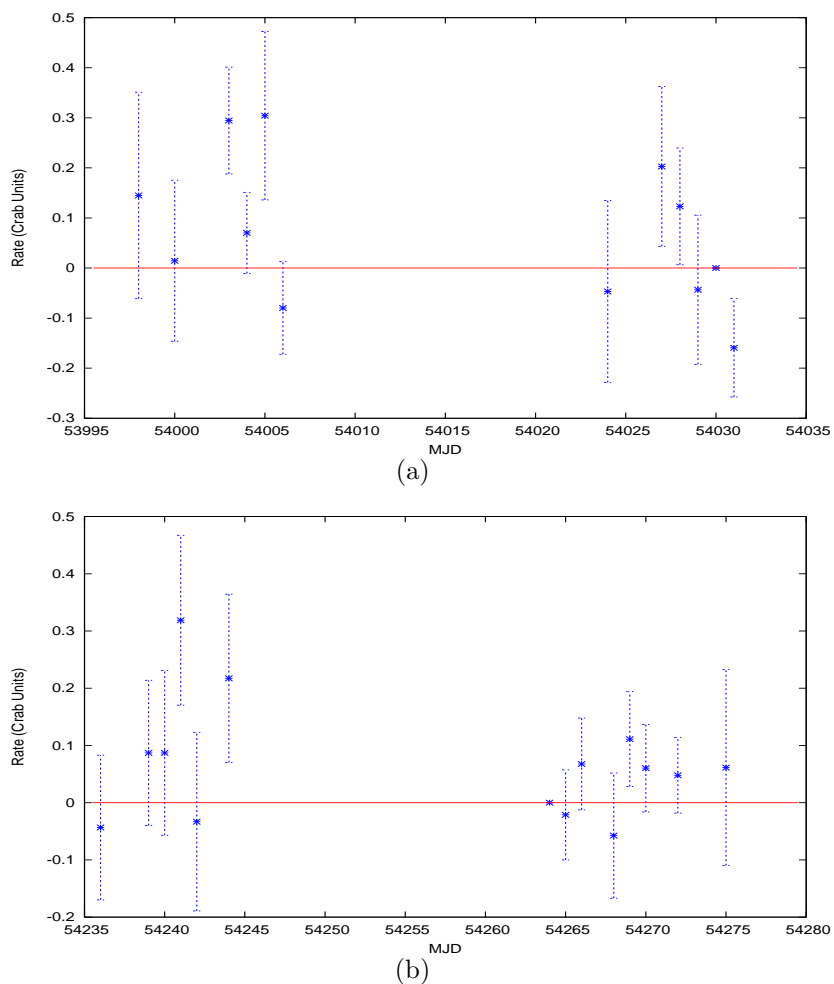


**Figure 5.13:** Two plots of night-averaged  $\gamma$ -ray light curves for 1ES 1959+650 in 2006-07. The top panel (a) shows the light curve for the early part of the season (20<sup>th</sup> September - 23<sup>rd</sup> October, 2006). The bottom panel (b) shows a light curve for the later part of the season (16<sup>th</sup> May - 24<sup>th</sup> June, 2007).

### 5.3. Analysis of Blazar Data

---

was that 1ES 1959+650 was not visible at zenith angles suitable for observations at the Whipple observatory site during the middle of the observing season. A fit of  $\chi^2/dof = 24.3/23$ , corresponding to a chance probability of 0.39, indicates that the source was not variable during this campaign.

The  $3\sigma$  upper limit for the entire 1ES 1959+650 data set was found to be 12.5% of the Crab Nebula rate. Figure 5.13 shows the light curves for the season. They are featureless (*i.e.* there were no significant flares detected). As was the case for 1ES 2344+514, it is possible that quiescent  $\gamma$ -ray emission from 1ES 1959+650 was below the sensitivity of the telescope and was therefore not detected.

#### **H 1426+428**

H 1426+428 was not detected from over 60 hours of on-source data. The *alpha* plot for H 1426+428 is shown in Figure 5.14. The  $3\sigma$  upper limit, calculated using the Helene method (Helene, 1983), was found to be 28% of the Crab Nebula rate.

There is no evidence of flared emission in the night-averaged light curve shown in Figure 5.15. There was no evidence of statistically significant  $\gamma$ -ray emission on run-by-run or night-by-night timescales. A fit of  $\chi^2/dof = 56.9/56$  for non-variable emission, corresponding to a chance probability of 0.44, is indicative of this.

#### **Summary**

Table 5.8 gives a summary of the results of the analyses performed for each blazar data set, including the nightly average  $\gamma$ -ray rate from the nights of strongest emission and mean emission over the course of the observing campaign (if they could be determined for the source).

### 5.3. Analysis of Blazar Data

---

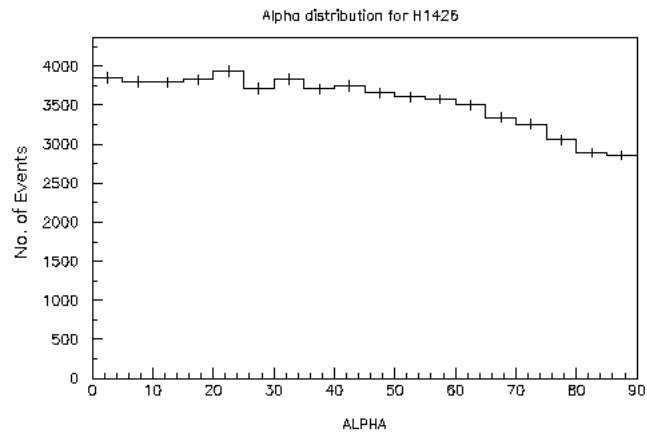


**Figure 5.14:** *Alpha* plot for all 2006-07 H 1426+428 on-source data analysed as TRACKING data. There is no evidence of an excess at small *alpha* values. *Alpha* in units of degrees.

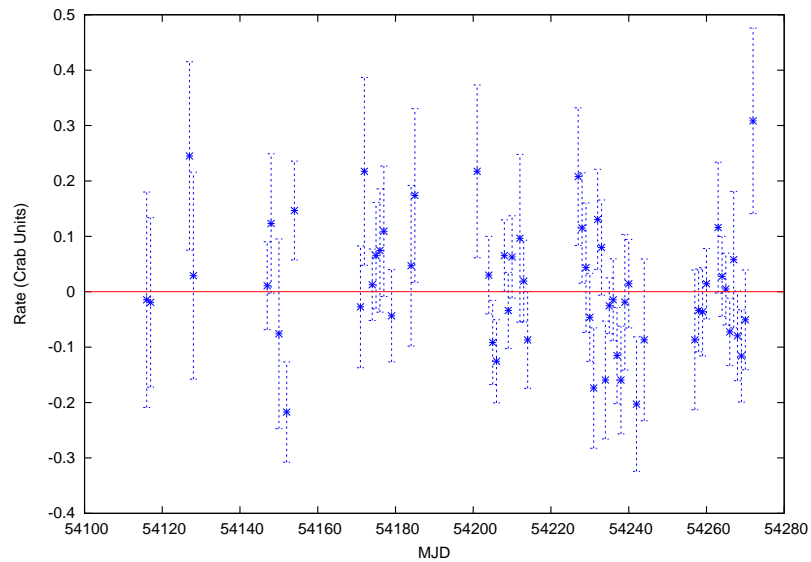


**Figure 5.15:** H 1426+428 light curve for the 2006-07 observing season. Data shown here were obtained 16<sup>th</sup> January - 21<sup>st</sup> June, 2007.

Object	Exposure [hours]	Overall Sig. [ $\sigma$ ]	Mean Rate/U.L. [ $\gamma \text{ min}^{-1}$ ]	Max. Sig. [ $\sigma$ ]	Max. Rate [ $\gamma \text{ min}^{-1}$ ]
Markarian 421	48.9	20.4	$0.79 \pm 0.04$	6.7	$2.86 \pm 0.43$
Markarian 501	42.6	7.7	$0.26 \pm 0.03$	8.4	$1.41 \pm 0.17$
1ES 2344+514	30.7	-	$< 0.26$	-	-
1ES 1959+650	20.7	-	$< 0.31$	-	-
H 1426+428	50.3	-	$< 0.71$	-	-

**Table 5.8:** Summary of  $\gamma$ -ray analysis for 2006-07 observing season. The quoted upper limits are  $3\sigma$  upper limits, calculated using the Helene method (Helene, 1983). The “Max. Sig.” and “Max. Rate” columns list the significance and rate detected on the night of highest emission.

### 5.3. Analysis of Blazar Data

---

# Chapter 6

## Optical Photometry

TeV blazars are known to exhibit variability in different wavebands across the electromagnetic spectrum. Variability has been seen to be strongly correlated at  $\gamma$ -ray and x-ray energies. Tentative hints of correlation between  $\gamma$ -ray emission and optical emission have been seen previously (*e.g.* Albert *et al.*, 2006b, 2007b).

During the 2006-07 observing season, optical data were collected from a number of observatories as part of a large-scale multiwavelength study. Some of these data were analysed as part of the work of this thesis. The optical monitoring programme is described in Section 6.1. The telescope, data reduction technique and photometry used are described in Section 6.2, Section 6.3 and Section 6.4 respectively. The estimation of the error associated with the photometry is outlined in Section 6.5. A simple measure of the variability exhibited by each of the blazars is explained in Section 6.6. Finally, the results of the optical photometry performed on each of the blazars studied before and after photometric normalisation are presented in Section 6.7 and Section 6.8.

## 6.1. Optical Monitoring Programme

---



**Figure 6.1:** Some of the telescopes located on the ridge of Mount Hopkins, Arizona at an altitude of  $\sim 2300$  m above sea level. Label **1** indicates the Whipple 10 m  $\gamma$ -ray telescope and **2** is the FLWO 1.2 m optical telescope. The FLWO 1.5 m Tillinghast telescope and 1.3 m PAIRITEL Infrared telescopes are labelled **3** and **4** respectively.

## 6.1 Optical Monitoring Programme

Since 2005, the Whipple 10 m telescope has primarily devoted observing time to the monitoring of AGN as part of a long-term dedicated multiwavelength programme, initiated and coordinated by the VERITAS Collaboration. A number of optical telescopes contributed data sets to this campaign. Among these was the Fred Lawrence Whipple Observatory (FLWO) 1.2 m telescope located adjacent to the Whipple 10 m  $\gamma$ -ray telescope on Mount Hopkins, Arizona (see Figure 6.1).

The data from the FLWO 1.2 m telescope were taken in service mode, meaning that observers had to set time aside specifically for these observations each night. Service time was allocated in the second and third trimesters (Spring and Summer) of the 2006-2007 observing season. All observations were taken with an  $r'$ -band filter from the SDSS photometric system filter set (Fukugita *et al.*, 1996) (see Figure 6.2). Due to the FLWO 1.2 m telescope's proximity to the Whipple 10 m telescope, they are subject to similar atmospheric conditions at the time of observation. This means that (except for the limitations of TeV observations due to the lunar cycle) light curves are well matched with regard to sampling. Unfortunately, however, due to weather and other factors optical obser-

## 6.1. Optical Monitoring Programme

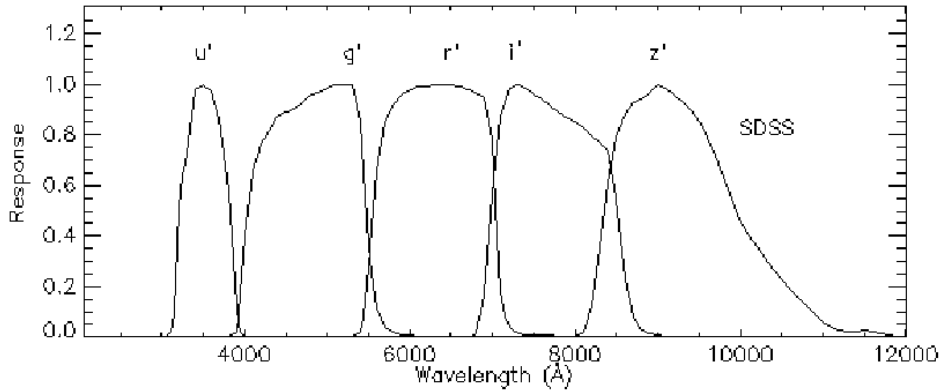


**Figure 6.2:** Graph showing the bandwidths of the SDSS range of optical filters. The  $r'$ -band filter was used for all images in this work.

Blazar	No. of Nights	MJD Range
Markarian 501	44	54168 - 54273
H 1426+428	40	54168 - 54273
Markarian 421	31	54117 - 54273
1ES 1959+650	24	54193 - 54273
1ES 2344+514	7	54232 - 54273

**Table 6.1:** Summary of optical  $r'$ -band data obtained at the FLWO 1.2 m telescope as part of this multiwavelength study.

vations could not be obtained every night for each object.

Table 6.1 outlines the extent of this optical dataset for each of the five blazars of interest in this work. The observations were only taken in the second and third trimesters (January to June 2007), meaning that only Markarian 421, Markarian 501 and H 1426+428 (due to their Right Ascensions) were well covered. By comparison, data collected for 1ES 2344+514 and 1ES 1959+650 did not have many corresponding observations at TeV energies.

## 6.2 The FLWO 1.2 m Telescope

The Fred Lawrence Whipple Observatory (FLWO) 1.2 m telescope primarily utilises the KeplerCam wide-field charge-coupled device (CCD) camera (Szentgyorgyi *et al.*, 2005). The primary purpose of the instrument is to provide multi-band photometry of the Kepler Input Catalog field (*i.e.* a catalogue of star systems that may contain Earth-sized extrasolar planets). The detector is comprised of four Fairchild CCD486 CCD chips. Each CCD has a  $4096 \times 4096$  pixel format with all pixels measuring  $15 \mu\text{m}$ . This provides a field of  $23.1 \text{ arcmin}^2$  (*i.e.* a plate scale of 0.338 seconds of arc per pixel) when using all four CCDs. KeplerCam was the instrument used to obtain all  $r'$ -band data presented in this thesis, although only the image formed on one of the CCDs was utilised from each frame.

The focal plane of the FLWO 1.2 m telescope is flattened with a custom-built fused silica doublet corrector. The corrector ensures equal throughput at all optical wavelengths and low field distortion.

The KeplerCam CCDs were fabricated in such a way that they are not subject to many physical defects, ensuring a good noise performance, quantum efficiency and linearity across the CCDs. The chips are also cryogenically cooled to reduce noise during observations. The standard image readout format is with pixels binned  $2 \times 2$ , with a corresponding readout time of 11 seconds. The CCD wells are very deep ( $\sim 65,000$  counts per pixel). This allows for long exposures without saturation effects such as “blooming”. Blooming, which occurs on all CCDs, is an effect whereby the charge in a pixels goes beyond saturation point and overflows into an adjacent pixel. This leads to erroneous pixel values and often leads to image streaks appearing in the image.

All images used for optical photometry in this work were obtained using the KeplerCam on the FLWO 1.2 m telescope. Each of the four CCDs making up the detector has its own amplifier. Due to the fact that CCD 2 offers slightly better performance than the other three, and

### 6.3. Data Reduction

---

owing to the complications introduced by having to normalise all four amplifiers in order to compare stars on them, the galaxy being investigated was centred in CCD 2 for all images and aperture photometry was only performed on objects in this part of the field.

## 6.3 Data Reduction

Data reduction was performed using IRAF<sup>1</sup>, a general purpose suite of programs used for the reduction and analysis of astronomical images (Tody, 1986, 1993). The suite is freely available and is written, developed and maintained by the National Optical Astronomical Observatories in Tucson, Arizona.

IRAF is arranged in a tree structure comprised of various *packages*. Each package contains a set of specific *tasks* (or subpackages). Every task has a set of parameters which may be adjusted by the operator to suit the current application. A standard set of reduction and analysis tasks for single-CCD images, called the **NOAO** package, is supplied with every installation. For multi-CCD images (like those obtained by KeplerCam) an external package, called **MSCRED**, is used (Valdes, 1998; Popescu *et al.*, 2005).

An IRAF image display server is necessary in order to display the images and complete certain tasks such as measuring the full-width-half-maximum of stars in the field. The display server used in this work was **ds9**.

In order to obtain an average of the images obtained on a given night, the data had to be correctly reduced, removing “additive” effects such as bias structure and gain variations across the CCD. A number of different types of image are required to complete a reduction:

- *Bias Frames*: These are exposures which have an exposure time of zero seconds and are used to remove bias structure. They are often

---

<sup>1</sup>Image Reduction and Analysis Facility, [www.iraf.net](http://www.iraf.net)

### 6.3. Data Reduction

---

called zero frames and are used to measure (and hence remove) DC offsets inherent in every pixel in the camera. Ten bias frames were obtained on each night so that average values of the offsets over a number of frames could be used for the photometry presented in this thesis.

- *Flat Frames:* These are short exposures, with the CCD evenly illuminated. They are used to correct for pixel-to-pixel gain variations in each image. There are two possible types of flat frame: sky/twilight flats and dome flats. Sky flats are obtained by illuminating the CCD by pointing the telescope at the sky during twilight. This usually provides a very even illumination. Dome flats are obtained by pointing the telescope at an evenly illuminated white screen inside the telescope dome. Twilight flats were not always obtainable, so dome flats were used throughout this work. At least ten flat frames were obtained each observing night.
- *Dark Frames:* For CCDs with a non-negligible amount of background current, dark frames are obtained by taking long exposures with the CCD covered. This provides a measure of the background “dark” current to be removed in each image. As the KeplerCam is cryogenically cooled, and owing to the short exposure times of the images used, the dark current is negligible and dark correction was not necessary.

Initially, all images must be overscan corrected. The overscan region is a section of the CCD which is not exposed along with the rest of the CCD chip. The “signal” in the rows of this strip are averaged to provide a measure of the pedestal (typically a few hundred digital counts) which has been injected into the image. The average value for each row of the overscan is then removed from values recorded by pixels in that row of the exposed part of the CCD accordingly. The overscan region is then trimmed from the useable frame.

### 6.3. Data Reduction

---

Reduction of images requires a series of carefully executed steps. IRAF has the functionality for this processing, but each step must be visually scrutinised to ensure high quality.

Below is an outline of the procedure used to reduce data, obtained at the FLWO 1.2 m telescope, to a single “night’s average” frame for each source suitable for photometry. The tasks listed are found in the IRAF MSCRED package.

- Combine bias frames into a single master bias frame using the `zerocombine` task. The images are overscan corrected and the overscan is trimmed from the image during the combination.
- Subtract master bias frame from all flat-field frames. Combine (*i.e.* average) all flat-field frames into a single master flat frame that corrects for gain differences across the CCD. Both these steps are done using the `flatcombine` task. Each flat-field frame is overscan corrected and the overscan region is trimmed from the image during combination.
- Subtract master bias from all science images obtained for the blazar that night. Divide all bias-corrected science images by the master flat frame. Both of these steps are done using the `ccdproc` task. Overscan correction and trimming is performed on the science images during this process.
- Combine the corrected science images produced by `ccdproc` into a single science frame (for that night’s data) using `combine`.
- Split the science frame up into its four constituent extensions using `mscsplit`. This step was only taken because the target object was contained on only one of the KeplerCam’s four CCDs.
- Discard the three extensions which do not contain the blazar of interest.

## 6.4. Optical Photometry

---

The remaining frame may be regarded as the nightly average for the blazar and photometry can then be carried out on this frame. This reduction procedure was followed for each night data was obtained for each of the blazars investigated. The photometry used is outlined in the following section.

## 6.4 Optical Photometry

CCD differential photometry offers a high degree of accuracy in the measurement of variability of a target (usually  $< 1\%$ , or  $\sim 2$  millimagnitudes for the targets presented in this thesis). In order to perform differential photometry, a number of standard “comparison” stars – exhibiting no variability – are selected within the field-of-view of the science image. A comparison is then made between the instrumental magnitude of the target of interest (*i.e.* the blazar) and the instrumental magnitudes of the comparison stars. The condition of the atmosphere at the time of observation is assumed to affect the comparison stars and the target equally, so high precision photometry is possible even on nights when the atmospheric condition is not optimal.

Once an image has been properly reduced, aperture photometry is performed on the blazar and all comparison stars in order to obtain the instrumental magnitudes needed for differential photometry. This is done by summing up the flux within an aperture that is placed around the star/galaxy (*i.e.* the target object). The background contribution within the aperture is estimated and subtracted leaving only the flux contribution from the object. An instrumental magnitude can then be calculated using this flux excess. The background estimate is made by summing the flux within an annulus placed outside of the aperture. This value is scaled by area to get an estimate of the expected background.

For the photometry presented in this work, the IRAF aperture photometry package, APPHOT, was used. The choice of aperture size is im-

## 6.4. Optical Photometry

---

portant for performing accurate photometry. If the aperture is too large, light from surrounding near-by objects may be included inadvertently. If the aperture size is too small, variation in the measured magnitude may arise due to differences in seeing changing the fraction of the object's light contained within the aperture. In general, a diameter of  $\sim 4 - 5$  times the full-width-half-maximum (FWHM) of the image of the object is optimum. The optimum aperture diameter may be found by using a series of aperture sizes for the same target and plotting aperture size against magnitude – so-called growth curves. The magnitude tends to increase with aperture size to a point where the plot is seen to plateau. The point where the plot levels off indicates the optimal aperture radius. Growth curves are produced for a number of stars in the field to find the best aperture size to use for the data set.

In practice, differential photometry is performed by comparing the magnitude of a variable target,  $m_d$ , to the magnitude of comparison star,  $m_c$ , which is assumed to be constant during the observing campaign. Standard differential photometry techniques, similar to those in Bailer-Jones & Mundt (2001), were performed to obtain light curves and associated errors. The differential light curve values were calculated as follows. Let  $F_i$  be the flux value (typically in units of analogue-to-digital units since exposure time is the same for all objects in the frame) for the  $i$ th reference star out of  $N$  reference stars in a frame. A new “comparison flux”,  $F_c$  is calculated by

$$F_c = \frac{1}{N} \sum_i^N F_i \quad (6.1)$$

The comparison magnitude,  $m_c$ , corresponding to this flux is, therefore,

$$m_c = -2.5 \log_{10} F_c \quad (6.2)$$

This magnitude is assumed to be constant over the course of the

## 6.5. Error Estimation

---

observing campaign. If  $F_s$  and  $m_s$  are the flux and magnitude of the blazar respectively, then the differential magnitude,  $m_d$ , is calculated by

$$m_d = m_s - m_c = 2.5 \log_{10} \left( \frac{F_c}{F_s} \right) \quad (6.3)$$

This method of averaging the reference star fluxes is preferred over magnitude averaging as it gives more weight to the brighter reference stars (*i.e.* those with a higher signal-to-noise ratio). If we call  $m_{d,k}$  the differential magnitude of the target in frame  $k$ , and if there are  $N$  frames in our data set, then the mean is subtracted such that

$$\sum_{k=1}^N m_{d,k} = 0 \quad (6.4)$$

## 6.5 Error Estimation

The science frames used for differential photometry in this work are all averages of between two and five images, each of which is a relatively long exposure (*i.e.* on the order of 30 seconds). These exposure times are sufficient so that it can be assumed that changes in atmospheric conditions will affect all stars in the frame equally due to the fact that there is sufficient time for thin cloud to move across the entire field of view during the exposure. Also, if  $t_{open}$  is the time taken for the shutter to open and  $t_{exp}$  is the exposure time, then  $t_{open} \ll t_{exp}$ , reducing any bias effects across the CCD due to the shutter opening time. If  $m_c$  is defined using non-variable reference stars, then changes in  $m_d$  are either due to noise or intrinsic variability in the target's luminosity. To distinguish between these two possibilities, the errors in  $m_d$  must be accurately measured and all comparison stars must be checked for variability (*i.e.* looking at the standard deviation of their light curves).

Assuming the reference stars have been well selected, the standard deviations of their non-variable differential light curves can be used to

## 6.5. Error Estimation

---

make an empirical estimate of the total photometric error for the target for a certain magnitude. This models the expected uncertainty in the target’s magnitude due to noise alone; something which would otherwise be difficult to do for a target exhibiting intrinsic variability. Another advantage of this approach is that it makes an estimate of both the formal and “informal” errors; the former being due to effects such as Poissonian noise in the target and the latter being dominated by imperfect flat-fielding.

The photometric uncertainties associated with each of the reference stars’ light curves was found using the method outlined in Lane *et al.* (2007), plotting the formal photometric error for the reference stars,  $\sigma_{iraf}$ , against the standard deviation of their light curve,  $\sigma_{rms}$ . The formal photometric error ( $\sigma_{iraf}$ ) is an average of the error on the instrumental magnitude calculated by IRAF after performing aperture photometry. A first-order polynomial is then fitted to this plot. The free parameters of this fit ( $a$  and  $b$ ) are used to find  $\delta m_i$ , the uncertainty in the light curve for the  $i$ th reference star, by

$$\delta m_i = a + b\sigma_{iraf} \quad (6.5)$$

The error in the relative magnitude,  $\delta m_{rel}$ , is found by combining the error in the magnitude of the target ( $\delta m_t$ ) and the error in the magnitude of the reference stars ( $\delta m_i$ ,  $i = 1 \dots N$ ) as follows

$$(\delta m_{rel})^2 = (\delta m_t)^2 + \left(\frac{1}{NF_c}\right)^2 \sum_i^N F_i^2 (\delta m_i)^2 \quad (6.6)$$

as outlined in Bailer-Jones & Mundt (2001).  $\delta m_t$  is found in a similar way to  $\delta m_i$  using Equation 6.5. One possible disadvantage of this method is that it relies on having two or more reference stars available so that a fit to the plot of  $\sigma_{iraf}$  against  $\sigma_{rms}$  can be found. However, at least two reference stars were usable in each dataset presented in this work.

## 6.6 Variability

Each light curve must be classified as variable or non-variable. To do this, the 99% confidence (*i.e.*  $2.576\sigma$ ) criterion employed in Jang & Miller (1997) and Romero *et al.* (1999) was adopted. For each light curve, the variability confidence level,  $C$ , is calculated as follows:

$$C = \frac{\sigma_{targ}}{\sigma_{comp}} \quad (6.7)$$

where  $\sigma_{targ}$  is the standard deviation of the differential light curve for the target (blazar) and  $\sigma_{comp}$  is the standard deviation for the differential light curve of a reference star. If  $C \geq 2.576$ , corresponding to a 99% confidence level, the target is said to be variable (Jang & Miller, 1997). In each case,  $\sigma_{comp}$  was calculated using the standard star which was the closest in magnitude to that of the blazar.

## 6.7 Results

After reducing the data and performing differential aperture photometry as outlined in the above sections, light curves were generated for the five targets of interest: Markarian 421, Markarian 501, H 1426+428, 1ES 1959+650 and 1ES 2344+514. The reference stars in each of these fields were analysed in a similar manner so that differential light curves were also obtained for them. Thus any large deviations in reference star light curves would be detected and these stars removed from the analysis. No account was made for light contributions from the host galaxy. All variations in the target blazar's light curves are, however, assumed to be due to variability of r'-band emission at the galactic core. This assumption is reasonable, as other studies have shown the galactic component of BL Lac optical emission to be steady (*e.g.* Nilsson *et al.*, 1999).

## 6.7. Results

---

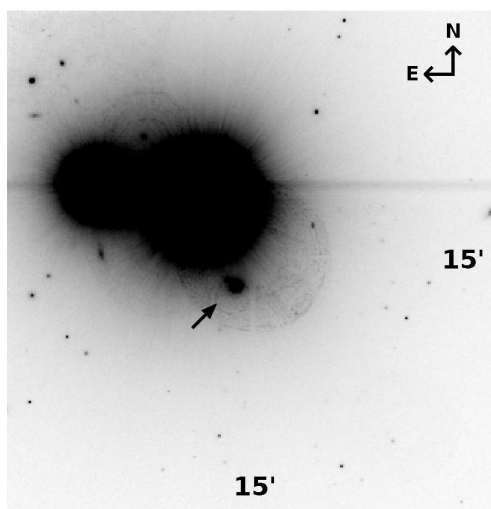


**Figure 6.3:** An image of Markarian 421 (centre, to the right and underneath the two bright stars) from the FLWO 1.2 m telescope taken on 16<sup>th</sup> March 2007. The image is an average of five 30-second exposures taken in succession and is typical of the images used for the photometry of Markarian 421 presented in this work.

### 6.7.1 Markarian 421

Optical photometry of Markarian 421 is complicated by the fact that it is located within the field-of-view of two optically-bright stars. The closer star (of the bright stars) to Markarian 421 is the largest: \*51 UMa. The second star in the system is HD 95976. Both of these objects are bright relative to Markarian 421. In astronomical images of this blazar, light from these two stars tends to bleed into the region of both Markarian 421 itself and the region of the standard reference stars in the field-of-view. Since seeing conditions change from night to night, the full width at half maximum of the stars varies, meaning the distance of the target from the light-containing region also varies. Careful selection of the aperture size is necessary to ensure that this effect does not cause variability in the blazar's light curve which is not intrinsic to the galactic core. However, the standard stars are displaced from these bright stars by a distance

## 6.7. Results

---

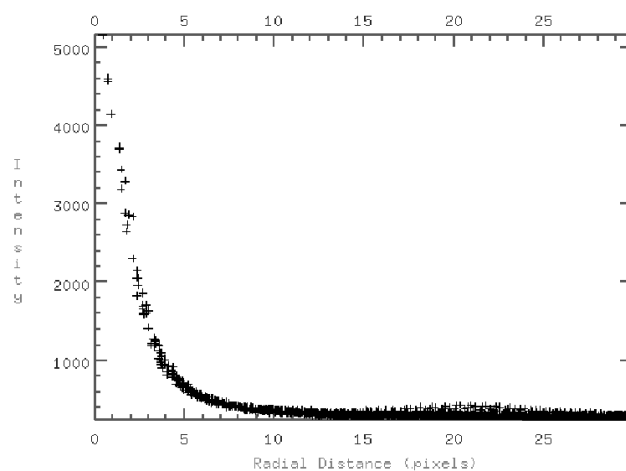


**Figure 6.4:** A radial profile of Markarian 421. The bump at a distance of  $\sim 22$  pixels (7.4 arcsec) distance from the centroid of the blazar is due to the companion galaxy U78. Further investigation showed that the influence of this companion was minimised at a radial distance of 14 pixels (4.7 arcsec). The x-axis is radial distance (in units of pixels) and the y-axis is intensity (in digital counts).

similar to the distance of the bright stars to Markarian 421 on each frame so that they are affected similarly. Since this is the case, the differential light curve for the standard stars should remain constant as the target's light curve varies.

Another complication in the field of Markarian 421 is the nearby companion galaxy U78 (B 1101+38 S). Figure 6.4 shows a radial profile of Markarian 421. A “bump” is clearly visible, peaking at a radial distance of around 22 pixels (7.4 arcsec) from the centroid of Markarian 421. Figure 6.5 shows a radial profile of the companion galaxy U78. It is clear from this plot that at radial distances greater than 8 pixels (2.7 arcsec) from the centroid of U78, light levels are dominated by contribution from Markarian 421. At radial distances less than 8 pixels from the centroid of U78, the light contribution is mainly from U78 itself. Since the centroid of U78 is known to be  $\sim 22$  pixels from that of Markarian 421, the minimum

## 6.7. Results

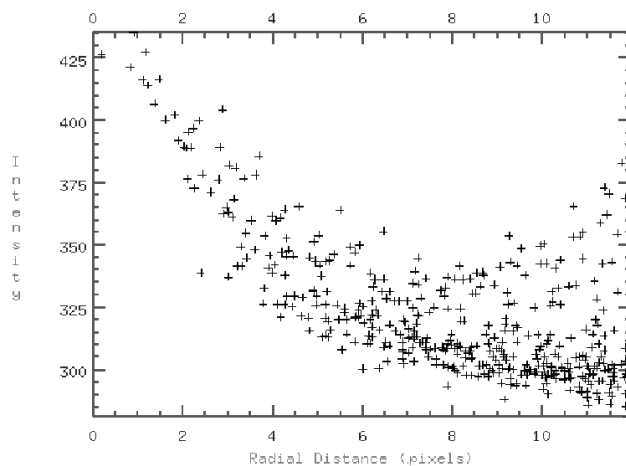


**Figure 6.5:** Radial profile of the galaxy U78 next to Markarian 421. The region in which the effect of light from U78 is minimised compared to that of Markarian 421 is at a radial distance of  $\sim 8$  pixels (2.7 arcsec) from the centroid of U78. The x-axis is radial distance (in units of pixels) and the y-axis is intensity (in digital counts).

in the composite profiles of Markarian 421 and U78 can be inferred to be at 14 pixels (4.7 arcsec) from the centroid of Markarian 421 (*i.e.* 22 - 8 pixels). This was therefore used as the optimum aperture radius when performing aperture photometry on Markarian 421. The annulus used to determine background was selected so that it did not contain a significant amount of light from U78. An inner radius of 25 pixels (8.5 arcsec) and a width of 5 pixels (1.7 arcsec) was used. These radii were selected as increasing the distance from the target centroid increases the area of the annulus, increasing the probability of contamination from other sources of light.

Although there are three standard reference stars shown (Villata *et al.*, 1998) in the finding chart for Markarian 421 (see Figure 6.6), only two of these were useable for this work. Reference star 3 could not be used due to its location in close proximity to the two bright, contaminating stars in the field of view.

## 6.7. Results

---

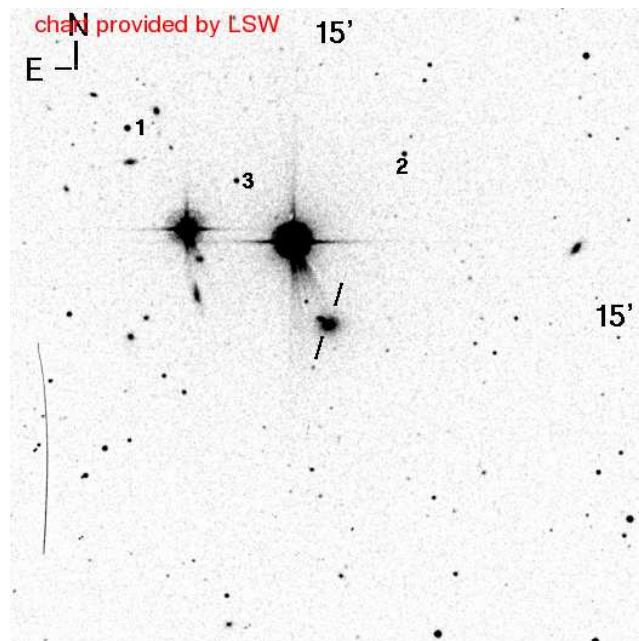


**Figure 6.6:** Finding chart for Markarian 421. Reference stars 1 and 2 were used here. Reference star 3 was unusable for this work due to its proximity to two bright stars. (Villata *et al.*, 1998).

## 6.7. Results

---

The differential light curves obtained for Markarian 421 and both reference stars are shown in Figure 6.7. The light curve of Markarian 421 has been shifted (by subtraction of the average differential magnitude of the light curve) so that it is seen to vary about 0 magnitudes. The reference star light curves were similarly shifted so that they were close to the target's light curve. The purpose for this was ease of reading. Both reference stars' light curves were plotted in this case. These were the only two reference stars used so variability in either light curve would cause variability to be exhibited in the target's light curve which is not intrinsic to the target. There are no significant variations in the light curve of either reference star.

Variability over  $\sim 0.45$  magnitudes makes Markarian 421 the most optically variable of the five blazars studied in this work. The confidence level of the variability was found to be  $C = 14.0$ , classifying it as variable. The uncertainties in the differential light curves were obtained using the method outlined in Section 6.5. While there were only two reference stars used and the validity of a straight-line fit could be questioned, the equation of the best-fit line was  $\sigma_{iraf} = 0.002 + 0.47\sigma_{rms}$ . Theoretically, the expected intercept for this type of plot should be zero. The intercept of the fit in this case was found to be very close to zero, indicating that the method was correct.

### 6.7.2 Markarian 501

Markarian 501 is located in a relatively uncrowded field. The nearest significant object to it is the galaxy B2 1652+39. This is located sufficiently far away ( $>30$  pixels radial distance from the centroid of Markarian 501) so that it did not affect the differential aperture photometry presented here.

There are 6 standard reference stars in the field-of-view (see Figure 6.9) at a range of distances from the target galaxy. Reference stars 1, 2, 3 and 4 (Villata *et al.*, 1998) were averaged to obtain the compar-

## 6.7. Results

---

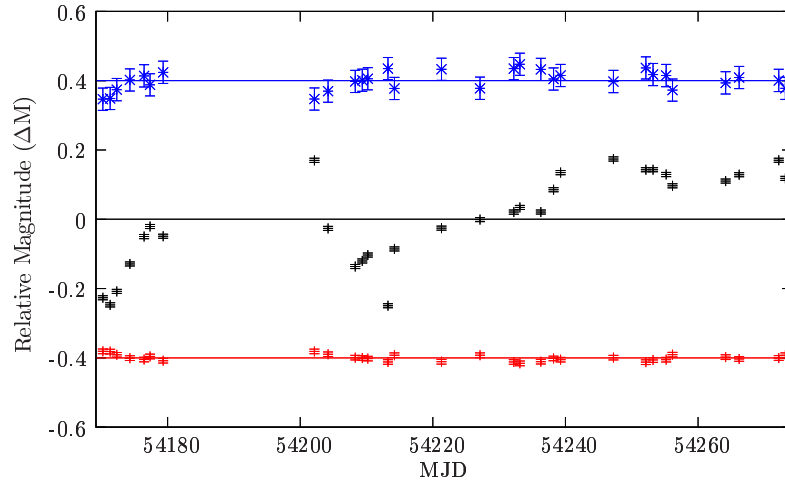


**Figure 6.7:** Differential aperture photometry light curves for Markarian 421 (black points). The straight line is the average magnitude which has been shifted to 0 so that variations are easy to read. The light curves obtained for reference stars 1 (red points) and 2 (blue points) are plotted to show they do not exhibit significant variability. The light curves of both reference stars have been shifted so that they are easily viewed on the same plot as the light curve of Markarian 421.

## 6.7. Results

---

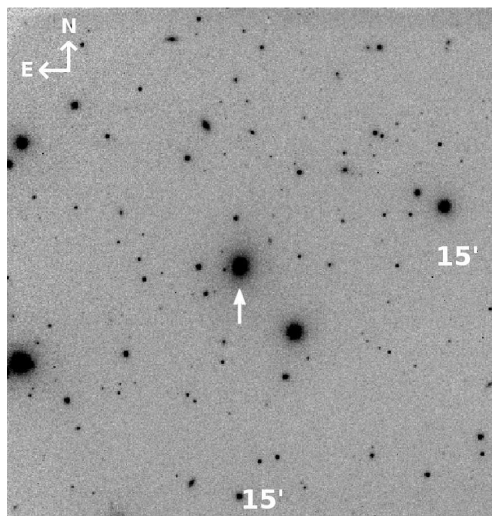


**Figure 6.8:** An image of Markarian 501 (large object near centre of image) from the FLWO 1.2 m telescope (taken on 29<sup>th</sup> April 2007). The image is an average of two 30-second exposures taken in succession and is typical of the images used for the photometry presented in this work.

ison flux used in the differential photometry. Reference stars 5 and 6 are of higher magnitude and were not stable (due to low signal-to-noise ratio) in all frames used for this purpose. A plot of  $\sigma_{iraf}$  against  $\sigma_{rms}$  for these four reference stars is shown in Figure 6.10 with the first-order polynomial fit matching the data points very well.

An aperture size of 15 pixels (5.1 arcsec) was chosen as it was  $\sim 4.5$  times the average full width half maximum of Markarian 501 over the entire data set. The background annulus was given an inner radius of 20 pixels (6.7 arcsec) from the centroid of the galaxy and 5 pixels width (1.7 arcsec). Each frame used was an average of two 30-second exposures.

The accuracy of this photometry method allows for the resolution of variability over a range of about 0.05 magnitudes in the differential light curve for Markarian 501 (see Figure 6.11). No significant variability was evident in the light curves of each of the reference stars used. The confidence level of variability is  $C = 5.4$  showing that the target is

## 6.7. Results

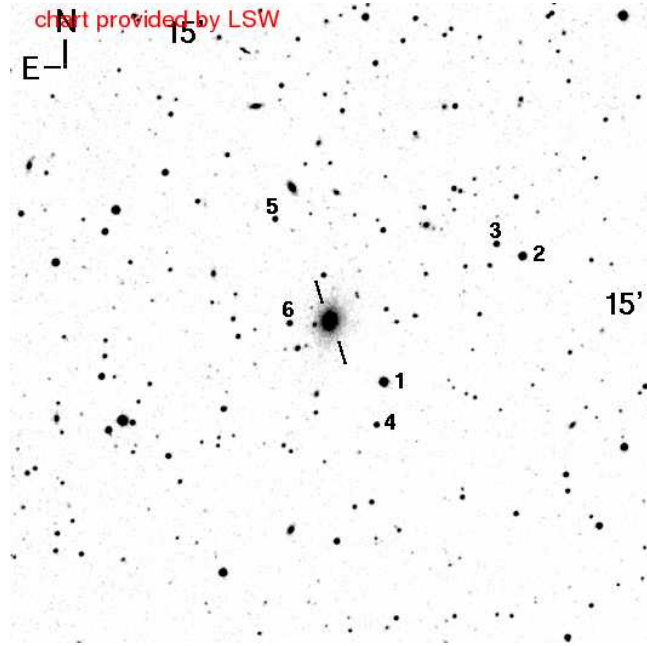


**Figure 6.9:** Finding chart for Markarian 501. The flux of reference stars 1, 2, 3 and 4 were averaged to give the comparison flux used in differential aperture photometry. (Villata *et al.*, 1998).

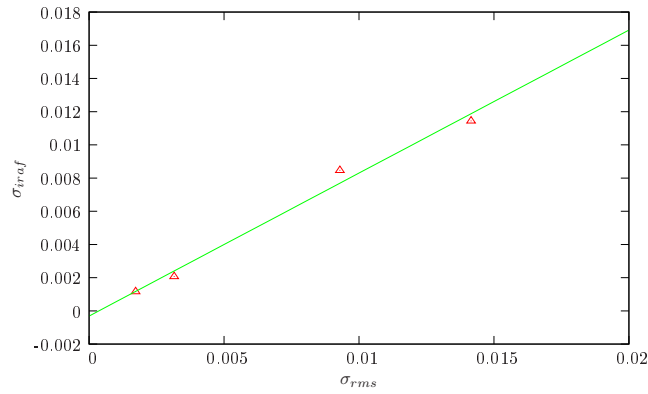


**Figure 6.10:** Plot of  $\sigma_{iraf}$  vs.  $\sigma_{rms}$ , used in the determination of errors in the differential photometry for Markarian 501. The first-order polynomial fit equation is  $\sigma_{iraf} = -0.0003 + 0.86\sigma_{rms}$ .

## 6.7. Results

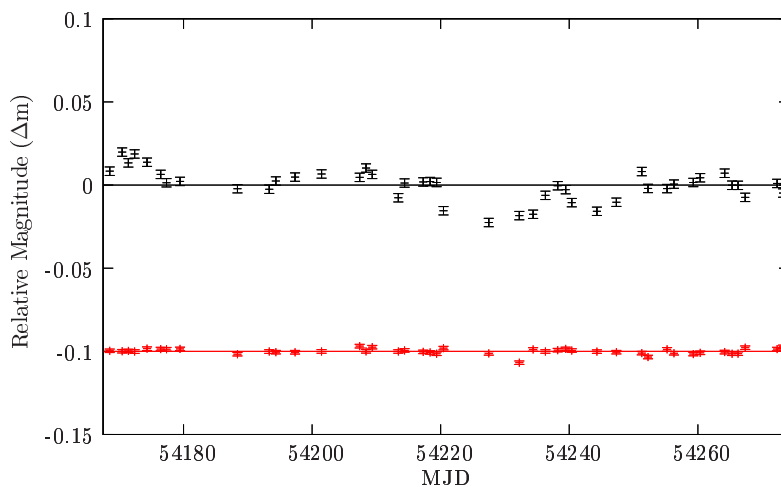


**Figure 6.11:** Differential aperture photometry light curves for Markarian 501 (black points). The straight line is the average magnitude which has been shifted to 0 so that variations are easy to read. The red points are the differential light curve for reference star 1.

variable.

### 6.7.3 H 1426+428

H 1426+428 is optically dim ( $\sim 16.5$  magnitude in  $r'$ -band) and is located in a sparse field. The exposures used in the photometry presented here were averages of two 2-minute exposures. The relatively deep exposures (compared to the other blazars included in the programme) were necessary to ensure a high signal-to-noise ratio in both the target galaxy and the reference stars.

Five of the reference stars (stars 1 - 4 and D in Figure 6.12) are located in close proximity to the blazar (Smith *et al.*, 1991). The three remaining reference stars (A, B and C in Figure 6.12) are displaced from the blazar by a larger distance. Reference stars A and C were partially or wholly located outside the image in a number of the frames and could not be used. Thus, the comparison flux (and magnitude) was found by

## 6.7. Results

---

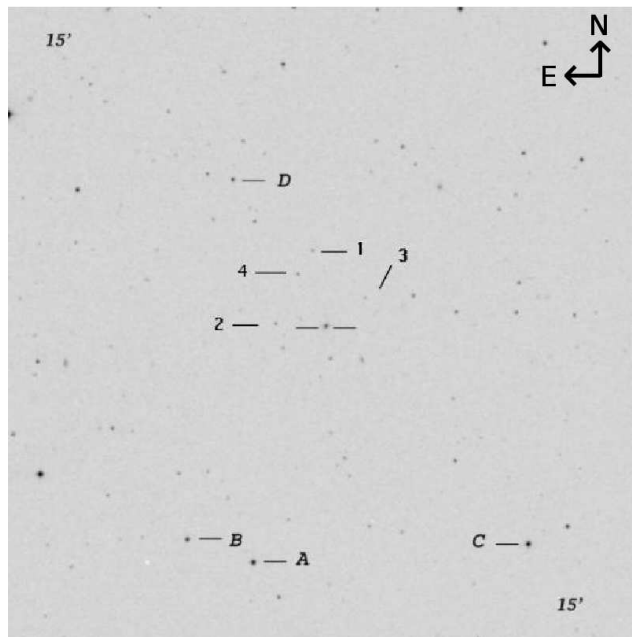


**Figure 6.12:** Finding chart for H 1426+428. Reference stars 1, 2, 3, 4 and B and D had their fluxes averaged to form the comparison flux used in the differential aperture photometry. Stars A and C were not fully contained on all frames. (Smith *et al.*, 1991).

## 6.7. Results

---

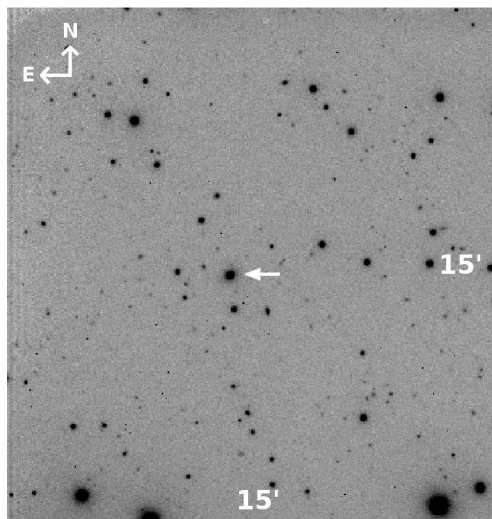


**Figure 6.13:** An image of H 1426+428 (bright object just left of centre) obtained at the FLWO 1.2 m telescope (taken on 18<sup>th</sup> April 2007). The image is an average of two 120-second exposures taken in succession and is typical of the images used for the photometry presented in this work.

averaging reference stars 1, 2, 3, 4, B and D. Although stars 1 - 4 were quite dim in a number of frames (due to atmospheric attenuation), their magnitude relative to the averaged reference flux remained steady.

As there were no significant nearby sources of contamination, an aperture radius of 15 pixels (5.1 arcsec, *i.e.*  $\sim 4.5$  times the average full-width half-maximum of the blazar's point spread function) was used for all photometry. An inner annulus radius of 20 pixels (6.7 arcsec) with an annulus width of 5 pixels (1.7 arcsec) was used to estimate the background. Figure 6.13 shows a typical nightly average frame. A plot of  $\sigma_{iraf}$  against  $\sigma_{rms}$  is shown in Figure 6.14, from which the uncertainties in the differential aperture photometry are calculated (see Section 6.5).

The differential aperture photometry light curve for H 1426+428 exhibits variability over 0.14 magnitudes (see Figure 6.15). The differential photometry errors are larger than those of the other blazars. This is due to the fact that H 1426+428 is a relatively dim object, as are most of

## 6.7. Results

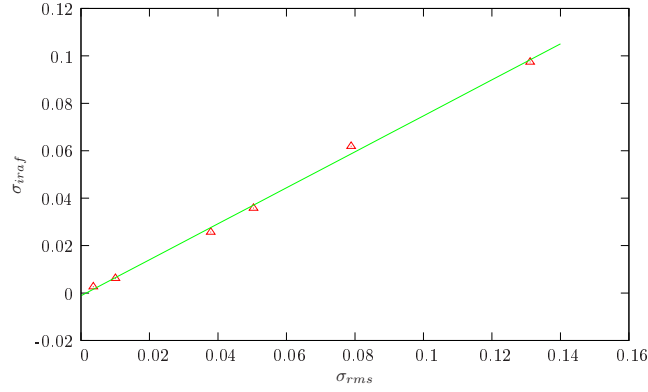


**Figure 6.14:** Plot of  $\sigma_{iraaf}$  vs.  $\sigma_{rms}$ , used in the determination of errors in the differential photometry for H 1426+428. The equation of the first-order polynomial fit is  $\sigma_{iraaf} = -0.001 + 0.76\sigma_{rms}$ .

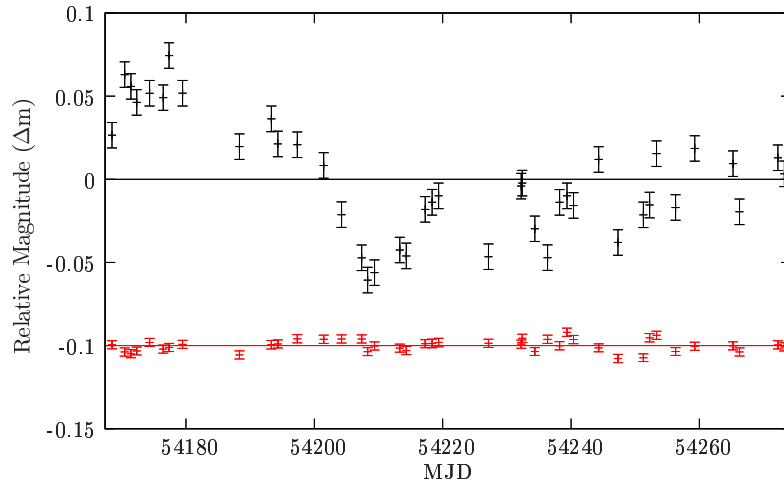


**Figure 6.15:** Differential aperture photometry light curves for H 1426+428 (black points). The straight line is the average magnitude which has been shifted to 0 so that variations are easy to read. The differential light curve for reference star B is also shown in the plot (red points).

## 6.7. Results

---

the standard stars. The signal-to-noise ratio for these objects is not as high as for those in the fields-of-view of the other blazars. Therefore, the uncertainties in the instrumental magnitudes calculated for the objects in each frame are relatively high. Variability is still significant (compared to the errors) however. The confidence level of variability is  $C = 3.5$ , so the source is classified as variable.

### 6.7.4 1ES 1959+650

Aperture photometry of 1ES 1959+650 was slightly complicated by the proximity of a bright star to the blazar. The radial plot in Figure 6.16 shows the centroid of the star at a radial distance of 16 pixels (5.4 arcsec) from the centroid of 1ES 1959+650. The star is visible to the upper right of the galaxy in Figure 6.17. As was the case with Markarian 421 (see Section 6.7.1), the aperture size was selected so that the effects of contamination from this star were minimised. An aperture size of 10 pixels (3.4 arcsec) was used. An annulus of 20-pixel (6.7 arcsec) inner radius and 5-pixel (1.7 arcsec) width was selected so that it did not include a significant amount of light from the star. Each nightly frame analysed was an average of two 60-second exposures.

Six of the seven reference stars in the field (see Figure 6.19) were averaged to find a comparison flux and magnitude (Villata *et al.*, 1998). One of the reference stars (star 5) was rejected as it was seen to exhibit unacceptable deviations across the data set. This reference star has exhibited variability in previous studies (Doroshenko *et al.*, 2007). The plot of  $\sigma_{iraf}$  against  $\sigma_{rms}$  for the six reference stars is shown in Figure 6.18 along with the associated first-order polynomial fit.

The  $r'$ -band variability exhibited by 1ES 1959+650 within the data set occurs over 0.2 magnitudes for most of the light curve (see Figure 6.20). The confidence level of variability is  $C = 10.4$ . There is an indication of relatively strong brightening towards the end of the light curve (*i.e.* a brightening of 0.2 magnitude above the average for the data within the

## 6.7. Results

---

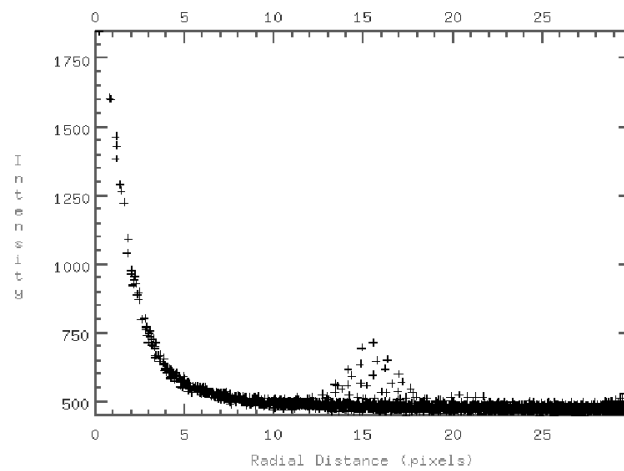


**Figure 6.16:** A radial profile of 1ES 1959+650. The star centred at a distance of 16 pixels (5.4 arcsec) from the centroid of 1ES 1959+650 is visible in the plot. Low-intensity points are found at a distance of  $\sim 16$  pixels also due to the fact that the plot is a radial profile and not a cross section. The aperture size used in the photometry of the galaxy was suitably selected to account for this possible source of contamination.

## 6.7. Results

---

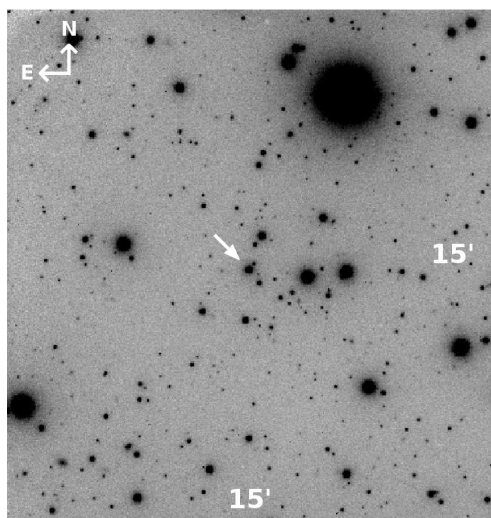


**Figure 6.17:** An image of 1ES 1959+650 (centre of image) obtained at the FLWO 1.2 m telescope on 29<sup>th</sup> April 2007. The image is an average of two 60-second exposures taken in succession and is typical of the images used for the photometry presented in this work.

final few days). The data are relatively sparse in this region of the plot however.

The uncertainties for each data point of the light curve are relatively small. This is due to the fact that the standard stars used and 1ES 1959+650 are relatively bright, increasing their signal-to-noise ratio.

### 6.7.5 1ES 2344+514

Only 3 standard stars were available in the field of 1ES 2344+514 (Fiorucci *et al.*, 1998). Of these, two were found to be steady enough for use (*i.e.* stars C1 and C2 in Figure 6.21). An aperture size of 15 pixels (5.1 arcsec) was used. A 5-pixel (1.7 arcsec) wide annulus with an inner radius of 20 pixels (6.7 arcsec) was used for background estimation.

Only 8 nights of data were obtained over the course of the campaign. Of these, only 7 were usable due to one of the nights being affected by bad

## 6.7. Results

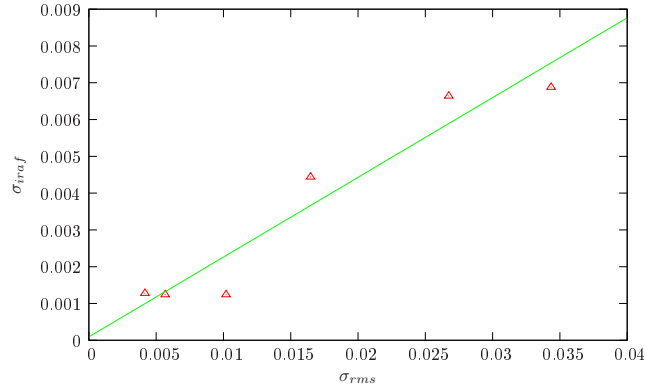


**Figure 6.18:** Plot of  $\sigma_{iras}$  vs.  $\sigma_{rms}$ , used in the determination of errors in the differential photometry for 1ES 1959+650. The equation of the first-order polynomial fit is  $\sigma_{iras} = 0.00009 + 0.22\sigma_{rms}$ .

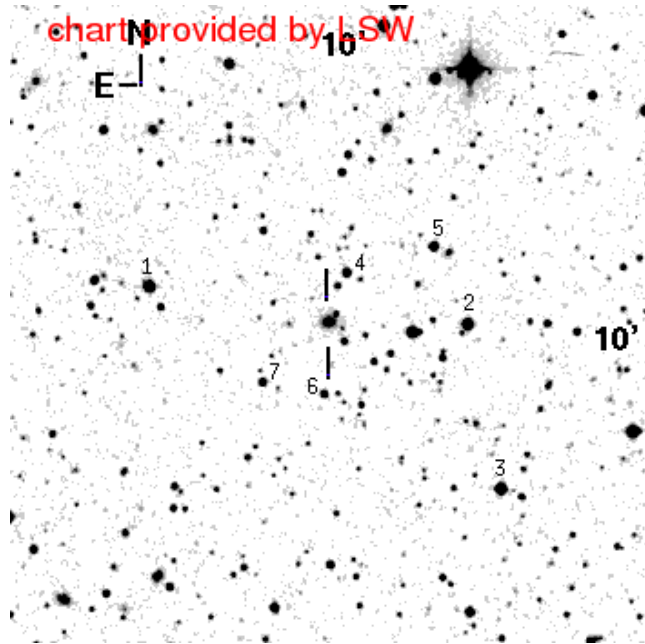


**Figure 6.19:** Finding chart for 1ES 1959+650. Reference stars 1, 2, 3, 4, 6 and 7 had their fluxes averaged to form the comparison flux used in the differential aperture photometry. (Villata *et al.*, 1998).

## 6.7. Results

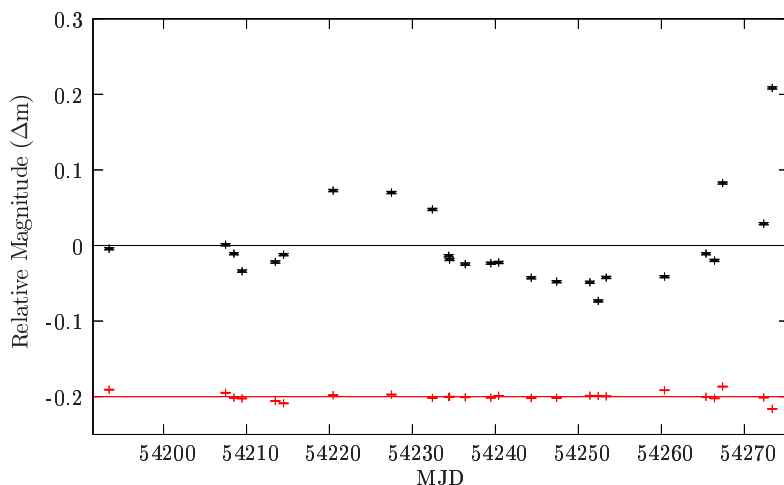


**Figure 6.20:** Plot of the differential light curve for 1ES 1959+650 (upper points), a straight line indicating the mean. The light curve has been shifted so that the average is zero. The differential light curve for reference star 1 (which was obtained in a similar manner) is shown also (lower points).

weather. Each night of data consisted of three 30-second exposures which were then combined to get an average. Photometry was then carried out on this master frame. An example of a typical frame used is shown in Figure 6.22

The photometry carried out followed the method outlined in Section 6.4. The light curve is shown in Figure 6.23. The sparse nature of the data set is quite obvious. However, variations  $>0.1$  magnitudes are apparent. As was the case with Markarian 421, only two reference stars could be used for the error analysis. The results using this method are credible however since the intercept is very close to zero ( $c \simeq 0.0005$ ), as one would expect for this type of plot.

Variations in brightness over 0.1 magnitudes are seen in the light curve. The variability confidence level is  $C = 4.1$ . The last two points on the light curve, separated by only 1 day, show a dimming of the source by around 50 millimagnitudes. This is regarded as fast optical variability

## 6.7. Results

---

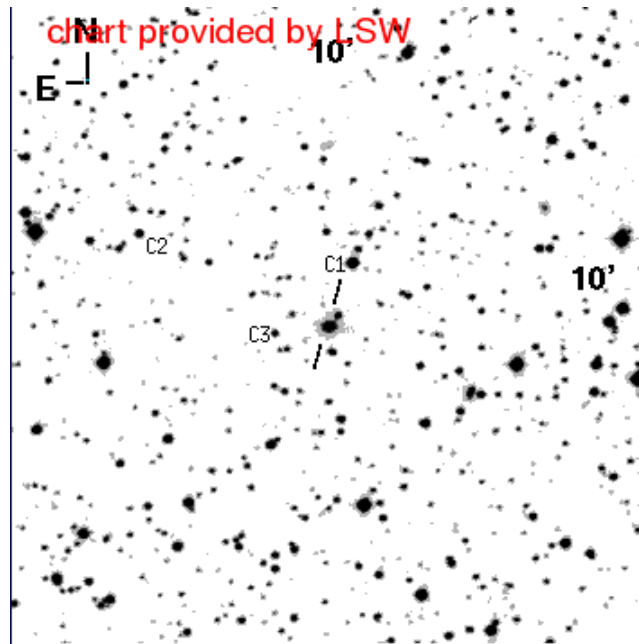


**Figure 6.21:** Finding chart for 1ES 2344+514. Reference stars C1 and C2 had their fluxes averaged in each frame to find a comparison flux used for all differential aperture photometry of the source. (Fiorucci *et al.*, 1998).

## 6.8. Photometric Normalisation

---

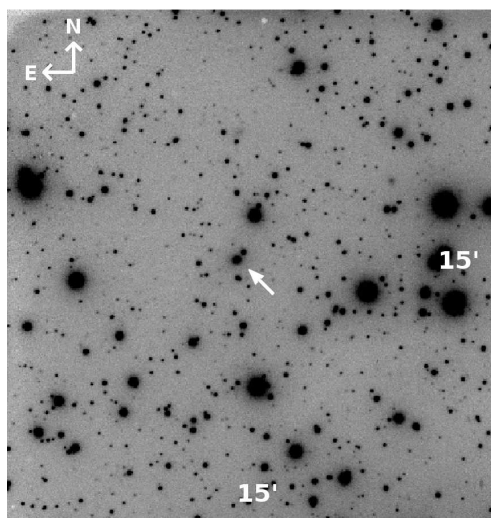


**Figure 6.22:** An image of 1ES 2344+514 (centre of image) obtained at the FLWO 1.2 m telescope on 30<sup>th</sup> May 2007. The image is an average of three 30-second exposures taken in succession and is typical of the images used for the photometry presented in this work.

for blazars.

## 6.8 Photometric Normalisation

The photometry discussed in the previous sections was pure differential photometry, with all light curves normalised so that they vary around 0 magnitude. A best-fit to the source magnitude is now found by comparing the differential magnitudes of multiple reference stars in the field to the known magnitudes of these reference stars.

To do this, the previously-calculated differential magnitude,  $m_d$ , was plotted against the real magnitudes (listed on the finding charts) for each of the standard stars used. An example of one of these plots is shown in Figure 6.24. The equation of the first-order fit to these data was then used to calculate the source magnitude for each point in its light curve.

The uncertainty associated with this method has two components:

## 6.8. Photometric Normalisation

---

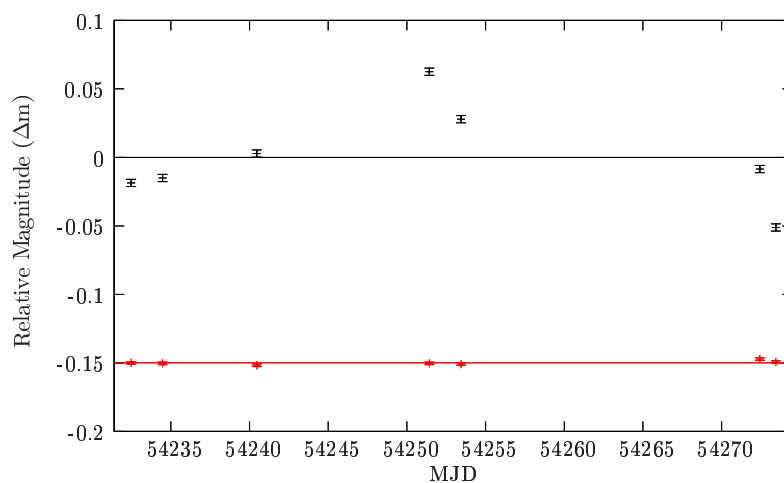


**Figure 6.23:** Plot of the differential light curve for 1ES 2344+514 (upper points), a straight line indicating the mean. The light curve has been shifted so that the average is zero. The differential light curve for reference star 1 (which was obtained in a similar manner) is shown also (lower points) as an indication that the photometry is consistent.

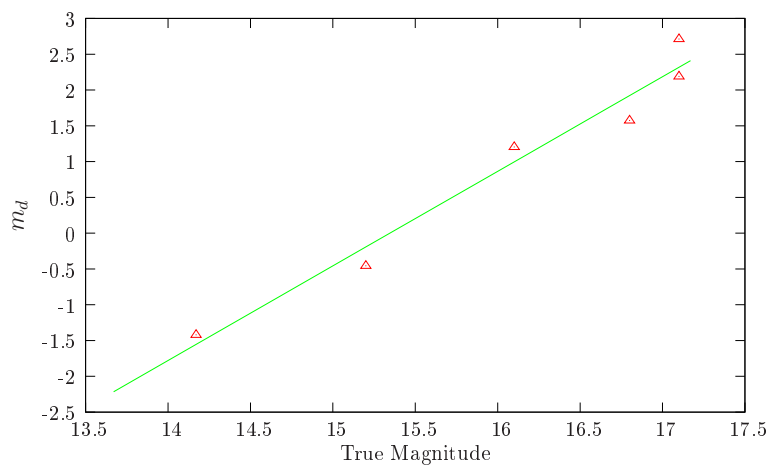


**Figure 6.24:** Plot of differential magnitude against actual magnitude, used to determine a best fit to the source magnitude.

## 6.8. Photometric Normalisation

---

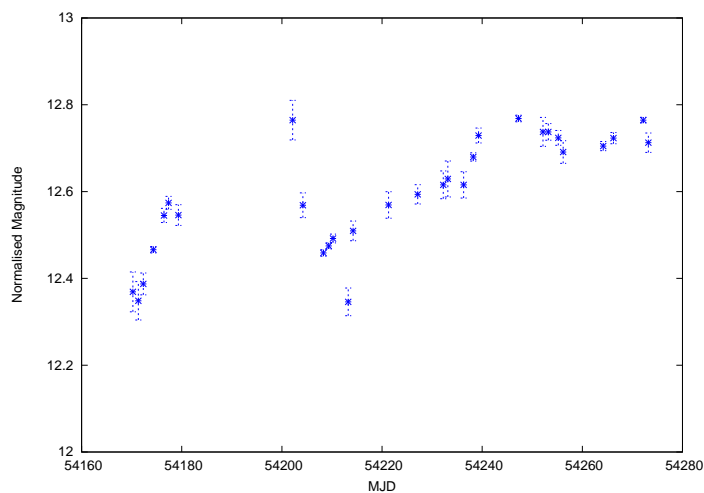


**Figure 6.25:** Light curve for Markarian 421 after differential magnitudes were normalised by a best fit to the source magnitude.

the error in the differential photometry and the uncertainty in the best fit. The uncertainty in the best fit was calculated by finding the scatter about the mean magnitude for each of the reference stars (*i.e.* the root-mean-square deviation on the reference star magnitude for each point in the light curve).

Figures 6.25 to 6.29 show the light curves of each of the five blazars monitored in this study after the best-fit magnitudes (and associated errors) have been calculated.

## 6.8. Photometric Normalisation

---

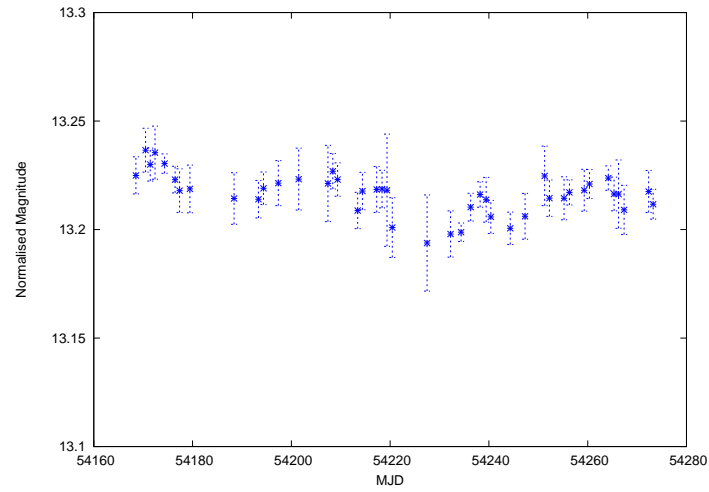


**Figure 6.26:** Light curve for Markarian 501 after differential magnitudes were normalised by a best fit to the source magnitude.

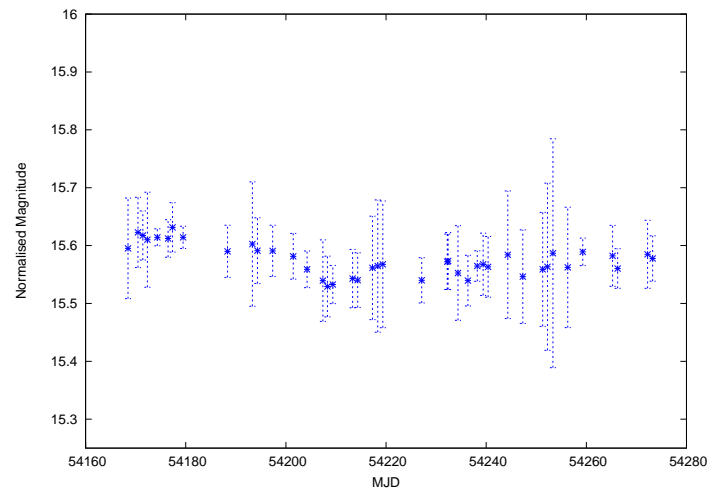


**Figure 6.27:** Light curve for H 1426+428 after differential magnitudes were normalised by a best fit to the source magnitude.

## 6.8. Photometric Normalisation

---

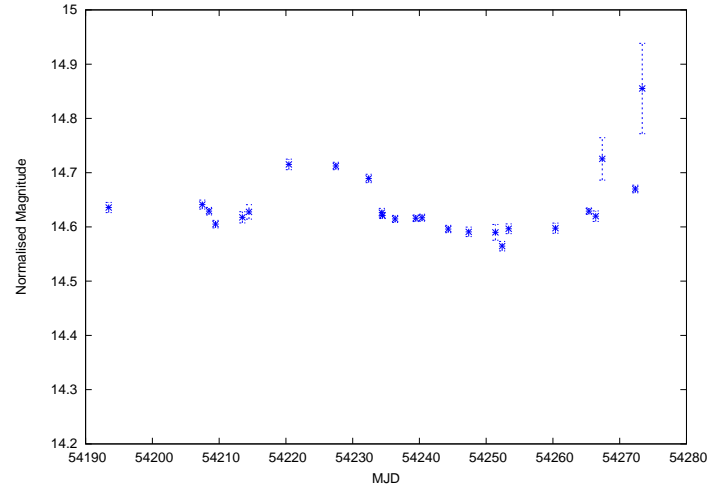


**Figure 6.28:** Light curve for 1ES 2344+514 after differential magnitudes were normalised by a best fit to the source magnitude.

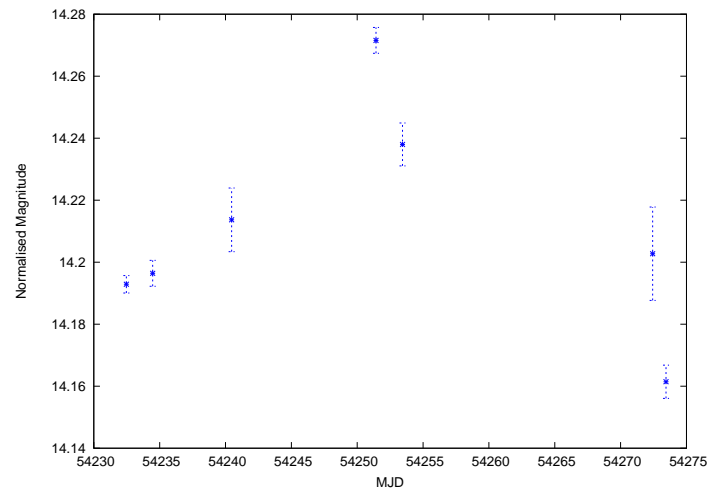


**Figure 6.29:** Light curve for 1ES 2344+514 after differential magnitudes were normalised by a best fit to the source magnitude.

## 6.8. Photometric Normalisation

---

# Chapter 7

## Variability & Correlation

The  $\gamma$ -ray light curves and the optical ( $r'$ -band) light curves, presented in Chapter 5 and Chapter 6 respectively, were examined in order to characterise their variability properties. A series of temporal analyses were carried out for the optical and  $\gamma$ -ray datasets of all five blazars, and correlations between emission in both energy bands was investigated for two of the sources. This thesis is concerned with the temporal characteristics of blazars in different energy bands. Therefore, spectral analysis has not been presented here.

This chapter outlines the temporal analysis of the light curves that are presented in Chapter 5 and Chapter 6. Hence, the terminology utilised throughout the chapter relates to time series analysis (*i.e.* “power” relates to the power of a signal in the frequency domain, as opposed to the spectral output power of the source).

The types of variability expected in blazar time series and their characteristics are outlined in Section 7.1. The long-term variability amplitudes and short-term variability amplitudes are examined in Section 7.2. The structure function, used to find the characteristic timescales of variability in the light curves, is presented in Section 7.3. Finally, the results of a correlation study to look for possible correlations between the optical data and  $\gamma$ -ray data are reported in Section 7.4.

### 7.1 Power Spectral Density Characteristics

The power spectral density (PSD) of a time-varying signal,  $x(t)$ , describes how the power of the signal is distributed among the constituent frequencies that comprise the signal. This distribution can be obtained by taking the Fourier transform of the signal. The characteristic statistical properties (*i.e.* the “colour”) of a signal can be distinguished by use of the PSD.

Although the PSD is a powerful and useful tool for characterising variability, it is not always possible to calculate it accurately. Calculation of the PSD requires that the Fourier Transform of the light curve be obtained. If the sampling of the light curve is sparse or uneven, the distorting effects of the windowing function (*i.e.* gain function by which the signal is multiplied before performing the Fourier Transform of a discretely sampled signal) can cause distortion in the Fourier transform. It then becomes impossible to discern structure in the light curve. Astronomical light curves are often both sparsely and unevenly sampled. In these cases, different statistical tools which are not as susceptible to sampling shortfalls, such as the structure function, may be employed to obtain information about the light curve which the PSD would otherwise provide. These tools are discussed in other sections of this chapter.

Some of the types of signal variation, characterised by differences in their power spectral densities, emphasising those processes which are pertinent to this thesis, are discussed in the following sections.

#### White Noise Processes

If all bands of a signal’s frequency bandwidth have the same power, the signal is considered to have white noise variability. This essentially means that the PSD is flat (*i.e.* has zero slope) across the measured Fourier frequency range (see Figure 7.1). White noise processes exhibit similar variations on long and short timescales. In the case of AGN emis-

## 7.1. Power Spectral Density Characteristics

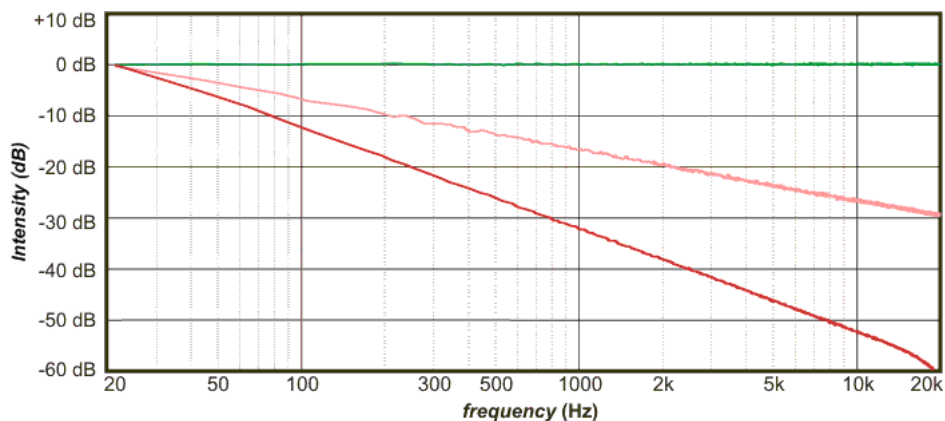


**Figure 7.1:** Examples of power spectral densities for white noise (green curve), pink noise (pink curve) and red noise (red curve) time-varying signals. The graph shows a plot of the intensity of signals plotted against frequency. (Credit: [www.doctoraudio.com](http://www.doctoraudio.com))

sion, white noise variability would suggest that emission is dominated by thermal emission of the accretion disk.

### Pink Noise Processes

Pink noise processes are processes for which the Fourier power is proportional to  $\frac{1}{f^\alpha}$ , where  $f$  is the Fourier frequency and  $0 < \alpha < 2$ . The PSD, therefore, has a negative slope, decreasing as the frequency increases. Pink noise with  $\alpha = 1$  is referred to as “flicker” (see Figure 7.1).

### Red Noise Processes

Red noise variability is also called  $1/f^2$  variability or Brown variability (Brownian motion is a “red noise” process). The variability is random, but each sample in the signal,  $x(t_i)$ , has a loose dependence on the value of the preceding sampled point,  $x(t_{i-1})$ . Most of the signal power is therefore concentrated in the lower frequencies of the Fourier transform and this power drops off quickly with increasing frequency (see Figure 7.1).

## 7.2. Variability Studies

---

For red noise processes, long timescale variability exceeds short timescale variability. Blazars are observed to exhibit red-noise (or pink-noise) variability at most wavelengths, suggesting that the emission is dominated by the jet which is fed by accretion of matter onto the central black hole.

## 7.2 Variability Studies

A number of statistical tools were used to quantitatively examine the variability of the  $\gamma$ -ray and optical r'-band light curves of all five blazars included in the multiwavelength campaign. The bulk variability over the course of the campaign was quantified by use of the fractional root-mean-square (RMS) variability amplitude. Shorter-term variability characteristics were examined using the fractional RMS point-to-point variability.

### 7.2.1 Fractional RMS Variability Amplitude

Fractional RMS variability amplitude,  $F_{var}$ , is a commonly-used (*e.g.* Edelson *et al.*, 1990, 2002) measure of the intrinsic amplitude of the variability of a time series which also allows for the effects of measurement noise of the time series. For a signal sampled at  $N$  discrete points (*i.e.*  $x_i$  for  $i = 1..N$ ),  $F_{var}$  is defined as

$$F_{var} = \frac{\sqrt{S^2 - \overline{\sigma_e^2}}}{\bar{x}} \quad (7.1)$$

where  $\bar{x}$  is the arithmetic mean of the flux values,  $x_i$ .  $S^2$  is the variance of the time series, defined by

$$S^2 = \frac{1}{N-1} \sum_{i=1}^N (x_i - \bar{x})^2 \quad (7.2)$$

and  $\overline{\sigma_e^2}$  is the mean square of the  $x_i$  measurement errors ( $\sigma_i$  for  $i = 1..N$ ), defined by

## 7.2. Variability Studies

---

$$\overline{\sigma_e^2} = \frac{1}{N} \sum_{i=1}^N \sigma_i^2 \quad (7.3)$$

A complete discussion of a conservative determination of the uncertainty in  $F_{var}$  is presented in Vaughan *et al.* (2003). The uncertainty in  $F_{var}$ ,  $\Delta F_{var}$ , is given by

$$\Delta F_{var} = \sqrt{\left( \sqrt{\frac{1}{2N}} \frac{\overline{\sigma_e^2}}{F_{var} \bar{x}^2} \right)^2 + \left( \frac{1}{\bar{x}} \sqrt{\frac{\overline{\sigma_e^2}}{N}} \right)^2} \quad (7.4)$$

$F_{var}$  is dimensionless and represents the variability amplitude normalised by the average flux of the source. It is used to compare the variability of sources of different luminosities, measuring the integrated variability amplitude for a given time series (Zhang *et al.*, 2005). In this regard, it measures the variability power of the total light curve (*i.e.* longterm variability) (Edelson *et al.*, 2002).

In cases where the mean-square measurement error exceeds the variance of the light curve, the square-root term in Equation 7.1 becomes imaginary. Thus, the value of  $F_{var}$  is not defined in these cases since any variability which may be present is at a level that is lower than the instrument can reasonably discern.

### 7.2.2 Point-to-point Fractional RMS Variability Amplitude

AGN tend to have steep “red noise” power spectral densities (*e.g.* Zhang *et al.*, 2005, 2002; Kataoka *et al.*, 2001), exhibiting large amounts of variability on long timescales. Therefore,  $F_{var}$  will be dominated by the variations on the longest timescales in the time series (Markowitz & Edelson, 2001). A parameter which is related to the  $F_{var}$  parameter – the point-to-point fractional RMS variability amplitude,  $F_{pp}$  – is instead used to characterise the short-term variability of the time series (Edelson

## 7.2. Variability Studies

---

*et al.*, 2002). It is defined as follows:

$$F_{pp} = \frac{1}{\bar{x}} \sqrt{\frac{1}{2(N-1)} \sum_{i=1}^{N-1} (x_{i+1} - x_i)^2 - \overline{\sigma_e^2}} \quad (7.5)$$

where  $\bar{x}$ ,  $N$  and  $\overline{\sigma_e^2}$  are defined in the same way as they were for equations 7.1, 7.3 and 7.2. The uncertainty in  $F_{pp}$  is given in the same way as it was for  $F_{var}$  (*i.e.* Equation 7.4). In calculating  $F_{pp}$ , differences in the gap times throughout the time series are not considered. For very unevenly sampled or small data sets this may lead to unrealistically high values of  $F_{pp}$ . However, the size and sampling of the data sets presented in this thesis (except the  $r'$  data set for 1ES 2344+514) are sufficient to obtain reasonable values.

If the measurement errors are greater than the variance of the light curve, then the square-root term in Equation 7.5 becomes imaginary and  $F_{pp}$  becomes meaningless. When this occurs,  $F_{pp}$  is classed as “undefined” (Edelson *et al.*, 2002). Physically, this means that the short term variability, if present, is at a smaller level than the instrument can discern within its sensitivity.

### 7.2.3 Results

The ratio of  $F_{var}$  to  $F_{pp}$  may be used to characterise the type of variability present in a time series. The larger the ratio, the steeper the slope of the power spectral density (Zhang *et al.*, 2005). Table 7.1 shows the  $F_{var}$  and  $F_{pp}$  values obtained for the  $\gamma$ -ray and optical  $r'$ -band data in the 2006-07 observing season with their associated uncertainties and the ratio of  $F_{var}$  to  $F_{pp}$  in each case. For white noise variability, the values  $F_{var}$  and  $F_{pp}$  should be similar as the variations on long and short timescales should be comparable. For red noise,  $F_{var}$  will be larger than  $F_{pp}$  since variations will predominantly be on longer timescales.

The  $r'$ -band light curve for Markarian 421 exhibited a fractional RMS

	<u>Optical</u>			<u><math>\gamma</math>-ray</u>		
	$F_{var} \pm \Delta F_{var}$	$F_{pp} \pm \Delta F_{pp}$	$\frac{F_{var}}{F_{pp}}$	$F_{var} \pm \Delta F_{var}$	$F_{pp} \pm \Delta F_{pp}$	$\frac{F_{var}}{F_{pp}}$
<b>Markarian 421</b>	$0.1260 \pm 0.00003$	$0.0530 \pm 0.00007$	2.38	$0.619 \pm 0.031$	$0.280 \pm 0.068$	2.21
<b>Markarian 501</b>	$0.0080 \pm 0.00007$	$0.0039 \pm 0.00015$	2.05	$0.951 \pm 0.664$	$0.678 \pm 0.174$	1.40
<b>1ES 1959+650</b>	$0.0516 \pm 0.00001$	$0.0307 \pm 0.00001$	1.68	0	0	—
<b>1ES 2344+514</b>	$0.0330 \pm 0.00001$	$0.0237 \pm 0.00001$	1.39	0	0	—
<b>H 1426+428</b>	$0.0315 \pm 0.00017$	$0.0133 \pm 0.00041$	2.37	0	0	—

**Table 7.1:** Table of  $F_{var}$  and  $F_{pp}$  values for each blazar. Values are given as 0 in cases where the mean-square measurement error exceeds the variance of the light curve. In these cases, variability (if present) is at a level so small that it cannot be discerned by the instrument within its sensitivity.

## 7.2. Variability Studies

---

variability amplitude,  $F_{var}$ , of nearly 0.13. The measured flux for Markarian 421 also contained a contribution from the host galaxy. The host galaxy contribution has been previously estimated to be  $\sim 15\%$  of the overall optical flux of Markarian 421 (Nilsson *et al.*, 1999). Thus,  $F_{var}$  should be 15% greater than quoted above, as the host galaxy only contributes to the mean flux and not the variability (see Equation 7.1). This level of variability is slightly lower than, but still consistent with, previous  $r'$ -band observations of Markarian 421. For instance, Błażejowski *et al.* (2005) found  $r'$ -band variability of  $F_{var} = 0.16$  during 2003 and 2004.

The equivalent measure of the variability at  $\gamma$ -ray energies shows Markarian 421 was much more variable in this energy regime with  $F_{var} = 0.62$ . This, again, is consistent with previous observations (Błażejowski *et al.*, 2005). In the case of both optical and  $\gamma$ -ray light curves, the ratio of  $F_{var}$  to  $F_{pp}$  is greater than 2, suggesting there is “red noise” variability in both data sets (Zhang *et al.*, 2005).

Błażejowski *et al.* (2005) presented optical and  $\gamma$ -ray values of  $F_{var}$  for Markarian 421 observations in the 2003-04 observing season. Similar to the work presented here, the data were grouped in one-day bins and no host galaxy contribution was subtracted from the optical data set. The value of  $0.62 \pm 0.03$  for the 2006-07 season for the  $\gamma$ -ray data agrees with the 2003-04 value (*i.e.* 0.61). The optical ( $r'$ -band)  $F_{var}$  presented in Błażejowski *et al.* (2005) was 0.16 which is  $\sim 30\%$  higher than the value obtained from the 2007 data. However, the 2007 value is consistent with  $r'$ -band observations taken during the 2005-06 season, which found  $F_{var} = 0.13$  (Horan *et al.*, 2009).

Markarian 501 does not exhibit as much fractional variability as was exhibited by Markarian 421. Looking at the  $r'$ -band data, the fractional RMS variability amplitude is less than 0.01. However, over 90% of the mean flux for Markarian 501 is due to the host galaxy (Nilsson *et al.*, 1999). The host galaxy only contributes to the mean flux level and not

## 7.2. Variability Studies

---

the variability, so the real variability amplitude is much larger. The ratio of  $F_{var}$  to  $F_{pp}$  is 2, so “red noise” variability is evident.

At  $\gamma$ -ray energies, Markarian 501 has a much higher value of  $F_{var}$  at around 0.95. This is due to the fact that a relatively low mean flux was detected while there were large variations throughout the campaign. Observations have previously shown that Markarian 501 exhibits more variability in higher energy bands (x-ray and  $\gamma$ -ray) than in lower energy bands (optical and radio). Albert *et al.* (2007f) observed maximum  $F_{var}$  values between  $\sim 0.6$  and  $\sim 1.2$  at TeV energies, which were in excess of maximum observed variability values at x-ray energies (Gliozzi *et al.*, 2006).

In the absence of statistically significant detections of 1ES 1959+650, 1ES 2344+514 or H 1426+428 at  $\gamma$ -ray energies, nothing definitive can be said about their variability properties in the TeV waveband over the course of this campaign. The ratios of the r'-band  $F_{var}$  to  $F_{pp}$  for 1ES 1959+650 and H 1426+428 both suggest “red noise” variability processes (*i.e.* ratio  $\sim 2$ ), as has been observed in previous blazar observations. For 1ES 2344+514, the ratio is closer to 1, which would suggest “white noise” variability. It must be noted, however, that the 1ES 2344+514 data set is very small (only 7 nights). There are large time gaps between the few points comprising the data set. As such, the fractional point-to-point variability amplitude may be abnormally high due to (possible) intrinsically slow variations only being sparsely sampled, giving high variations on a point-to-point basis.

Markarian 421 and Markarian 501 both exhibit larger fractional variability in higher energy bands over the course of this campaign (*i.e.* optical variability is lower than that observed at  $\gamma$ -ray energies in both cases). This is consistent with previous observations which have shown optical and radio bands exhibiting lower variability than x-ray and  $\gamma$ -ray bands (*e.g.* Błażejowski *et al.*, 2005). Fossati *et al.* (2000) showed that a similar effect could be seen when comparing x-ray variability with  $\gamma$ -ray

### 7.3. The Structure Function

---

variability (*i.e.* higher  $F_{var}$  in the  $\gamma$ -ray band).

## 7.3 The Structure Function

In the examination of time-varying signals, the characteristic timescales of variability may be studied by using the structure function (Rutman, 1978). This is a robust analysis tool which quantifies the mean differences in the fluxes of a time series as a function of the separation in the sampling interval,  $\tau$ . Calculation of the structure function does not require that the time series of interest be evenly or densely sampled. This makes it useful in astronomical applications where data sets are often unevenly and sparsely sampled. The information obtained from the structure function is similar to a power spectral analysis (see Section 7.1), but is better suited to the investigation of non-periodic processes (Hughes *et al.*, 1992).

The structure function was calculated for the optical light curves presented in Chapter 6 and the  $\gamma$ -ray light curves presented in Chapter 5. This analysis was carried out to look for characteristic timescales (*i.e.* flare rise/fall times) in each time series. The characteristic timescales of some of the light curves are later used to simulate light curves with similar temporal characteristics. The calculation of the structure function and the determination of characteristic rise times are discussed in the following sections.

### 7.3.1 Structure Function Calculation

Simonetti *et al.* (1985) introduced the structure function to examine the flicker present in radio light curves of a number of extragalactic sources. A structure function of order  $M$  removes polynomials of order  $M - 1$  from the time series. The result then depends only on any stationary random process (one whose mean and variance do not change over time) present in the time series and any remaining higher order trends. Therefore, the first-order structure function will remove any DC components in the time

### 7.3. The Structure Function

---

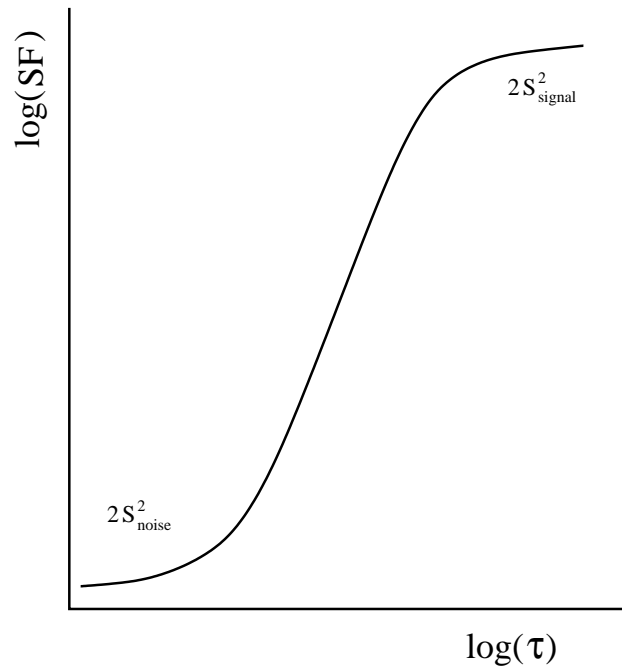


**Figure 7.2:** Schematic of an ideal structure function plotted on a log-log scale.  $S^2$  is the variance of the signal for which the structure function is being calculated. Adapted from Hughes *et al.* (1992).

### 7.3. The Structure Function

---

series. The normalised first-order structure function for a time series,  $x(t_i)$ , is defined as

$$SF^{(1)}(\tau) = \frac{1}{N(\tau)} \sum_{i=1}^N \left( \frac{[x(t_i + \tau) - x(t_i)]}{\bar{x}} \right)^2 \quad (7.6)$$

where  $\tau$  is the time lag,  $\bar{x}$  is the mean flux for the data set and  $N$  is the number of pairs of data points which are separated by  $\Delta t$  such that

$$\tau - \frac{\Delta\tau}{2} < \Delta t \leq \tau + \frac{\Delta\tau}{2} \quad (7.7)$$

where  $\Delta\tau$  is the width of the bin in which  $SF^{(1)}(\tau)$  has been calculated. The value of  $\Delta\tau$  was chosen such that all  $SF(\tau)$  values were obtained from more than 5 pairs of flux values. A detailed methodology for the construction of the structure function may be found in Spangler *et al.* (1989).

Hughes *et al.* (1992) discusses the shape of the first-order structure function and how it is related to the intrinsic properties of the data set. The structure function of a signal is related to the variance of the signal,  $S^2$ , and its autocorrelation function (*i.e.* cross correlation of a time series with itself),  $\rho(\tau)$ , by

$$SF^{(1)}(\tau) = 2S^2(1 - \rho(\tau)) \quad (7.8)$$

On short timescales, the measurement noise in the light curve has an autocorrelation (*i.e.*  $\rho(\tau)$  in Equation 7.8) close to zero, which leads to the lower plateau in the structure function plot at a level of around twice the variance of the noise. At timescales beyond the longest correlation timescale, the structure function value plateaus at twice the variance of the time series. The structure function is normally plotted against time lag,  $\tau$ , on a log-log graph. In practice, variation in the structure functions on the longest timescales (*i.e.* beyond and along the upper plateau) are not thought to be significant and are usually caused by the light curve

### 7.3. The Structure Function

---

containing a finite number of flares and uneven sampling of the time series. Figure 7.2 shows an ideal example of a structure function plot, with the short and long timescale plateaus shown.

The curve linking the two plateaus offers information about the intrinsic variation of the source. The occurrence of “breaks” from a straight-line curve (*i.e.* changes in slope, intermediate plateaus or dips) in the curve linking the  $2S_{noise}^2$  plateau and the  $2S_{signal}^2$  plateau indicate periodicities in flux variations. These periodicities are the characteristic timescales for the variability in the time series (*i.e.* flare rise time). The breaks occur because variations correlated on these timescales will cause  $x(t_i + \tau) - x(t_i)$  (from Equation 7.6) to be small. The structure function is thus closely related to the power spectral density of the time series (Section 7.1), since the power spectral density is equivalent to the Fourier transform of the autocorrelation (Hughes *et al.*, 1992).

Calculation of the structure function only requires that the light curve is discretely sampled. However, more accurate structure functions may be obtained from those light curves for which the sampling is dense and even. Those with few samples, or large gaps in the sampling, are subject to *windowing* effects whereby certain time lags (in the structure function) are not as well sampled as others due to a lack of pairs for that particular time lag. In calculating the structure function,  $\Delta\tau$  (the structure function bin width in Equation 7.7) is the “window” employed. The following sections present the structure functions ( $\gamma$ -ray and optical r'-band) for the five blazars studied and discuss any features apparent on visual inspection. Two-day bins (*i.e.*  $\Delta\tau = 2$  days) were used to calculate the structure function in all cases so that at least 5 pairs were used to calculate the value of each point in the plot. As it is often difficult to accurately discern real features in structure function curves by visual inspection, a more complete search for features is presented in subsequent sections.

### 7.3. The Structure Function

---

#### Markarian 421

Figure 7.3 shows the  $\gamma$ -ray and r'-band structure functions for Markarian 421. By visual inspection, there appears to be a break in the  $\gamma$ -ray structure function at  $\sim 5 - 8$  days.

The optical data are more evenly sampled than the  $\gamma$ -ray data, so the optical structure function is more clearly defined. There appears to be a prominent break at around 6 - 8 days. The break might indicate the “roll-over” of the  $2S_{signal}^2$  plateau (*i.e.* upper plateau in Figure 7.2) since no further obvious plateaus are apparent in the curve at larger lags.

A best-fit structure function was found for the optical light curve using Monte Carlo simulations of light curves with similar temporal characteristics to those of the real data set. This are discussed in more detail in Section 7.3.2.

#### Markarian 501

The normalised  $\gamma$ -ray structure function (shown in Figure 7.4) appears to exhibit the expected profile (positive slope) on visual inspection. Features suggesting characteristic timescales are not easy to discern by visual inspection, however, the curve seems to break at  $\sim 15 - 20$  days.

The optical structure function is well sampled and follows the expected profile for a structure function. There may be a break at 2 - 3 days, though this consists of only one data point. There is, however, more evidence for a less positive (or negative) slope in the curve at 3 - 4 days. This plateau may be evidence for a possible characteristic timescale, although it is not as definitive as features of the optical structure function for Markarian 421. In the case of Markarian 501, no prominent upper ( $2S_{signal}^2$ ) plateau is evident, suggesting that the longest timescale for the light curve is longer than the time covered by this data set ( $\sim 65$  days). The break at 3 - 4 days may be evidence of a shorter timescale, suggesting flicker or shot noise.

A best-fit for this structure function was found using Monte Carlo

### 7.3. The Structure Function

---

simulations of light curves (generated using similar temporal characteristics to the real light curve) as presented in Section 7.3.2.

#### **1ES 1959+650**

Both the  $\gamma$ -ray and optical light curves obtained for 1ES 1959+650 are relatively poorly and sparsely sampled. In particular, the  $\gamma$ -ray light curve has a large gap in the middle. More importantly, no  $\gamma$ -ray excess was detected in the light curve. This means that the structure function analysis will be dominated by the measurement error and should exhibit a flat profile (*i.e.* the  $2S_{noise}^2$  plateau in Figure 7.2).

Both structure functions generated (see Figure 7.5) are scattered and have large uncertainty in each data point due to relatively poor sampling of the light curve. The  $\gamma$ -ray structure function exhibits a flat profile, as expected. Determination of any characteristic timescale in the  $r'$ -band structure function is quite difficult.

#### **1ES 2344+514**

The optical data set for 1ES 2344+514 consisted of only 7 nights of  $r'$ -band data. As such, the structure function plot is poorly sampled (only 2 points). This makes determination of characteristic timescales from the structure function plot impossible.

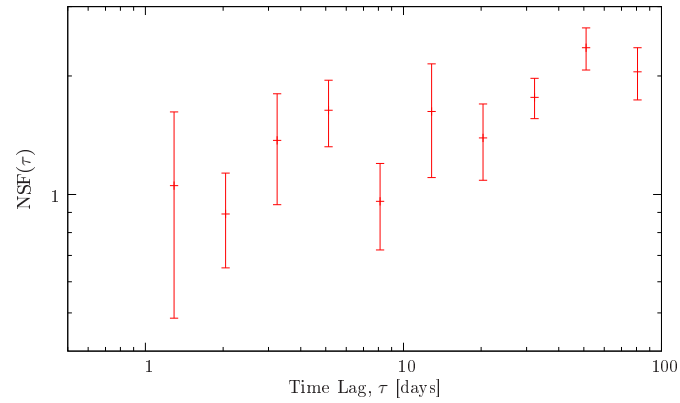
The  $\gamma$ -ray structure function (see Figure 7.6) is dominated by measurement noise. As such, a flat profile is to be expected. The structure function does not follow the expected rising profile (Figure 7.2). This is likely due to the fact that there was no significant  $\gamma$ -ray excess detected throughout the data set. As such, nothing definite can be said about a characteristic timescale for the data.

#### **H 1426+428**

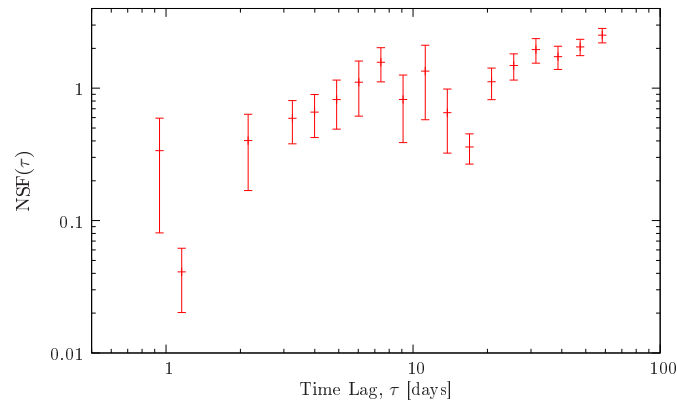
The flat nature of the  $\gamma$ -ray structure function (see Figure 7.7) would again suggest that the light curve for H 1426+428 is dominated by mea-

### 7.3. The Structure Function

---



(a)  $\gamma$ -ray

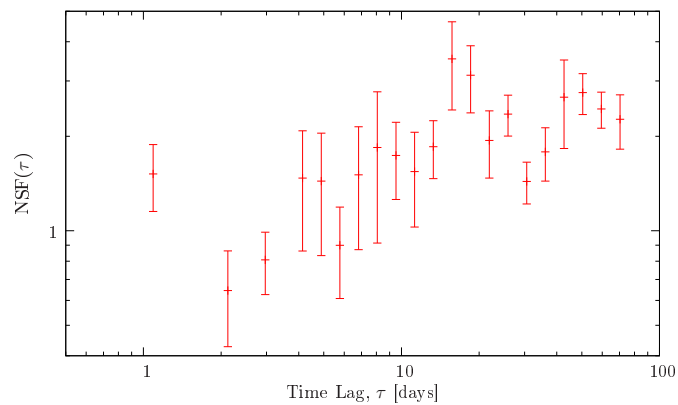


(b) Optical  $r'$ -band

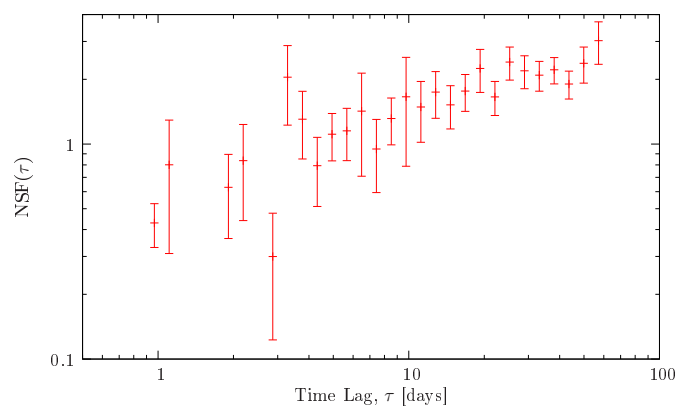
**Figure 7.3:** Plots of the structure function for Markarian 421. The top panel (a) is the normalised structure function for the  $\gamma$ -ray data and the bottom (b) is the normalised structure function for the optical  $r'$ -band data.

### 7.3. The Structure Function

---



(a)  $\gamma$ -ray

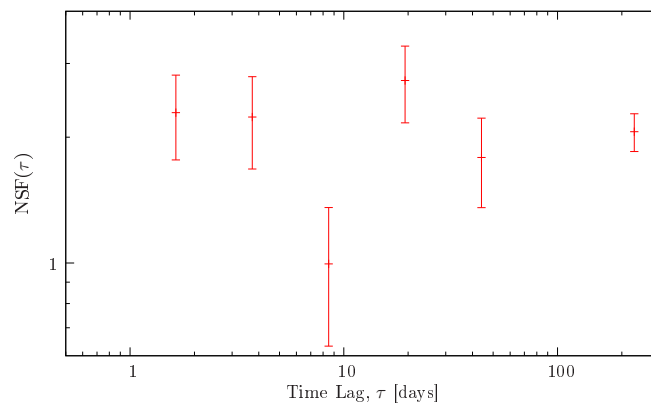


(b) Optical  $r'$ -band

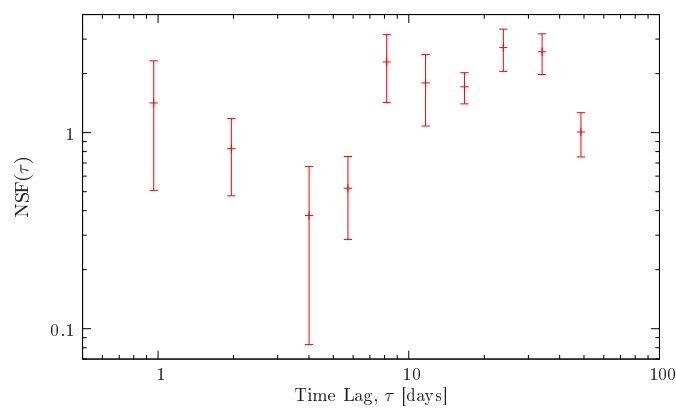
**Figure 7.4:** Plots of the structure function for Markarian 501. The top panel (a) is the normalised structure function for the  $\gamma$ -ray data and the bottom (b) is the normalised structure function for the optical  $r'$ -band data.

### 7.3. The Structure Function

---



(a)  $\gamma$ -ray



(b) Optical  $r'$ -band

**Figure 7.5:** Plots of the structure function for 1ES 1959+650. The top panel (a) is the normalised structure function for the  $\gamma$ -ray data and the bottom (b) is the normalised structure function for the optical  $r'$ -band data.

### 7.3. The Structure Function

---

surement error, hence the structure function only shows the flat  $2S_{noise}^2$  plateau.

The optical structure function, on the other hand, exhibits a typical shape (positive slope; see Figure 7.2), with a possible break in the curve at  $\sim 10 - 20$  days suggesting a corresponding characteristic timescale in the variability of this well-sampled light curve.

#### 7.3.2 Structure Function Simulation and Fitting

There is no definitive or objective way to quantify the position of features, such as changes in slope, in structure function analysis. Visual inspection of the curve may leave features open to interpretation. To overcome this, a reasonable model for the light curve may be assumed in order to simulate light curves<sup>1</sup> with similar properties.

A large number of simulated light curves were generated for a given characteristic timescale value. The structure function was calculated for each of these simulated light curves and the average structure function for that characteristic timescale was obtained. The average structure function was compared with the structure function of the real light curve. These steps were then repeated for a number of different values of characteristic timescale until the best-fit structure function was found.

The assumed model and the fitting methodology are described in the following sections.

#### Structure Function Modelling

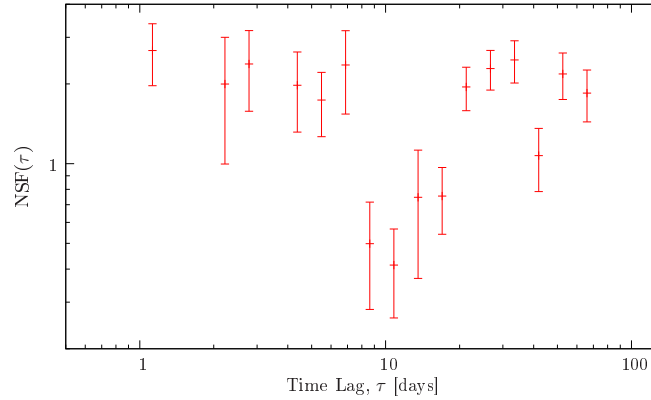
The variability in the light curve being modelled was assumed to be due to random processes (Zhang *et al.*, 2005). Therefore, the simulated light curve was comprised of a superposition of flares randomly separated in time. The frequency of flares was estimated by counting the number of up-down transitions ( $3\sigma$ -level) in the real light curves (for the 2006-07

---

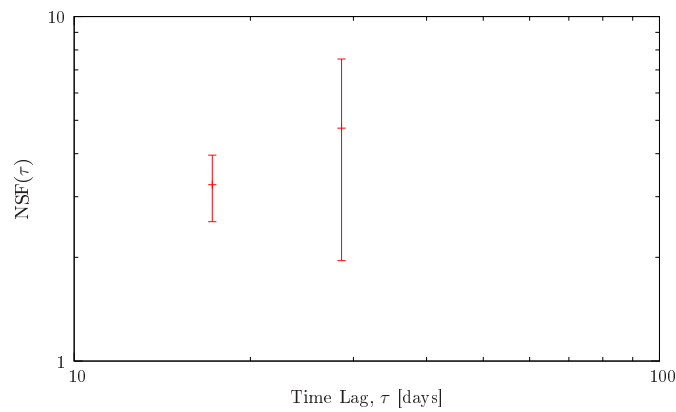
<sup>1</sup>Software to simulate light curves based on characteristics of real light curves was provided by Prof. J. H. Buckley, Washington University in St. Louis, MI, USA.

### 7.3. The Structure Function

---



(a)  $\gamma$ -ray

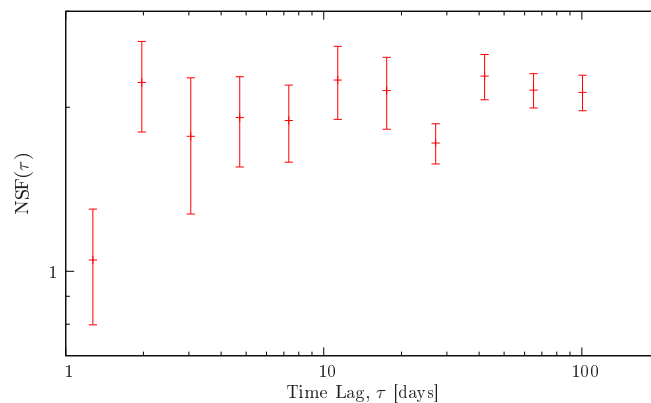


(b) Optical  $r'$ -band

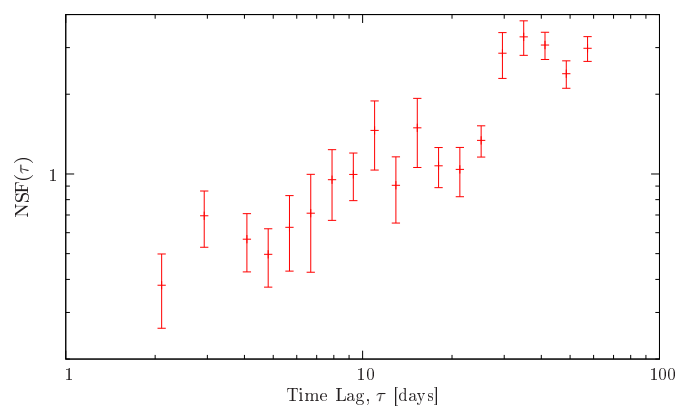
**Figure 7.6:** Plots of the structure function for 1ES 2344+514. The top panel (a) is the normalised structure function for the  $\gamma$ -ray data and the bottom (b) is the normalised structure function for the optical  $r'$ -band data.

### 7.3. The Structure Function

---



(a)  $\gamma$ -ray



(b) Optical  $r'$ -band

**Figure 7.7:** Plots of the structure function for H 1426+428. The top panel (a) is the normalised structure function for the  $\gamma$ -ray data and the bottom (b) is the normalised structure function for the optical  $r'$ -band data.

### 7.3. The Structure Function

---

observing season). Each simulated flare was given a triangular shape with equal rise time,  $t_{rise}$ , and fall time,  $t_{fall}$  (*i.e.*  $t_{rise} = t_{fall} =$  characteristic timescale). X-ray observations of Markarian 421 have previously shown this to be a reasonable assumption (Fossati *et al.*, 2008). Each flare,  $f(t)$ , centred at  $t_p$  was defined by

$$f(t) = \begin{cases} A(t - (t_p - t_{rise}))/t_{rise} & \text{for } (t_p - t_{rise}) < t \leq t_p \\ -A(t - (t_p + t_{fall}))/t_{fall} & \text{for } t_p < t \leq (t_p + t_{fall}) \end{cases} \quad (7.9)$$

where  $A$  is the amplitude of the flare. Each flare was given the same amplitude. Tanihata *et al.* (2001) used a power-law distribution of amplitudes, but this method was not followed here as it introduces extra free parameters and does not improve the fit. However, the flare amplitudes were allowed to “pile up” if they occurred at almost (or exactly) the same time, meaning the amplitudes of simultaneously occurring flares would be added. The simulated light curves were sampled at exactly the same time intervals as the corresponding real light curves.

The flux values for the simulated light curves were scaled so that they had the same mean and variance as the flux values for the real data set. Measurement error was added to the simulations by Gaussian deviates (Press *et al.*, 1992) so that it was at the same level as that of the real light curve. Finally, Gaussian fluctuations were added to the flux values in the simulated curve. Light curves created in this manner were used to find the best-fit structure function, thus determining the characteristic timescale of the real light curve.

#### Fitting Method

A large number of random light curves were generated using the procedure outlined above and a structure function was generated for each one. Typically, 10,000 simulated light curves and corresponding structure functions were generated for each characteristic timescale (*i.e.* rise time,

### 7.3. The Structure Function

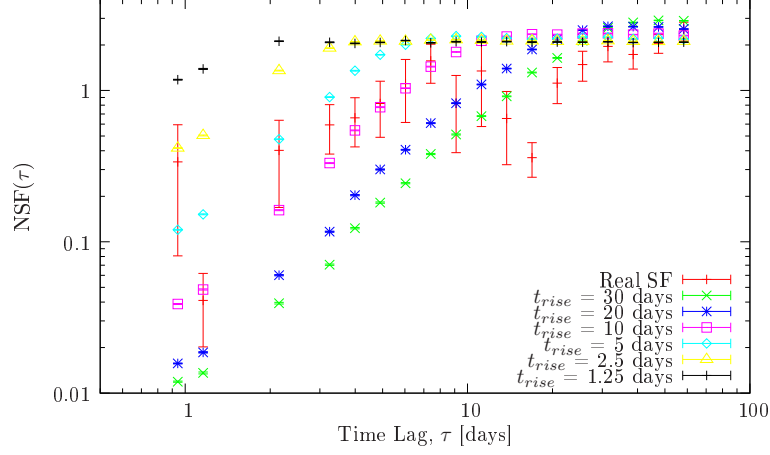


**Figure 7.8:** Average structure functions for a range of characteristic timescales ( $t_{rise}$ ) plotted along with the real Markarian 421 optical structure function (red points).

equal to the fall time) value tested. The average structure function for each rise time was compared to the structure function for the real data set and a goodness-of-fit value was determined. Since the data points in the structure function are correlated, the standard  $\chi^2$  value could not be used. Instead, a test statistic,  $G$ , was defined:

$$G(t_{rise}) = \frac{\sum_{i=1}^n (SF_i^{(1)} - \overline{SF}_i)^2}{N_i} \quad (7.10)$$

where  $n$  is the number of bins in the structure function,  $N_i$  is the number of data pairs contributing to the  $i^{th}$  bin of the structure function,  $SF_i^{(1)}$  is a single measured structure function point and  $\overline{SF}_i$  is the average fit structure function point. A plot of  $G$  versus rise characteristic timescale (where different values of  $t_{rise}$  are tested as the rise time in each simulation) will have a minimum at the characteristic timescale of the light curve.

The average simulated structure function rises to a plateau at the characteristic timescale of the simulated light curves. A plot showing a number of these average structure functions for different characteristic

### 7.3. The Structure Function

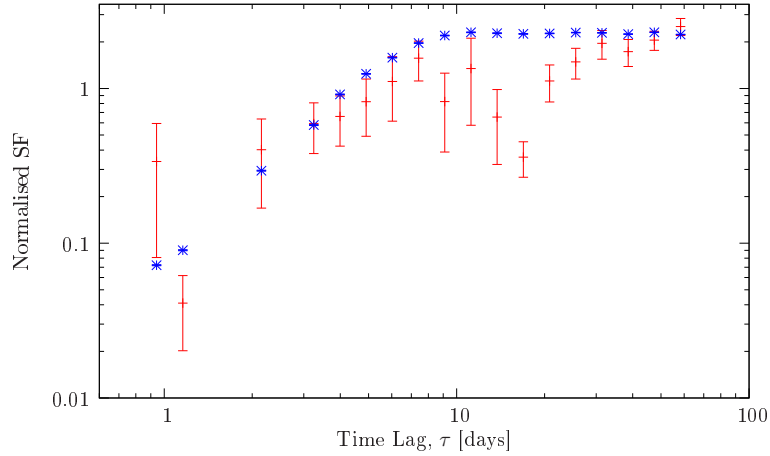


**Figure 7.9:** Plot of the best-fit structure function to simulated data (asterisks) plotted along with the real structure function for the  $r'$ -band Markarian 421 data set.

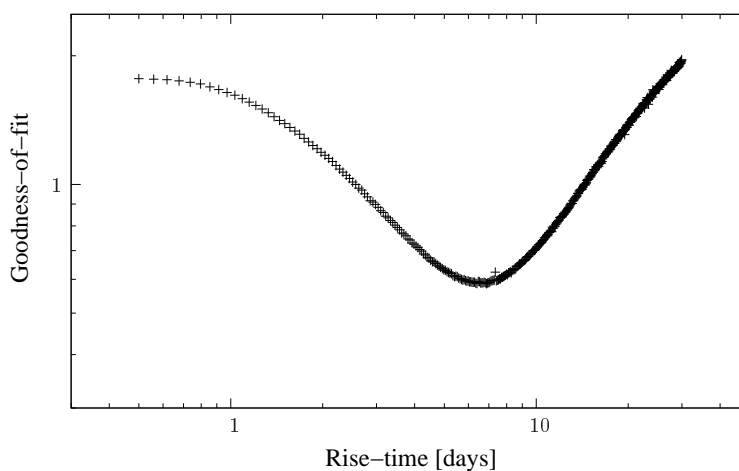
timescales is shown in Figure 7.8. The figure also shows the real optical structure function for Markarian 421 (similar to Figure 7.3(b)). The light curves used to generate the average structure functions were sampled at the same time intervals as the Markarian 421  $r'$ -band light curve presented in Chapter 6.

Figure 7.9 shows an example of this fitting method applied to the optical  $r'$ -band data for Markarian 421 while Figure 7.10 shows the goodness-of-fit plot. The real structure function is seen to begin to plateau at around the same time lag as the modelled best-fit at  $\sim 7$  days. A minimum occurs in the corresponding goodness-of-fit plot at 6.8 days. This suggests a minimum characteristic timescale of 6.8 days for the Markarian 421 data (assuming the fit model is accurate). Figure 7.11 shows an example of a simulated light curve with the same characteristic timescale as the real optical  $r'$ -band light curve (Figure 7.11(a)). The structure function for this simulated light curve is shown in Figure 7.11(b). The curve of the structure function is seen to plateau at around the same time lag as the real light curve (*i.e.*  $\sim 7$  days).

In the case of Markarian 501, the minimum characteristic timescale

### 7.3. The Structure Function

---



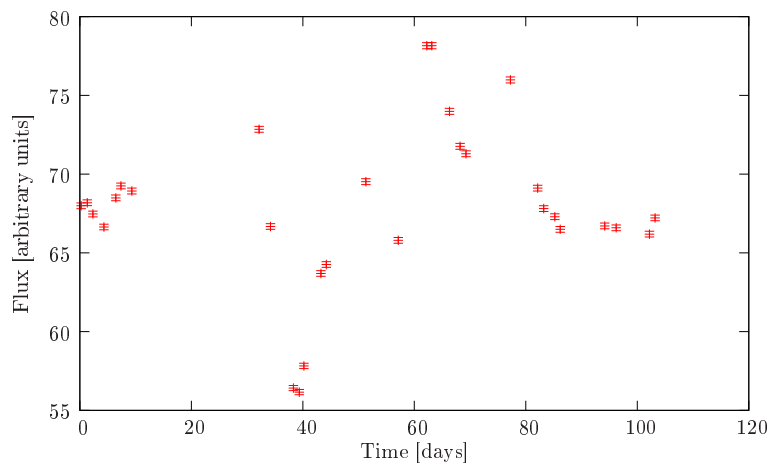
**Figure 7.10:** Plot of the goodness-of-fit parameter,  $G(t_{rise})$ , plotted against rise time. A minimum occurs at 6.8 days, corresponding to the characteristic timescale of variability for the light curve.

for the optical light curve variability was found to be 3.1 days, assuming the fit model is reasonable. For Markarian 501, the longest optical characteristic timescale appears to be longer than the duration of the FLWO 1.2 m observing campaign since no upper plateau is evident in the structure function. The average simulated structure function, however, fitted the real structure function best for a characteristic timescale of 3.1 days. At this value, the plateau in the average simulated structure function coincided with the point in the real optical structure function occurs where the break occurs.

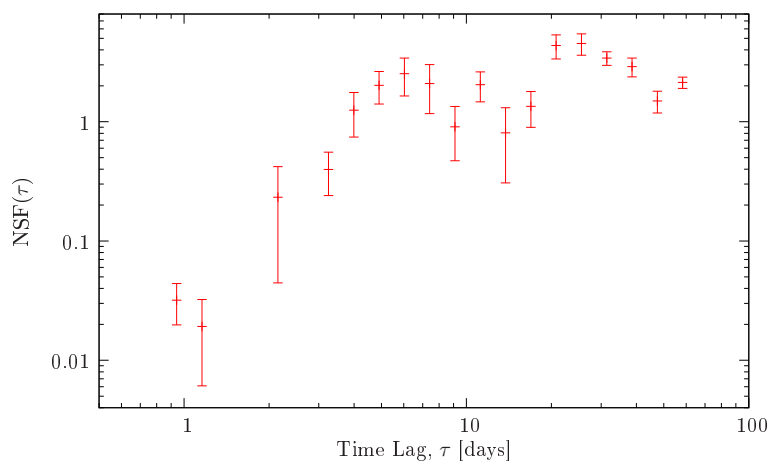
The characteristic timescale values that were found using this fitting method were used when simulating light curves so that they possessed the same temporal characteristics as the real light curves to find the chance probability for correlations, which is discussed further in Section 7.4.

### 7.3. The Structure Function

---



(a) Simulated Light Curve



(b) Structure Function of Simulation

**Figure 7.11:** Example of a simulated lightcurve. The light curve was simulated with the same time intervals and temporal characteristics (including characteristic timescale of 6.8 days) as the Markarian 421 r'-band light curve presented in Chapter 6. The structure function of the simulated lightcurve is also shown.

---

## 7.4 Correlation Analysis

Blazars are known to exhibit temporal variability across the electromagnetic spectrum. Variability correlations between different wavelengths may indicate which processes are driving emission or constrain emission models. Correlation between x-ray emission and  $\gamma$ -ray emission has been clearly shown in previous studies (*e.g.* Fossati *et al.*, 2008), lending support to the standard model in which an electron population produces the x-ray emission by synchrotron radiation and the  $\gamma$ -ray component is produced by inverse Compton scattering involving the same population of electrons.

Correlations between optical and  $\gamma$ -ray emission are not as well defined. As mentioned in Chapter 6, there has been tentative evidence that optical flaring might lead flaring in higher energy bands ( $\gamma$ -ray or x-ray). The discovery of  $\gamma$ -ray emission from 1ES 1011+496 (Albert *et al.*, 2006a) by MAGIC was made after observations were triggered by optical emission that was considerably higher than the source's four-year mean flux. Observations which led to the detection of  $\gamma$ -rays from Markarian 180 Albert *et al.* (2007a) were triggered in a similar manner. It is not clear if the detections of these sources during heightened levels of  $\gamma$ -ray emission at (or nearly at) the same time as heightened optical flux were chance occurrences.

In the case of two of the sources studied (Markarian 421 and Markarian 501), the relationship between the  $\gamma$ -ray flux and optical flux was examined using flux-flux plots. This is described in Section 7.4.1. The discrete correlation function (DCF) – a more formal method of measuring correlations in unevenly sampled data – was then used to investigate any possible correlation present. As no source variability is evident in the  $\gamma$ -ray data for 1ES 1959+650, 1ES 2344+514 and H 1426+428, no correlation analysis was conducted for these three objects. Calculation of the DCF is described in the Section 7.4.2. The limitations of the DCF and calculation of chance probability for accidental correlations are dis-

## 7.4. Correlation Analysis

---

cussed in Section 7.4.3. The results of DCF analysis for Markarian 421 and Markarian 501 are then presented and discussed in Section 7.4.4.

### 7.4.1 Flux-Flux Correlation

Figure 7.12 shows flux-flux correlation plots for both Markarian 421 and Markarian 501. These plots were produced by pairing optical flux measurements with  $\gamma$ -ray flux measurements taken within one day of each other. These datasets were normalised by dividing each flux value by the mean flux for that waveband. A scatter plot was then produced. Trends in the flux-flux plot may be indicative of a correlation in emission between the two bands.

The flux-flux plots shown in Figure 7.12 do not exhibit any obvious trends. A weighted least-squares linear fit was made to the data in both cases. This fit took account of the uncertainty in the  $\gamma$ -ray and optical fluxes.

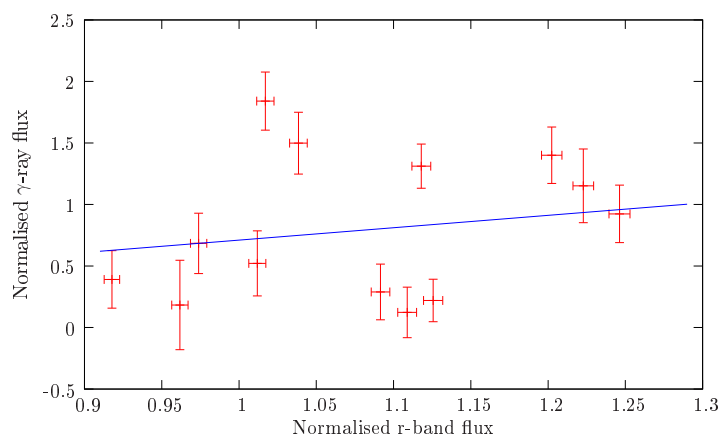
In the case of Markarian 421, a  $\chi^2$  goodness-of-fit of  $\chi^2/dof = 76.1/11$  showed that the data were not well fitted by the linear fit. Similarly for Markarian 501, a  $\chi^2/dof = 1222/10$  suggests that the fit does not show any evidence for a linear correlation.

The seeming lack of trends may indicate that the light curves are not sampled densely enough to resolve correlations on timescales of 1 day or that optical emission and  $\gamma$ -ray emission simply may not be correlated on one-day timescales. To examine the correlation over a different range of timescales, the discrete correlation function was used.

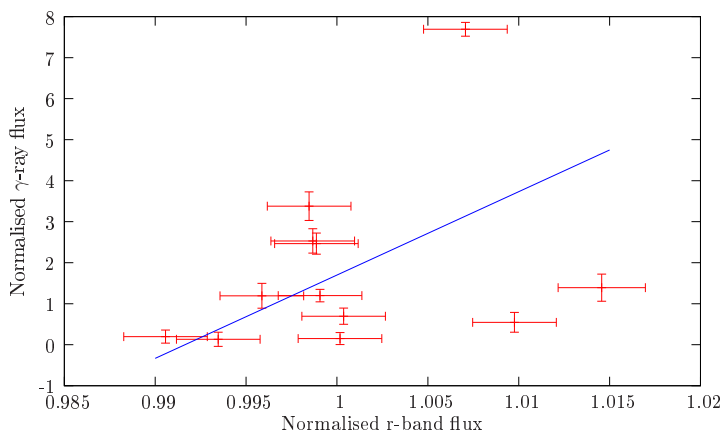
### 7.4.2 Discrete Correlation Function

Given two continuous, stationary stochastic functions (*i.e.* random processes whose probability distribution does not change when shifted in time),  $a(t)$  and  $b(t)$ , defined at all  $t$ , the classical correlation function,  $CF(\tau)$ , is defined as

## 7.4. Correlation Analysis



(a) Markarian 421



(b) Markarian 501

**Figure 7.12:** Flux-flux correlation plots for optical  $r'$ -band and  $\gamma$ -ray band. The top panel is the flux-flux plot for Markarian 421. The bottom panel is the flux-flux plot for Markarian 501. Weighted linear least-squares fits are shown in both cases. The  $\chi^2/dof$  values for these fits are given in the text. In both cases, only optical/ $\gamma$ -ray pairs of observations taken within 24 hours of each other were used in the plot, meaning that only a subset of each data set was utilised. However, the data were normalised using the average flux for the entire data set so the average normalised flux may not be 1.0 in the plots.

## 7.4. Correlation Analysis

---

$$CF(\tau) = \frac{E\{[a(t) - \bar{a}][b(t + \tau) - \bar{b}]\}}{\sigma_a \sigma_b} \quad (7.11)$$

where  $E(f)$  is the (mathematical) expectation value for  $f$  (*i.e.* the average for a stochastic process; Press *et al.*, 1992),  $\bar{a}$  and  $\bar{b}$  are the mean values of  $a(t)$  and  $b(t)$  respectively,  $\sigma_a$  and  $\sigma_b$  are the standard deviations of  $a(t)$  and  $b(t)$  respectively and  $\tau$  is a time gap or lag (Oppenheim & Schaffer, 1975). While this is useful for continuous functions, astronomical data can rarely be regarded as continuous. They are usually a time series of discrete points. In this case, the discrete correlation function (DCF), introduced by Edelson & Krolik (1988), may be applied to the data. It is an approximation of  $CF(\tau)$  which can deal with unevenly sampled data, as is often the case with astronomical data sets.

To construct the DCF (as per Edelson *et al.*, 1995) of two discrete time series,  $x(t_i)$  and  $y(t_j)$ , both data sets are first normalised to zero mean and unit dispersion:

$$x'(t_i) = \frac{x(t_i) - \bar{x}}{\sigma_x} \quad (7.12)$$

$$y'(t_j) = \frac{y(t_j) - \bar{y}}{\sigma_y} \quad (7.13)$$

where  $\bar{x}$  is the mean value and  $\sigma_x$  is the standard deviation of  $x(t)$  (similar nomenclature for  $y(t)$ ). For each pairing of the points in  $x'(t)$  and  $y'(t)$ , the time lag  $\Delta t_{ij}$  and the unbinned DCF (*i.e.*  $UDCF$ ) are found:

$$\Delta t_{ij} = t_i - t_j \quad (7.14)$$

$$UDCF_{ij} = x'(t_i)y'(t_j) \quad (7.15)$$

In other words, to find  $\Delta t_{12}$ , the second value in  $t_j$  is subtracted from the first value in  $t_i$ . The  $UDCF$  values are now binned so that all values of  $UDCF_{ij}$  for which the corresponding  $\Delta t_{ij}$  fall in the time bin centred

## 7.4. Correlation Analysis

---

on  $T_{lag}$ , *i.e.*

$$T_{lag} - \frac{\Delta t_{bin}}{2} < \Delta t_{ij} \leq T_{lag} + \frac{\Delta t_{bin}}{2} \quad (7.16)$$

are included in the calculation of the DCF at that time lag:

$$DCF(T_{lag}) = \frac{1}{N} \sum UDCF_{ij} \quad (7.17)$$

Here,  $N$  is the number of  $UDCF$  pairs that are included in the  $T_{lag}$  bin. The selection of the bin-width,  $\Delta t_{bin}$ , depends on the sampling frequencies of the light curves and the required resolution. In constructing the DCF,  $\Delta t_{bin}$  was selected such that at least of five  $UDCF_{ij}$  values contributed to each  $DCF(T_{lag})$  bin.

The uncertainty of the DCF value from each DCF bin is given by the standard error on the mean for the  $UDCF_{ij}$  values which contribute to that bin. That is

$$\Delta DCF(T_{lag}) = \frac{\sigma_{T_{lag}}}{\sqrt{N_{T_{lag}}}} \quad (7.18)$$

where  $\sigma_{T_{lag}}$  is the standard deviation of the  $N_{T_{lag}}$   $UDCF_{ij}$  values which contribute to the  $DCF(T_{lag})$  bin. A positive value of DCF at a certain time lag (or lead) indicates a possible correlation between the two time series at that time lag. A negative DCF value may indicate an anti-correlation at that time lag. The discrete auto correlation function is found by calculating the DCF for a time series with itself (*i.e.* for  $x(t) = y(t)$ ) and investigates how well a time series correlates with a copy of itself. This function is important as it may expose periodicity (intrinsic or spurious) in the time series. Features appearing in the discrete autocorrelation function of a time series can consequentially affect the discrete correlation of that time series with a different time series.

## 7.4. Correlation Analysis

---

### 7.4.3 DCF Limitations and Chance Probability

Although the DCF does not require a time series to be evenly sampled or densely sampled, it does have some limitations. Very poorly sampled light curves containing only a few data points, for instance, will not have sufficient  $UDCF_{ij}$  values (Equation 7.15) to produce a meaningful DCF when the pairs are binned.

Features in the discrete autocorrelation function of either (or both) of the light curves being correlated may also influence the DCF. Low-frequency variations in a light curve can cause mis-estimates of the real time lags present in the data and possibly lead to spurious correlations (Welsh, 1999).

Since spurious features which do not relate to intrinsic correlations may appear in a DCF, it is important to quantify the confidence which may be placed in DCF peaks. Peaks at (or close to) zero lag are of particular interest because, in this region, the DCF is identical to the linear cross correlation coefficient. Using an *a-priori* hypothesis of a correlation at zero lag, a Monte Carlo method for finding the chance probability of obtaining DCF values was used. Assuming the flares occur randomly in time, the probability of finding a certain value of DCF at zero lag was found. A large number of simulated light curves were generated ( $\sim 100,000$ ). This was done by simulating flares with the same characteristic rise-time found by structure function analysis of the light curve being modelled using the fit model outlined in Section 7.3.2. Optical light curves were simulated for this work as characteristic times were easier to obtain from the optical structure functions. A DCF was calculated for each simulated optical light curve with the real  $\gamma$ -ray light curve. The frequency with which values of DCF (at zero lag) occurred by chance for the simulated light curves was histogrammed. This histogram was normalised and then integrated to form an integral probability distribution. An example of this type of histogram is shown in Figure 7.13.

Even though the simulated light curves have been generated so that

## 7.4. Correlation Analysis

---

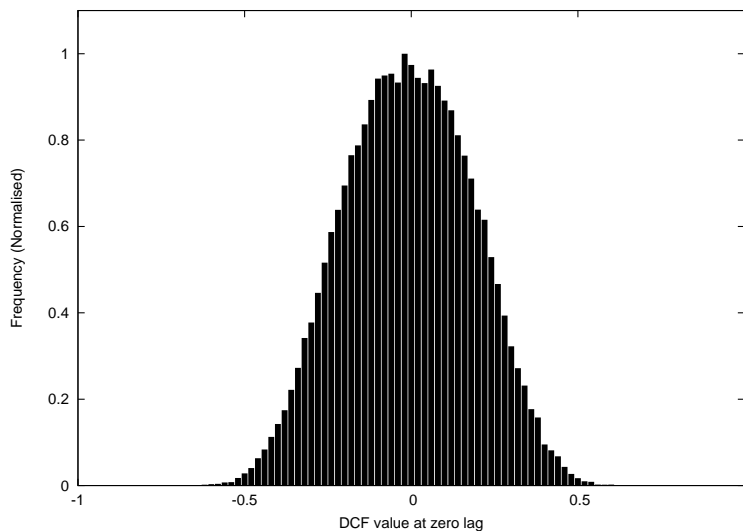


**Figure 7.13:** Example of a normalised histogram of DCF values at zero lag obtained for 100,000 simulated light curves, used to estimate the probability of getting a certain value of DCF at zero lag by chance alone.

flares occur at random times, most of them have a substantial DCF value at some time lag by chance. The chance probability of obtaining a particular DCF value at zero lag may be used to make a quantitative statement about the chance probability of certain DCF values occurring.

The use of a similar statistical treatment for finding the chance probability of obtaining apparent correlations at other, non-zero, time lags is complicated by a substantial trials factor. An approximation was used to give some quantitative information about the chance probability however. First, a test was performed to ascertain the extent by which the histogram of DCF values obtained for simulated light curves (and, hence, the chance probability distribution) changes at different values of time lag. A set of 100,000 simulated light curves was generated. For each of these simulations, the DCF was calculated with a real light curve in the  $\gamma$ -ray waveband. The DCF values for a certain value of  $T_{lag}$  were histogrammed. This distribution was integrated to construct an integral

## 7.4. Correlation Analysis

---

chance probability distribution. This was repeated over a series of time lags and these were all plotted on one graph for comparison. The distributions, though different, were not seen to vary greatly over the range of time lags tested (see examples shown in Figure 7.17 and Figure 7.20). In order to estimate the trials factor associated with searching for correlations over a range of time lags, the assumption was made that the probability distributions did not vary over the entire range of time lag values.

Next, the probability of finding the DCF value of interest by chance at the relevant time lag was found using the same Monte Carlo method used for zero lag. As probabilities at different time lags are being tested, however, there is a trials factor which must be taken into account. The number of points in the DCF plot,  $n$ , was taken as a first-order approximation of this, as we are assuming that the probability distribution does not vary across the range of time lags tested. The number of points in the DCF depends on the selection of  $\Delta t_{bin}$ , where  $\Delta t_{bin}$  was selected so that all  $DCF(T_{lag})$  bins contained at least 5  $UDCF_{ij}$  values. The probability of finding the DCF value by chance,  $P_c$ , in  $n$  trials was then taken as approximately  $(n \times P_c)$ .

### Test of Methodology: X-Ray/ $\gamma$ -ray Correlation

Correlations between blazar emission in the VHE  $\gamma$ -ray band and the x-ray band have been seen in previous studies. As an example of the technique employed to quantify the significance of features in the DCF obtained for the  $\gamma$ -ray band and the optical  $r'$ -band, the technique was applied to an x-ray time series. The x-ray data were RXTE All-Sky Monitor (ASM) “quicklook” (*i.e.* non-rigorous analysis) light curves which are freely available on the RXTE website<sup>2</sup>.

The structure function for the x-ray time series was calculated, as outlined in Section 7.3. The best-fit structure function was found using

---

<sup>2</sup><http://xte.mit.edu/>

## 7.4. Correlation Analysis

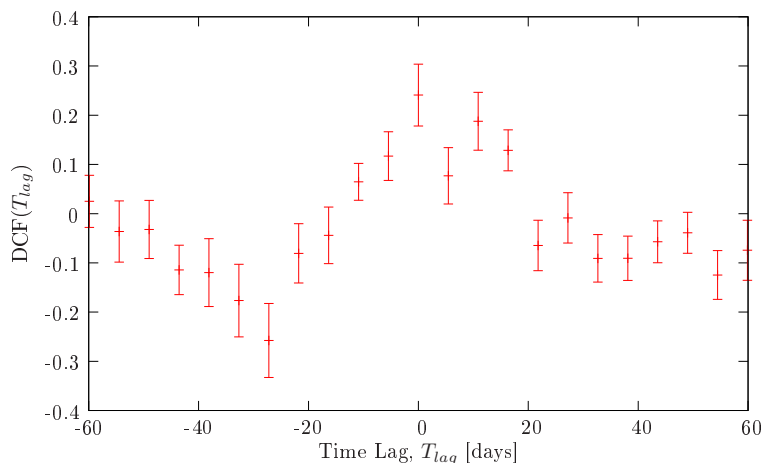


**Figure 7.14:** Example Markarian 421 DCF plot for  $\gamma$ -ray (Whipple 10 m telescope) and x-ray data (RXTE). The x-ray data were obtained between 2<sup>nd</sup> September 2006 and 31<sup>st</sup> May 2007. The  $\gamma$ -ray light curve is presented in Chapter 5. The DCF was constructed so that features with a positive lag would suggest  $\gamma$ -ray emission lagging x-ray emission.

the Monte Carlo method outlined in Section 7.3.2. From this fit, the time series was seen to have a characteristic timescale of 4.23 days.

The DCF was constructed for the Whipple 10 m  $\gamma$ -ray light curve and RXTE light curve (see Figure 7.14). A prominent peak is evident around  $T_{lag} = 0$  days. At  $T_{lag} = 0$  days, the DCF has a value of 0.241. The probability of obtaining this value of DCF by chance was found. A large number (10,000) simulated light curves were generated so that they had the same temporal characteristics as the RXTE x-ray light curve. For each of the simulated light curves, the DCF value at  $T_{lag} = 0$  days was obtained. The distribution of the DCF values was then used to find the chance probability of obtaining a DCF value of 0.241 at zero lag. The probability was found to be 3.8%.

Next, the x-ray time series was altered so that the flux values (along with their associated uncertainties) were re-ordered, while the dates for the observations were left untouched. This effectively randomised the

## 7.4. Correlation Analysis

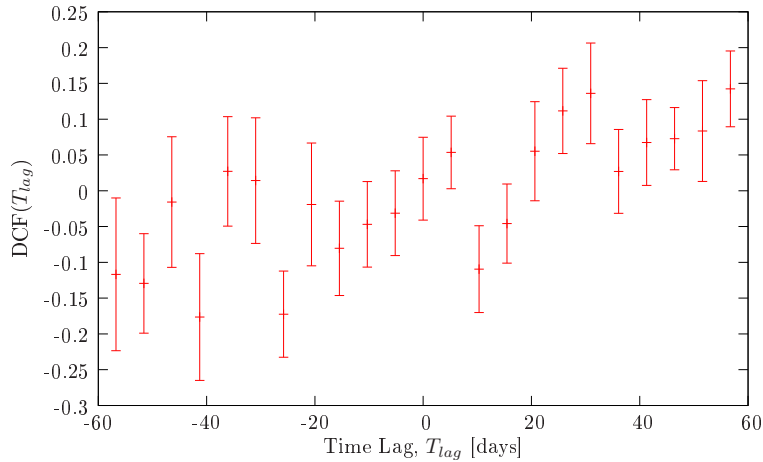


**Figure 7.15:** Example Markarian 421 DCF plot for  $\gamma$ -ray (Whipple 10 m telescope) and RXTE x-ray data for which the flux values have been randomly interchanged with one another. The DCF was constructed so that features with a positive lag would suggest  $\gamma$ -ray emission lagging x-ray emission.

time series so that there was no underlying physical reason for correlations between the re-ordered light curve and the Whipple 10 m light curve. Figure 7.15 shows the DCF constructed for the Whipple 10 m  $\gamma$ -ray lightcurve and the re-ordered RXTE light curve. There was no prominent peak at  $T_{lag} = 0$  days, as had been the case for the DCF constructed using the correctly-ordered x-ray light curve. The DCF value at zero lag was found to be 0.017. The chance probability for this value (at  $T_{lag} = 0$  days) was found to be 39.2%.

A small peak occurred in the DCF at  $\sim 30$  days, where the DCF value was 0.136. Since the light curve had been re-ordered in a random fashion, any peak in the DCF should occur due to coincidental correlation. The probability of such a peak occurring by chance at  $T_{lag} = 30$  days was found using a method similar to the one used to find the chance probability at  $T_{lag} = 0$  days. However, as outlined in Section 7.4.3, the use of this method at non-zero lags is complicated by a trials factor which must be taken into account. As an approximation, the number of points

## 7.4. Correlation Analysis

---

in the DCF was used as the trials factor. The DCF binning was set so that the sampling was similar to the sampling used in the DCF analysis for the optical  $r'$ -band and the VHE  $\gamma$ -ray band, presented in the sections that follow. The probability of obtaining a value of  $DCF = 0.136$  at  $T_{lag} = 30$  days was found to be 15.1%. Taking the trials factor (*i.e.* 20 points in DCF plot) into account, the expectation value for obtaining this DCF value is greater than one. Hence, the feature is shown to have occurred by chance.

### 7.4.4 Results

The results of DCF analysis, looking for correlations between the  $\gamma$ -ray and  $r'$ -band data for Markarian 421 and Markarian 501, are presented in this section. The results of a quantitative approach to estimating the chance probability for features in the DCF are also reported. Possible explanations for features which appear in the DCF are discussed.

The DCF was calculated for  $\gamma$ -ray and x-ray light curves for both Markarian 421 and Markarian 501. A strong correlation near zero lag was found. This correlation has been reported in previous observations and has been confirmed by many multiwavelength campaigns (*e.g.* Fossati *et al.*, 2008; Błażejowski *et al.*, 2005). Therefore, the results of the DCF for these two bands are only outlined for Markarian 421 but not reported here in detail. A more detailed investigation of this correlation will be reported in a future paper based on this multiwavelength campaign. A one-zone synchrotron self-Compton (SSC) model explains the dynamics of this correlation well, whereby the x-ray photons which are generated by synchrotron radiation in the emitting region are upscattered to produce  $\gamma$ -ray photons by inverse Compton processes.

#### Markarian 421

The DCF of the  $\gamma$ -ray light curve with the  $r'$ -band light curve is shown in Figure 7.16. The use of different bin sizes was investigated. Five-day

## 7.4. Correlation Analysis

---

bins were used to construct the DCF so that features in the plot were discernible without oversampling, which would increase the uncertainty of the data points due to low numbers of  $UDCF_{ij}$  values contributing to each DCF bin. The use of smaller bins, providing more points in the DCF plot, did not allow for more features in the plot to be discerned and also increased the uncertainty in each peak. By using larger bin sizes, some features in the plot could no longer be resolved.

There does not appear to be a prominent feature at zero lag in the DCF. However, a number of peaks appear at various positive and negative lags. A peak with a value of 0.57 occurs at a lag of  $-50$  days, suggesting optical emission lagging  $\gamma$ -ray by 50 days. A feature at  $+40$  days lag may also suggest an anti-correlation (*i.e.* low state of optical emission 40 days before a  $\gamma$ -ray peak). However, both of these points are poorly sampled leading to large uncertainty in both values of DCF (*i.e.* uncertainties of 0.31 and 0.36 respectively). For instance, the local minimum at  $T_{lag} = 40$  days was only found with a minimum number (5) of  $UCDF_{ij}$  contributions.

Peaks at lags of  $+10$  and  $-10$  days both have large DCF values of 0.46 and 0.40 respectively. These are well-sampled points with relatively low associated uncertainties. Correlations which are close to zero lag might indicate that similar processes drive the emission in both wavebands and, hence, are of interest. However, the symmetry of these peaks about zero lag raises suspicion as to their origin. The peaks still appeared in the DCF plot when the binning was altered. The likelihood of such correlations happening by chance was investigated more thoroughly.

100,000 light curves were simulated with similar characteristics to those of the  $r'$ -band light curve. The characteristic rise time for the flares in these simulations was found using the best-fit structure function for the light curve (Section 7.3.2). The DCF values at zero lag were found for the simulated light curves with the real  $\gamma$ -ray light curve. The chance probability of obtaining a DCF value of 0.5 or greater was found

## 7.4. Correlation Analysis

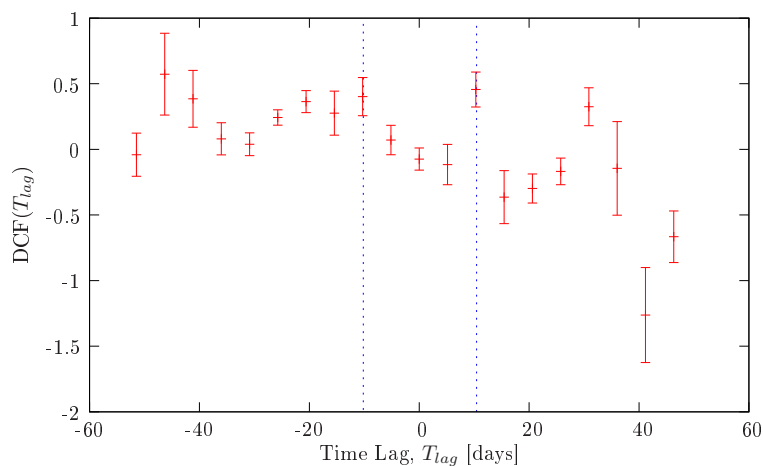


**Figure 7.16:** Markarian 421 DCF plot for  $\gamma$ -ray and  $r'$ -band optical data. The DCF was constructed so that features with a positive lag would suggest  $\gamma$ -ray emission lagging optical emission.

to be only  $\sim 1\%$ .

The chance probability distributions at different lag values are shown in Figure 7.17. Although the distribution does change with lag time, it does not change dramatically until larger lags are being tested. The chance probability of obtaining a 0.5 DCF value at 10 days lag was found to be 5.6%. The probability of finding the same DCF value at  $-10$  days lag (*i.e.* 10 days lead) was found to be 6.4%. Given the trials factor (20 points used to construct DCF), the expectation value of these features happening by chance is greater than 1.00. Therefore, it is assumed that they are due to features occurring in the optical and  $\gamma$ -ray light curves that are not intrinsically associated with each other but happen to correlate by chance.

Looking at the discrete autocorrelation functions for the Markarian 421  $\gamma$ -ray and optical light curves (Figure 7.18), some features which may contaminate their cross correlation (Welsh, 1999) are apparent. In particular, two large peaks appear in the  $\gamma$ -ray autocorrelation at  $\pm 10$

## 7.4. Correlation Analysis

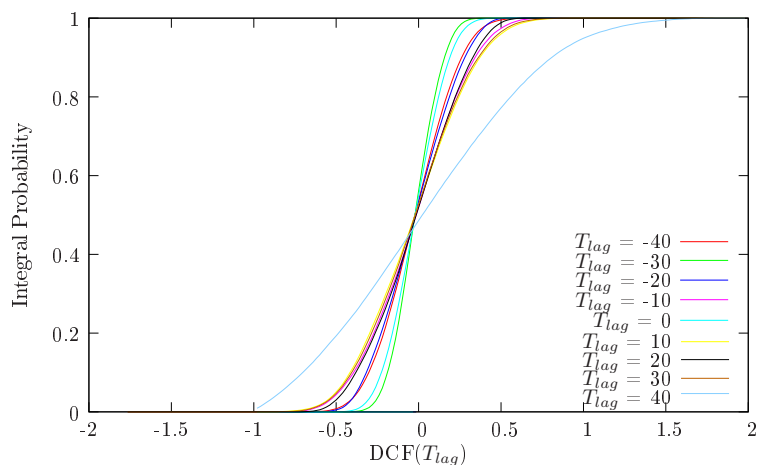


**Figure 7.17:** Chance probability distributions for different time lags found by integrating histogram of values obtained for the DCF of Markarian 421  $\gamma$ -ray light curve with 100,000 simulated “optical” light curves. All but one (distribution for  $T_{lag} = 40$  days) are very similar. All  $T_{lag}$  values shown in the legend are in units of days.

days lag. It is thought that these peaks in the autocorrelation function were the cause of the peaks found in the DCF at lags of  $\pm 10$  days. These features in the autocorrelation function, along with the approximation of the chance probability for these features, would suggest that there is no good evidence for any lag in emission.

### Markarian 501

Figure 7.19 shows the DCF of the  $\gamma$ -ray and optical  $r'$ -band data for Markarian 501. The DCF was constructed by binning  $UDCF_{ij}$  values in 5-day bins. This reduced uncertainty for the data points without loss of resolution of features in the curve. As was the case for Markarian 421, and consistent with most emission models, there is no evidence for correlation at zero lag. At non-zero lag, the highest peak occurs at a lag of  $-30$  days (*i.e.* a 30-day  $\gamma$ -ray lead) at a DCF level of 0.27. The next most prominent peak is at a lag of 20 days, but this peak has a DCF

## 7.4. Correlation Analysis

---

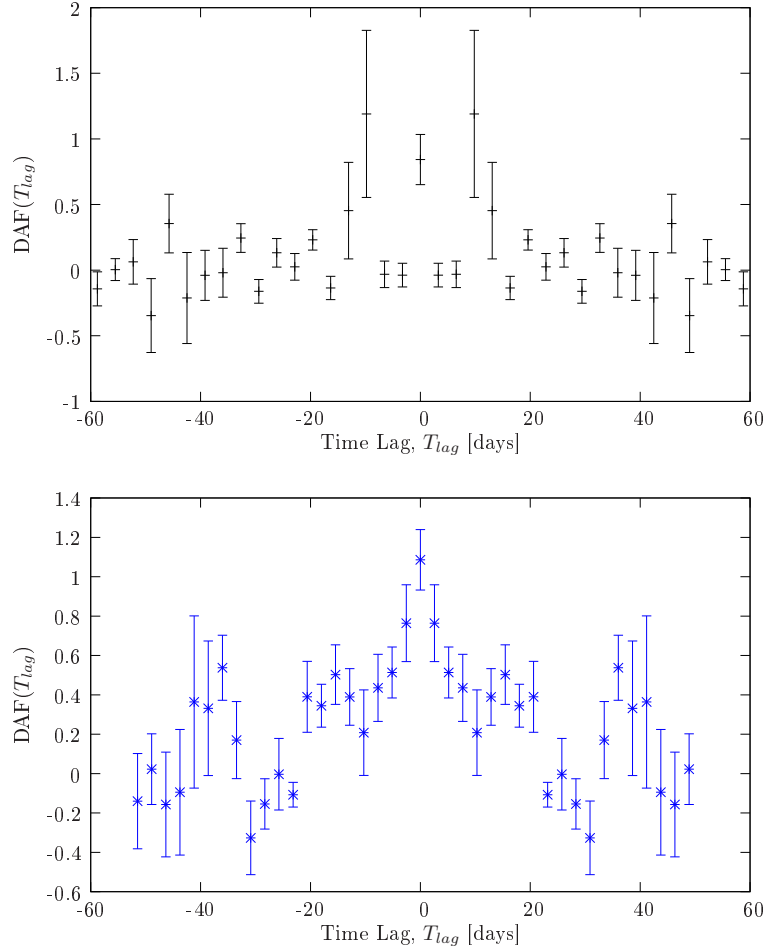


**Figure 7.18:** Discrete autocorrelation functions for Markarian 421. The top panel shows the discrete autocorrelation function for the  $\gamma$ -ray light curve. A large feature at  $\pm 10$  days lag may contaminate the DCF. The bottom panel is the discrete autocorrelation function for the optical data, plotted on the same time scale as the  $\gamma$ -ray discrete autocorrelation function.

## 7.4. Correlation Analysis

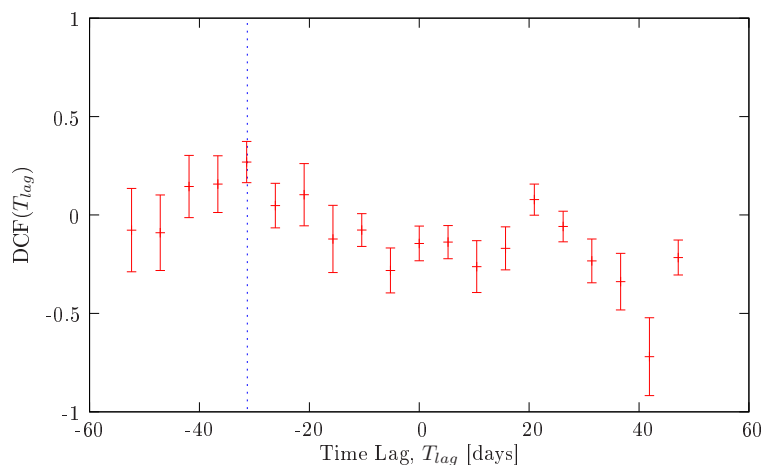


**Figure 7.19:** Markarian 501 DCF plot for  $\gamma$ -ray and  $r'$ -band optical data. The DCF was constructed so that features with a positive lag would suggest  $\gamma$ -ray lagging optical emission.

value of 0.08, which is insignificant.

The chance probability of finding a peak of certain DCF value at zero lag was found by simulating 100,000 light curves with similar characteristics (found by structure function analysis) to the Markarian 501  $r'$ -band optical light curve, as described in Section 7.4.3. The chance probability of finding a peak of 0.08 at zero lag was found to be 26%. The probability of finding the highest peak value of 0.27 at zero lag was found to be 2%. These values do not take account of trials, having observed these peaks at non-zero lag.

The variation of the chance probability distribution at different lag values is shown in Figure 7.20. The chance probability of finding a DCF value of 0.27 at a time lag of  $-30$  days was found to be  $\sim 5\%$ . If the number of points in the DCF plot (*i.e.* 20) is taken as the trials value, the expectation value of finding this value (or greater) in one of the points in the DCF is  $\sim 100\%$ . The same treatment for the 0.08 peak at a lag of 20 days results in a similar probability of observing such a value by chance. Therefore, there is no strong evidence for correlation at any time

## 7.4. Correlation Analysis

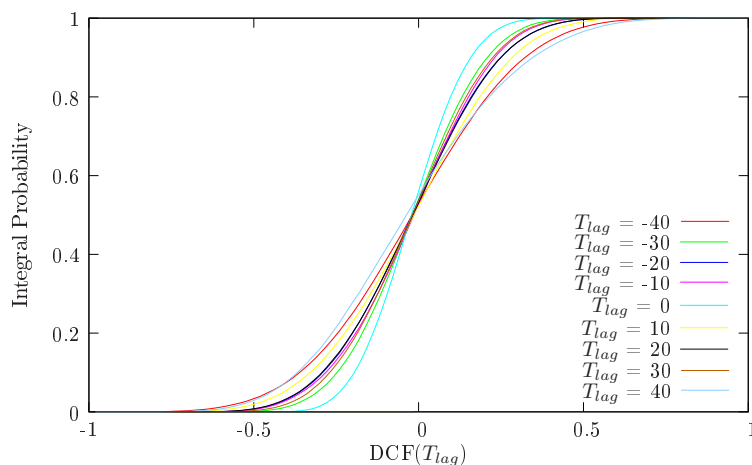


**Figure 7.20:** Chance probability distributions for different time lags found by integrating histogram of values obtained for the DCF of Markarian 501  $\gamma$ -ray light curve with 100,000 simulated “optical” light curves. All distributions are very similar over most DCF values.  $T_{lag}$  values shown in the legend are in units of days.

lead or lag between these data sets.

The discrete autocorrelations for the  $\gamma$ -ray and optical r'-band light curves are shown in Figure 7.21. There are no significant features in the autocorrelations which could have contaminated the DCF. This is also evidenced by the fact that the DCF plot does not exhibit peaks which are symmetrical about zero-lag. Symmetrical peaks in the DCF can be indicative of contamination from the autocorrelation since autocorrelation plots are symmetrical about zero lag.

## 7.4. Correlation Analysis

---

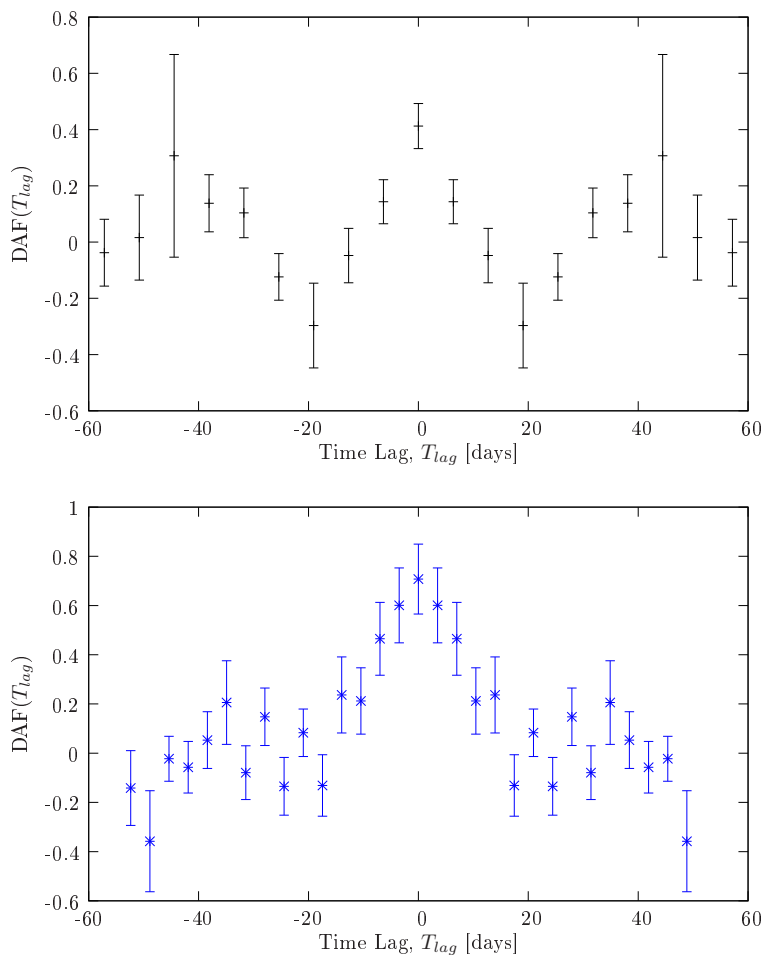


**Figure 7.21:** Discrete autocorrelation functions (DAF) for Markarian 501. The top panel shows the DAF for the  $\gamma$ -ray light curve. The bottom panel is the DAF for the optical data, plotted on the same time scale as the  $\gamma$ -ray DAF. Neither of the DAFs have significant contaminating features.

# Chapter 8

## Interpretation and Conclusions

### 8.1 Summary

The work of this thesis includes a thorough reduction and analysis of TeV  $\gamma$ -ray and  $r'$ -band optical data from five known TeV-emitting blazars, which are a class of AGN. The data were obtained at the Whipple 10 m  $\gamma$ -ray telescope and the 1.2 m optical telescope, both located on Mt. Hopkins in southern Arizona, USA. The nature of the  $\gamma$ -ray and optical emission during the observation campaign was characterised and compared to similar observations made previously. The data were then scrutinised for possible correlations between emission in both energy bands.

An extensive search of Hillas parameter space was undertaken in order to define a  $\gamma$ -ray domain more suited to the analysis of 2006-07 data than standard Supercuts 2000. This resulted in a more sensitive (*i.e.* better signal-to-noise ratio) analysis while maintaining a reasonable  $\gamma$ -ray rate. Two of the five blazars studied (Markarian 421 and Markarian 501) were detected with high statistical significance. Significant flaring was also detected over the course of the observing campaign for both of these blazars. Flux upper limits ( $3\sigma$ -level) were presented for 1ES

## 8.2. Discussion

---

1959+650, 1ES 2344+514 and H 1426+428. None of these blazars exhibited significant  $\gamma$ -ray flaring activity during the campaign.

Well-sampled differential  $r'$ -band light curves were obtained for Markarian 421, Markarian 501, H 1426+428 and 1ES 1959+650, while only seven nights of data were obtained in the case of 1ES 2344+514. These data were obtained during the course of the TeV observing campaign and could therefore be compared to the TeV light curves for correlations.

Various temporal analyses were conducted for each of the  $\gamma$ -ray and  $r'$ -band light curves to quantify characteristics relating to their variability. In particular, a structure function analysis was performed. Simulated light curves were then used to find a best-fit to some of the better-sampled light curves. Thus, the characteristic rise-times for the flares in the data set were ascertained.

In the case of Markarian 421 and Markarian 501, correlation analyses were performed using the discrete correlation function (DCF). A Monte Carlo method was used to find the chance probabilities for peaks occurring in the DCF which might indicate correlation between the bands. There was no evidence of significant correlation between the  $r'$ -band emission and TeV  $\gamma$ -ray band emission.

## 8.2 Discussion

A discussion of the results of the  $\gamma$ -ray and optical analyses is presented here along with a separate discussion about correlations.

### 8.2.1 TeV $\gamma$ -ray Analysis

The cumulative significance method outlined in Chapter 5 optimises the parameters used to select  $\gamma$ -ray like events by defining a contiguous “ $\gamma$ -ray domain” within Hillas parameter space. By using this method, a set of selection criteria were found which increased the signal-to-noise ratio in a data set which was already known to have a significant  $\gamma$ -ray excess.

## 8.2. Discussion

---

It is worth noting that the  $\gamma$ -ray domain selected using the cumulative significance method is both contiguous and geometrically regular. This is the case for almost all methods of  $\gamma$ -ray selection (see Section 5.1.1). Selection methodologies based on the use of non-contiguous and/or irregular regions of parameter space are non-trivial. However, previous studies of the use of non-contiguous selection regions have not shown evidence for an improvement in the sensitivity of the analysis.

The *alpha* cut of  $9.5^\circ$ , given by both the cumulative significance method and the single parameter variation method, is considerably lower (*i.e.* tighter) than the nominal value of  $15^\circ$  used in Supercuts 2000. This is the main difference between the optimised parameter cuts used to analyse the 2006-07 data and Supercuts 2000 and is due to the fact that the 2006-07 cuts were optimised for maximum significance.

As discussed in Chapter 5, recent testing of the Whipple 10 m telescope has shown that it has a small systematic pointing error, the extent of which depends on the telescope's elevation. The definition of *alpha* for each event assumes that the source is located at the centre of the telescope camera's field-of-view. This assumption is not entirely correct when taking the pointing error into account. The Whipple 10 m telescope camera has been moved slightly during maintenance work since the data presented in this thesis were obtained. This makes characterisation of the pointing offset for the 2006-07 season difficult. However, if a suitable method of characterising the pointing error is devised using the data obtained during the season, a software correction could be applied in any re-analysis. The effect of implementing a software pointing correction during the analysis of data obtained in the 2007-08 observing season has been to increase the sensitivity of the analysis.

Although Markarian 421 was detected with high significance ( $>20\sigma$ ), maximum flux levels were lower than those detected in previous campaigns. Flux levels of  $\sim 3$ -5 times that of the Crab Nebula flux have not been uncommon for TeV  $\gamma$ -ray observations (Błażejowski *et al.*, 2005;

## 8.2. Discussion

---

Fossati *et al.*, 2008). The highest night-averaged flux level detected during this campaign was  $\sim 1.1$  times the Crab Nebula flux in this energy band. However, the fractional root-mean-square (RMS) variability amplitude is similar to that obtained in previous observing campaigns such as Błażejowski *et al.* (2005). This may suggest that the variability level of the source relative to its mean flux level remains constant, regardless of flare amplitudes.

The detection of Markarian 501 is consistent with previous observations of the source; low-level or undetectable emission between rapid flaring outbursts (Albert *et al.*, 2007f; Aharonian *et al.*, 1999b, 2001b). The flares detected during the 2006-07 season reached a maximum which was less than the Crab Nebula flux. Flares at levels of  $\sim 10$  times that of the Crab Nebula have been detected in previous observations (Aharonian *et al.*, 1999b). VERITAS observations of Markarian 501 in the previous season (2005-06) detected relatively low-level flux with no significant flares, although it was not monitored on a nightly basis during that season (Hanna *et al.*, 2008).

There was no evidence of statistically significant  $\gamma$ -ray excess for 1ES 1959+650, 1ES 2344+514 or H 1426+428 during the 2006-07 observing season. However, in comparison to Markarian 421 and Markarian 501, these objects have not been observed at levels exceeding the flux sensitivity of the Whipple 10 m telescope very frequently in the past (Gutierrez *et al.*, 2006; Konopelko, 1999; Newbold, 2007).

### 8.2.2 Optical Data Analysis

Accurate photometry of the SDSS  $r'$ -band optical data obtained at the FLWO 1.2 m telescope allowed for the resolution of variability on 0.01 magnitude scales. The five blazars studied exhibited varying amounts of variability in their light curves. Similar to the  $\gamma$ -ray band, Markarian 421 was the most variable at  $r'$ -band optical wavelengths with variations over  $>0.4$  magnitudes. In contrast, Markarian 501 exhibited variability

## 8.2. Discussion

---

over only  $\sim 0.05$  magnitudes, even though it was the only other blazar (included in this campaign) which exhibited detectable variability at TeV energies.

The fractional RMS variability amplitude varied considerably for the blazars monitored, but was much smaller in the  $r'$ -band than at  $\gamma$ -ray energies. This follows a general trend of increased variability for observations at higher energies which has been shown in many multiwavelength studies, with the x-ray and  $\gamma$ -ray bands exhibiting more fractional variability than the optical and radio bands (Błażejowski *et al.*, 2005).

### 8.2.3 Correlation

No evidence for correlations between optical ( $r'$ -band) and  $\gamma$ -ray emission could be found for Markarian 421 or Markarian 501 during this observation campaign. The MAGIC collaboration have detected two blazars after optical brightening triggered TeV observations: Markarian 180 (Albert *et al.*, 2006b) and 1ES 1011+496 (Albert *et al.*, 2007b). In both cases, the level of optical flux increased significantly above a multi-year average, triggering target-of-opportunity observations. In the case of Markarian 180, the optical flux increased by 50% above a three-year mean level. The nightly integrated TeV flux, however, was consistent with steady emission. In the case of 1ES 1011+496, the optical brightness increased slowly (over half a year) before reaching the target-of-opportunity trigger level for TeV observations. Again, steady TeV emission was detected, with no evident flares. Observations in the previous season, while the optical flux was much lower, resulted in only a marginal ( $\sim 3\sigma$ ) signal, corresponding to a TeV flux level 40% lower than the observed flux when the optical flux was higher. The detection of  $\gamma$ -ray emission from these two high-frequency peaked BL Lacs (HBLs) would suggest that there may be evidence for optical and  $\gamma$ -ray correlation. In the case of both detections however, a slow, steady rise in optical flux was evident before  $\gamma$ -ray emission was detected. Although optical variation was evident in

---

### 8.3. Interpretation and Conclusions

---

the 2006-07 data presented in this thesis, it occurred over much shorter timescales. Longer-term optical and  $\gamma$ -ray light curves may be necessary in order to observe any correlation present.

Wagner (1996) presented evidence for short timescale correlations between optical and high-energy (HE; MeV - GeV)  $\gamma$ -ray emission from ten blazars which had previously been detected by EGRET. Low photon-count limitations and poor ( $< 1$ -day) sampling are noted as caveats for these findings, however. This study did not include simultaneous TeV observations and so no conclusions could be drawn about optical/TeV correlations. Short timescale correlations between optical band and HE band is expected by certain leptonic emission models (Bloom *et al.*, 1997).

### 8.3 Interpretation and Conclusions

In the context of a one-zone Synchrotron Self-Compton (SSC) emission model, the trend of increasing variability at higher energies may be interpreted as the high-energy photons, which are characterised by shorter synchrotron cooling times (*e.g.* for the Crab Nebula,  $t_{cool} \simeq 50$  years for 20 keV photons and  $t_{cool} \simeq 1300$  years for 40 keV photons), being generated by energetic particles in the relativistic jet. A state of higher flux would suggest a change in the population of electrons causing the emission. A freshly injected population of electrons has a flatter high-energy slope and a higher maximum energy than an aging electron population. This scenario would lead to a shift in the Inverse Compton peak to higher energies in the spectral energy distribution, which has been seen in some multiwavelength studies of TeV blazars (*e.g.* Albert *et al.*, 2007f). In the 2006-07 observing season, Markarian 421 was observed to exhibit  $\sim 5$  times more short term  $\gamma$ -ray variability ( $F_{pp}$ ) than optical variability during the campaign. In the case of Markarian 501, the  $\gamma$ -ray band exhibited over 170 times more short term variability than the optical band. Due to the long synchrotron cooling times of the optically

### 8.3. Interpretation and Conclusions

---

emitting electrons, the lower level of variability seen in the optical band (when compared to the variability exhibited in the  $\gamma$ -ray band) during the 2006-07 season is expected. This difference in cooling times between the high-energy and low-energy emitting electrons is one possible explanation for the lack of a tight correlation between the optical and TeV bands. If flaring is rapid, pile-up of flares may occur in the optical band where cooling times longer. This may hide the underlying shot structure responsible for the flaring behaviour.

Single-zone SSC models have been largely successful in explaining the x-ray and  $\gamma$ -ray emission of blazars via synchrotron and inverse Compton processes. However, these models have been less successful at accounting for the optical and radio (*i.e.* lower-energy) spectral energy distributions (SEDs), generally underestimating their observed flux considerably. Błażejowski *et al.* (2005) modified the one-zone model to include two additional emission sites; one site of radio emission and one site of optical emission, both located farther along the jet than the x-ray/ $\gamma$ -ray zone but separated from each other. Each site of emission in this modified model has a different SED, which allows for better spectral fitting in different energy bands. If low-energy and high-energy emissions occur in physically separated regions of the jet, then correlation between emission in these bands would not be expected over the timescales examined in this thesis. As such, the findings of this thesis favour a model which incorporates multiple zones of emission.

External Compton models suggest that synchrotron processes in a single electron population are responsible for the infrared to x-ray component of the blazar's spectral energy distribution. The seed photons, which are scattered to higher energies by inverse Compton processes, are thought to be ambient photons in some region of the active galaxy that is external to the relativistic jet. As is the case with the one-zone SSC model, external Compton models predict that optical emission and  $\gamma$ -ray emission should be correlated due to fact that the electron population –

## 8.4. Future Studies

---

the source of the optical emission (Section 3.2.1) – is thought to scatter the ambient photons to higher energies at one site of emission. Therefore, the findings of this thesis run contrary to the predictions of external Compton models.

Generally, hadronic models are not favoured over leptonic models when describing the processes responsible for TeV blazar emission. For instance, Aharonian (2000) suggested a model which fits the spectral energy distribution of both Markarian 421 and Markarian 501 very well. However, regions of the jet with magnetic fields of 30 - 100 G were required for the model to fit the observations. By comparison, magnetic fields of  $\leq 1$  G are typically required for most SSC models.

Although a correlation was not found between  $\gamma$ -ray and optical emission over the time frame of this study, given the above multi-zone SSC emission model, it may be possible that correlations do exist albeit on longer timescales. Shocks moving along the jet will encounter each site of emission in turn. The result of this would be that optical (and radio) emission would lag x-ray and  $\gamma$ -ray considerably. Therefore, the nature of the optical/ $\gamma$ -ray relationship for HBLs, if one exists, may only clearly reveal itself in longer-term studies. With this in mind, it is worth noting that the blazar monitoring programme at the Whipple 10 m telescope is currently in its third year and should continue into the future. The multiwavelength observations of Markarian 421 in the 2005-06 observing season will be presented in Horan *et al.* (2009). Observations of the other blazars over multiple seasons will be presented in further publications.

## 8.4 Future Studies

The work presented in this thesis has been conducted in the context of a larger multiwavelength observation campaign that was initiated by the VERITAS Collaboration in 2005. Observations at infrared, radio and x-ray wavelengths have been taken as part of this campaign. Optical data

#### 8.4. Future Studies

---

in the B-band, V-band and R-band (*i.e.* UVBRI filter set as opposed to SDSS filter set) have also been obtained from a number of observatories around the world<sup>1</sup>. These data will be combined with the data presented in this thesis to form the basis of a comprehensive multiwavelength study. Spectral analysis will be conducted as part of these studies.

One particular strength of this type of observing campaign is that the sources have been monitored at all wavelengths regardless of flux level in a particular waveband. Hence, the spectral energy densities of the blazars for nights when the flux in a certain waveband was high may be compared to the spectral energy density on nights when the flux was low in that band. Spectral energy density fitting may then be used to constrain model parameters for different flux level scenarios.

Multiwavelength observations of the five blazars discussed in this thesis have continued in the 2007-08 observing season. The multiwavelength observing campaign is planned to continue for at least one more year providing an incredibly rich, well-sampled data set across the electromagnetic spectrum.

The Whipple 10 m telescope will continue to be used to monitor blazars in this manner, as part of the multiwavelength campaign, for the foreseeable future. However, the current generation of imaging atmospheric Cherenkov telescopes, such as VERITAS, have surpassed the capability of the Whipple 10 m telescope by having superior energy thresholds, angular resolution, flux sensitivity and energy resolution. If a similar blazar monitoring campaign was initiated with VERITAS used in place of the Whipple 10 m telescope at TeV energies, more features could be discerned in the TeV light curves obtained since the flux sensitivity would be much greater. It is also likely that emission from the blazars would be detected while they were in a quiescent state. The superior energy resolution offered by the telescope would provide more accurate SEDs and more of the spectrum would be covered due to the lower en-

---

<sup>1</sup>see <http://veritas.sao.arizona.edu/content/blogspot/6/40/> for a list of collaborators.

## 8.5. The Future of $\gamma$ -ray Astronomy

---

ergy threshold of the system. However, the amount of observation time required to conduct such a study would be difficult to obtain given the limited amount of observation time available to such telescopes ( $\sim 800$  hours per year).

## 8.5 The Future of $\gamma$ -ray Astronomy

The development of the field of very high energy astrophysics over the past two decades has been nothing short of extraordinary. Twenty years ago, only a single source of TeV  $\gamma$ -rays had yet been detected at a high level of statistical significance. Since then, the development pace for the technology and techniques has been rapid.

The race for higher sensitivity and lower energy thresholds in very high energy  $\gamma$ -ray astronomy has driven the establishment of current generation instruments such as VERITAS, HESS and MAGIC. Although these observatories have only come online in the last number of years, the future of ground-based  $\gamma$ -ray astronomy is already being shaped. The HESS Collaboration are constructing the HESS II: an additional 30 m telescope married to their current array of four 12 m telescopes (Horns *et al.*, 2007). MAGIC will also soon finish construction of MAGIC II: an additional 17 m telescope to work stereoscopically with the currently operated 17 m telescope, which will utilise a new type of triggering system and hybrid photomultiplier detectors (Baixeras *et al.*, 2005). These additions will drive energy thresholds lower still, opening the  $\gamma$ -ray window that little bit farther.

Looking beyond the “upgrades” to current generation observatories, the next generation of ground-based observatories are already being discussed. The Cherenkov Telescope Array (CTA) and the Advanced Gamma-ray Imaging System (AGIS) are, respectively, the European and American efforts currently being posited as a possible step forward. A number of possible designs have been proposed for both projects. AGIS, for in-

## 8.5. The Future of $\gamma$ -ray Astronomy

---

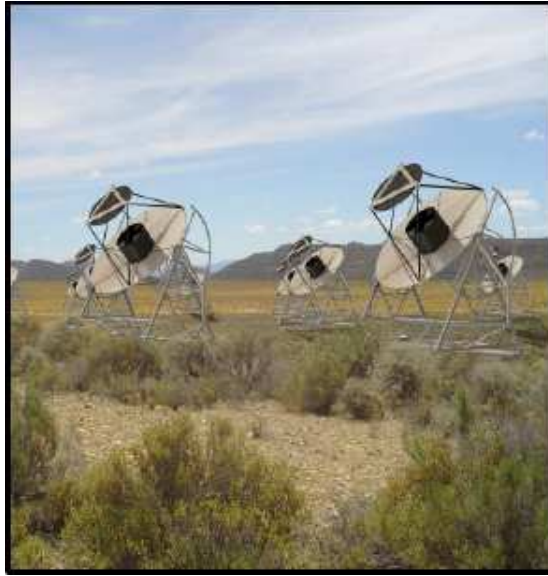


**Figure 8.1:** Artist's concept of one possible design for AGIS.

stance, may be a  $1 \text{ km}^2$  array of telescopes with opening apertures of 10 - 12 m. The use of different sized telescopes throughout the array, different spacing schemes and possible new technologies are all being explored for use in the designs. CTA design concepts have been similar to those of AGIS but include the possibility of a site in the northern hemisphere as well as a site in the southern hemisphere. AGIS and CTA may eventually merge into one world-wide collaboration to construct telescopes which can overcome some of the inescapable shortfalls of the current generation of observatories. An artist's concept of AGIS is shown in Figure 8.1.

With the current generation of VHE  $\gamma$ -ray telescopes producing detections at an unprecedented rate, and with the next generation already in development, the future of the Whipple 10 m telescope is somewhat uncertain. However, given the limited amount of observation time available (due to the dependence on the lunar cycle) and the relatively small number of VHE  $\gamma$ -ray observatories in existence, there is still a place for

## 8.5. The Future of $\gamma$ -ray Astronomy

---

Whipple 10 m telescope in the future of  $\gamma$ -ray astronomy. Although no longer the most sensitive telescope in the VHE waveband, it still has the ability to detect blazars when they are flaring at or near the flux level of the Crab Nebula, for instance. This means that it could still have the capability to discover emission of VHE  $\gamma$ -rays from blazars that were not previously known to emit in this band, while also acting as a trigger for known TeV blazars if they flare. It may also be used to act as a testbed for new technologies which could subsequently be utilised on newer observatories, reducing the negative impact this would otherwise have on their duty cycle. Clearly, the Whipple 10 m telescope remains a valuable scientific instrument and will continue to be one for a number of years to come.

One of the major developments which will influence the entire field of high-energy astrophysics in the coming years is the recent launch of NASA's GLAST mission. This high-energy  $\gamma$ -ray satellite will close the energy gap which has existed between ground-based and space-borne experiments, leading to a variety of new discoveries. The satellite was launched in June 2008 (Figure 8.2). GLAST's unprecedented sensitivity, large field of view and angular resolution (for its energy band) will offer those working on ground-based experiments a new scheme for triggering observations as well as new scientific basis for observing different potential sources of TeV  $\gamma$ -rays.

Overall, the future of  $\gamma$ -ray astronomy looks incredibly promising. Longterm observations and population studies of the rapidly-growing catalogue of TeV  $\gamma$ -ray sources will undoubtedly reveal much about the processes which underlie their emission. The implications of these findings can only add to our understanding of physics in general.

## 8.5. The Future of $\gamma$ -ray Astronomy

---



**Figure 8.2:** The launch of GLAST which took place on 11<sup>th</sup> of June, 2008.

## 8.5. The Future of $\gamma$ -ray Astronomy

---

# Appendix A

## Data Files

ON Run	OFF Run	Date	Exp. Time
		[yyyy-mm-dd]	[min]
gt031906	gt031907	2006-09-30	27.5
gt032013	gt032014	2006-10-19	27.5
gt032110	gt032111	2006-10-23	27.5
gt032125	gt032126	2006-10-27	27.5
gt032148	gt032149	2006-10-30	14.0
gt032224	gt032225	2006-11-16	27.5
gt032242	gt032243	2006-11-17	27.5
gt032244	gt032245	2006-11-17	27.5
gt032263	gt032264	2006-11-18	27.5
gt032281	gt032282	2006-11-19	27.5
gt032363	gt032364	2006-11-23	27.5
gt032473	gt032474	2006-12-14	27.5
gt032475	gt032476	2006-12-14	27.5
gt032489	gt032490	2006-12-15	27.5
gt032503	gt032504	2006-12-16	20.0

Continued on next page...

---

ON Run	OFF Run	Date	Exp. Time
gt032505	gt032506	2006-12-16	27.5
gt032521	gt032522	2006-12-21	27.5
gt032580	gt032581	2007-01-10	27.5
gt032615	gt032616	2007-01-16	27.5
gt032638	gt032639	2007-01-17	27.5
gt032658	gt032659	2007-01-24	27.5
gt032678	gt032679	2007-02-07	27.5
gt032698	gt032699	2007-02-09	17.0
gt032712	gt032713	2007-02-13	27.5
gt032740	gt032741	2007-02-17	27.5
gt032849	gt032850	2007-03-12	11.0
gt032878	gt032879	2007-03-14	27.5
gt032894	gt032895	2007-03-15	27.5
gt032913	gt032914	2007-03-16	27.5

---

**Table A.1:** Crab pairs used to optimise cuts for the 2006-07 season.

---

<b>ON Run</b>	<b>OFF Run</b>	<b>Date</b>	<b>Exp. Time</b>
		[yyyy-mm-dd]	[min]
gt032388	gt032387	2006-11-25	27.5
gt032389	-	2006-11-25	25.0
gt032414	-	2006-11-28	16.0
gt032511	-	2006-12-16	27.5
gt032531	gt032530	2006-12-21	27.5
gt032532	-	2006-12-21	27.5
gt032533	-	2006-12-21	27.5
gt032534	-	2006-12-21	9.0
gt032599	gt032600	2007-01-15	27.5
gt032601	-	2007-01-15	27.5
gt032602	-	2007-01-15	27.4
gt032623	gt032624	2007-01-16	27.5
gt032625	-	2007-01-16	27.5
gt032628	-	2007-01-16	27.4
gt032645	-	2007-01-17	27.5
gt032646	gt032647	2007-01-17	27.5
gt032663	-	2007-01-27	27.5
gt032664	gt032665	2007-01-27	27.5
gt032670	-	2007-01-28	27.5
gt032721	gt032722	2007-02-16	27.5
gt032723	-	2007-02-16	27.5
gt032724	-	2007-02-16	27.5
gt032727	-	2007-02-16	27.5
gt032744	-	2007-02-17	27.5
gt032745	gt032746	2007-02-17	27.5

---

Continued on next page...

---

ON Run	OFF Run	Date	Exp. Time
gt032747	-	2007-02-17	27.5
gt032749	-	2007-02-17	27.5
gt032788	-	2007-02-19	27.5
gt032789	-	2007-02-19	27.5
gt032799	-	2007-02-21	27.5
gt032800	-	2007-02-21	27.5
gt032801	gt032802	2007-02-21	27.5
gt032815	-	2007-02-23	27.5
gt032818	-	2007-02-23	27.5
gt032825	-	2007-02-25	27.5
gt032826	-	2007-02-25	27.5
gt032836	-	2007-03-09	27.5
gt032845	-	2007-03-11	27.5
gt032846	-	2007-03-11	21.5
gt032855	gt032856	2007-03-12	25.0
gt032857	-	2007-03-12	27.5
gt032858	-	2007-03-12	27.5
gt032869	-	2007-03-13	27.5
gt032870	-	2007-03-13	27.5
gt032871	gt032872	2007-03-13	27.5
gt032885	-	2007-03-15	10.0
gt032886	-	2007-03-15	27.5
gt032887	gt032888	2007-03-15	27.5
gt032901	-	2007-03-15	27.5
gt032902	-	2007-03-15	27.5
gt032903	-	2007-03-15	27.5
gt032923	gt032924	2007-03-16	27.5

---

Continued on next page...

---

ON Run	OFF Run	Date	Exp. Time
gt032925	-	2007-03-16	27.5
gt032926	-	2007-03-16	27.5
gt032947	-	2007-03-17	14.0
gt032955	-	2007-03-18	27.5
gt032957	-	2007-03-18	24.0
gt032973	-	2007-03-20	27.5
gt032974	gt032975	2007-03-20	27.5
gt032976	-	2007-03-20	27.5
gt032999	gt033000	2007-03-25	27.5
gt033014	-	2007-04-08	27.5
gt033015	-	2007-04-08	27.5
gt033017	gt033018	2007-04-08	19.5
gt033024	gt033025	2007-04-11	27.5
gt033026	-	2007-04-11	27.5
gt033028	-	2007-04-11	27.5
gt033029	-	2007-04-11	27.5
gt033030	-	2007-04-11	9.5
gt033031	gt033032	2007-04-11	14.0
gt033051	-	2007-04-14	27.5
gt033052	gt033053	2007-04-14	27.5
gt033054	-	2007-04-14	27.5
gt033068	-	2007-04-15	27.5
gt033069	-	2007-04-15	24.0
gt033070	gt033071	2007-04-15	27.5
gt033072	gt033073	2007-04-15	27.5
gt033088	-	2007-04-16	27.5
gt033090	-	2007-04-16	27.5

---

Continued on next page...

---

ON Run	OFF Run	Date	Exp. Time
gt033091	-	2007-04-16	27.5
gt033092	gt033093	2007-04-16	27.5
gt033105	-	2007-04-18	27.5
gt033106	-	2007-04-18	27.5
gt033107	-	2007-04-18	27.5
gt033108	-	2007-04-18	27.5
gt033124	-	2007-04-19	27.5
gt033125	-	2007-04-19	21.5
gt033126	-	2007-04-19	27.5
gt033137	-	2007-04-20	27.5
gt033138	-	2007-04-20	27.5
gt033139	gt033140	2007-04-20	10.0
gt033182	-	2007-05-08	27.0
gt033183	-	2007-05-08	27.5
gt033190	-	2007-05-09	27.5
gt033191	-	2007-05-09	27.5
gt033197	gt033198	2007-05-10	27.5
gt033199	-	2007-05-10	27.5
gt033200	-	2007-05-10	27.5
gt033209	-	2007-05-11	27.5
gt033210	-	2007-05-11	27.5
gt033211	gt033212	2007-05-11	27.5
gt033220	-	2007-05-12	27.5
gt033221	-	2007-05-12	27.5
gt033234	-	2007-05-13	22.0
gt033252	-	2007-05-15	27.5
gt033253	-	2007-05-15	11.0

---

Continued on next page...

---

ON Run	OFF Run	Date	Exp. Time
gt033254	-	2007-05-15	27.5
gt033255	-	2007-05-15	27.5
gt033292	-	2007-05-18	27.5
gt033294	-	2007-05-18	27.5
gt033359	-	2007-06-06	27.5
gt033374	-	2007-06-08	18.0
gt033383	-	2007-06-09	27.5

---

**Table A.2:** Markarian 421 data analysed for this thesis.

---

<b>ON Run</b>	<b>OFF Run</b>	<b>Date</b>	<b>Exp. Time</b>
		[yyyy-mm-dd]	[min]
gt032756	-	2007-02-17	27.5
gt032757	-	2007-02-17	27.5
gt032811	-	2007-02-21	27.5
gt032812	-	2007-02-21	25.5
gt032824	-	2007-02-23	27.5
gt032829	-	2007-02-25	27.5
gt032830	-	2007-02-25	27.5
gt032911	-	2007-03-15	27.5
gt032930	-	2007-03-16	27.5
gt032931	gt032932	2007-03-16	27.5
gt032952	-	2007-03-17	9.0
gt032968	-	2007-03-18	27.5
gt032969	-	2007-03-18	20.0
gt032985	-	2007-03-20	27.5
gt032986	-	2007-03-20	15.0
gt032987	-	2007-03-20	27.5
gt033004	-	2007-03-25	23.0
gt033005	-	2007-03-25	27.5
gt033009	gt033010	2007-03-26	27.5
gt033011	-	2007-03-26	13.5
gt033064	-	2007-04-14	27.5
gt033065	gt033066	2007-04-14	22.0
gt033080	-	2007-04-15	27.5
gt033081	-	2007-04-15	27.5
gt033083	gt033084	2007-04-15	22.5

---

Continued on next page...

---

ON Run	OFF Run	Date	Exp. Time
gt033099	-	2007-04-16	27.5
gt033100	-	2007-04-16	27.5
gt033114	-	2007-04-18	7.5
gt033115	-	2007-04-18	27.5
gt033116	gt033117	2007-04-18	27.5
gt033118	-	2007-04-18	27.5
gt033119	-	2007-04-18	20.5
gt033132	-	2007-04-19	27.5
gt033147	-	2007-04-20	27.5
gt033148	-	2007-04-20	27.5
gt033149	-	2007-04-20	27.5
gt033155	-	2007-04-23	27.5
gt033156	-	2007-04-23	27.5
gt033157	-	2007-04-23	27.5
gt033158	-	2007-04-23	19.5
gt033164	-	2007-04-23	24.0
gt033165	-	2007-04-23	7.0
gt033166	-	2007-04-23	24.0
gt033171	-	2007-04-24	27.5
gt033172	-	2007-04-24	23.5
gt033195	-	2007-05-09	19.5
gt033205	gt033206	2007-05-10	27.5
gt033207	-	2007-05-10	27.5
gt033218	gt033219	2007-05-11	27.5
gt033229	gt033230	2007-05-12	27.5
gt033231	-	2007-05-12	25.0
gt033238	-	2007-05-13	27.5

---

Continued on next page...

---

ON Run	OFF Run	Date	Exp. Time
gt033239	-	2007-05-13	27.5
gt033240	-	2007-05-13	27.5
gt033241	gt033242	2007-05-13	27.5
gt033261	-	2007-05-15	27.5
gt033262	-	2007-05-15	27.5
gt033263	-	2007-05-15	27.5
gt033274	-	2007-05-16	27.5
gt033275	gt033276	2007-05-16	14.0
gt033286	-	2007-05-17	27.5
gt033287	-	2007-05-17	20.0
gt033300	gt033301	2007-05-18	27.5
gt033302	-	2007-05-18	27.5
gt033310	gt033311	2007-05-19	27.5
gt033312	-	2007-05-19	13.0
gt033321	-	2007-05-20	25.0
gt033322	-	2007-05-20	15.0
gt033332	-	2007-05-21	25.0
gt033339	-	2007-05-22	27.5
gt033340	-	2007-05-22	27.5
gt033345	-	2007-05-23	27.5
gt033346	-	2007-05-23	27.5
gt033353	-	2007-05-24	27.5
gt033362	-	2007-06-06	27.5
gt033370	-	2007-06-07	27.5
gt033372	-	2007-06-07	23.0
gt033379	gt033380	2007-06-08	27.5
gt033388	gt033389	2007-06-09	27.5

---

Continued on next page...

---

ON Run	OFF Run	Date	Exp. Time
gt033429	gt033430	2007-06-13	27.5
gt033431	-	2007-06-13	27.5
gt033432	-	2007-06-13	27.5
gt033441	gt033442	2007-06-14	27.5
gt033443	-	2007-06-14	27.5
gt033444	-	2007-06-14	26.0
gt033455	gt033456	2007-06-15	27.5
gt033457	-	2007-06-15	27.5
gt033458	-	2007-06-15	27.5
gt033459	-	2007-06-15	27.5
gt033477	gt033478	2007-06-17	27.5
gt033490	gt033491	2007-06-18	25.0
gt033492	-	2007-06-18	27.5
gt033501	-	2007-06-19	27.5
gt033502	-	2007-06-19	27.5
gt033511	-	2007-06-21	27.5
gt033512	-	2007-06-21	27.5
gt033513	-	2007-06-21	14.0
gt033519	gt033520	2007-06-21	13.0
gt033521	-	2007-06-21	27.5
gt033527	-	2007-06-22	27.5
gt033535	gt033536	2007-06-23	14.5
gt033542	-	2007-06-24	27.5

---

**Table A.3:** Markarian 501 data analysed for this thesis.

---

<b>ON Run</b>	<b>OFF Run</b>	<b>Date</b>	<b>Exp. Time</b>
		[yyyy-mm-dd]	[min]
gt031801	gt031802	2006-09-20	27.5
gt031813	-	2006-09-22	27.5
gt031824	-	2006-09-25	27.5
gt031825	-	2006-09-25	27.5
gt031828	-	2006-09-25	27.5
gt031845	-	2006-09-26	27.5
gt031846	-	2006-09-26	27.0
gt031847	-	2006-09-26	26.0
gt031848	-	2006-09-26	27.5
gt031863	-	2006-09-27	27.5
gt031878	-	2006-09-28	27.5
gt031879	-	2006-09-28	27.5
gt031962	-	2006-10-16	17.0
gt031995	gt031996	2006-10-19	27.5
gt032019	gt032020	2006-10-20	27.5
gt032021	-	2006-10-20	27.5
gt032043	gt032044	2006-10-21	27.5
gt032067	gt032068	2006-10-22	27.5
gt032091	gt032092	2006-10-23	27.5
gt032093	-	2006-10-23	27.5
gt033279	-	2007-05-16	27.5
gt033314	-	2007-05-19	27.5
gt033324	-	2007-05-20	27.5
gt033333	-	2007-05-21	27.5
gt033342	-	2007-05-22	24.0

---

Continued on next page...

---

ON Run	OFF Run	Date	Exp. Time
gt033356	-	2007-05-24	27.5
gt033433	gt033434	2007-06-13	17.5
gt033435	-	2007-06-13	27.5
gt033446	gt033447	2007-06-14	20.0
gt033448	-	2007-06-14	27.5
gt033449	-	2007-06-14	27.5
gt033461	gt033462	2007-06-15	27.5
gt033463	-	2007-06-15	27.5
gt033464	-	2007-06-15	27.5
gt033482	gt033483	2007-06-17	14.0
gt033484	-	2007-06-17	27.5
gt033494	gt033495	2007-06-18	27.5
gt033496	-	2007-06-18	27.5
gt033497	-	2007-06-18	27.5
gt033504	gt033505	2007-06-19	15.0
gt033506	-	2007-06-19	27.5
gt033507	-	2007-06-19	27.5
gt033508	-	2007-06-19	22.5
gt033516	-	2007-06-20	27.5
gt033517	-	2007-06-20	27.5
gt033522	gt033523	2007-06-21	26.0
gt033524	-	2007-06-21	27.5
gt033544	-	2007-06-24	13.0

---

**Table A.4:** 1ES 1959+650 data analysed for this thesis.

---

<b>ON Run</b>	<b>OFF Run</b>	<b>Date</b>	<b>Exp. Time</b>
		[yyyy-mm-dd]	[min]
gt031814	-	2006-09-22	27.5
gt031830	-	2006-09-25	27.5
gt031835	gt031836	2006-09-25	15.0
gt031881	-	2006-09-28	27.5
gt031882	gt031883	2006-09-28	14.0
gt031884	-	2006-09-28	27.5
gt031885	-	2006-09-28	27.5
gt031896	gt031897	2006-09-30	27.5
gt031898	-	2006-09-30	27.5
gt031899	-	2006-09-30	27.5
gt031900	-	2006-09-30	13.0
gt031922	gt031923	2006-10-02	27.5
gt031939	-	2006-10-13	23.5
gt031970	-	2006-10-16	19.0
gt031971	-	2006-10-16	27.5
gt031985	gt031986	2006-10-17	27.5
gt031987	-	2006-10-17	27.5
gt031988	-	2006-10-17	27.5
gt032003	gt032004	2006-10-19	27.5
gt032027	-	2006-10-20	27.5
gt032029	-	2006-10-20	27.5
gt032050	gt032051	2006-10-21	27.5
gt032052	-	2006-10-21	27.5
gt032075	-	2006-10-22	27.5
gt032099	-	2006-10-23	27.5

---

Continued on next page...

---

ON Run	OFF Run	Date	Exp. Time
gt032101	-	2006-10-23	27.5
gt032141	-	2006-10-29	27.5
gt032143	-	2006-10-29	20.5
gt032181	-	2006-11-14	27.5
gt032182	gt032183	2006-11-14	27.5
gt032184	-	2006-11-14	27.5
gt032212	-	2006-11-16	27.5
gt032213	gt032214	2006-11-16	27.5
gt032215	-	2006-11-16	27.5
gt032231	-	2006-11-17	27.5
gt032232	gt032233	2006-11-17	14.5
gt032234	-	2006-11-17	27.5
gt032252	-	2006-11-18	27.5
gt032272	-	2006-11-19	27.5
gt032294	-	2006-11-20	27.5
gt032307	-	2006-11-21	27.5
gt032309	-	2006-11-21	27.5
gt032325	-	2006-11-22	27.5
gt032327	-	2006-11-22	27.5
gt032328	-	2006-11-22	27.5
gt032347	gt032348	2006-11-23	27.5
gt032349	-	2006-11-23	27.5
gt032350	-	2006-11-23	27.5
gt032372	-	2006-11-25	27.5
gt032374	gt032375	2006-11-25	27.5
gt032419	-	2006-12-10	18.0
gt032423	-	2006-12-10	27.5

---

Continued on next page...

---

ON Run	OFF Run	Date	Exp. Time
gt032430	-	2006-12-11	27.5
gt032437	gt032438	2006-12-12	27.5
gt032439	-	2006-12-12	11.0
gt032463	-	2006-12-14	22.5
gt032466	-	2006-12-14	23.0
gt032479	-	2006-12-15	18.0
gt032481	-	2006-12-15	27.5
gt032495	-	2006-12-16	15.0
gt032496	-	2006-12-16	27.5
gt032497	-	2006-12-16	27.5
gt032513	-	2006-12-21	27.5
gt032514	-	2006-12-21	27.5
gt032515	-	2006-12-21	27.5
gt032536	-	2006-12-22	27.5
gt032537	-	2006-12-22	27.5
gt032538	-	2006-12-22	27.5
gt032566	gt032567	2007-01-09	19.0
gt032575	-	2007-01-11	27.5
gt032611	-	2007-01-16	27.5
gt032633	-	2007-01-17	27.5

---

**Table A.5:** 1ES 2344+514 data analysed for this thesis.

---

<b>ON Run</b>	<b>OFF Run</b>	<b>Date</b>	<b>Exp. Time</b>
		[yyyy-mm-dd]	[min]
gt032630	-	2007-01-16	27.5
gt032651	-	2007-01-17	27.5
gt032654	-	2007-01-17	14.0
gt032667	-	2007-01-27	5.0
gt032668	-	2007-01-27	27.5
gt032672	-	2007-01-28	27.5
gt032728	gt032729	2007-02-16	27.5
gt032730	-	2007-02-16	27.5
gt032731	-	2007-02-16	27.5
gt032732	-	2007-02-16	27.5
gt032753	gt032754	2007-02-17	27.5
gt032755	-	2007-02-17	27.5
gt032790	-	2007-02-19	21.0
gt032806	-	2007-02-21	27.5
gt032807	-	2007-02-21	27.5
gt032819	-	2007-02-23	26.5
gt032820	-	2007-02-23	27.5
gt032821	gt032822	2007-02-23	27.5
gt032860	-	2007-03-12	24.5
gt032861	-	2007-03-12	19.5
gt032876	gt032877	2007-03-13	22.0
gt032890	-	2007-03-14	27.5
gt032891	-	2007-03-14	27.5
gt032892	gt032893	2007-03-14	16.0
gt032906	-	2007-03-15	27.5

---

Continued on next page...

---

ON Run	OFF Run	Date	Exp. Time
gt032908	gt032909	2007-03-15	27.5
gt032927	gt032928	2007-03-16	27.5
gt032929	-	2007-03-16	27.5
gt032949	-	2007-03-17	15.0
gt032950	-	2007-03-17	22.5
gt032961	-	2007-03-18	14.0
gt032962	-	2007-03-18	22.5
gt032980	-	2007-03-20	27.5
gt032981	gt032982	2007-03-20	27.5
gt032983	-	2007-03-20	27.5
gt033001	-	2007-03-25	6.5
gt033002	gt033003	2007-03-25	27.5
gt033008	-	2007-03-26	27.5
gt033033	-	2007-04-11	22.0
gt033059	-	2007-04-14	27.0
gt033060	-	2007-04-14	27.5
gt033061	-	2007-04-14	27.5
gt033062	gt033063	2007-04-14	11.0
gt033076	-	2007-04-15	27.0
gt033077	-	2007-04-15	27.5
gt033078	gt033079	2007-04-15	19.5
gt033095	gt033096	2007-04-16	8.5
gt033097	-	2007-04-16	27.5
gt033098	-	2007-04-16	27.5
gt033110	-	2007-04-18	27.5
gt033111	-	2007-04-18	27.5
gt033112	-	2007-04-18	27.5

---

Continued on next page...

---

ON Run	OFF Run	Date	Exp. Time
gt033113	-	2007-04-18	27.5
gt033128	-	2007-04-19	27.5
gt033129	-	2007-04-19	27.5
gt033130	gt033131	2007-04-19	27.5
gt033141	-	2007-04-20	27.5
gt033142	-	2007-04-20	27.5
gt033144	gt033145	2007-04-20	27.5
gt033152	gt033153	2007-04-22	16.5
gt033154	-	2007-04-22	27.5
gt033160	-	2007-04-23	27.5
gt033162	gt033163	2007-04-23	27.5
gt033168	-	2007-04-24	27.5
gt033169	gt033170	2007-04-24	27.5
gt033177	gt033178	2007-05-07	27.5
gt033179	-	2007-05-07	7.0
gt033184	gt033185	2007-05-08	17.5
gt033186	-	2007-05-08	27.5
gt033194	-	2007-05-09	27.5
gt033201	-	2007-05-10	27.5
gt033202	-	2007-05-10	14.0
gt033203	-	2007-05-10	27.5
gt033215	gt033216	2007-05-11	27.5
gt033225	-	2007-05-12	27.5
gt033227	gt033228	2007-05-12	27.5
gt033235	-	2007-05-13	27.5
gt033237	-	2007-05-13	27.5
gt033244	-	2007-05-14	22.5

---

Continued on next page...

---

ON Run	OFF Run	Date	Exp. Time
gt033257	-	2007-05-15	27.5
gt033258	-	2007-05-15	27.5
gt033259	-	2007-05-15	27.5
gt033260	-	2007-05-15	27.5
gt033268	-	2007-05-16	27.5
gt033273	-	2007-05-16	27.5
gt033282	-	2007-05-17	27.5
gt033283	-	2007-05-17	14.0
gt033295	-	2007-05-18	27.5
gt033306	gt033307	2007-05-19	21.0
gt033318	-	2007-05-20	27.5
gt033319	-	2007-05-20	27.5
gt033337	-	2007-05-22	27.5
gt033352	-	2007-05-24	27.5
gt033360	gt033361	2007-06-06	27.5
gt033366	-	2007-06-07	27.5
gt033367	-	2007-06-07	27.5
gt033368	-	2007-06-07	27.5
gt033376	gt033377	2007-06-08	27.5
gt033378	-	2007-06-08	27.5
gt033384	gt033385	2007-06-09	27.5
gt033386	-	2007-06-09	27.5
gt033387	-	2007-06-09	27.5
gt033409	-	2007-06-12	27.5
gt033424	gt033425	2007-06-13	27.5
gt033426	-	2007-06-13	17.0
gt033427	-	2007-06-13	27.5

---

Continued on next page...

---

ON Run	OFF Run	Date	Exp. Time
gt033437	gt033438	2007-06-14	27.5
gt033439	-	2007-06-14	27.5
gt033440	-	2007-06-14	27.5
gt033451	gt033452	2007-06-15	27.5
gt033453	-	2007-06-15	27.5
gt033454	-	2007-06-15	27.5
gt033466	gt033467	2007-06-16	27.5
gt033474	gt033475	2007-06-17	27.5
gt033476	-	2007-06-17	27.5
gt033487	gt033488	2007-06-18	27.5
gt033489	-	2007-06-18	27.5
gt033499	-	2007-06-19	27.5
gt033500	-	2007-06-19	27.5
gt033510	-	2007-06-20	15.5

---

**Table A.6:** H 1426+428 data analysed for this thesis.

---

ON Run	OFF Run	Date	Exp. Time
gt031802	-	2006-09-20	27.5
gt031836	-	2006-09-25	27.5
gt031838	-	2006-09-25	27.5
gt031840	-	2006-09-25	27.5
gt031852	-	2006-09-26	27.5
gt031856	-	2006-09-26	27.5
gt031858	-	2006-09-26	27.5
gt031860	-	2006-09-26	27.5
gt031872	-	2006-09-27	27.5
gt031874	-	2006-09-27	27.5
gt031876	-	2006-09-27	27.5
gt031883	-	2006-09-28	27.5
gt031887	-	2006-09-28	27.5
gt031889	-	2006-09-28	27.5
gt031891	-	2006-09-28	27.5
gt031893	-	2006-09-28	27.5
gt031897	-	2006-09-30	27.5
gt031903	-	2006-09-30	27.5
gt031905	-	2006-09-30	27.5
gt031907	-	2006-09-30	27.5
gt031918	-	2006-10-01	20.0
gt031923	-	2006-10-02	27.5
gt031925	-	2006-10-02	27.5
gt031927	-	2006-10-02	27.5
gt031964	-	2006-10-16	27.5
gt031966	-	2006-10-16	17.0

---

Continued on next page...

---

<b>ON Run</b>	<b>OFF Run</b>	<b>Date</b>	<b>Exp. Time</b>
		[yyyy-mm-dd]	[min]
gt031969	-	2006-10-16	27.5
gt031973	-	2006-10-16	27.5
gt031980	-	2006-10-17	10.0
gt031982	-	2006-10-17	12.0
gt031984	-	2006-10-17	27.5
gt031986	-	2006-10-17	27.5
gt031991	-	2006-10-17	27.5
gt031996	-	2006-10-19	27.5
gt031999	-	2006-10-19	27.5
gt032004	-	2006-10-19	27.5
gt032007	-	2006-10-19	27.5
gt032009	-	2006-10-19	27.5
gt032011	-	2006-10-19	27.5
gt032020	-	2006-10-20	27.5
gt032032	-	2006-10-20	27.5
gt032034	-	2006-10-20	27.5
gt032036	-	2006-10-20	17.0
gt032044	-	2006-10-21	27.5
gt032046	-	2006-10-21	12.0
gt032048	-	2006-10-21	27.5
gt032051	-	2006-10-21	27.5
gt032055	-	2006-10-21	27.5
gt032057	-	2006-10-21	27.5
gt032061	-	2006-10-21	27.5
gt032066	-	2006-10-22	27.5
gt032068	-	2006-10-22	27.5
gt032071	-	2006-10-22	27.5

---

Continued on next page...

---

<b>ON Run</b>	<b>OFF Run</b>	<b>Date</b>	<b>Exp. Time</b>
		[yyyy-mm-dd]	[min]
gt032077	-	2006-10-22	27.5
gt032080	-	2006-10-22	27.5
gt032085	-	2006-10-22	27.5
gt032092	-	2006-10-23	27.5
gt032097	-	2006-10-23	27.5
gt032100	-	2006-10-23	27.5
gt032104	-	2006-10-23	27.5
gt032106	-	2006-10-23	27.5
gt032108	-	2006-10-23	27.5
gt032111	-	2006-10-23	27.5
gt032121	-	2006-10-27	27.5
gt032123	-	2006-10-27	27.5
gt032126	-	2006-10-27	27.5
gt032168	-	2006-11-11	27.5
gt032183	-	2006-11-14	27.5
gt032190	-	2006-11-14	27.5
gt032209	-	2006-11-16	27.5
gt032214	-	2006-11-16	27.5
gt032219	-	2006-11-16	27.5
gt032221	-	2006-11-16	27.5
gt032223	-	2006-11-16	27.5
gt032225	-	2006-11-16	27.5
gt032230	-	2006-11-17	10.0
gt032233	-	2006-11-17	27.5
gt032236	-	2006-11-17	27.5
gt032238	-	2006-11-17	27.5
gt032240	-	2006-11-17	27.5

---

Continued on next page...

---

<b>ON Run</b>	<b>OFF Run</b>	<b>Date</b>	<b>Exp. Time</b>
		[yyyy-mm-dd]	[min]
gt032243	-	2006-11-17	27.5
gt032245	-	2006-11-17	27.5
gt032248	-	2006-11-18	27.5
gt032254	-	2006-11-18	27.5
gt032256	-	2006-11-18	27.5
gt032258	-	2006-11-18	27.5
gt032260	-	2006-11-18	27.5
gt032264	-	2006-11-18	27.5
gt032271	-	2006-11-19	27.5
gt032273	-	2006-11-19	27.5
gt032275	-	2006-11-19	27.5
gt032277	-	2006-11-19	27.5
gt032279	-	2006-11-19	27.5
gt032282	-	2006-11-19	27.5
gt032284	-	2006-11-19	27.5
gt032286	-	2006-11-19	20.0
gt032289	-	2006-11-20	27.5
gt032293	-	2006-11-20	27.5
gt032298	-	2006-11-20	27.5
gt032304	-	2006-11-21	27.5
gt032308	-	2006-11-21	27.5
gt032313	-	2006-11-21	27.5
gt032317	-	2006-11-21	27.5
gt032321	-	2006-11-21	27.5
gt032324	-	2006-11-22	27.5
gt032333	-	2006-11-22	27.5
gt032335	-	2006-11-22	27.5

---

Continued on next page...

---

<b>ON Run</b>	<b>OFF Run</b>	<b>Date</b>	<b>Exp. Time</b>
		[yyyy-mm-dd]	[min]
gt032342	-	2006-11-22	27.5
gt032346	-	2006-11-23	27.5
gt032348	-	2006-11-23	27.5
gt032357	-	2006-11-23	9.0
gt032360	-	2006-11-23	27.5
gt032364	-	2006-11-23	27.5
gt032366	-	2006-11-23	27.5
gt032369	-	2006-11-24	27.5
gt032375	-	2006-11-25	27.5
gt032378	-	2006-11-25	27.5
gt032380	-	2006-11-25	27.5
gt032387	-	2006-11-25	27.5
gt032404	-	2006-11-27	27.5
gt032406	-	2006-11-27	27.5
gt032413	-	2006-11-28	27.5
gt032429	-	2006-12-11	27.5
gt032433	-	2006-12-11	27.5
gt032438	-	2006-12-12	27.5
gt032443	-	2006-12-12	27.5
gt032450	-	2006-12-13	27.5
gt032457	-	2006-12-13	27.5
gt032469	-	2006-12-14	27.5
gt032474	-	2006-12-14	27.5
gt032476	-	2006-12-14	27.5
gt032485	-	2006-12-15	27.5
gt032490	-	2006-12-15	27.5
gt032500	-	2006-12-16	27.5

---

Continued on next page...

---

<b>ON Run</b>	<b>OFF Run</b>	<b>Date</b>	<b>Exp. Time</b>
		[yyyy-mm-dd]	[min]
gt032502	-	2006-12-16	27.5
gt032504	-	2006-12-16	27.5
gt032506	-	2006-12-16	27.5
gt032509	-	2006-12-16	27.5
gt032517	-	2006-12-21	27.5
gt032519	-	2006-12-21	27.5
gt032522	-	2006-12-21	27.5
gt032525	-	2006-12-21	27.5
gt032530	-	2006-12-21	27.5
gt032540	-	2006-12-22	8.5
gt032549	-	2006-12-22	18.0
gt032560	-	2007-01-08	27.5
gt032567	-	2007-01-09	27.5
gt032569	-	2007-01-09	13.0
gt032572	-	2007-01-09	27.5
gt032577	-	2007-01-10	27.5
gt032581	-	2007-01-10	27.5
gt032589	-	2007-01-15	27.5
gt032591	-	2007-01-15	18.0
gt032593	-	2007-01-15	27.5
gt032595	-	2007-01-15	27.5
gt032597	-	2007-01-15	27.5
gt032600	-	2007-01-15	27.5
gt032616	-	2007-01-16	27.5
gt032618	-	2007-01-16	27.5
gt032624	-	2007-01-16	27.5
gt032635	-	2007-01-17	27.5

---

Continued on next page...

---

<b>ON Run</b>	<b>OFF Run</b>	<b>Date</b>	<b>Exp. Time</b>
		[yyyy-mm-dd]	[min]
gt032637	-	2007-01-17	27.5
gt032639	-	2007-01-17	27.5
gt032647	-	2007-01-17	27.5
gt032659	-	2007-01-24	27.5
gt032665	-	2007-01-27	27.5
gt032676	-	2007-02-07	27.5
gt032713	-	2007-02-13	27.5
gt032719	-	2007-02-16	27.5
gt032722	-	2007-02-16	27.5
gt032729	-	2007-02-16	27.5
gt032741	-	2007-02-17	27.5
gt032746	-	2007-02-17	27.5
gt032754	-	2007-02-17	27.5
gt032761	-	2007-02-18	27.5
gt032778	-	2007-02-19	18.0
gt032798	-	2007-02-21	27.5
gt032802	-	2007-02-21	27.5
gt032822	-	2007-02-23	27.5
gt032833	-	2007-03-09	27.5
gt032850	-	2007-03-12	27.5
gt032852	-	2007-03-12	27.5
gt032856	-	2007-03-12	25.0
gt032867	-	2007-03-13	27.5
gt032872	-	2007-03-13	27.5
gt032877	-	2007-03-13	20.0
gt032879	-	2007-03-14	27.5
gt032883	-	2007-03-14	27.5

---

Continued on next page...

---

<b>ON Run</b>	<b>OFF Run</b>	<b>Date</b>	<b>Exp. Time</b>
		[yyyy-mm-dd]	[min]
gt032888	-	2007-03-14	27.5
gt032893	-	2007-03-14	27.5
gt032895	-	2007-03-15	27.5
gt032899	-	2007-03-15	27.5
gt032909	-	2007-03-15	27.5
gt032914	-	2007-03-16	27.5
gt032924	-	2007-03-16	27.5
gt032928	-	2007-03-16	27.5
gt032932	-	2007-03-16	27.5
gt032940	-	2007-03-17	12.5
gt032975	-	2007-03-20	27.5
gt032982	-	2007-03-20	27.5
gt033000	-	2007-03-25	27.5
gt033003	-	2007-03-25	27.5
gt033010	-	2007-03-26	27.5
gt033018	-	2007-04-08	27.5
gt033025	-	2007-04-11	27.5
gt033032	-	2007-04-11	27.5
gt033039	-	2007-04-12	10.5
gt033053	-	2007-04-14	27.5
gt033055	-	2007-04-14	27.5
gt033063	-	2007-04-14	27.5
gt033066	-	2007-04-14	21.0
gt033071	-	2007-04-15	27.5
gt033073	-	2007-04-15	27.5
gt033079	-	2007-04-15	27.5
gt033084	-	2007-04-15	27.5

---

Continued on next page...

---

<b>ON Run</b>	<b>OFF Run</b>	<b>Date</b>	<b>Exp. Time</b>
		[yyyy-mm-dd]	[min]
gt033089	-	2007-04-16	27.5
gt033093	-	2007-04-16	27.5
gt033096	-	2007-04-16	27.5
gt033117	-	2007-04-18	27.5
gt033131	-	2007-04-19	27.5
gt033140	-	2007-04-20	14.5
gt033145	-	2007-04-20	27.5
gt033153	-	2007-04-22	15.0
gt033163	-	2007-04-23	27.5
gt033178	-	2007-05-07	27.5
gt033185	-	2007-05-08	27.5
gt033193	-	2007-05-09	27.5
gt033198	-	2007-05-10	27.5
gt033206	-	2007-05-10	27.5
gt033212	-	2007-05-11	27.5
gt033216	-	2007-05-11	27.5
gt033219	-	2007-05-11	27.5
gt033230	-	2007-05-12	27.5
gt033242	-	2007-05-13	27.5
gt033265	-	2007-05-16	27.5
gt033276	-	2007-05-16	27.5
gt033288	-	2007-05-17	11.5
gt033293	-	2007-05-18	10.0
gt033301	-	2007-05-18	27.5
gt033307	-	2007-05-19	27.5
gt033311	-	2007-05-19	27.5
gt033361	-	2007-06-06	27.5

---

Continued on next page...

---

ON Run	OFF Run	Date	Exp. Time
		[yyyy-mm-dd]	[min]
gt033377	-	2007-06-08	27.5
gt033380	-	2007-06-08	27.5
gt033385	-	2007-06-09	27.5
gt033389	-	2007-06-09	27.5
gt033425	-	2007-06-13	27.5
gt033430	-	2007-06-13	27.5
gt033438	-	2007-06-14	27.5
gt033442	-	2007-06-14	27.5
gt033447	-	2007-06-14	27.5
gt033452	-	2007-06-15	27.5
gt033456	-	2007-06-15	27.5
gt033462	-	2007-06-15	27.5
gt033475	-	2007-06-17	27.5
gt033478	-	2007-06-17	27.5
gt033483	-	2007-06-17	23.0
gt033488	-	2007-06-18	27.5
gt033491	-	2007-06-18	27.5
gt033495	-	2007-06-18	27.5
gt033505	-	2007-06-19	27.5
gt033520	-	2007-06-21	27.5
gt033523	-	2007-06-21	27.5
gt033528	-	2007-06-22	16.0
gt033536	-	2007-06-23	16.0

---

**Table A.7:** Darkfield data used to calculate the 2006-07 tracking ratio.

---

# Bibliography

- Abdo, A. A. *et al.*: 2007, *Astrophys. J. Lett.*, **664**, L91
- Abraham, J. *et al.*: 2007, *Science*, **318**, 938
- Abraham, J. *et al.*: 2008, *Astropart. Phys.*, **29**, 188
- Acciari, V. A. *et al.*: 2008a, *Astrophys. J.*, **679**, 397
- Acciari, V. A. *et al.*: 2008b, *Astrophys. J.*, **679**, 1427
- Aharonian, F. *et al.*: 2001a, *Astronomy and Astrophysics*, **370**, 112
- Aharonian, F. *et al.*: 2001b, *Astrophys. J.*, **546**, 898
- Aharonian, F. *et al.*: 2002a, *Astronomy and Astrophysics*, **393**, L37
- Aharonian, F. *et al.*: 2002b, *Astronomy and Astrophysics*, **384**, L23
- Aharonian, F. *et al.*: 2002c, *Astronomy and Astrophysics*, **393**, 89
- Aharonian, F. *et al.*: 2003a, *Astronomy and Astrophysics*, **406**, L9
- Aharonian, F. *et al.*: 2003b, *Astronomy and Astrophysics*, **403**, L1
- Aharonian, F. *et al.*: 2004a, *Astronomy and Astrophysics*, **421**, 529
- Aharonian, F. *et al.*: 2004b, *Astrophys. J.*, **614**, 897
- Aharonian, F. *et al.*: 2004c, *Astronomy and Astrophysics*, **425**, L13
- Aharonian, F. *et al.*: 2005a, *Science*, **307**, 1938

## BIBLIOGRAPHY

---

- Aharonian, F. *et al.*: 2005b, *Astronomy and Astrophysics*, **442**, 1
- Aharonian, F. *et al.*: 2005c, *Science*, **309**, 746
- Aharonian, F. *et al.*: 2005d, *Astronomy and Astrophysics*, **436**, L17
- Aharonian, F. *et al.*: 2005e, *Astronomy and Astrophysics*, **430**, 865
- Aharonian, F. *et al.*: 2005f, *Astronomy and Astrophysics*, **439**, 1013
- Aharonian, F. *et al.*: 2005g, *Astronomy and Astrophysics*, **431**, 197
- Aharonian, F. *et al.*: 2006a, *Astronomy and Astrophysics*, **460**, 743
- Aharonian, F. *et al.*: 2006b, *Astronomy and Astrophysics*, **449**, 223
- Aharonian, F. *et al.*: 2006c, *Nature*, **440**, 1018
- Aharonian, F. *et al.*: 2006d, *Astronomy and Astrophysics*, **455**, 461
- Aharonian, F. *et al.*: 2006e, *Astronomy and Astrophysics*, **448**, L19
- Aharonian, F. *et al.*: 2006f, *Astrophys. J.*, **636**, 777
- Aharonian, F. *et al.*: 2007a, *Astrophys. J. Lett.*, **664**, L71
- Aharonian, F. *et al.*: 2007b, *Astronomy and Astrophysics*, **472**, 489
- Aharonian, F. *et al.*: 2007c, *Astronomy and Astrophysics*, **473**, L25
- Aharonian, F. *et al.*: 2007d, *Astrophys. J.*, **661**, 236
- Aharonian, F. *et al.*: 2007e, *Astronomy and Astrophysics*, **475**, L9
- Aharonian, F. *et al.*: 2007f, *Astronomy and Astrophysics*, **466**, 543
- Aharonian, F. *et al.*: 2008a, *Astronomy and Astrophysics*, **484**, 435
- Aharonian, F. *et al.*: 2008b, *Astrophys. J.*, **In Press**
- Aharonian, F. *et al.*: 2008c, *Astronomy and Astrophysics*, **477**, 353

## BIBLIOGRAPHY

---

- Aharonian, F. A.: 2000, *New Astronomy*, **5**, 377
- Aharonian, F. A. *et al.*: 1999a, *Astronomy and Astrophysics*, **342**, 69
- Aharonian, F. A. *et al.*: 1999b, *Astronomy and Astrophysics*, **349**, 11
- Aharonian, F. A. *et al.*: 2004d, *Nature*, **432**, 75
- Aharonian, F. A. *et al.*: 2007g, *Astronomy and Astrophysics*, **469**, L1
- Aielli, G. *et al.*: 2007, *Nucl. Phys. B Supl.*, **166**, 96
- Albert, J. *et al.*: 2006a, *Astrophys. J. Lett.*, **642**, L119
- Albert, J. *et al.*: 2006b, *Astrophys. J. Lett.*, **648**, L105
- Albert, J. *et al.*: 2006c, *Astrophys. J. Lett.*, **638**, L101
- Albert, J. *et al.*: 2006d, *Astrophys. J.*, **639**, 761
- Albert, J. *et al.*: 2006e, *Science*, **312**, 1771
- Albert, J. *et al.*: 2007a, *Astrophys. J. Lett.*, **666**, L17
- Albert, J. *et al.*: 2007b, *Astrophys. J. Lett.*, **667**, L21
- Albert, J. *et al.*: 2007c, *Astrophys. J.*, **662**, 892
- Albert, J. *et al.*: 2007d, *Astronomy and Astrophysics*, **474**, 937
- Albert, J. *et al.*: 2007e, *Astrophys. J.*, **663**, 125
- Albert, J. *et al.*: 2007f, *Astrophys. J.*, **669**, 862
- Albert, J. *et al.*: 2008, *Astrophys. J. Lett.*, **675**, L25
- Aliu, E. *et al.*: 2008, *Science*, **322**, 1221
- Amenomori, M. *et al.*: 2000, *Phys. Rev. D*, **62**, **11**, 112002
- Amenomori, M. *et al.*: 2003, *Astrophys. J.*, **598**, 242

## BIBLIOGRAPHY

---

- Amenomori, M. *et al.*: 2005, *Astrophys. J.*, **633**, 1005
- Arbeiter, C., Pohl, M. & Schlickeiser, R.: 2002, *Astronomy and Astrophysics*, **386**, 415
- Atkins, R. *et al.*: 2003, *Astrophys. J.*, **595**, 803
- Badran, H. M. & Weekes, T. C.: 2001, Proc. 29th Int Cosmic Ray Conf., Pune, volume 7, 2892
- Bailer-Jones, C. A. L. & Mundt, R.: 2001, *Astronomy and Astrophysics*, **367**, 218
- Baixeras, C. *et al.*: 2005, Proc 29th Int. Cosmic Ray Conf., Pune, volume 5, 227
- Beckmann, V. *et al.*: 2002, *Astronomy and Astrophysics*, **383**, 410
- Bednarek, W.: 1998, *Astronomy and Astrophysics*, **336**, 123
- Beilicke, M.: 2007, *Astrophysics. Space Sci.*, **309**, 139
- Beilicke, M. *et al.*: 2007, American Institute of Physics Conference Series, volume 921, 147–149
- Bell, A. R.: 1978, *Mon. Not. R. Astr. Soc.*, **182**, 147
- Bhat, P. N. *et al.*: 2000, *Bulletin of the Astronomical Society of India*, **28**, 455
- Blandford, R. D. & Levinson, A.: 1995, *Astrophys. J.*, **441**, 79
- Blandford, R. D. & Ostriker, J. P.: 1978, *Astrophys. J. Lett.*, **221**, L29
- Blandford, R. D. & Rees, M. J.: 1978, Proc. Pittsburgh Conf. on BL Lac Objects, 328–341
- Błażejowski, M. *et al.*: 2005, *Astrophys. J.*, **630**, 130

## BIBLIOGRAPHY

---

- Bloom, S. D. & Marscher, A. P.: 1996, *Astrophys. J.*, **461**, 657
- Bloom, S. D. *et al.*: 1997, *Astrophys. J. Lett.*, **490**, L145
- Boone, L. M. *et al.*: 2002, *Astrophys. J. Lett.*, **579**, L5
- Bosch-Ramon, V. *et al.*: 2007, *Astronomy and Astrophysics*, **473**, 545
- Böttcher, M.: 2002, *Bulletin of the Astronomical Society of India*, **30**, 115
- Böttcher, M., Mukherjee, R. & Reimer, A.: 2002, *Astrophys. J.*, **581**, 143
- Böttcher, M. *et al.*: 2003, *Astrophys. J.*, **596**, 847
- Bradbury, S. M. & Rose, H. J.: 2002, *Nucl. Instrum. Methods A*, **481**, 521
- Bradbury, S. M. *et al.*: 1997, *Astronomy and Astrophysics*, **320**, L5
- Buckley, J. H. *et al.*: 1996, *Astrophys. J. Lett.*, **472**, L9+
- Carrigan, S. *et al.*: 2007, Proc. 30th Int. Cosmic Ray Conference, Merida, volume In Press
- Carson, J.: 2007, *J. Phys. Conf. Ser.*, **60**, 115
- Casares, J. *et al.*: 2005, *Mon. Not. R. Astr. Soc.*, **364**, 899
- Catanese, M. & Weekes, T. C.: 1999, *Publ. Astr. Soc. Pacific*, **111**, 1193
- Catanese, M. *et al.*: 1995, Proc. Int. Workshop Towards a Major Cherenkov Detector IV, Padua, 335
- Catanese, M. *et al.*: 1997, *Astrophys. J. Lett.*, **487**, L143
- Catanese, M. *et al.*: 1998, *Astrophys. J.*, **501**, 616

## BIBLIOGRAPHY

---

- Cawley, M. F.: 1993, Towards a Major Atmospheric Cherenkov Detector II for TeV Astro/Particle Physics, 176
- Celik, O. *et al.*: 2007, Proc. 30th Int. Cosmic Ray Conf., Merida, volume In Press
- Chadwick, P. M. *et al.*: 1998, *Astrophys. J.*, **503**, 391
- Chadwick, P. M. *et al.*: 1999, *Astropart. Phys.*, **11**, 145
- Cocconi, G.: 1959, Proc. 6th Int. Cosmic Ray Conf., Moscow, volume 2, 309
- Cranshaw, T. E.: 1963, Cosmic Rays, Clarendon Press
- Daniel, M. K. *et al.*: 2005, *Astrophys. J.*, **621**, 181
- Dar, A. & Laor, A.: 1997, *Astrophys. J. Lett.*, **478**, L5
- Davies, J. M. & Cotton, E. S.: 1957, *Solar Energy Sci. Eng.*, **1**, 16
- de Naurois, M.: 2007, *Astrophysics. Space Sci.*, **309**, 277
- Dermer, C. D.: 1995, *Astrophys. J. Lett.*, **446**, L63
- Dermer, C. D. & Schlickeiser, R.: 1993, *Astrophys. J.*, **416**, 458
- Dermer, C. D., Sturmer, S. J. & Schlickeiser, R.: 1997, *Astrophys. J. Suppl.*, **109**, 103
- Dingus, B. L.: 2007, The First GLAST Symposium, volume 921 of *AIP Conference Series*, 438–439
- Djannati-Atai, A. *et al.*: 1999, *Astronomy and Astrophysics*, **350**, 17
- Djannati-Ataï, A. *et al.*: 2002, *Astronomy and Astrophysics*, **391**, L25
- Djannati-atai, A. *et al.*: 2007a, Proc. 30th Int. Cosmic Ray Conf., Merida, volume In Press

## BIBLIOGRAPHY

---

- Djannati-atai, A. *et al.*: 2007b, Proc. 30th Int. Cosmic Ray Conf., Merida, volume In Press
- Döring, M. *et al.*: 2001, Proc. 27<sup>th</sup> Int. Cosmic Ray Conf., Hamburg, volume 1, 2985
- Doroshenko, V. T. *et al.*: 2007, *Astrophysics*, **50**, 40
- Drury, L. O., Markiewicz, W. J. & Voelk, H. J.: 1989, *Astronomy and Astrophysics*, **225**, 179
- Dunlea, S.: 2001, Ph.D. thesis, University College Dublin (unpublished)
- Edelson, R. *et al.*: 1995, *Astrophys. J.*, **438**, 120
- Edelson, R. *et al.*: 2002, *Astrophys. J.*, **568**, 610
- Edelson, R. A. & Krolik, J. H.: 1988, *Astrophys. J.*, **333**, 646
- Edelson, R. A., Krolik, J. H. & Pike, G. F.: 1990, *Astrophys. J.*, **359**, 86
- Falcone, A. D., Cui, W. & Finley, J. P.: 2004a, *Astrophys. J.*, **601**, 165
- Falcone, A. D. *et al.*: 2004b, *Astrophys. J.*, **613**, 710
- Fazio, G. G. *et al.*: 1968, *Canadian J. Phys.*, **46**, 451
- Fegan, D.: 1997, *J. Phys. G (Nucl. Phys.)*, **23**, 1013
- Feroci, M. *et al.*: 2007, *Nucl. Instrum. Methods A*, **581**, 728
- Fiorucci, M., Tosti, G. & Rizzi, N.: 1998, *Publ. Astr. Soc. Pacific*, **110**, 105
- Fossati, G. *et al.*: 1998, *Mon. Not. R. Astr. Soc.*, **299**, 433
- Fossati, G. *et al.*: 2000, *Astrophys. J.*, **541**, 153
- Fossati, G. *et al.*: 2008, *Astrophys. J.*, **677**, 906

## BIBLIOGRAPHY

---

- Fukugita, M. *et al.*: 1996, *Astron. J.*, **111**, 1748
- Gaidos, J. A. *et al.*: 1996, *Nature*, **383**, 319
- Gaisser, T. K.: 1990, *Cosmic Rays and Particle Physics*, Cambridge University Press, 1990
- Ghisellini, G.: 1999, *Astropart. Phys.*, **11**, 11
- Ghisellini, G. & Maraschi, L.: 1989, *Astrophys. J.*, **340**, 181
- Ghisellini, G., Maraschi, L. & Dondi, L.: 1996, *Astron. Astrophys. Suppl. Ser.*, **120**, C503
- Ghosh, K. K. *et al.*: 2000, *Astrophys. J. Suppl.*, **127**, 11
- Giebels, B. *et al.*: 2002, *Astrophys. J.*, **571**, 763
- Ginzburg, V. L. & Syrovatskii, S. I.: 1965, *Ann. Rev. Astron. Astrophys.*, **3**, 297
- Ginzburg, V. L. & Syrovatskii, S. I.: 1969, *Ann. Rev. Astron. Astrophys.*, **7**, 375
- Giommi, P., Padovani, P. & Perlman, E.: 2000, *Mon. Not. R. Astr. Soc.*, **317**, 743
- Giommi, P. *et al.*: 2001, *Blazar Demographics and Physics*, volume 227 of *ASP Conf. Series*, 227
- Giroletti, M. *et al.*: 2004, *Astrophys. J.*, **600**, 127
- Gliozzi, M. *et al.*: 2006, *Astrophys. J.*, **646**, 61
- Gregory, P. C. & Taylor, A. R.: 1978, *Nature*, **272**, 704
- Grube, J.: 2007, Ph.D. thesis, University of Leeds (unpublished)
- Gupta, A. C. *et al.*: 2008, *New Astronomy*, **13**, 375

## BIBLIOGRAPHY

---

- Gutierrez, K. *et al.*: 2006, *Astrophys. J.*, **644**, 742
- Hanna, D. *et al.*: 2008, *Nucl. Instrum. Methods A*, **588**, 26
- Harrison, F. A. *et al.*: 2000, *Astrophys. J.*, **528**, 454
- Hartman, R. C. *et al.*: 1999, *Astrophys. J. Suppl.*, **123**, 79
- Hayashida, N. *et al.*: 1998, *Astrophys. J. Lett.*, **504**, L71
- Heidt, J. & Wagner, S. J.: 1996, *Astronomy and Astrophysics*, **305**, 42
- Helene, O.: 1983, *Nucl. Instrum. Methods A*, **212**, 319
- Hillas, A. M.: 1985, Proc. 19<sup>th</sup> Int. Cosmic Ray Conf., La Jolla, volume 3, 445–448
- Hillas, A. M.: 1996, *Space Sci. Rev.*, **75**, 17
- Hillas, A. M. *et al.*: 1998, *Astrophys. J.*, **503**, 744
- Hinton, J.: 2007, Proc. 30th Int. Cosmic Ray Conf., Merida, volume In Press
- Hinton, J. *et al.*: 2007, Proc. 30th Int. Cosmic Ray Conf., Merida, volume In Press
- Hoffman, C. M. *et al.*: 1999, *Reviews of Modern Physics*, **71**, 897
- Holder, J. *et al.*: 2003, *Astrophys. J. Lett.*, **583**, L9
- Holder, J. *et al.*: 2006, *Astropart. Phys.*, **25**, 391
- Holt, S., Neff, S. G. & Urry, C. M.: 1992, Testing the AGN Paradigm, Springer Verlag
- Holt, S. S. *et al.*: 1980, *Astrophys. J. Lett.*, **241**, L13
- Hoppe, S. *et al.*: 2007, Proc. 30th Int. Cosmic Ray Conf., Merida, volume In Press

## BIBLIOGRAPHY

---

- Horan, D.: 2007, Proc. AAS/AAPT Joint Meeting, volume 209, 109.09
- Horan, D. *et al.*: 2002, *Astrophys. J.*, **571**, 753
- Horan, D. *et al.*: 2004, *Astrophys. J.*, **603**, 51
- Horan, D. *et al.*: 2007, *Astrophys. J.*, **655**, 396
- Horan, D. *et al.*: 2009, Submitted to *Astrophys. J.*, **In Press**
- Horns *et al.*, D.: 2007, *J. Phys. Conf. Ser.*, **60**, 119
- Hughes, P. A., Aller, H. D. & Aller, M. F.: 1992, *Astrophys. J.*, **396**, 469
- Jang, M. & Miller, H. R.: 1997, *Astron. J.*, **114**, 565
- Jelley, J. V.: 1958, Cherenkov Radiation, New York: Pergamon
- Jones, T. W., O'dell, S. L. & Stein, W. A.: 1974, *Astrophys. J.*, **188**, 353
- Kataoka, J. *et al.*: 2001, *Astrophys. J.*, **560**, 659
- Kerrick, A. D.: 1994, *IAU Circular*, **5996**, 1
- Kerschhaggl, M. *et al.*: 2007, Proc. 30th Int. Cosmic Ray Conf., Merida, volume In Press
- Kildea, J.: 2007, The First GLAST Symposium, volume 921 of *AIP Conference Series*, 339–340
- Kildea, J. *et al.*: 2007, *Astropart. Phys.*, **28**, 182
- Klebesadel, R. W., Strong, I. B. & Olson, R. A.: 1973, *Astrophys. J. Lett.*, **182**, L85
- Konigl, A.: 1981, *Astrophys. J.*, **243**, 700
- Konopelko, A.: 1999, Proc. 26th Int. Cosmic Ray Conf., Salt Lake City, volume 3, 426

## BIBLIOGRAPHY

---

- Konopelko, A. *et al.*: 2007, *Astrophys. J.*, **658**, 1062
- Kosack, K. *et al.*: 2004, *Astrophys. J. Lett.*, **608**, L97
- Kosack, K. *et al.*: 2007, Proc. 30th Int. Cosmic Ray Conf., Merida, volume In Press
- Koyama, K. *et al.*: 1995, *Nature*, **378**, 255
- Krawczynski, H. *et al.*: 2004, *Astrophys. J.*, **601**, 151
- Krennrich, F. *et al.*: 2001a, *Astrophys. J. Lett.*, **560**, L45
- Krennrich, F. *et al.*: 2001b, Peak Response Energy of the Whipple Telescope in 2000 and 2001, Whipple Collaboration Internal Communication (unpublished)
- Krennrich, F. *et al.*: 2002, *Astrophys. J. Lett.*, **575**, L9
- Krennrich, F. *et al.*: 2003, Proc. 28th Int. Cosmic Ray Conf., Tsukuba, volume 5, 2603
- Lane, C. *et al.*: 2007, *Astrophys. J. Lett.*, **668**, L163
- Lang, M. J. *et al.*: 2004, *Astronomy and Astrophysics*, **423**, 415
- Latronico, L., Spandre, G. & *et al.*: 2007, *Nucl. Instrum. Methods A*, **581**, 160
- Le Bohec, S. & Holder, J.: 2003, *Astropart. Phys.*, **19**, 221
- Le Bohec, S. *et al.*: 2004, *Astrophys. J.*, **610**, 156
- Lee, V.: 2008, Ph.D. thesis, Washington University in St. Louis (unpublished)
- Lemiere, A. *et al.*: 2007, Proc. Int. Cosmic Ray Conf., Merida, volume In Press

## BIBLIOGRAPHY

---

- Lessard, R. W.: 1999, Supercuts 2000, Whipple Collaboration Internal Memo (unpublished)
- Lessard, R. W. *et al.*: 2001, *Astropart. Phys.*, **15**, 1
- Lewis, D. A.: 1990, *Experim. Astron.*, **1**, 213
- Lynden-Bell, D.: 1969, *Nature*, **223**, 690
- Mannheim, K.: 1993, *Astronomy and Astrophysics*, **269**, 67
- Mannheim, K.: 1998, *Science*, **279**, 684
- Maraschi, L., Ghisellini, G. & Celotti, A.: 1992, *Astrophys. J. Lett.*, **397**, L5
- Markowitz, A. & Edelson, R.: 2001, *Astrophys. J.*, **547**, 684
- Marscher, A. P. & Gear, W. K.: 1985, *Astrophys. J.*, **298**, 114
- Mastichiadis, A. & Kirk, J. G.: 1997, *Astronomy and Astrophysics*, **320**, 19
- Mohanty, G. *et al.*: 1998, *Astropart. Phys.*, **9**, 15
- Moriarty, P. *et al.*: 1997, *Astropart. Phys.*, **7**, 315
- Muraishi, H. *et al.*: 2000, *Astronomy and Astrophysics*, **354**, L57
- Nagai, T. *et al.*: 2003, Proc. 28th Int. Cosmic Ray Conf., Tsukuba, volume 5, 2635
- Nepomuk Otte, A. *et al.*: 2007, Proc. 30th Int. Cosmic Ray Conf., Merida, volume In Press
- Neshpor, I. Y., Kalekin, R. O. & *et al.*: 1995, Proc. 24th Int. Cosmic Ray Conf., Rome, volume 2, 385
- Neshpor, Y. I. *et al.*: 2001, *Astronomy Reports*, **45**, 249

## BIBLIOGRAPHY

---

- Newbold, M.: 2007, Proc APS Four Corners Section/SPS Zone 16 Joint Fall Meeting, Flagstaff, 6
- Nieppola, E., Tornikoski, M. & Valtaoja, E.: 2006, *Astronomy and Astrophysics*, **445**, 441
- Nilsson, K. *et al.*: 1999, *Publ. Astr. Soc. Pacific*, **111**, 1223
- Nishiyama, T.: 1999, Proc. 26th Int. Cosmic Ray Conf., Salt Lake City, volume 3, 370
- Oppenheim, A. V. & Schafer, R. W.: 1975, Digital Signal Processing, Prentice-Hall Inc., 1975
- Padovani, P.: 1999, BL Lac Phenomenon, volume 159 of *Astronomical Society of the Pacific Conference Series*, 339
- Padovani, P.: 2007, *Astrophysics. Space Sci.*, **309**, 63
- Padovani, P. & Giommi, P.: 1995, *Astrophys. J.*, **444**, 567
- Petry, D. *et al.*: 1996, *Astronomy and Astrophysics*, **311**, L13
- Petry, D. *et al.*: 2002, *Astrophys. J.*, **580**, 104
- Pfeffermann, E. & Aschenbach, B.: 1996, Roentgenstrahlung from the Universe, 267–268
- Pian, E. *et al.*: 1998, *Astrophys. J. Lett.*, **492**, L17+
- Piccinotti, G. *et al.*: 1982, *Astrophys. J.*, **253**, 485
- Piner, B. G. & Edwards, P. G.: 2004, *Astrophys. J.*, **600**, 115
- Piran, T.: 1999, *Physics Reports*, **314**, 575
- Piron, F. *et al.*: 2000, GeV-TeV Gamma Ray Astrophysics Workshop: Towards a Major Atmospheric Cherenkov Detector VI, volume 515 of *American Institute of Physics Conference Series*, 113

## BIBLIOGRAPHY

---

- Piron, F. *et al.*: 2001, *Astronomy and Astrophysics*, **374**, 895
- Plaga, R.: 2008, *New Astronomy*, **13**, 73
- Poggiani, R.: 2006, *Astrophysics. Space Sci.*, **306**, 17
- Pohl, M. & Schlickeiser, R.: 2000, *Astronomy and Astrophysics*, **354**, 395
- Popescu, R. *et al.*: 2005, *Serbian Astronomical Journal*, **170**, 123
- Press, W. H. *et al.*: 1992, *Numerical Recipes in C. The Art of Scientific Computing*, Cambridge: University Press, 1992, 2nd ed.
- Punch, M. *et al.*: 1991, Proc. 22<sup>th</sup> Int. Cosmic Ray Conf., Dublin, 464
- Punch, M. *et al.*: 1992, *Nature*, **358**, 477
- Quinn, J.: 1997, Ph.D. thesis, University College Dublin (unpublished)
- Quinn, J. *et al.*: 1996, *Astrophys. J. Lett.*, **456**, L83+
- Quinn, J. *et al.*: 1999, *Astrophys. J.*, **518**, 693
- Ramana Murthy, P. V. & Wolfendale, A. W.: 1993, *Gamma-Ray Astronomy - 2nd Edition*, Cambridge University Press, 1993
- Rebillot, P. F. *et al.*: 2006, *Astrophys. J.*, **641**, 740
- Rees, M. J.: 1966, *Nature*, **211**, 468
- Rees, M. J.: 1967, *Mon. Not. R. Astr. Soc.*, **137**, 429
- Rees, M. J.: 1984, *Ann. Rev. Astron. Astrophys.*, **22**, 471
- Reynolds, P. T. *et al.*: 1993, *Astrophys. J.*, **404**, 206
- Romero, G. E., Cellone, S. A. & Combi, J. A.: 1999, *Astron. Astrophys. Suppl. Ser.*, **135**, 477

## BIBLIOGRAPHY

---

- Rose, J. H., Akerlof, W. C. & et al.: 1995, Proc. 24th Int. Cosmic Ray Conf., Rome, volume 3, 766
- Rosswog, S. & Brüggen, M.: 2007, Introduction to High-Energy Astrophysics, Cambridge University Press
- Rutman, J.: 1978, *IEEE Proc.*, **66**, 1048
- Schmidt, M.: 1963, *Nature*, **197**, 1040
- Schmitt, J. L.: 1968, *Nature*, **218**, 663
- Schroedter, M.: 2002, Proc. Meeting of the High Energy Astrophysics Division of the AAS, Albuquerque, B17.052
- Schroedter, M.: 2004, Ph.D. thesis, University of Arizona (unpublished)
- Schroedter, M. *et al.*: 2005, *Astrophys. J.*, **634**, 947
- Schubnell, M. S.: 1994, Proc. 185th AAS Meeting, volume 26 of *Bulletin of the American Astronomical Society*, 1467
- Sikora, M., Begelman, M. C. & Rees, M. J.: 1994, *Astrophys. J.*, **421**, 153
- Sikora, M. & Madejski, G.: 2001, High Energy Gamma-Ray Astronomy, International Symposium, volume 558 of *American Institute of Physics Conference Series*, 275
- Simonetti, J. H., Cordes, J. M. & Heeschen, D. S.: 1985, *Astrophys. J.*, **296**, 46
- Smith, A. *et al.*: 2007, *Astrophysics. Space Sci.*, **309**, 299
- Smith, D. A. *et al.*: 2006, *Astronomy and Astrophysics*, **459**, 453
- Smith, P. S., Jannuzi, B. T. & Elston, R.: 1991, *Astrophys. J. Suppl.*, **77**, 67

## BIBLIOGRAPHY

---

- Smith et al., A. W.: 2008, *In Prep*.
- Sokolov, A. & Marscher, A. P.: 2005, *Astrophys. J.*, **629**, 52
- Spangler, S. *et al.*: 1989, *Astronomy and Astrophysics*, **209**, 315
- Steinle, H. *et al.*: 2006, *Chinese Astronomy and Astrophysics Supl.*, **6**, 365
- Stickel, M., Fried, J. W. & Kuehr, H.: 1993, *Astron. Astrophys. Suppl. Ser.*, **98**, 393
- Sullivan, G. *et al.*: 2001, Proc. 27th Int. Cosmic Ray Conf., Hamburg, volume 7, 2773
- Superina, G. *et al.*: 2007, Proc. 30th Int. Cosmic Ray Conf., Merida, volume In Press
- Swordy, S.: 2008a, *The Astronomer's Telegram*, **1422**, 1
- Swordy, S.: 2008b, *The Astronomer's Telegram*, **1415**, 1
- Szentgyorgyi, A. H. *et al.*: 2005, Proc. 207th Meeting of the American Astronomical Society, volume 37 of *Bulletin of the American Astronomical Society*, 1339
- Takahashi, T. *et al.*: 1996, *Astrophys. J. Lett.*, **470**, L89+
- Takahashi, T. *et al.*: 2000, *Astrophys. J. Lett.*, **542**, L105
- Tanihata, C. *et al.*: 2001, *Astrophys. J.*, **563**, 569
- Tavani, M. *et al.*: 2006, Space Telescopes and Instrumentation II: Ultraviolet to Gamma Ray, volume 6266 of *Proc. SPIE Conf.*, 3
- Teshima, M.: 2008, *The Astronomer's Telegram*, **1491**, 1
- Teshima, M. *et al.*: 2007, Proc. 30th Int. Cosmic Ray Conf., Merida, volume In Press

## BIBLIOGRAPHY

---

- Tody, D.: 1986, Instrumentation in Astronomy VI, Tucson, volume 627 of *Proc. SPIE Conf.*, 733
- Tody, D.: 1993, Astronomical Data Analysis Software and Systems II, volume 52 of *Astronomical Society of the Pacific Conference Series*, 173
- Toner, J. A. *et al.*: 2007, Proc. 30<sup>th</sup> Int. Cosmic Ray Conf., Merida, volume In Press
- Tsuchiya, K. *et al.*: 2004, *Astrophys. J. Lett.*, **606**, L115
- Urry, C.: 2004, AGN Physics with the Sloan Digital Sky Survey, volume 311 of *Astronomical Society of the Pacific Conference Series*, 49
- Urry, C. M. & Padovani, P.: 1995, *Publ. Astr. Soc. Pacific*, **107**, 803
- Valdes, F. G.: 1998, Astronomical Data Analysis Software and Systems VII, volume 145 of *Astronomical Society of the Pacific Conference Series*, 53
- Vaughan, S. *et al.*: 2003, *Mon. Not. R. Astr. Soc.*, **345**, 1271
- Villata, M. *et al.*: 1998, *Astron. Astrophys. Suppl. Ser.*, **130**, 305
- Villata, M. *et al.*: 2000, *Astron. Astrophys. Suppl. Ser.*, **144**, 481
- Wagner, S. J.: 1996, *Astron. Astrophys. Suppl. Ser.*, **120**, C495
- Wagner, S. J. *et al.*: 1995, *Astronomy and Astrophysics*, **298**, 688
- Weedman, D. W.: 1986, Quasar Astronomy, Cambridge and New York, Cambridge University Press, 1986
- Weekes, T. C.: 1988, *Physics Reports*, **160**, 1
- Weekes, T. C.: 2000, GeV-TeV Gamma Ray Astrophysics Workshop: Towards a Major Atmospheric Cherenkov Detector VI, volume 515 of *American Institute of Physics Conference Series*, 3

## BIBLIOGRAPHY

---

- Weekes, T. C.: 2003, *Very High Energy Gamma-Ray Astronomy*, The Institute of Physics Publishing, 2003
- Weekes, T. C. & Turver, K. E.: 1977, *Recent Advances in Gamma-Ray Astronomy*, volume 124 of *ESA Special Publication*, 279–286
- Weekes, T. C. *et al.*: 1989, *Astrophys. J.*, **342**, 379
- Welsh, W. F.: 1999, *Publ. Astr. Soc. Pacific*, **111**, 1347
- Zhang, Y. H. *et al.*: 2002, *Astrophys. J.*, **572**, 762
- Zhang, Y. H. *et al.*: 2005, *Astrophys. J.*, **629**, 686